Towards an integrated approach for the development of architectured materials

Justin Dirrenberger

Sorbonne Université
UFR 919 - Ingénierie

Mémoire d'habilitation

en vue de l'obtention de l'habilitation à diriger des recherches

présenté et soutenu publiquement par

Justin DIRRENBERGER

le 18 décembre 2018

Vers une approche intégrée pour le développement des matériaux architecturés

Towards an integrated approach for the development of architectured materials

Jury

Véronique AUBIN, Professeur, CentraleSupélec	Rapporteur
Jean-François CARON, Directeur de recherche, ENPC	Rapporteur
Damien FABREGUE, Professeur, INSA Lyon	Rapporteur
Jean-Pierre CHEVALIER, Professeur, CNAM	Examinateur
Hélène DUMONTET, Professeur, Sorbonne Université	Examinateur
Samuel FOREST, Directeur de recherche, ENSMP	Examinateur

HDR

Contents

List of Notations

Tensors, tensor algebra and operators

x	0^{th}-order tensor (scalar)
$\underline{\boldsymbol{x}}$ or x_i	1^{st}-order tensor (vector)
$\underset{\sim}{\boldsymbol{x}}$ or x_{ij}	2^{nd}-order tensor
$\underset{\approx}{\boldsymbol{x}}$ or x_{ijkl}	4^{th}-order tensor
$\underset{\sim}{\boldsymbol{I}}$ or I_{ij}	2^{nd}-order identity tensor
$\underset{\approx}{\boldsymbol{I}}$ or I_{ijkl}	4^{th}-order identity tensor
$x = \underline{\boldsymbol{a}} \cdot \underline{\boldsymbol{b}}$	$x = a_i b_i$
$\underline{\boldsymbol{x}} = \underset{\sim}{\boldsymbol{a}} \cdot \underline{\boldsymbol{b}}$	$x_i = a_{ij} b_j$
$\underset{\sim}{\boldsymbol{x}} = \underset{\sim}{\boldsymbol{a}} \cdot \underset{\sim}{\boldsymbol{b}}$	$x_{ij} = a_{ik} b_{kj}$
$x = \underset{\sim}{\boldsymbol{a}} : \underset{\sim}{\boldsymbol{b}}$	$x = a_{ij} b_{ij}$
$\underset{\sim}{\boldsymbol{x}} = \underset{\approx}{\boldsymbol{a}} : \underset{\sim}{\boldsymbol{b}}$	$x_{ij} = a_{ijkl} b_{kl}$
$x = \underset{\approx}{\boldsymbol{a}} :: \underset{\approx}{\boldsymbol{b}}$	$x = a_{ijkl} b_{ijkl}$
$\underset{\sim}{\boldsymbol{x}} = \underline{\boldsymbol{a}} \otimes \underline{\boldsymbol{b}}$	$x_{ij} = a_j b_j$
$\underset{\sim}{\boldsymbol{x}} = \underline{\boldsymbol{a}} \overset{s}{\otimes} \underline{\boldsymbol{b}} = \frac{1}{2}\left(\underline{\boldsymbol{a}} \otimes \underline{\boldsymbol{b}} + \left(\underline{\boldsymbol{a}} \otimes \underline{\boldsymbol{b}}\right)^T\right)$	$x_{(ij)} = \frac{1}{2}\left(a_i b_j + a_j b_i\right)$
$\underset{\approx}{\boldsymbol{x}} = \underset{\sim}{\boldsymbol{a}} \otimes \underset{\sim}{\boldsymbol{b}}$	$x_{ijkl} = a_{ij} b_{kl}$
δ_{ij}	Kronecker symbol
$\left\|\left\|\underline{\boldsymbol{x}}\right\|\right\|$	Euclidean norm of a vector
$I_1(\underset{\sim}{\boldsymbol{x}})$ or $\mathrm{Tr}\,\underset{\sim}{\boldsymbol{x}}$ or x_{ii}	1^{st} invariant of a tensor (trace)
$I_2(\underset{\sim}{\boldsymbol{x}})$ or $\frac{1}{2}\left(\left(\mathrm{Tr}\,\underset{\sim}{\boldsymbol{x}}\right)^2 - \mathrm{Tr}\left(\underset{\sim}{\boldsymbol{x}}^2\right)\right)$	2^{nd} invariant of a tensor
$I_3(\underset{\sim}{\boldsymbol{x}})$ or $\mathrm{Det}\,\underset{\sim}{\boldsymbol{x}}$	3^{rd} invariant of a tensor (determinant)
$\underset{\sim}{\boldsymbol{x}}^{-1}$	Inverse of an invertible tensor
$\underset{\sim}{\boldsymbol{x}}^T$	Transpose of a tensor
$\mathrm{Div}\,\underset{\sim}{\boldsymbol{x}}$ or $\nabla \cdot \underset{\sim}{\boldsymbol{x}}$ or $x_{ij,j}$	Divergence of a tensor
$\nabla \underset{\sim}{\boldsymbol{x}}$ or $\nabla \otimes \underset{\sim}{\boldsymbol{x}}$	Gradient of a tensor
$\dot{\underset{\sim}{\boldsymbol{x}}} = \frac{d\underset{\sim}{\boldsymbol{x}}}{dt}$	Time derivative of a tensor
$\underset{\approx}{\boldsymbol{J}}$	Spherical projector for 2^{nd}-order symmetric tensors
$\underset{\approx}{\boldsymbol{K}}$	Deviatoric projector for 2^{nd}-order symmetric tensors

Mechanical tensors

$\mathscr{E}^{el}$	Elastic strain energy density
$\underset{\sim}{\boldsymbol{\sigma}}$ or σ_{ij}	Cauchy stress tensor
$\underset{\sim}{\boldsymbol{\varepsilon}}$ or ε_{ij}	Engineering strain tensor
$\underset{\approx}{\boldsymbol{c}}$ or c_{ijkl} or c_{IJ}	Elastic moduli tensor
$\underset{\approx}{\boldsymbol{s}}$ or s_{ijlk} or s_{IJ}	Compliance tensor
$\underset{\sim}{\boldsymbol{\sigma}}^{\text{sph}} = \frac{1}{3}\left(\text{Tr}\,\underset{\sim}{\boldsymbol{\sigma}}\right)\underset{\sim}{\boldsymbol{I}}$	Spherical stress tensor
$\underset{\sim}{\boldsymbol{\sigma}}^{\text{dev}} = \underset{\sim}{\boldsymbol{\sigma}} - \underset{\sim}{\boldsymbol{\sigma}}^{\text{sph}}$	Deviatoric stress tensor
$\underset{\sim}{\boldsymbol{X}}$	Kinematic hardening tensor
$\underset{\approx}{\boldsymbol{H}}$	Hill tensor
$\underline{\boldsymbol{v}}$	Velocity field
$\underline{\boldsymbol{u}}$	Displacement field
$\underline{\boldsymbol{f}}$	Body forces
$\underline{\boldsymbol{F}}$	Surface forces
E	Young's modulus
μ	Shear modulus
k	Bulk modulus
ν	Poisson's ratio
P_v	Viscoplastic parameter
K	Kinematic viscosity
n	Inverse strain-rate sensitivity
$\dot{e}^{\text{p}}$	Plastic energy rate density
$\tau^{(\text{s})}$	Resolved shear stress on slip system (s)
$\dot{\gamma}$	Viscoplastic slip rate
p	Accumulated plastic strain
$\dot{d}_1$	Intrinsic dissipation power density

Finite element notations

$[x]$	n-dimensional matrix
$\{x\}$	Column-vector
$[N]$	Shape function matrix
$[B]$	Deformation operator
$[K]$	Stiffness matrix

Mathematical morphology

A	Random closed set
A^c	Complementary set of A
$\check{A} = \{-x, x \in A\}$	Transposed set of A
K	Compact set
P	Probability of an event
$p = P\{x \in A\}$	Probability of x to be in A
$q = P\{x \in A^c\} = 1 - p$	Probability of x to be in A^c
$C(h) = P\{x \in A, x + h \in A\}$	Covariance $C(h)$
$Q(h) = P\{x \in A^c, x + h \in A^c\}$	Covariance $Q(h)$
$\overline{W}_2(x, x + h)$	2^{nd} order central correlation function
$A \oplus \check{K}$	Dilation by a compact K
$A \ominus \check{K}$	Erosion by a compact K
$A_K = A \ominus \check{K} \oplus K$	Opening by a compact K
$A^K = A \oplus \check{K} \ominus K$	Closing by a compact K
$\mu(A)$	Measure of A
μ_n	Lebesgue measure in $\mathbb{R}^n$
θ_k	Radon measure on locally compact topological spaces
$\mathscr{L}(A)$	Perimeter of A in $\mathbb{R}^2$
$\mathscr{A}(A)$	Area of A in $\mathbb{R}^2$
$\mathscr{S}(A)$	Area of A in $\mathbb{R}^3$
$\mathscr{V}(A)$	Volume of A
S_S	Surface fraction
V_V	Volume fraction
$Z(x)$	Random function or physical property
$E\{Z(x)\}$	Mathematical expectation of $Z(x)$
D_Z^2	Variance of $Z(x)$
D_Z	Standard deviation of $Z(x)$
$\overline{Z}(V)$	Average value over V of $Z(x)$
A_n	Integral range of dimension n
ϵ_{abs}	Absolute error
ϵ_{rel}	Relative error

Introduction Part I

0 Introduction

Materiam superabat opus

— Ovid, Metamorphoses, II, 5 (I^{st} century A.D.)

0.1 Introduction

The time period that is sanctuarised for writing an *habilitation* thesis is a critical moment in the life of a scientist. Analysing the past in order to shape the future, that is the aim of the present effort. At first, the compilation of works presented in this manuscript might appear quite heterogeneous, rightfully so! Although diverse, the research presented is actually consistent, following its own specific direction. With this document, my main challenge is to summarise six years of reflections, experiences, arbitrary choices, numerous failures and few successes, which are representative of the work conducted until now; but also to propose a research direction that I wish to pursue next. The underlying question supporting most of my work could be simplified as *How does morphology induce functionality within materials and structures?* Narrow-mindedly, one could argue that this question is not relevant for materials science, but rather mechanical design. As a matter of fact, my approach to materials science is transdisciplinary, or cross-fertilised, taking viewpoints and considerations from other academic fields in order to shed new light on a given topic and, from time to time, innovate. I have found that there is an unfathomable excitement about doing scientific research that can be implemented in real-life applications, and am truly humbled to have had the opportunity of working as such on projects with national research institutes and private industrial partners. It is now obvious for the reader that most of my work has been focused on trying to solve applied science problems. Nevertheless, while working on materials engineering, unexpected developments might sometimes arise, calling for an investigation of more fundamental questions. Another comment that could be drawn by looking at my work is the apparent dispersion of efforts due to the multiplicity of topics, which is true to a certain extent, but necessary in the sense that most projects I have been involved with

included research on the processing, characterising, modelling, and designing of engineering materials, each of these topics being dependent on the others. It became clear that only a holistic, systemic approach, *i.e.* encompassing all the aspects of the problem, could allow our research to produce and deliver satisfying answers. Hopefully this manuscript will testify for the relevance of such an approach. As stated in the title of the manuscript, I propose to research further towards an integrated approach for the development of architectured materials.

0.2 A personal brief

A career in scientific research and higher education had not been an obvious path for me until quite recently. Starting out with an apprenticeship, I obtained a technical degree in applied physics, and pursued a *Diplôme d'ingénieur* curriculum in materials science and engineering. Through my studies I had the opportunity to spend 6 months at EPFL in Lausanne, Switzerland, as an intern in the Laboratory of Construction Materials, working on the early-age mechanical properties of white cement. This was my first hands-on experience with research, and my first encounter with microstructural modelling and simulation. Subsequently, I chose to follow a master of science program in parallel of my last year of engineering school in order to enroll for PhD the following year. In this program, I was fortunate enough to meet my PhD advisors. In 2009, after conducting my master's project at Schlumberger, studying the effect of carbonation on the mechanical properties of cementitious materials used for sealing depleted oil reservoirs, I started working on my PhD at Ecole Nationale Supérieure des Mines de Paris. For 3 incredibly formative years, I explored the topics of homogenisation theory, computational methods, microstructural modelling, mathematical morphology, composite materials, additive manufacturing, mechanics of architectured materials, already making connections in-between these fields. In 2012, I defended my thesis on the computational determination of the effective properties of architectured materials. Quickly after that, willing to pursue a career in research without the constraints of private companies, I was recruited at Conservatoire National des Arts et Métiers (Cnam) in Paris as a Maître de Conférences (CNU 33, chimie des matériaux), joining the PIMM laboratory which is a mixed research unit between Arts et Métiers-ParisTech, Cnam, and CNRS. Research at PIMM is much focused on the processing of industrial materials (metals, polymers), induced microstructures, mechanical properties, and durability. When I joined PIMM, alongside classical topics (micromechanics, fatigue, advanced steels...) I started developing my own research topics mainly through external collaborations, firstly on large-scale additive manufacturing, then on the mechanics of architectured chiral metamaterials. Since then, the core of my research activity has evolved towards the design, processing, and modelling of architectured materials.

0.3 Outline

The manuscript is divided into 3 parts: the present introductory part, a scientific overview part, and a conclusion and proposal for future work. The main scientific overview part is made of 3 chapters corresponding to the different spatial scales probed in the works presented. The first

chapter deals with spatial scales typical for materials science, from the nanometre up to one hundred microns approximately, with 2 projects I have been involved in, including one on the processing of nanocomposites, and one on the very high cycle fatigue of metallic materials. The second chapter is dedicated to the millimetre scale, which is characteristic of architectured materials in the sense of [Ashby and Bréchet, 2003]. The chapter will be subdivided into 7 sections concerned with the processing, modelling, and design of architectured materials, which constitutes the core of my research. The third chapter is a summary of the work conducted at the structural or architectural scale, with large-scale additive manufacturing and automation, at PIMM, firstly in collaboration with architects and designers, now with Laboratoire Navier at Ecole des Ponts, and XtreeE, a technological company which I co-founded. All the bibliographical references are gathered at the end of the manuscript.

Scientific overview Part II

1 Microstructural representativity

The infinite variety in the properties of the solid materials we find in the world is really the expression of the infinite variety of the ways in which the atoms and molecules can be tied together, and of the strength of those ties.

— Sir William Henry Bragg, Concerning the Nature of Things (1925)

Materials science comes from the following fact: microstructural heterogeneities play a critical role in the macroscopic behaviour of a material [Besson et al., 2010, Bornert et al., 2001, Jeulin and Ostoja-Starzewski, 2001, François et al., 2012, Torquato, 2001, Ostoja-Starzewski, 2008]. Constitutive modelling, thanks to an interaction between experiments and simulation, is usually able to describe the response of most materials in use. Such phenomenological models, including little to no information about the microstructure, cannot necessarily account for local fluctuation of properties. In this case, the material is considered as a homogeneous medium. Studying the behaviour of heterogeneous materials involves developing enriched models including morphological information about the microstructure [Smith and Torquato, 1988, Yeong and Torquato, 1998, Torquato, 1998, Decker et al., 1998, Jeulin, 2000, Kanit et al., 2006, Peyrega et al., 2011, Jean et al., 2011a, Escoda et al., 2015, Bargmann et al., 2018, Soyarslan et al., 2018]. These models should be robust enough to predict effective properties depending on statistical data (volume fraction, n-point correlation function, etc.) and the physical nature of each phase or constituent. As a matter of fact, advanced models are often restricted to a limited variety of materials. Although isotropic and anisotropic polycrystalline metals, for instance, have been extensively studied by the means of both analytical and computational tools [Cailletaud et al., 2003, Kanit et al., 2003, Madi et al., 2007, Berdin et al., 2013, Fritzen et al., 2013, Benedetti and Barbe, 2013, Hor et al., 2014, Kowalski et al., 2016, Peng et al., 2018], some material configurations (architectured materials, materials with infinite contrast of properties, nanocomposites, materials exhibiting nonlinear behaviour, etc.) call for further development of models and tools for describing their effective behaviour.

1.1 Representative volume element

The question of representativity has been a topic of interest in scientific communities for half a century, especially in the field of materials science, micromechanics and microscopy. Indeed, microstructural heterogeneities play a critical role on the macroscopic physical properties of materials. One common way to account for this underlying complexity is resorting to homogenisation techniques. Most homogenisation approaches, including analytical and computational, require the existence of a representative volume element (RVE). Several definitions have been given for the RVE over the past 50 years. A review of this topic can be found in [Gitman et al., 2007]. The classical definition of RVE is attributed to [Hill, 1963], who stated that for a given material the RVE is a sample that is structurally typical of the whole microstructure, i.e. containing a sufficient number of heterogeneities for the macroscopic properties to be independent of the boundary values of traction and displacement. Later, [Beran, 1968] emphasised the role of statistical homogeneity, especially in a volume-averaged sense. This also means that the RVE size considered should be larger than a certain microstructural length for which moduli fluctuate. [Hashin, 1983] made a review on analysis of composite materials in which he referred to statistical homogeneity as a practical necessity. [Sab, 1992] considered that the classical RVE definition for a heterogeneous medium holds only if the homogenised properties tend towards those of a similar periodic medium. This entails that the response over an RVE should be independent of boundary conditions (BC). From numerical simulations on VEs of various sizes, [Terada et al., 2000] concluded that from a practical viewpoint RVE should be as large as possible. [Ostoja-Starzewski, 2002] considers the RVE to be only defined over a periodic unit-cell or a non-periodic cell containing an infinite number of heterogeneities. [Drugan and Willis, 1996] introduced explicitly the idea of minimising the RVE size, meaning that the RVE would be the smallest material volume for which the apparent and effective properties coincide. Besides, it is worth noticing that for a given material the RVE size for physical property A, *e.g.* thermal conductivity, is *a priori* different from the RVE size for physical property B, *e.g.* elastic moduli. Thus, one has to consider an RVE that depends on the specific investigated property.

Many definitions refer to the separation of scales as a necessary condition for the existence of a RVE. This condition is not always met, *i.e.* with percolating media or materials with microstructural gradient of properties. This separation of scale involves a comparison between different characteristic lengths:

- d, size of microstructural heterogeneities;
- l, size of the RVE considered;
- L, characteristic length of the applied load.

Previous considerations regarding characteristic lengths can be summarised as follows:

$$d \ll l \ll L \tag{1.1}$$

Nevertheless, Inequality 1.1 is a necessary but not sufficient condition for the applicability of homogenisation. As a matter of fact, quasi-uniform loading, *i.e.* $l \ll L$, has to be enforced. Let us consider a measurable property, such as a mechanical strain field. The spatial average of its measured value over a finite volume V converges towards the mathematical expectation of its measured value over a series of samples smaller than V (ensemble average). It is the ergodicity hypothesis. Moreover, ergodicity implies that one sample (or realisation) of volume V contains the statistical information necessary for the description of its microstructure. Also, this entails that heterogeneities are small enough in comparison to the RVE size, *i.e.* $d \ll l$. If and only if these two conditions are met ($d \ll l$ and $l \ll L$), the existence and uniqueness of an equivalent homogeneous medium for both cases of random and periodic materials can be rigorously proven [Sab, 1992]. Homogenisation is therefore possible.

Taking into account these definitions, and assuming ergodicity for the heterogeneous media considered, [Kanit et al., 2003] proposed a method based on a statistical analysis for computing the minimal RVE size for a given physical property $Z(x), \forall x \in V$ and precision in the estimate of effective properties. The computed RVE size was found to be proportional to the integral range [Matheron, 1971], which corresponds to a volume of statistical correlation. For a volume V larger than the integral range, $Z(x)$ is considered as a noncorrelated random variable. This approach was implemented in many papers in order to estimate RVE sizes for morphological, elastic and thermal properties, usually resorting to finite element simulations on periodic unit cells of increasing size [Kanit et al., 2003, Jean et al., 2011a]. The rate of convergence of the mean value for apparent properties, with respect to the size of the considered system, is related to the size of the statistical RVE, *i.e.* a microstructure with slow rate of convergence would yield large RVE sizes.

For non-periodic materials, the problem of representativity of samples can be addressed by means of a probabilistic approach giving size-dependent intervals of confidence, which is a well-known approach used in geostatistics [Matheron, 1971]. The approach presented [Kanit et al., 2003] is based on the scaling effect on the variance of effective properties in simulations of random media. Several assumptions have to be considered regarding the statistics of the microstructures considered.

Ergodicity hypothesis The ergodicity hypothesis is fulfilled for a property or a random function Z when the statistical properties of its measured value (mathematical expectation, variance, etc.) over a finite volume V (spatial average) converge to those estimated over series of independent samples smaller than V (ensemble average), when the volume V goes to infinity. Ergodicity implies that one realisation of a volume $V \geq V_{\mathrm{RVE}}$ contains all the statistical information necessary to the description of its microstructure.

Stationarity hypothesis The stationarity hypothesis is assumed for a property or a random function Z when its mathematical expectation is constant with respect to time and space.

Statistical homogeneity hypothesis A random structure is considered statistically homogeneous, when it is stationary, which means that its probabilistic properties are invariant by translation.

1.1.1 RVE size determination for media with finite integral range

Let us consider a microstructure that fulfills the ergodicity and stationarity conditions for a given physical quantity $Z(x)$ regarded as a random function with average $E\{Z(x)\}$ and point variance D_Z^2. The ensemble variance $D_Z^2(V)$ of its average value $\overline{Z}(V)$ over the domain Ω with volume V can be obtained using the centered second-order correlation function $\overline{W}_2$ in this way:

$$D_Z^2(V) = \frac{1}{V}\iint_\Omega \overline{W}_2(x-y)dxdy \tag{1.2}$$

with

$$\overline{W}_2(h) = E\left\{\left(Z(x)-\overline{Z}\right)\left(Z(x+h)-\overline{Z}\right)\right\} \tag{1.3}$$

For determining the RVE size for the physical property Z one can rely on the geostatistical notion of integral range [Matheron, 1975, Lantuéjoul, 1991, Cailletaud et al., 1994, Jeulin, 2001, Jeulin and Ostoja-Starzewski, 2001, Lantuéjoul, 2002]. The integral range A_n is homogeneous to a volume of dimension n in $\mathbb{R}^n$. For $n=3$, the integral range is given by:

$$A_3 = \frac{1}{D_Z^2}\int_{\mathbb{R}^3} \overline{W}_2(h)dh \tag{1.4}$$

The physical interpretation of the integral range is such that for a given volume V, one can define $n = \dfrac{V}{A_3}$ volume elements for which the i average values $Z_i(V')$ over the n sub-volumes $V' = \dfrac{V}{n}$ are uncorrelated random variables. Hence, for a large specimen, *i.e.* $V \gg A_3$, Equation 1.2 can be rewritten introducing the point variance of Z, D_Z^2 as follows:

$$D_Z^2(V) = D_Z^2\frac{A_3}{V} \tag{1.5}$$

Let us analyse this asymptotic relation. First, in general one has no guarantee on the finiteness of point variance D_Z^2 [Matheron, 1971]: let us consider a large domain Ω and a smaller domain $V \subset \Omega$ that is attainable by means of experimentation or computation, one can then compute an experimental variance which is in fact a function of Ω supported by V, that will increase with Ω. If the variance over V is finite, it should be regarded as a limit of the experimental variance for

$\Omega \rightarrow +\infty$. D_Z^2 can be computed over V as follows:

$$\begin{aligned} D_Z^2 &= \frac{1}{V}\int_V \left(Z(x)-\overline{Z}\right)^2 dV \\ &= \frac{1}{V}\int_V Z^2(x)-\overline{Z}^2 dV \\ &= \frac{1}{V}\int_V Z^2(x)dV-\left(\frac{1}{V}\int_V Z(x)dV\right)^2 \end{aligned} \tag{1.6}$$

On the other hand, the ensemble variance $D_Z^2(V')$ is computed from the average values $\overline{Z_i}$ over n sub-volumes:

$$\begin{aligned} D_Z^2(V') &= \frac{1}{n}\sum_{i=1}^{n}\left(Z_i(V')-\overline{Z_i}\right)^2 \\ &= \frac{1}{n}\sum_{i=1}^{n} Z_i^2(V')-\overline{Z_i}^2 \\ &= \frac{1}{n}\sum_{i=1}^{n} Z_i^2(V')-\left(\frac{1}{n}\sum_{i=1}^{n} Z_i(V')\right)^2 \end{aligned} \tag{1.7}$$

Equation 1.7 uses the average value of the average values $\overline{Z_i}$ over n sub-volumes V', which is expected to converge towards the effective property Z_{eff} when $V \rightarrow +\infty$. If Z_{eff} is already known, it might be of interest to use it instead of $\overline{Z_i}$ in order to obtain a better estimate.

If $Z(x)$ is the indicator function of the stationary random set A, then one can obtain analytically the variance of the local volume fraction as a function of the point variance as follows:

$$D_Z^2 = p - p^2 = p(1-p) \tag{1.8}$$

with p, probability for a point x to belong to the random set A, which is equivalent to the volume fraction of A in V.

The asymptotic scaling law given in Equation 1.5 can be used for any additive variable Z over the domain Ω. In the case of elastic properties for instance, average stress $\langle \underset{\sim}{\boldsymbol{\sigma}} \rangle$ or strain $\langle \underset{\sim}{\boldsymbol{\varepsilon}} \rangle$ fields have to be computed. For determining the RVE size for a given property Z, one thus has to know its integral range A_3. There is no theoretical covariance for mechanical fields. However, there are two ways to estimate it; first by assuming that $\overline{Z}$ is equal to the arithmetic average of properties (rule of mixture) for a biphasic medium, hence Equation 1.6 yields:

$$D_Z^2 = p(1-p)\,(Z_1 - Z_2)^2 \tag{1.9}$$

with Z_1 and Z_2, respectively property Z of phase 1 and 2. D_Z^2 can also be estimated computationally on the largest virtual sample available, in order to minimise boundary layer effects and obtain a converged value. The approach proposed by [di Paola, 2010] consists in taking only into account the inner part of the simulation volume. This could present an advantage for determining the point variance.

Once the point variance has been estimated for a given property, the integral range can be obtained using the procedure proposed by [Matheron, 1989] for any random function: consider realisations of domains Ω with an increasing volume V (or non-overlapping sub-domains of large simulations, with a wide range of sizes), the parameter A_3 can be estimated by fitting the obtained variance according to Equation 1.5:

$$\log D_Z^2(V) = \log D_Z^2 + \log A_3 - \log V \tag{1.10}$$

Following the method proposed in [Kanit et al., 2003], itself based on the approach developed in [Cailletaud et al., 1994], considering a large number n of realisations (or sub-volumes), the following sampling error in the estimation of the effective properties arises:

$$\epsilon_{\text{abs}} = \frac{2D_Z(V)}{\sqrt{n}} \tag{1.11}$$

From which the relative error ϵ_{rel} can be defined:

$$\epsilon_{\text{rel}} = \frac{\epsilon_{\text{abs}}}{\overline{Z}} = \frac{2D_Z(V)}{\overline{Z}\sqrt{n}} \Rightarrow \epsilon_{\text{rel}}^2 = \frac{4D_Z^2 A_3}{\overline{Z}^2 nV} \tag{1.12}$$

Hence a volume size that we will consider statistically representative can be defined for a prescribed property Z, number of realisations n and relative error (*e.g.* 5%):

$$V_{\text{RVE}} = \frac{4D_Z^2 A_3}{\epsilon_{\text{rel}}^2 \overline{Z}^2 n} \tag{1.13}$$

This RVE size then depends on the point variance D_Z^2, integral range A_3 and mean value $\overline{Z}$, 3 parameters that are estimated from simulations.

1.1.2 Generalisation of the statistical approach to microstructures with non-finite integral range

The method presented above is now adapted and generalised to the case of media with non-finite integral range, especially Poisson linear varieties and Boolean random models made of Poisson linear varieties, *e.g.* Poisson fibers, which will be used hereafter for modelling non-woven architectured materials. Since the integral range of linear Poisson varieties is not finite [Jeulin, 1991], Equation 1.5 does not apply anymore. It was proposed in [Lantuéjoul, 1991] to

use a modified scaling law with exponent $\gamma \neq 1$. The variance can thus be rewritten as follows [Jeulin, 2011]:

$$D_Z^2(V) = D_Z^2\left(\frac{A_3^*}{V}\right)^\gamma \tag{1.14}$$

which yields by linearization,

$$\log D_Z^2(V) = \log D_Z^2 + \gamma \log A_3^* - \gamma \log V \tag{1.15}$$

A_3^* is not the integral of the centered second-order correlation function $\overline{W}_2(h)$ anymore, as defined before in Equation 1.4. Nonetheless, it is homogeneous to a volume of material and can readily be used to determine RVE sizes which can then be obtained by updating the previous definition for relative error (Eq. 1.12), hence yielding an updated definition of the RVE size:

$$V_{\text{RVE}} = A_3^{*\,\gamma}\sqrt{\frac{4D_Z^2}{\epsilon_{\text{rel}}^2 \overline{Z}^2 n}} \tag{1.16}$$

The generalised integral range A_3^* and scaling-law exponent γ can be estimated from simulations as it was done in [Kanit et al., 2003], [Altendorf et al., 2014] and [Dirrenberger et al., 2014]. When considering statistical RVE sizes of microstructures with non-finite integral range for other properties than morphological ones, for which there is no information about the theoretical value of the point variance D_Z^2, it may be useful to reformulate Equation 1.14 as follows:

$$D_Z^2(V) = KV^{-\gamma} \tag{1.17}$$

with $K = D_Z^2 A_3^{*\gamma}$, leaving only 2 parameters to identify from the statistical data obtained by simulation. The method for determining statistical RVE sizes has been studied and used for media with finite integral range in the references [Kanit et al., 2003, Kanit et al., 2006, Madi et al., 2005, Madi et al., 2007, Pelissou et al., 2009, Jean et al., 2011a, Jean et al., 2011b, Oumarou et al., 2011, Altendorf et al., 2014, Teixeira-Pinto et al., 2016, Bironeau et al., 2016]. This approach is implemented for media with infinite integral range in [Dirrenberger et al., 2014], for the case of Poisson fibers. Similar considerations have been made in [Doškář et al., 2018], but using the SEPUC approach [Zeman and Šejnoha, 2007, Niezgoda et al., 2010].

In most papers, the authors resorted to periodic boundary conditions (PBC) since [Kanit et al., 2003] showed from computational experiments that mean apparent properties obtained with PBC converge faster towards the effective properties than with the Dirichlet and Neumann-type BC. Nevertheless, KUBC and SUBC can be useful since they correspond to the Voigt and Reuss bounds in elasticity. They can thus be used for bounding the effective properties of random architectured materials. If the microstructure features a matrix phase, tighter bounds can be obtained by choosing elementary volumes including only the matrix at the boundary, as

shown in [Salmi et al., 2012a].

1.2 Evaluation of morphological representative sample sizes for nanolayered polymer blends

Although most of the previous works were related to micromechanics of composite materials, in the context of Adrien Bironeau's PhD thesis [Bironeau, 2016, Bironeau et al., 2016, Zhu et al., 2016, Bironeau et al., 2017, Feng et al., 2018], we had the opportunity to study the RVE size for morphological properties of polymer blends in order to optimise functional properties, *e.g.* permeability, optical refraction, etc. In particular, we focused on nanolayered films, in which two different polymers are combined in a nanostratified structure, composed of numerous alternating thin layers. The nanolayer coextrusion is a continuous process capable of producing films at a large scale with up to thousands of layers, thus yielding individual layer thickness down to several nanometres. Originally developed in the 1960s by Dow Chemical, USA (US Patent No. 3239197; [Tollar, 1966]), this process was thoroughly investigated by Baer's group to study nanoscale polymer interactions [Liu et al., 2003] and produce films with unique optical properties [Kazmierczak et al., 2007], as well as enhanced mechanical [Kerns et al., 1999] or gas barrier properties [Wang et al., 2009]. In our laboratory, the process has been recently used to control the architecture at the micro-/nanoscale of multiphase polymer systems, like polymer blends [Boufarguine et al., 2013], nanocomposites [Miquelard-Garnier et al., 2013, Li et al., 2014] or triblock copolymers [Roland et al., 2016]. Since multilayered coextrusion results in materials exhibiting more or less regular microstructures, the development of a characterisation method enabling a full description of the morphological features of multilayered systems is of prime importance. When the number of layers is too large for individual characterisation, resorting to statistical approaches becomes mandatory in order to account for the behaviour of the whole material. In this case, a large density of microstructural heterogeneities complies with the requirements of classical RVE definitions, hence enabling the correlation between microstructural features and macroscopic performance. This approach is desirable when optimising the process and investigating the effect of process parameters on the layer thickness distribution. As a matter of fact, the RVE size will depend on such process parameters, for the statistical rate of convergence of apparent properties is intrinsically related to the microstructural variability induced by the process. In this work, the layer heterogeneities are characterised by very small, nanometric, length scales, which makes their observation difficult. Appropriate methods, such as atomic force microscopy (AFM) or transmission electron microscopy, are available, but with reduced regions of interest under observation, of a few squared microns at best, hence bringing back the question of representativity for the micrographs acquired this way. This practical problem of scale separation and representativity is very similar to what has been encountered by other authors in the literature when trying to evaluate RVE sizes on various materials, such as fibrous media [Dirrenberger et al., 2014], collagen fibrils [Altendorf et al., 2012], concrete [Huet, 1990, Pelissou et al., 2009] or particle-reinforced composites [Salmi et al., 2012b]. In order to tackle the problem of sample representativity, the statistical method proposed by

Polymer	Commercial name	Density (g/cm^3)[1]	MFI[1]	η^* at 225°C , $\dot{\gamma} = 5s^{-1}$
PMMA	Altuglas VM100	1.18	14.5g/10min at 230°C /3.8kg	791 Pa.s
PS	Crystal 1340	1.05	4.0g/10min at 200°C /5kg	786 Pa.s

Table 1.1: Rheological properties of the polymers used in this work

[Kanit et al., 2003], although initially developed by [Hersant and Jeulin, 1976], for determining RVE sizes will be implemented for morphological properties of nanolayered polymer films, *i.e.* the layer thickness t and volume fraction V_V, based on AFM micrographs.

1.2.1 Materials and characterisation techniques

Materials

Nanolayered polymer PS–PMMA films were considered in this work. Poly(methyl methacrylate) (PMMA) was graciously supplied by Altuglas International (Altuglas VM100), whereas polystyrene (PS) was provided by Total Petrochemical (Crystal 1340). The melt flow indexes (MFIs), densities and complex viscosity $\eta*$ in the extrusion conditions (225°C , $\dot{\gamma} = 5s^{-1}$), determined using an Anton Paar rheometer in plate/plate configuration, are given in Table 1.1.

Process

PS–PMMA nanolayered films are manufactured using a multilayer coextrusion process. The processing route consists of two 20-mm single-screw extruders with melt gear pumps, a three-layer coextrusion feed-block (A-B-A), a series of layer-multiplying elements, an exit flat die and a thermally regulated chill roll as illustrated in Fig. 1.1. PMMA was extruded to form the outer skin layers and PS the core layer. The inclusion of gear pumps into the coextrusion system enables an additional degree of control over the relative thickness ratio of the layered polymers as they enter the A-B-A feed-block. In this study, the mass fraction of polymer B in the film was set and kept constant by adjusting the flow rate through the speed of the melt gear pumps. The initial three-layer polymer flow subsequently enters a mixing section, composed of a sequence of layer-multiplying elements. The melt was initially cut in half vertically, and then each half was compressed and restretched to its original width, hence doubling the number of layers with each layer-multiplying element. A series of n elements combines two polymers producing $2^{n+1} + 1$ alternating layers, as shown in Fig. 1.1.

Here, 10 multiplying elements were used, giving films containing 2049 layers. Finally, after passing through the last layer-multiplying element, the nanolayered structure was formed into a thin sheet by passing through a flat die, 150 mm wide and 1.5 mm thick. At the die exit, the

[1] Obtained from the technical datasheet.

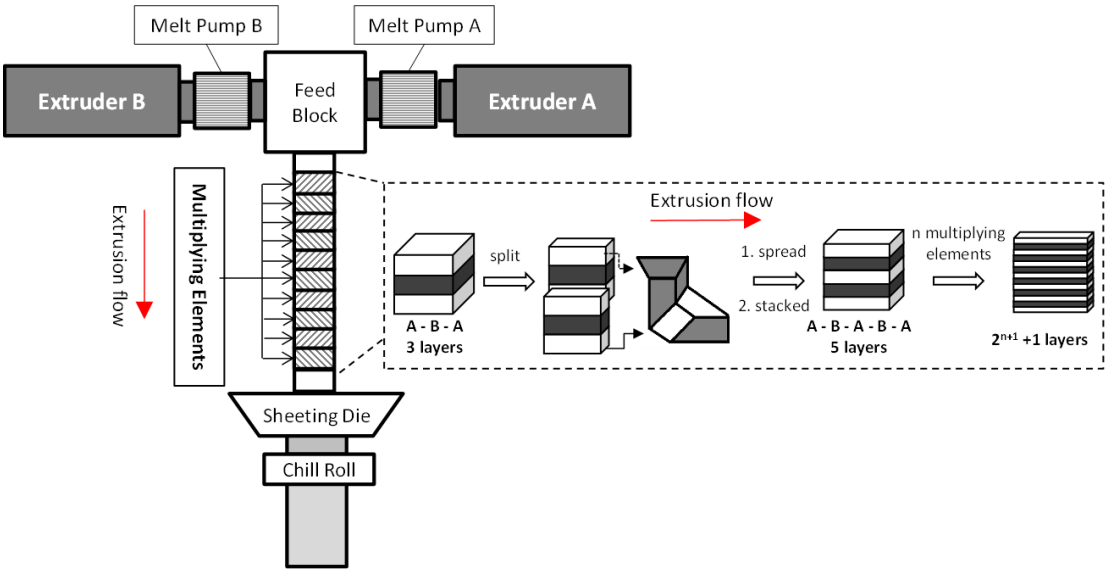

Figure 1.1: Principle of the multiplication of layer by the multilayer coextrusion process to fabricate the films

nanolayered samples were stretched and quenched, using a water-cooled chill roll at 95°C , and collected. The resulting sample is a rectangular film made of alternating layers of PS and PMMA, architectured as a one-dimensional (1D) stacking. The sample has PS/PMMA compositions by weight of 10/90 and a thickness of approximately 250 µm. Based on these parameters, the nominal PS layer thickness is 27 nm (Eq. 1.18) and the theoretical volume fraction is 11%.

$$\text{Nominal thickness}^{\text{PS}} = \text{Nominal thickness}^{\text{Film}} \frac{{V_V}^{\text{PS}}}{\text{Number of layers}^{\text{PS}}} \tag{1.18}$$

Characterisation techniques

AFM images were obtained in tapping mode using a multimode microscope controlled by a Nanoscope V controller (Veeco), operated under ambient atmosphere. The tips (silicon, spring constant 40 N/m, oscillation frequency ca. 300 kHz) were obtained from BudgetSensors. The radius of curvature of the tips was less than 10 nm. Phase, height and amplitude images were acquired simultaneously. Specimens were cut from the centre of the extruded films and sectioned perpendicular to their surface with an ultramicrotome 2088 Ultrotome V (LKB) at a cutting speed of 1 mm/s. Images were recorded at full resolution (4096 × 4096 pixels), with a scan rate of 0.5 Hz. This resolution yields a pixel size of 7 nm. AFM images were taken from extrusion direction. The phase signal was described as a measure of the energy dissipation involved in the contact between the tip and the sample, which depends on a number of factors, including viscoelasticity, adhesion and topography. As these factors are different between PS and PMMA, the thickness of layers was measured from the AFM phase images (Fig. 1.2), which most clearly revealed the layered film structure. On the obtained images, PS and PMMA appear in brown and gold colour,

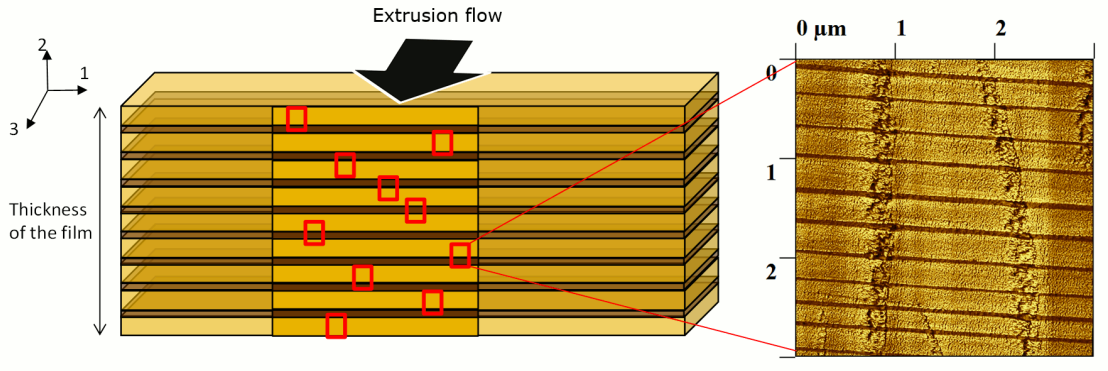

Figure 1.2: AFM specimen and image analysis principle. The arrow represents the extrusion flow direction (left); AFM image of partial cross section of the sample (vertical lines are compression lines due to sample preparation, right).

	3 layers	10 layers	30 layers	100 layers	200 layers	300 layers	500 layers
Number of realisations	275	81	28	10	5	3	2
Average sample size (nm)	738	2441	6949	20143	40287	60076	100717
Total number of PS layers	825	810	840	1000	1000	900	1000
Number of measured PS layers	822	808	800	822	822	742	822

Table 1.2: Characteristics of each volume series

respectively.

Image analysis

Since the film has finite dimensions, 10 images of around 100 layers were taken all along the thickness of the film as represented in Fig. 1.2. The sample was composed of 1024 PS layers; a large fraction of PS layers (ca. 80%) was measured indeed. In order to determine the RVE, these 10 images were divided into nonoverlapping, neighbour squares of equal size. Thus, due to the regular nature of the microstructure, it was possible to obtain statistical data for more than 100 layers by compiling them. In the end, seven series of images containing respectively 3, 10, 30, 100, 200, 300 and 500 layers of PS were obtained, as shown in Fig. 1.3, for the first four series. The horizontal lines on these AFM images were chatter marks due to sample compression during microtoming. The characteristics for each series are given in Table 1.2. The number of realisations corresponds to the number of samples considered within one series.

Thicknesses of PS layers were measured from AFM phase images with the image analysis software Gwyddion. Through the software, a phase profile can be extracted showing the variation of phase degree. It is noteworthy that the profile is averaged over 128 pixels whatever be the image size. This integrated height is larger than the thickness of the cut and compression lines,

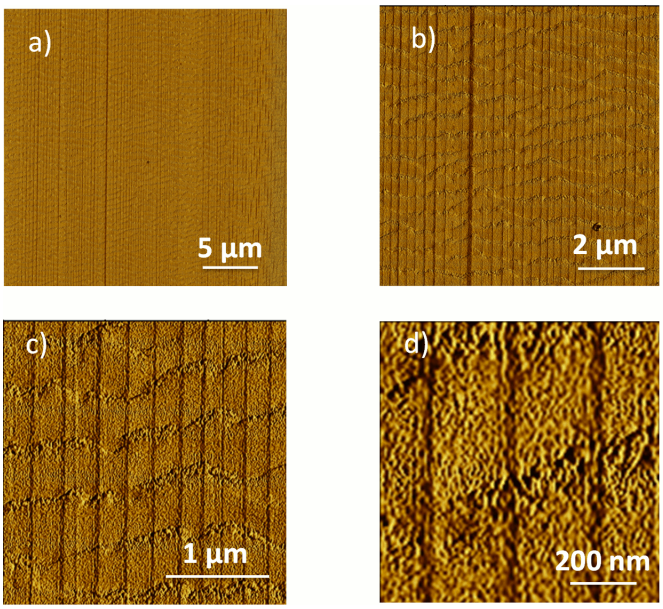

Figure 1.3: AFM phase images of PMMA/PS (90/10 wt%) film with (A) 100 layers, (B) 30 layers, (C) 10 layers and (D) 3 layers.

which appear during the sample preparation. Moreover, these lines are perpendicular to the layers. Hence, they are included in the profile noise, and the measurements of layer thickness are not affected. Each layer is represented by one peak on the profile. The thickness of each layer is determined according to an arbitrary procedure which consists of measuring the full width at half-maximum height of the peak. This step is similar to a manual threshold. As the thickness of layers is in the range of tens of nanometres, *i.e.* a few pixels in terms of AFM imaging, it is critical to analyse all possible sources of error. Various types of error can exist in this case: uncertainties of measurement, systematic error, and sampling error. The size of the AFM tip, AFM controller, image compression and acquisition definition were considered as uncertainties of measurement. The manual threshold and bias due to the operator were considered as systematic error. The sampling, which depends on the size of the considered system, *i.e.* the total number of layers which will be measured, can be a source of error if the number of analysed layers is too small. This last point is fundamental for our study as the sampling error can be related to the RVE size, given the assumptions of statistical homogeneity and ergodicity for the considered material. Both assumptions will be made from now on in order to provide a consistent ground for applying the approach developed by [Kanit et al., 2003]. Tips used have a curvature radius of $R = 10$ nm. The in-plane resolution of AFM is related to the radius of curvature of the tip, as well as the vertical detection limit ($\Delta z = 0.1$ nm in our case, given by the manufacturer), and the size of the feature being characterised. The in-plane detection limit is approximated by Eq. 1.19.

$$\Delta x = 2\sqrt{2R\Delta z} \tag{1.19}$$

The value estimated from Eq. 1.19 is $\Delta x = 2.8$ nm, which is considerably small in comparison

with the theoretical value of PS layers (27 nm). Therefore, the uncertainty of measurement due to the AFM tip size was considered negligible. To reinforce this assertion, a comparative study has been done with a thinner tip ($R = 2$ nm) and results regarding the layer thickness were the same. All images were acquired by the same operator with the same AFM controller at a constant image resolution (4096 × 4096 pixels at a scan rate of 0.5 Hz) in order to avoid image resolution bias. However, it is worth noting that the images were acquired with the highest resolution attainable for this AFM apparatus. The acquisition definition can have a crucial importance on measurements if not chosen cautiously. The minimal acceptable resolution can be defined by a criterion, *e.g.* that one pixel represents less than 10% of the measured feature. AFM images are recorded as raw data, without algorithmic compression, hence no error due to image file compression was considered. Concerning threshold, with this measurement method, the systematic error on thickness was estimated to one pixel. The size of the pixel depends on the size of the image and the resolution. Here, the systematic error was 27000/4096, being 7 nm. Moreover, this measurement method overestimates the value by including the external pixels in the measure. So, for each value measured on the profile, the value of systematic error was subtracted in order to improve accuracy.

1.2.2 Representativity of AFM samples

There are several morphological criteria (granulometry, anisotropy, etc.) that can be used to characterise random structures. We focus here on the spatial arrangement of a given random structure. It is characterised by, at least, three properties: covariance, distance function and anisotropy. Since this work does not deal with multiscale and/or anisotropic models of random structures, we will only consider the covariance. The covariance $C(x, x+h)$ of random set A is given by:

$$C(x, x+h) = P\{x \in A, x+h \in A\} \tag{1.20}$$

If A is a stationary random set, $C(x, x+h) = C(h)$. If A is ergodic, $C(h)$ can be estimated from the volume fraction of $A \cap A_{-h}$:

$$C(h) = V_V(A \cap A_{-h}) = V_V\left(A \ominus \check{h}\right) \tag{1.21}$$

The erosion by $\{x, x+h\}$ results in variations in $C(h)$ which depend on vector h (modulus $|h|$ and orientation α). The covariance $Q(h)$ of the complementary random set A^c can also be considered, although it does not give any information compared to $C(h)$:

$$Q(0) = q = 1 - p \tag{1.22}$$

$$Q(h) = P\left\{x \in A^c, x+h \in A^c\right\} = 1 - 2C(0) + C(h) \tag{1.23}$$

The covariance of a random set in $\mathbb{R}^3$ is subject to the following properties:

- $C(0) = P\{x \in A\} = p$;
- $\frac{1}{\pi}\int_0^{4\pi} -\left(\frac{\partial C(h,\alpha)}{\partial |h|}\right)_{h=0} d\alpha = S_V(A)$ when the partial derivative remains finite;
- if $C(0) - C(h) \simeq |h|^\beta$ for $h \to 0$, with $0 < \beta < 1$, the boundary of A has a non integer *Haussdorf* dimension $d = 3 - \beta$, and A is a fractal set;
- $C(\infty) = p^2$, the covariance of a stationary ergodic random set reaches a sill, the events are independent;
- For a given orientation α, $C(h)$ reaches a sill at a certain distance a_α, or range, that we consider as the characteristic length scale of the random structure: $C(a_\alpha) = C(\infty) = V_V(A)^2 = p^2$;
- The presence of multiple scales in the random structure is characterised inflections of the experimental covariance;
- Periodicity of the structure results in periodicity of the covariance.

Correlation functions are useful for studying physical properties within random structures. The centered second-order correlation function can be deduced from the covariance. For the case of a two-phase medium with properties $Z = Z_1$ when $x \in A$ and $Z = Z_2$ when $x \in A^c$, it yields:

$$\begin{aligned} \overline{W}_2(h) &= E\{(Z(x+h) - E\{Z\})(Z(x) - E\{Z\})\} \\ &= (Z_1 - Z_2)^2 \left(C(h) - p^2\right) \\ &= (Z_1 - Z_2)^2 \left(Q(h) - q^2\right) \end{aligned} \tag{1.24}$$

The integral range A_n presented in Section 1.1.1 is obtained from the centered second-order correlation function in this way:

$$A_n = \frac{1}{D_Z^2}\int_{\mathbb{R}^n} \overline{W}_2(h)\, dh \tag{1.25}$$

In the case of concern for this work, *i.e.* nanolayered polymer blends ideally structured as a 1D stacking, morphological variability is induced in only one direction, the microstructural morphology being constant in both directions 2 and 3. Eqs. 1.4 and 1.5 can thus be reformulated as Eqs. 1.26 and 1.27 by considering the sample size L, or length of the sample, *e.g.* in µm:

$$D_Z^2(L) = D_Z^2 \frac{A_1}{L} \tag{1.26}$$

with A_1, the integral range in $\mathbb{R}$ defined as :

$$A_1 = \frac{1}{D_Z^2}\int_{\mathbb{R}} \overline{W}_2(h) dh \tag{1.27}$$

By adapting Eq. 1.16 to the 1D case, it yields:

$$L_{\mathrm{RVE}} = A_1^{*\,\gamma}\sqrt{\frac{4D_Z^2}{\epsilon_{\mathrm{rel}}^2\overline{Z}^2 n}} \tag{1.28}$$

This RVE size then depends on the point variance D_Z^2, integral range A_1 and mean value $\overline{Z}$. These three parameters are estimated from the image analytically, except when considering the volume fraction which is equal to the length fraction L_L, for which D_Z^2 is known explicitly:

$$D_{L_L}^2 = L_L\,(1 - L_L) \tag{1.29}$$

For the specific case of PS layer thickness, the theoretical thickness can be obtained from the length fraction as follows:

$$t_{\mathrm{th}} = L_L\frac{L}{N} \tag{1.30}$$

with L, size of the sample and N, the number of PS layers within the sample, which is a constant imposed by the number of multiplying elements used during the coextrusion process and the sample size L . Hence, Eq. 1.31 can be adapted in the following way for the point variance of PS layer thickness:

$$D_t^2 = \left(\frac{L}{N}\right)^2 L_L\,(1 - L_L) \tag{1.31}$$

The coefficient A_1^* and scaling-law exponent γ can be estimated from image analysis as it was done by [Kanit et al., 2003], [Altendorf et al., 2014] and [Wang et al., 2015], by considering the ensemble variance $D_Z^2(L)$ versus L and identifying the ordinate at the origin for the scaling law, hence yielding $D_Z^2 A_1^{*\gamma}$ from which exponent γ and point variance D_Z^2 are known, leaving only A_1^* to be evaluated. Furthermore, Eq. 1.17 can be updated for present problem:

$$D_Z^2\,(L) = KL^{-\gamma} \tag{1.32}$$

with $K = D_Z^2 A_1^{*\gamma}$, leaving only two parameters to be identified from the statistical analysis. Eq. 1.28 can thus be updated in this way:

$$L_{\mathrm{RVE}} = \sqrt[\gamma]{\frac{4K}{\epsilon_{\mathrm{rel}}^2\overline{Z}^2 n}} \tag{1.33}$$

1.2.3 Results and discussion

Morphological measurements have been performed on the six different populations of sample size.

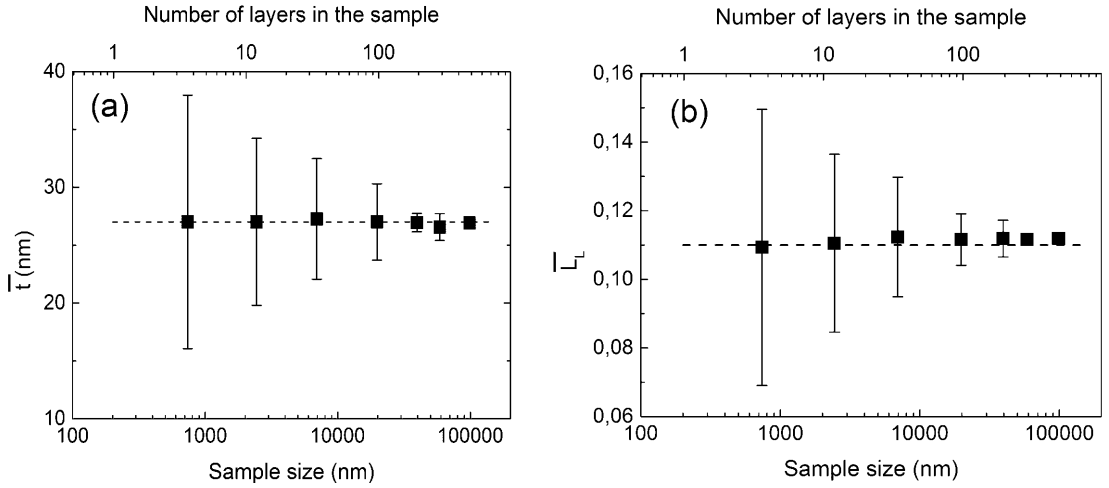

Figure 1.4: Mean values for the PS layer thickness t (a) and volume fraction L_L (b) varying with sample size.

Mean value and distribution

The mean volume fraction of PS layers V_V is equal to both the surface fraction S_S and length fraction $\overline{L_L}$ of PS, since the microstructural morphology is stationary. L_L has been computed over n realisations for a given sample size L in nm. The mean PS layer thickness $\overline{t}$ was also estimated from image analysis with respect to the size of the sample. Both $\overline{L_L}$ and $\overline{t}$ are plotted as functions of the sample size in Fig. 1.4. The mean values obtained for the largest sample size considered ($L = 98862$nm) are $\overline{L_L} = 11.19 \pm 0.03\%$ for the volume fraction and $\overline{t} = 26.9 \pm 0.1$nm. Morphological fluctuations are inherent to the stochastic nature of real-life materials. As expected, no bias occurs for both the layer thickness and volume fraction, whatever the size of the realisations.

The observed distributions of thickness and volume fraction of PS layers for each sample size L are shown in Fig. 1.5 (a) and (b), respectively. For each property, the distributions were similar whatever be the considered system. As represented in red lines in Fig. 1.5, normal distribution curves have been fitted to the experimental data. Experimental data and fit are in good agreement. For each population, the mean value of the normal distribution curve was equal to $\overline{t}$. This result confirms the implicit hypothesis of standard deviation calculation made with Eq. 1.12 from which the statistical analysis is done.

Covariance

In order to check for morphological regularity of the material considered, the two-point geometrical covariance was computed for the sample shown in Fig. 1.6(a), which was transformed into the binary image (Fig. 1.6(b)) by manual thresholding and morphological opening and closure operations. The considered sample was approximately 2×2µm, including seven PS layers and a

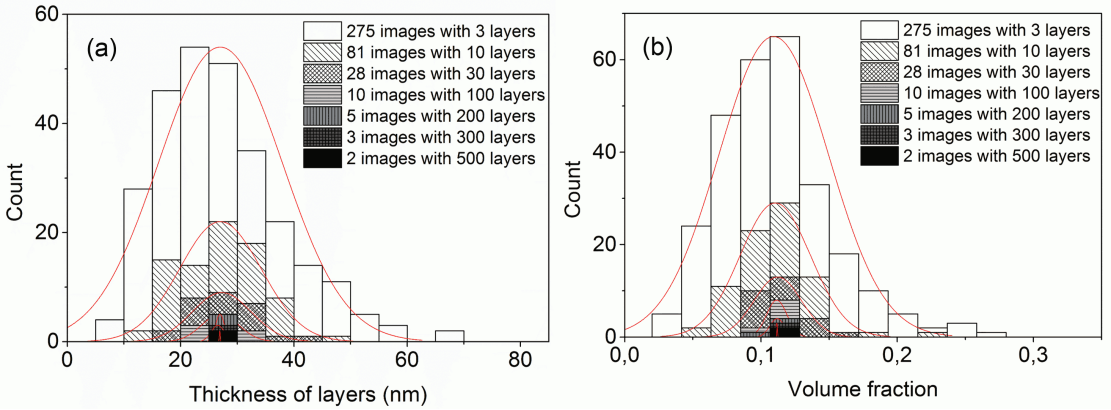

Figure 1.5: Distribution of statistical population as a function of (a) thickness of layers and (b) volume fraction. The red lines represent the normal distribution curves.

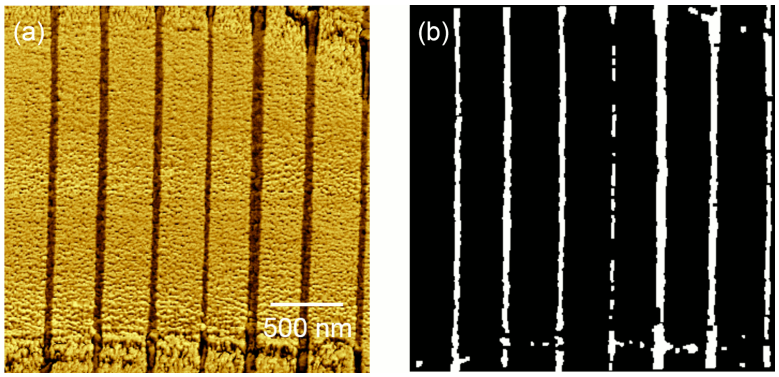

Figure 1.6: (a) AFM micrograph used for the covariance study and (b) binary image for computing the covariance.

volume fraction of PS layers of 11.4%.

Its covariance was estimated along the horizontal direction, the orientation of vector $\underline{\boldsymbol{h}}$, which corresponds to direction 2 in Fig. 1.2. The regular quasi-periodic character of the material is clearly apparent on the covariance plot shown in Fig. 1.7, yielding a distance of 280 nm between the centres of two neighbouring PS layers. The first point C_0 corresponds to the volume fraction of the sample: $V_V = 0.114$, whereas the sill C_∞ corresponds to ${V_V}^2 = 0.013$.

Morphological representativity

Results regarding the volume fraction are presented in Fig. 1.8. Variance for the mean PS layer thickness as a function of the sample size is shown in Fig. 1.9. The γ exponents of the scaling law for each morphological property were estimated from the results of image analysis, by fitting the slope of the variance curves. Values of K are estimated from Fig. 1.8 and 1.9 based on Eq. 1.32. From Fig. 1.8, two slopes are identified for the power law, indicating the existence of

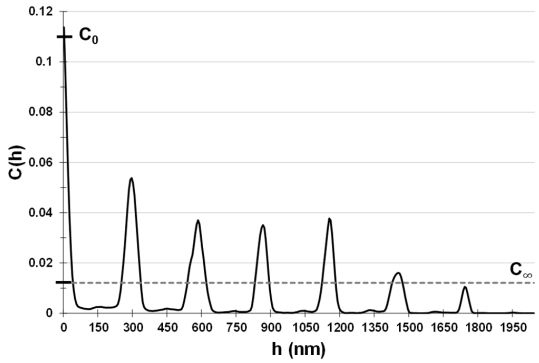

Figure 1.7: Covariance computed horizontally on the image shown in Fig. 1.6(b).

two scales of heterogeneities. The first-scale, or local, variability is intrinsic to the microstructure induced by the extrusion process: it encompasses the effects of short-range physical phenomena, such as flow nonlinearities, local thermal inhomogeneity and interfacial interactions. This first scale of variability is always present although its effects become blunter for a larger system; it is characterised by a consistent γ exponent of $0.66 - -0.75$ for both properties, which should be compared to the theoretical value of 0.5 obtained for random fibres in 2D [Jeulin, 2016]. The second scale of variability to consider is seen only for sample sizes higher than 10^4 nm; its origin could be described as boundary effect patterns during the process. Indeed, due to higher shear rate prescribed to the melt at the wall while passing through multiplying elements, layers in the vicinity of the wall become thinner than others. If this phenomenon occurs at each multiplying step, the final sample is constituted of patterns with long-range varying layer thickness sequences. The tipping point between the slopes could then be interpreted as the characteristic length of such pattern. In our case, the pattern dimension can be estimated to be 2.0×10^4nm, corresponding to approximately 100 layers, *i.e.* about 10% of the film thickness. Rather than considering this a limitation of the statistical approach invoked for the case of films with finite dimensions, we propose to use this method for the characterisation of microstructural variability, in order to study the effect of process parameters on the quality of nanolayered films. As a matter of fact, this statistical approach allows for the discrimination of multiple sources of variability and interpretation of their physical meaning. The second scale of variability appears to accelerate the statistical convergence with respect to the size of the system, for volume fraction ($\gamma = 4.45$), as well as for the mean layer thickness ($\gamma = 4.22$). Also such exponents are expected for random media with zero integral range, which is the case for the periodic part of the microstructure, as revealed by the quasiperiodic behaviour of the covariance in Fig. 1.7. Nevertheless, in this study, sample series containing 100 layers or more have a low number of realisations (≤ 10). More samples would be necessary in order to obtain a better accuracy for these series.

Using Eq. 1.33, it is now possible to determine statistical RVE sizes from image analysis. Estimates for RVE sizes are presented in Table 1.3 for the different morphological properties (volume fraction and layer thickness of PS), for various relative errors and numbers of realisations ($n = \{1; 10; 50\}$), using the first-scale variability parameters, since only small size samples are

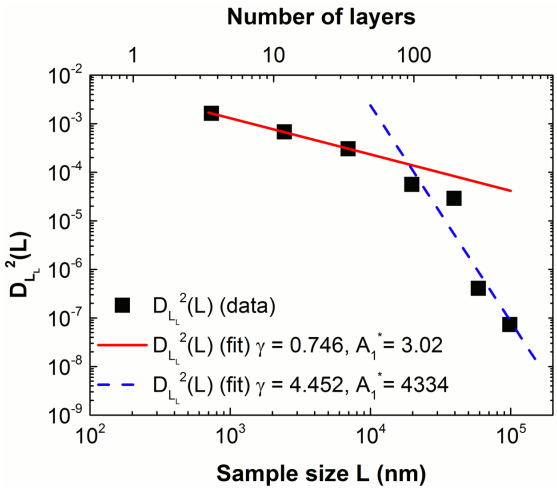

Figure 1.8: Variance $D^2_{L_L}(L)$ of the volume fraction of PS depending on sample size L, computed from image analysis.

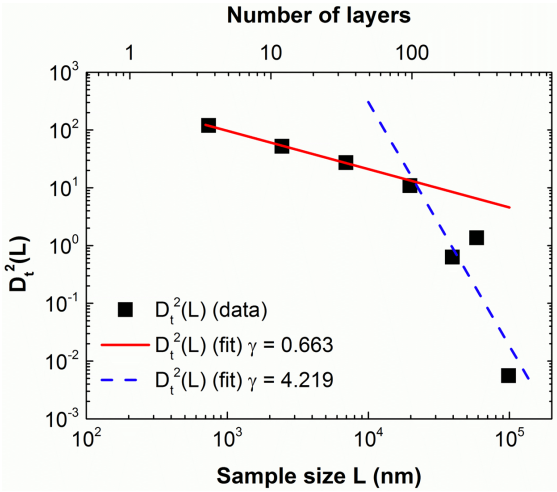

Figure 1.9: Variance $D^2_t(L)$ of the thickness of PS depending on sample size L, computed from image analysis.

Z	γ	K	n	ϵ_{rel}	L_{RVE}(nm)	$\overline{N}$
PS volume fraction	0.746	7.08×10^{-2}	1	5%	9.92×10^{5}	4043
	0.746	7.08×10^{-2}	10	5%	4.53×10^{4}	185
	0.746	7.08×10^{-2}	50	5%	5.24×10^{3}	21
	0.746	7.08×10^{-2}	1	10%	1.55×10^{5}	630
	0.746	7.08×10^{-2}	10	10%	7.07×10^{3}	29
	0.746	7.08×10^{-2}	50	10%	8.17×10^{2}	3
PS layer thickness	0.663	9.43×10^{3}	1	5%	3.23×10^{6}	13173
	0.663	9.43×10^{3}	10	5%	1.00×10^{5}	409
	0.663	9.43×10^{3}	50	5%	8.85×10^{3}	36
	0.663	9.43×10^{3}	1	10%	4.00×10^{5}	1628
	0.663	9.43×10^{3}	10	10%	1.24×10^{4}	51
	0.663	9.43×10^{3}	50	10%	1.09×10^{3}	4

Table 1.3: L_{RVE} size estimated using Eq. 1.33 for PS volume fraction and layer thickness.

readily accessible with AFM. RVE sizes presented in this table for $n = 1$ are always larger than the volume element sizes achieved throughout this work: $L = 100$ µm on average for the largest. Nevertheless, the precision for a given sample size can be obtained from multiple realisations of smaller samples. As an example, for $\overline{t}_{\text{PS}}$, if $L = 12$ µm, and $\epsilon_{\text{rel}} = 10\%$, one must analyse 10 realisations in order to obtain the same statistical convergence as for one realisation with $L = 400$ µm. Precaution should be taken regarding the bias induced by boundary layer effects on mean values by choosing smaller elementary samples when considering physical properties rather than morphological ones.

From both practical and acquisition time viewpoints, for mean value and distribution of layer thickness for a given precision, it is better to analyse images with fewer layers. So, the power-law parameters to be considered for the determination of a representative sample size are those related to the first-scale variability. In order to characterise long-range boundary effects due to the manufacturing process, large samples have to be considered. Such image acquisition might be inaccessible through AFM, and therefore large samples can be reconstructed from smaller contiguous nonoverlapping samples, as it was done in this work.

1.2.4 Conclusions and perspectives

Nanolayered PS–PMMA polymer blend films were manufactured and morphologically characterised through AFM and image analysis. Representativity of hundreds of nanoscale heterogeneous samples was investigated. The statistical approach introduced by [Kanit et al., 2003] was adapted and implemented for the case of 1D nanolayered materials based on image analysis of microstructural samples. RVE sizes were determined for both PS volume fraction and mean

layer thickness. The study of the ensemble variance convergence with respect to the size of the system revealed two regimes for the scaling power law, indicating the presence of two scales of morphological heterogeneities within the material.

In summary, three functions are enabled by the present approach:

- To predict RVE size for a given property and precision;
- To reach the same precision with either one large sample or several smaller samples;
- To discriminate and characterise multiple scales of variability in heterogeneous media.

Further work will include the morphological modelling of such materials in order to generate populations of virtual samples for computation of physical properties, *e.g.* mechanical, thermal, electrical, etc. As the rate of statistical convergence with respect to the size of the system informs us about variations induced in the microstructure, the current approach will be applied for different factors of influence, *i.e.* blend compositions, morphologies and process parameters. This work is a useful step further towards understanding the relationship between process parameters, induced microstructures and functional properties.

1.3 RVE size determination for viscoplastic properties in polycrystalline materials

Another case of application appeared during the PhD work of Shaobo Yang [Yang, 2018, Yang et al., 2019] concerned with the study of the dissipative behaviour of polycrystalline copper in very high cycle fatigue regime. In order to compare and interpret experimental results, we resorted to polycrystalline aggregate simulations using finite element analysis. To validate the approach, the representativity of our simulations had to be assessed, which is the aim of the present section.

1.3.1 Introduction

In the past decades, full-field numerical simulation of polycrystalline materials based on finite element analysis has been widely developed to investigate the mechanical behaviour, allowing the analysis of stress and strain fields at a scale that is not easily assessable experimentally [Barbe et al., 2001, Roters et al., 2011]. Most of the authors in the literature dedicated to the simulation of polycrystals usually consider a population of virtual polycrystalline samples made of several hundred grains, validating this arbitrary choice by analysing the mean value and standard deviation for a given property computed on such population [Shenoy et al., 2007, Shenoy et al., 2008, Robert et al., 2012, Martin et al., 2014, Sweeney et al., 2015, Cruzado et al., 2017, Cruzado et al., 2018]. Nevertheless, the development

of full-field simulation of polycrystalline materials results in shedding new light on the relationship between the microstructural description at the dislocation or grain scale and the local mechanical behaviour [Cailletaud et al., 2003]. The homogenised macroscopic response of a polycrystalline material sample will depend on its size, hence yielding the question of representativity for such virtual samples.

Using this approach, [Kanit et al., 2003] studied the RVE sizes of a two-phase 3D Voronoi mosaic for linear elasticity, thermal conductivity and volume fraction, under uniform displacement, traction and periodic boundary conditions (PBC). The results showed that the PBC held an advantage of convergence rate of the mean apparent properties in comparison to other boundary conditions, due to the vanishing of boundary layer effects. A slow rate of convergence for the considered properties would yield a large RVE sizes [Dirrenberger et al., 2014]. Also considering the large calculation cost in the case of crystal plasticity, it is preferable to rely on PBC in order to optimise the computation strategy, as it was done in other investigations [Pelissou et al., 2009, Jean et al., 2011a].

The statistical method of [Kanit et al., 2003] was implemented for the estimation of RVE size, not only for linear mechanical properties and morphological property, but also for plastic properties: [Madi et al., 2006] evaluated the RVE size for 2D/3D viscoplastic composite materials. In their study, the macroscopic strain rate of the 2D/3D material was modeled using a Norton flow rule. Based on the von Mises criterion, an apparent viscoplastic parameter P_v^{app} was firstly defined as the coupling of two parameters of the Norton flow rule K and n, *i.e.* $P_v^{\text{app}} = \frac{1}{K^n}$. The authors showed that the value of P_v^{app} converged towards a constant value with an increasing volume of simulation and that the RVE size for P_v^{app} was found to be smaller than the ones for elastic moduli. In the present study, we relied on this definition of the apparent viscoplastic parameter, as it is adapted for describing the nonlinear behaviour of a macroscopically isotropic polycrystalline viscoplastic material.

As a matter of fact, the concept of RVE has often been used in investigations associated with the average mechanical response of 2D and 3D polycrystalline material. The definition of RVE size can stem from finite element meshing considerations or convergence of mean values for a considered property. For instance, [Barbe et al., 2001] described the RVE for a cubic polycrystalline mesh as an equilibrium between the number of grains (238) and the average number of integration points per grain (660) attainable within typical computational means. More recently, [Sweeney et al., 2015] estimated the energetic parameter of CoCr stent material in high cycle fatigue by averaging in 5 RVEs with 138-140 grains. [Cruzado et al., 2017, Cruzado et al., 2018] simulated the cyclic deformation of metallic alloys with 20 RVEs and a size of 300 grains, which showed an error less than 10% for elastoviscoplastic properties. Similar determination of material RVE size can also be found in [Shenoy et al., 2007, Shenoy et al., 2008, Martin et al., 2014, Gillner and Münstermann, 2017, Teferra and Graham-Brady, 2018]. In these references, RVE size is defined as a few realisations with a few hundred grains which can realise a convergence of mean properties. However, these analyses do not allow for a rigorous statistical definition of the

RVE size.

Rather than relying solely on the convergence of mean properties, the method proposed in [Kanit et al., 2003] makes use of the rate of convergence of the ensemble variance of the mean properties with respect to the volume size, thus enabling the definition and estimation of a statistical RVE size for each considered property. However, no one ever assessed the RVE size for polycrystalline material in the framework of CPFEM with the statistical RVE method. Additional consideration has to be made regarding the apparent properties to be considered as criteria for RVE size determination in viscoplasticity. The first one should be the definition of intrinsic dissipation within the context of crystal plasticity. Secondly, the definition of the apparent viscoplastic parameter will be considered in the crystal plasticity framework. Meanwhile, for the crystal plasticity behaviour, material heterogeneity is mainly due to the local grain orientation, which can introduce strong stress concentrations, leading to early onset of plasticity. Both grain orientation and the choice of crystal plastic behaviour are likely to influence directly the value of RVE size for mechanical properties, as it will be discussed in the paper.

1.3.2 Crystal plasticity constitutive model

The material involved in this paper was pure polycrystalline copper. Both anisotropic crystal elasticity and plasticity were considered for its behaviour. The cubic elasticity is characterised by 3 independent elastic constants, taken from [Musienko et al., 2007]. The crystal plasticity model considered in the present work was introduced and implemented by [Méric et al., 1991, Cailletaud, 1992] in the finite element code ZeBuLoN/ZSet[1]. The Meric-Cailletaud model was chosen for its ability to account for kinematic hardening. This model is popular within the crystal plasticity community and has been used in many previous works on computational mechanics for polycrystalline material [Barbe et al., 2001, Diard et al., 2005, Gérard et al., 2009]. For the sake of conciseness, the crystal plasticity model and its parameters will not be presented here, for more details the enquiring reader can refer to [Yang et al., 2019].

1.3.3 Computational approach

Periodic three-dimensional mesh generation

In this paper, a methodology is employed for generating and meshing 3D random polycrystals. The associated mesh optimisation approach and statistical work of mesh quality are fully presented in the reference paper [Quey et al., 2011]. The corresponding algorithms are implemented and distributed in an open-source software package: Neper[2]. Using Neper, the Voronoi tesselation can be constructed with a periodicity constraint, needed for PBC. For the sake of simplicity and comparison with results from the literature, an isotropic morphological and crystallographic texture is considered. To do so, the three Euler-Bunge angles (α,β,γ) in the Z-X-Z type are

[1] http://www.zset-software.com
[2] http://neper.sourceforge.net/

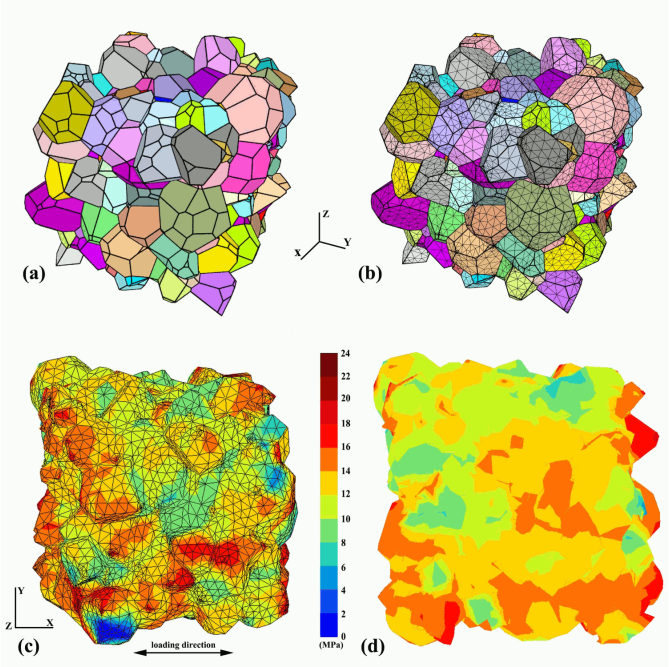

Figure 1.10: (a) 3D microstructural model of a polycrystalline aggregate (343 grains); (b) meshing with tetrahedral elements; (c) von Mises equivalent stress map with a macroscopic tensile strain of 0.01%; (d) XY-section of (c)

used for the orientation of each grain. Afterwards, the microstructural model is meshed with linear tetrahedral elements as shown in Fig. 1.10(b). At least 300 elements were used for each grain, which is a reasonable value considering the usual practice in the full-field simulation literature [Cailletaud et al., 2003, Roters et al., 2011, Cruzado et al., 2017]. The grain size in the generated microstructure follows a normal distribution function with a mean value of 20µm and a standard deviation of 13.5µm. Fig. 1.10(c) represents an example of equivalent von Mises stress distribution at a macroscopic strain of 0.01%, and the stress map within the grains is observed by slicing perpendicularly to the Z axis, as shown in Fig. 1.10(d).

Definition of apparent elastic properties

The micromechanical linear elastic behaviour at each integration point in the finite element simulation is described by the generalised Hooke law using the fourth-rank elastic moduli tensor $\underset{\approx}{\boldsymbol{c}}$, such that:

$$\underset{\sim}{\boldsymbol{\sigma}} = \underset{\approx}{\boldsymbol{c}} : \underset{\sim}{\boldsymbol{\varepsilon}} \tag{1.34}$$

with $\underset{\sim}{\boldsymbol{\sigma}}$ second-order symmetric *Cauchy* stress tensor, $\underset{\sim}{\boldsymbol{\varepsilon}}$ second-order symmetric engineering strain tensor. For a given volume V, the fourth-rank tensor of apparent moduli $\underset{\approx}{\boldsymbol{C}}^{\text{app}}$ can be

defined by the macroscopic relations:

$$\underset{\sim}{\boldsymbol{\Sigma}} = \langle \underset{\sim}{\boldsymbol{\sigma}} \rangle = \frac{1}{V} \int_V \underset{\sim}{\boldsymbol{\sigma}} \, dV = \underset{\approx}{\boldsymbol{C}}^{\text{app}} : \underset{\sim}{\boldsymbol{E}} \tag{1.35}$$

where $\underset{\sim}{\boldsymbol{\Sigma}}$ and $\underset{\sim}{\boldsymbol{E}}$ are respectively the macroscopic stress and strain second-rank tensors. For an elementary volume V large enough ($V > V_{\text{RVE}}$), the apparent properties do not depend on the boundary conditions [Huet, 1990, Sab, 1992] and equal to the effective properties of the considered material, so that:

$$\underset{\approx}{\boldsymbol{C}}^{\text{app}} = \underset{\approx}{\boldsymbol{C}}^{\text{eff}} \tag{1.36}$$

For determining an apparent bulk modulus k^{app} over V, let us apply the following macroscopic strain tensor in order to solve the micromechanical KUBC problem:

$$\underset{\sim}{\boldsymbol{E}}_k = \begin{bmatrix} \frac{1}{9} & 0 & 0 \\ 0 & \frac{1}{9} & 0 \\ 0 & 0 & \frac{1}{9} \end{bmatrix} \tag{1.37}$$

An apparent bulk modulus k^{app} can be defined from the elastic strain energy density for the macroscopic strain using the Hill–Mandel lemma [Hill, 1967], such that:

$$k^{\text{app}} \hat{=} 2\mathscr{E}^{el}\left(\underset{\sim}{\boldsymbol{E}}_k\right) = \langle \underset{\sim}{\boldsymbol{\sigma}} : \underset{\sim}{\boldsymbol{\varepsilon}} \rangle = \langle \underset{\sim}{\boldsymbol{\sigma}} \rangle : \langle \underset{\sim}{\boldsymbol{\varepsilon}} \rangle = \underset{\sim}{\boldsymbol{\Sigma}} : \underset{\sim}{\boldsymbol{E}}_k = \text{Tr}\,\underset{\sim}{\boldsymbol{\Sigma}} \tag{1.38}$$

k^{app} can be regarded as an estimate of k^{eff}.

Considering the shear modulus μ^{app} over V, let us apply the following macroscopic strain tensor in order to solve the micromechanical KUBC problem:

$$\underset{\sim}{\boldsymbol{E}}_\mu = \begin{bmatrix} 0 & \frac{1}{2} & 0 \\ \frac{1}{2} & 0 & 0 \\ 0 & 0 & 0 \end{bmatrix} \tag{1.39}$$

An apparent shear modulus μ^{app} can be defined from the elastic strain energy density for the macroscopic strain given in Equation 1.39 using the Hill–Mandel lemma, such that:

$$\mu^{\text{app}} \hat{=} 2\mathscr{E}^{el}\left(\underset{\sim}{\boldsymbol{E}}_\mu\right) = \langle \underset{\sim}{\boldsymbol{\sigma}} : \underset{\sim}{\boldsymbol{\varepsilon}} \rangle = \langle \underset{\sim}{\boldsymbol{\sigma}} \rangle : \langle \underset{\sim}{\boldsymbol{\varepsilon}} \rangle = \underset{\sim}{\boldsymbol{\Sigma}} : \underset{\sim}{\boldsymbol{E}}_\mu = \Sigma_{12} \tag{1.40}$$

μ^{app} can be regarded as an estimate of μ^{eff}.

Definition of apparent plastic property

The notion of apparent viscoplastic parameter is considered as defined in [Madi et al., 2006] for characterising viscoplasticity. For the concerned polycrystalline copper, two hypotheses are made:

1) The von Mises criterion is defined for isotropic material behaviour. In the present case, although the local material behaviour is anisotropic, the macroscopic behaviour is considered isotropic, since the grains have been generated with a statistically isotropic distribution of orientation. Therefore, the von Mises criterion is suitable for macroscopic numerical considerations. Based on von Mises criterion, the total plastic deformation is equal to the sum of micro shear deformation on all activated slip systems for each element of volume, as described in the following equations:

$$\dot{e}^{\mathrm{p}} = \underset{\sim}{\boldsymbol{\Sigma}} : \dot{\underset{\sim}{\boldsymbol{E}}}^{\mathrm{vp}} = \sum_{(\mathrm{s})=1}^{12} \tau^{(\mathrm{s})} \dot{\gamma}^{(\mathrm{s})} = \sigma^{\mathrm{eq}} \dot{p} \tag{1.41}$$

where, $\dot{e}^{\mathrm{p}}$ is the macroscopic plastic energy rate density, $\dot{\underset{\sim}{\boldsymbol{E}}}^{\mathrm{vp}}$, the viscoplastic macroscopic strain tensor, $\tau^{(\mathrm{s})}$, the resolved shear stress on slip system s, $\dot{\gamma}^{(\mathrm{s})}$, the slip rate, $\sigma^{\mathrm{eq}} = \sqrt{3J_2\left(S_{ij}\right)}$, the equivalent uniaxial tensile stress, which is associated with $J_2\left(S_{ij}\right)$ the second invariant of the deviatoric part S_{ij} of the macroscopic stress tensor $\underset{\sim}{\boldsymbol{\Sigma}}$. p is the accumulated plastic strain. Local quantities, such as the resolved shear stress and plastic slip rate on each slip systems are computed in the local material frame, and expressed in the macroscopic frame prior to averaging.

2) The apparent global plastic strain rate can be also approximated by a simple Norton flow rule:

$$\dot{p} = \left(\frac{\sqrt{3J_2\left(S_{ij}\right)}}{K^{\mathrm{app}}} \right)^{n^{\mathrm{app}}} \tag{1.42}$$

Generally, this assumption is only valid if each phase has the same parameters n and K, as stated by [Rougier et al., 1993] in the case of creep. We assume the same K and n parameters for each slip system in pure polycrystalline copper. By combining Eqs. 1.41 and 1.42, it yields:

$$\dot{e}^{\mathrm{p}} = \sqrt{3J_2\left(S_{ij}\right)} \left(\frac{\sqrt{3J_2\left(S_{ij}\right)}}{K^{\mathrm{app}}} \right)^{n^{\mathrm{app}}} \tag{1.43}$$

By using the viscoplastic parameter $P_v^{\mathrm{app}} = \dfrac{1}{K^n}$ introduced in [Madi et al., 2006]:

$$\dot{e}^{\mathrm{p}} = \underset{\sim}{\boldsymbol{\Sigma}} : \dot{\underset{\sim}{\boldsymbol{E}}}^{\mathrm{vp}} = \sum_{(\mathrm{s})=1}^{12} \tau^{(\mathrm{s})} \dot{\gamma}^{(\mathrm{s})} = P_v^{\mathrm{app}} \left(\sqrt{3J_2\left(S_{ij}\right)} \right)^{n^{\mathrm{app}}+1} \tag{1.44}$$

For each realisation, uniaxial tensile testing is carried out using PBC with prescribed macroscopic strain rate. As pure copper is rather strain rate insensitive at room temperature

[Carreker and Hibbard, 1953], only one strain rate is considered for the test ($10^{-3}\mathrm{s}^{-1}$). From the simulation, values for $\sqrt{3J_2\left(S_{ij}\right)}$ and $\dot{e}^{\mathrm{p}}$ are obtained. From Eq. 1.44, the value of P_v^{app} is identified.

Furthermore, in order to determine the RVE size of polycrystalline copper for viscoplasticity, the intrinsic dissipation energy density during tensile test was also chosen as one property to estimate the RVE size. For each slip system, the intrinsic dissipation power density $\dot{d}_1^{(\mathrm{s})}$ is defined as the plastic power $\tau^{(\mathrm{s})}\dot{\gamma}^{(\mathrm{s})}$ minus the stored power associated with isotropic hardening, $r^{(\mathrm{s})}\dot{q}^{(\mathrm{s})}$, and kinematic hardening, $x^{(\mathrm{s})}\dot{\alpha}^{(\mathrm{s})}$, as proposed by [Chrysochoos et al., 1989], hence:

$$\dot{d}_1^{(\mathrm{s})} = \tau^{(\mathrm{s})}\dot{\gamma}^{(\mathrm{s})} - x^{(\mathrm{s})}\dot{\alpha}^{(\mathrm{s})} - r^{(\mathrm{s})}\dot{q}^{(\mathrm{s})} \tag{1.45}$$

The intrinsic dissipation energy density during the tensile test is computed as the volume average of the time integral of Eq. 1.45.

Determination of RVE size

In order to determine the RVE size of polycrystalline copper for viscoplasticity, we are relying on the approach introduced in Section 1.1.

1.3.4 Results and discussion

According to the approach described in Section 1.1, several realisations were generated for statistical analysis, with different number of grains, ranging from 8 to 343, as listed in Tab. 1.4. The generated microstructure has a mean grain diameter of 20 µm. Thus, the actual volume size is directly related to the number of grains. For the sake of simplicity, we used the number of grains in place of the volume size (V). Generally, the number of realisations n should be different for each domain size in order to achieve a similar measurement error for all sizes considered. The relative measurement error for all domain sizes were controlled at under 1% for elastic properties, under 3% for intrinsic dissipation. On the contrary, the measurement error remains high, just under 120% for apparent viscoplastic parameter P_v^{app}, likely due to the large intrinsic variability of the property. To accomplish the generation and meshing of microstructures, a computer equipped with an Intel Core i7-4750HQ CPU 2.0GHz and 8GB RAM was used. The consumed time of meshing, as well as elastic and plastic calculations for one realisation is also presented for reference in Tab. 1.4.

Isotropy of mean apparent moduli

The microstructures in this work are expected to be macroscopically isotropic, this assumption needs to be assessed. For that purpose, six computations are necessary for finding the 21 components of apparent elastic tensor $\underset{\approx}{\boldsymbol{C}}^{\mathrm{app}}$ on each realisation. The standard deviation decreases

Number of grains (V)	8	27	64	125	216	343
Mesh generation time (min)	0.25	1.5	6	13	22	35
Elastic computation time (s)	1.2	3.0	6.7	15	27	42
Plastic computation time (min)	2.0	6.7	18	38	98	194
Realisations for μ^{app}	514	140	56	28	16	10
Realisations for k^{app}	466	112	41	19	15	10
Realisations for d_1^{app}	352	90	40	28	14	8
Realisations for P_v^{app}	56	38	26	16	12	6

Table 1.4: Number of realisations used for the considered domain sizes

with increasing volume size. The resulting tensors can be found in [Yang et al., 2019] but have been omitted here, for the sake of conciseness. The averaged tensor components obtained for 343 grains are characteristic of isotropic elasticity since $\overline{C}_{11} \sim \overline{C}_{22} \sim \overline{C}_{33}$ and $\overline{C}_{12} \sim \overline{C}_{13} \sim \overline{C}_{23}$ with a maximal error of 5%, and $\overline{C}_{44} \sim \overline{C}_{55} \sim \overline{C}_{66}$ are approximately equal to $\frac{\overline{C}_{11} - \overline{C}_{12}}{2}$ with a maximal error of 10%. The remaining components should vanish in the isotropic case, and here, they take up less than 1% of $\overline{C}_{11}$. It can be also observed that the elastic moduli tensor components have not reached their converged values for smaller volumes, which is likely due to a bias of representatively as studied by [Hazanov and Huet, 1994, Huet, 1997, Hazanov, 1998].

Apparent elastic and plastic properties

After confirming the isotropy of the generated microstructures, elastic properties μ^{app} and k^{app} are investigated, as well as the intrinsic dissipation and the apparent viscoplastic parameter for all realisations. Fig. 1.11 illustrates the changes of the four apparent parameters with respect to volume size, including mean value and standard deviation. Increasing the volume size, the mean values of μ^{app} and k^{app} increase gradually and stabilise respectively at 49031 ± 1085 MPa and 130972 ± 2385 MPa on the 343 volume size, which are consistent with typical values for polycrystalline copper. Similar convergence behaviour can be observed for d_1^{app}. Its mean value reaches 53 J/m^3 with the corresponding intervals of confidence of 4.3 J/m^3 on the 343 volume size, which is in the same magnitude level as previous studies for metals, such as [Chrysochoos and Martin, 1989, Chrysochoos et al., 2009].

The definition of P_v^{app} consists of two parameters, K^{app} and n^{app}. The fluctuation of both parameters may yield a large change of P_v^{app} in magnitude. The relative error around 9% on $\log P_v^{\text{app}}$ is a little higher than for elastic properties and intrinsic dissipation, mostly due to a smaller number of realisations. When the volume size increases to 343, the fluctuation tends to weaken, and the averaged value of $\log P_v^{\text{app}}$ stabilises at -10.74, with a fluctuation range of ± 0.8. Interestingly, this value is also approximately equal to the combination of the two parameters of the single crystal constitutive law, $K = 5$ and $n = 10$, producing the value of $10^{-10.7}$ as the

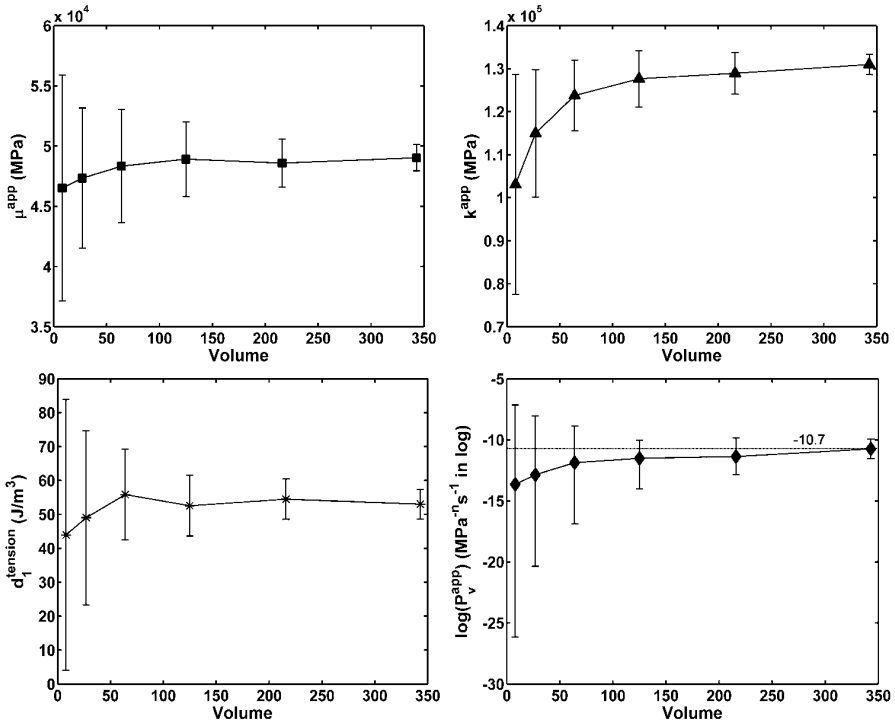

Figure 1.11: The mean values for the apparent properties with increasing volume size. The error bars correspond to plus and minus 2 standard deviations

definition of $P_v = \frac{1}{K^n}$. The apparent parameters K^{app} and n^{app} converge at 29.06 and 7.32 for 343 grains, with a relative error of about 3% for both K^{app} and n^{app}.

Variance and RVE size

The evolution of the ensemble variance with respect to volume is plotted in Fig. 1.12 for each four properties considered. Parameters γ and K are identified using Eq. 1.17. Values of γ are close to 1 for μ^{app}, k^{app}, and d_1^{app}. For P_v^{app}, γ reaches a value of 4.9, indicating a much faster statistical convergence rate than for the other properties.

One of the advantages of relying on microstructural computation is the ability to consider each grain or phase individually. For this purpose, Fig. 1.13 illustrates the impact of grain orientation on crystal plasticity, by analysing the local heterogeneities of the plastic behaviour in a realisation with 343 grains, including von Mises equivalent stress and plastic power evolution with respect to the equivalent macroscopic stress. The curves for the two properties were drawn for each grain and the whole volume. As shown in the von Mises curves, grains in the volume hold different equivalent stress, ranging from 6 MPa to 16 MPa. Some grains actually remain in the elastic regime during the tensile test. Meanwhile, grains yield heterogeneous plastic power depending on the grain orientation for the same stress level, as shown on the right hand side in Fig. 1.13.

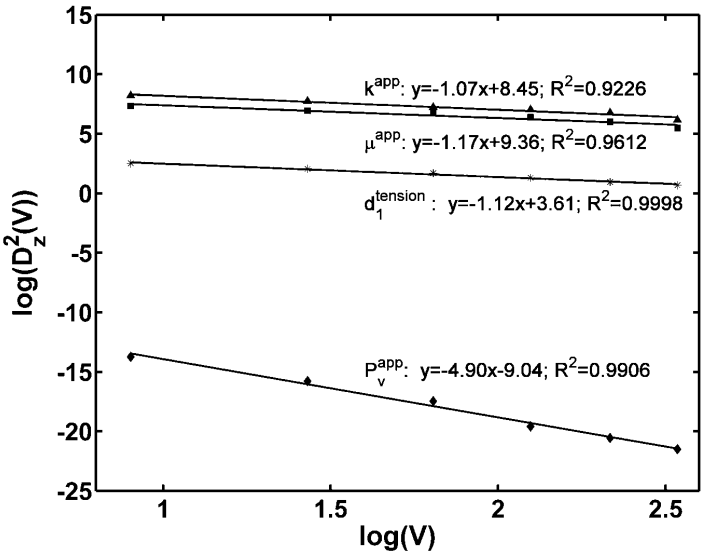

Figure 1.12: Variance for the elastic and viscoplastic properties depending on the volume of simulation V

These heterogeneities are related to the local grain orientation, local anisotropic elasticity and anisotropic crystal plasticity framework.

Using Eq. 1.16, RVE sizes are computed using the parameters identified hereabove, results are summarised in Tab. 1.5. In practical use, for a 5% relative error, a volume size of 135 grains can be considered for elastic properties, while for intrinsic dissipation and apparent viscoplastic parameter, the volume sizes must be larger than 1010 grains and 1445 grains, respectively. If a higher precision is required, more realisations can be also considered, *e.g.* for a precision of 1% with $n = 50$ realisations, $V_{\mathrm{RVE}}^{\mu^{\mathrm{app}}} = 71$, $V_{\mathrm{RVE}}^{k^{\mathrm{app}}} = 54$, $V_{\mathrm{RVE}}^{d_1^{\mathrm{app}}} = 545$, and $V_{\mathrm{RVE}}^{P_v^{\mathrm{app}}} = 1254$.

In the case of isotropic plasticity behaviour, the RVE size for the viscoplastic parameter, used by [Madi et al., 2006] was found to be smaller than for the elastic moduli ones. A different conclusion with the present results is likely due to the difference of material behaviour, *i.e.* anisotropic elasticity and crystal plasticity. Crystal plasticity highly depends on the grain orientation, as different activated slip systems produce different plastic deformations. The effect of anisotropic elasticity appears to yield lower statistical heterogeneity than the crystal plasticity behaviour, *i.e.* yielding a smaller RVE size in comparison.

Based on Fig. 1.13, it appears that plastic deformation takes place in most grains during the tensile test, but localisation operates only in a minority of grains, *i.e.* less than 10% of them. This plastic strain localisation and stress concentration phenomenon could explain a high γ exponent for P_v^{app}. As a matter of fact, a pattern of localisation will form for any number of grains due to the morphological and material anisotropies. Therefore, a large number of grains is not needed for ensemble variance convergence on the averaged value of the viscoplastic parameter. Results

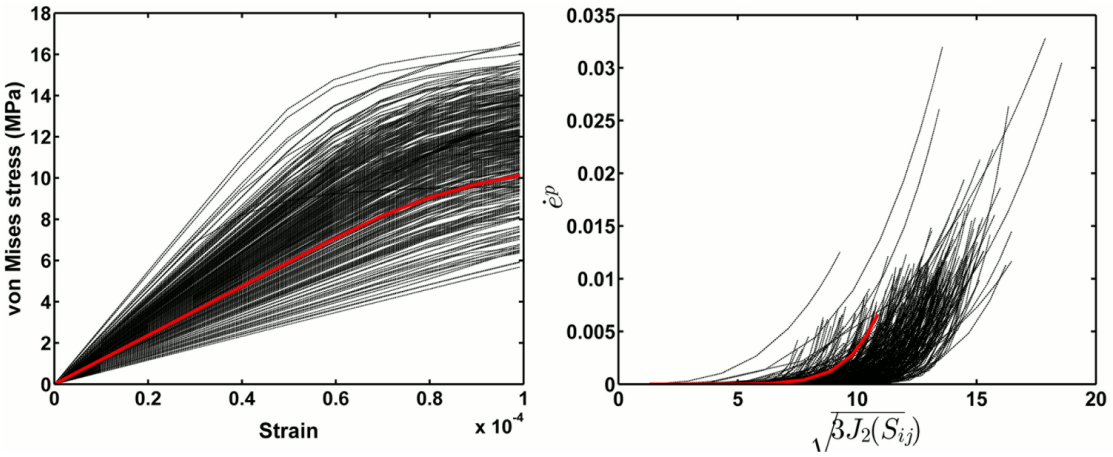

Figure 1.13: Tensile curves (left) and plastic power evolution with respect to the equivalent uniaxial tensile stress (right) for each grain in a 343 grains sample (black lines represent grains; red line is for the whole volume)

Z	γ	K	ϵ_{rel}	V_{RVE}
μ^{app}	1.07	2.82×10^8	1%	2756
	1.07	2.82×10^8	2%	753
	1.07	2.82×10^8	5%	135
	1.07	2.82×10^8	10%	37
k^{app}	1.17	2.29×10^9	1%	1504
	1.17	2.29×10^9	2%	461
	1.17	2.29×10^9	5%	96
	1.17	2.29×10^9	10%	29
d_1^{app}	1.12	4.07×10^3	1%	17894
	1.12	4.07×10^3	2%	5190
	1.12	4.07×10^3	5%	1010
	1.12	4.07×10^3	10%	293
P_v^{app}	4.90	9.12×10^{-10}	1%	2788
	4.90	9.12×10^{-10}	2%	2101
	4.90	9.12×10^{-10}	5%	1445
	4.90	9.12×10^{-10}	10%	1089

Table 1.5: V_{RVE} size estimated using Eq. 1.16 for polycrystalline copper with $n = 1$ realisation

from Eq. 1.16 and Table 1.5 might lead to another conclusion: the RVE size for P_v^{app} is rather large and only decreases slowly with increasing the relative error. This is due to the high intrinsic point variance of P_v^{app}, *i.e.* K in Eq. 1.16. This variability is related to the nonlinear nature of the localisation phenomenon. This large point variance counterbalances the effect of a fast ensemble variance convergence. One could argue that the point variance of P_v^{app} is likely to be related to a strong material heterogeneity as induced in the present work by elastic anisotropy and crystal plasticity.

1.3.5 Conclusions and perspectives

Aiming at computing the intrinsic dissipation of pure copper based on a crystal plasticity framework, virtual polycrystalline samples were generated, and the RVE size for various mechanical properties was estimated. A statistical analysis method was used to determine the RVE size of polycrystalline pure copper for four properties, including two isotropic elastic properties: shear and bulk modulus, the viscoplastic parameter, and intrinsic dissipation energy density during a tensile test. The main conclusions are listed below:

1. The statistical RVE method developed by [Kanit et al., 2003] is applicable to viscoplastic polycrystalline materials modelled within a crystal plasticity finite element framework;
2. RVE sizes obtained are smaller for elastic properties than for plastic properties, likely due to the anisotropic elastoviscoplastic model chosen for the material behaviour, as well as the polycrystalline nature of the samples, both inducing stronger heterogeneities in the mechanical fields. This conclusion is opposite to the ones made by [Madi et al., 2006], while considering an isotropic elastoplastic biphasic material;
3. The computational microstructural study allowed to characterise the local heterogeneities associated with plasticity, hence giving an insight on the microstructural behaviour explaining the statistical macroscopic trends observed;
4. The viscoplastic parameter is related to the nonlinear phenomenon of plastic localisation, inducing strong local variability. This inherent intrinsic heterogeneity leads to a high point variance, which itself will invariably yield larger RVE size in comparison to linear properties.

The statistical analysis provided in this work can be applied to other polycrystalline materials for various properties, given that a microstructural morphological model is available for generating a virtual statistical sampling population. Introducing more information about the microstructure of materials appears as a necessity for improving the predictive capability of such statistical techniques. Further work will involve the extension of the present approach to the fatigue of metallic polycrystalline materials. The fatigue strength of polycrystalline materials is a longstanding problem in mechanical design, especially in the very high cycle fatigue regime, where the stress level is much lower than tra-

ditional fatigue limit [Bathias and Paris, 2004, Stanzl-Tschegg et al., 2007, Phung et al., 2014, Torabian et al., 2016a, Torabian et al., 2016b, Torabian et al., 2017b, Torabian et al., 2017a]. In order to reduce experiment duration time, many authors have resorted to the method of self-heating tests, in which the thermomechanical response of the material during cyclic loading is analysed and the intrinsic dissipation is taken as the fatigue damage indicator to evaluate fatigue strength at various stress levels in the high and very high cycles fatigue domain [Luong, 1995, La Rosa and Risitano, 2000, Boulanger et al., 2004, Doudard et al., 2010, Chrysochoos et al., 2008, Connesson et al., 2011, Blanche et al., 2015, Guo et al., 2015]. Physically, coming from the irreversibility of the plastic deformation, intrinsic dissipation is assumed to be related to the microplastic deformation in gigacycle fatigue regime, *i.e.* the crystal slipping behaviour at the grain scale. The approach developed in the present work could thus be used to determine the RVE size associated with intrinsic dissipation during very-high cycle fatigue. Relying on full-field crystal plasticity finite element analysis could thus further our understanding of the damage phenomena taking place at the microscale.

1.4 Outlook

The use of morphological descriptors can be a very efficient way to improve modelling, in the case of homogenisation for instance. The statistical method developed in [Cailletaud et al., 1994] and [Kanit et al., 2003] was generalised in [Dirrenberger et al., 2014] to media with non-finite integral range. In the present chapter we presented new developments regarding RVE size determination, on two different case studies, which are testimonies of the possibilities opened by applying mathematical morphology to the analysis of complex, heterogeneous materials at multiple scales. In the first case, the method was applied to a 1-D heterogeneous multilayered composite material in order to evaluate sampling representativity for microstructural characterisation. The analysis of variance evolution with respect to the system size allowed us to link morphological fluctuation to instabilities taking place during extrusion processing. In the second case, our aim was to extend the statistical definition of RVE size to the case of nonlinear viscoplastic behaviour, which is generally considered for crystal plasticity finite element simulations. In order to assess the representativity of virtual polycrystalline samples of copper in this context, the dissipated energy density and viscoplastic parameter were considered. Hopefully, assessing the problem of representativity in realistic virtual microstructures will help furthering our understanding of the damage mechanisms happening within metallic materials, in the context of thermomechanical fatigue for instance. Now assuming that underlying microstructures are well understood, let us consider a larger scale, the millimetre scale, where materials can be architectured.

2 Architectured materials

Form follows function—that has been misunderstood.
Form and function should be one, joined in a spiritual union.

— Frank Lloyd Wright, The Future of Architecture (1953)

2.1 Introduction to architectured materials

Architectured materials are a rising class of materials that bring new possibilities in terms of functional properties, filling the gaps and pushing the limits of Ashby's materials performance maps [Ashby and Bréchet, 2003]. The term architectured materials encompasses any microstructure designed in a thoughtful fashion, such that some of its materials properties, *e.g.* yield strength/density, have been improved in comparison to those of its constituents, due to both structure and composite effects, which depend on the multiphase morphology, *i.e.* the relative topological arrangement between each phase [Ashby and Bréchet, 2003, Bouaziz et al., 2008, Bréchet and Embury, 2013].

There are many examples: particulate and fibrous composites, foams, sandwich structures, woven materials, lattice structures, etc. with different objectives. For instance, developing architectured porous materials for structural, acoustic and insulation properties [Caty et al., 2008, Fallet et al., 2008], entangled monofilament of pearlitic steel [Courtois et al., 2012, Rodney et al., 2016], sandwich composite structures [Kolopp et al., 2013, Piollet et al., 2013, Piollet, 2014, Piollet et al., 2016], segmented interlocking structures [Dyskin et al., 2001, Estrin et al., 2003, Molotnikov et al., 2007, Schaare et al., 2009, Estrin et al., 2011, Mather et al., 2012, Krause et al., 2012, Molotnikov et al., 2013, Molotnikov et al., 2015, Feng et al., 2015, Khandelwal et al., 2015, Djumas et al., 2016, Djumas et al., 2017], asymmetric frictional materials [Bafekrpour et al., 2014, Bafekrpour et al., 2015], woven and non-woven textile composites [Mezeix et al., 2009, Lewandowski et al., 2012, Dirrenberger et al., 2014], porous metallic glasses [Sarac et al., 2014], hierarchical composites [Henry and Pimenta, 2018], crumpled metal-

lic foils [Bouaziz et al., 2013], etc.

One can play on many parameters in order to obtain architectured materials, but all of them are related either to the microstructure or the geometry. Parameters related to the microstructure can be optimised for specific needs using a materials-by-design approach, which has been thoroughly developed by chemists, materials scientists and metallurgists. Properties improvements related to microstructural design are intrinsically linked to the synthesis and processing of materials and are therefore due to micro and nanoscale phenomena, taking place at a scale ranging from 1 nm to 10 µm. This scale is below the scope of the present chapter, but has been extensively studied in the literature [Olson, 2001, Freeman, 2002, Embury and Bouaziz, 2010].

Until now, most architectured materials in the literature have been obtained empirically. By capitalising on the concept of localised processing of thin structures, our efforts at the PIMM laboratory have been focused on developing systematic tools to determine materials architecturation patterns, for a given set of requirements. For instance, these patterns come as an output from a computational shape-optimisation loop developed around a heuristic generative geometry module, based on cellular automata (CA), and a cost function evaluation module, based on the finite element (FE) method. This cost function has to be minimised for given constraints [Bendsøe and Sigmund, 2004]. In the case of linear elastic problems, the cost function can be related to the elastic energy density computed by numerical homogenisation at the scale of the structure [Allaire, 2002]. The cost function value is then used as a feedback, and an optimised shape is generated accordingly following a specific evolution algorithm. The spatial resolution associated with the shape-optimisation can be chosen to be relevant for localised laser treatment, *i.e.* 1 mm, corresponding to a representative scale of the underlying microstructure; this allows us to use homogenised behaviour for each grid-cell in the simulation [Dirrenberger, 2012].

From a macroscopic viewpoint, parameters related to the geometry have mainly been the responsibility of structural and civil engineers for centuries: to efficiently distribute materials within structures. An obvious example would be the many different strategies available for building bridges. At the millimetre scale, materials can be considered as structures, *i.e.* one can enhance the bending stiffness of a component by modifying its geometry while keeping the lineic mass (for beams) or surfacic mass (for plates) unchanged [Weaver and Ashby, 1996]. On the other hand, one might need a lower flexural strength for specific applications, with the same lineic and/or surfacic masses. This can be achieved with strand structures, *i.e.* by creating topological interfaces in the material. Processing remains the key technological issue for further development of architectured materials as the microstructure, the shape, and the scale of the material depend on it, as shown on Fig. 2.1. Progress is made every day in terms of material processing at the lab scale, as it was done in [Schaedler et al., 2011] by using a bottom-up approach of sequential processing techniques in order to fabricate ultralight metallic microlattice materials [Schaedler and Carter, 2016]. There is still a long way to go for the industry to actually apply architectured materials in product manufacturing; our work aims at fostering material processing enabling the use of architectured materials in the industry.

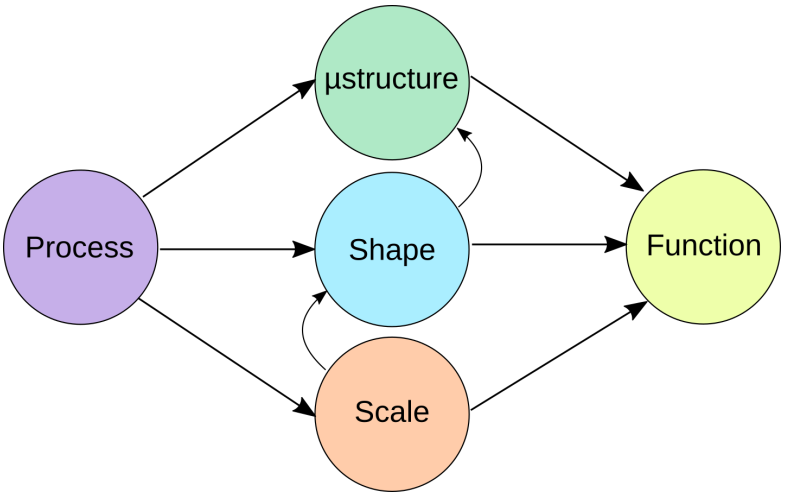

Figure 2.1: Functionality is enabled by the microstructure, shape, and scale, all of which depend on material processing

Architectured materials lie between the microscale and the macroscale, as shown on Figure 2.2. This class of materials involves geometrically engineered distributions of microstructural phases at a scale comparable to the scale of the component [Ashby and Bréchet, 2003, Bouaziz et al., 2008, Bréchet and Embury, 2013], thus calling for enriched models of continuum mechanics in order to determine the effective properties of materials [Geers and Yvonnet, 2016, Matouš et al., 2017], *e.g.* generalised continua theories, in order to describe the behaviour of architectured materials, such as strain-gradient elasticity [Auffray et al., 2015], and strain-gradient plasticity. This topic has been especially fruitful these last few years in the mechanics of materials community [Lebée and Sab, 2012, Trinh et al., 2012, Chen et al., 2014, Auffray et al., 2015, Placidi and El Dhaba, 2015, Rosi and Auffray, 2016, Andreaus et al., 2016, Placidi et al., 2017, dell'Isola et al., 2017]; this results in the availability of versatile models able to describe the various situations encountered with architectured materials. Given mature processing techniques, architectured materials are promised to a bright future in industrial applications due to their enticing customisable specific properties and the opportunity for multifunctionality.

When considering actual applications, one engineering challenge is to predict the effective properties of such materials; computational homogenisation using finite element analysis is a powerful tool to do so. Homogenised behaviour of architectured materials can thus be used in large structural computations, hence enabling the dissemination of architectured materials in the industry. Furthermore, computational homogenisation is the basis for computational topology optimisation [Allaire, 2002, Bendsøe and Sigmund, 2004, Guest and Prévost, 2006, Challis et al., 2008, Xu et al., 2016a, Vicente et al., 2016, Xu et al., 2016b, Salonitis et al., 2017, Asadpoure et al., 2017, Khakalo and Niiranen, 2017, Wang et al., 2017b] which will give rise to the next generation of architectured materials as it can already be seen in the works of [Laszczyk et al., 2009, Andreassen et al., 2014, Vermaak et al., 2014, Körner and Liebold-Ribeiro, 2015, Hopkins et al., 2016, Kotani and Ikeda, 2016, Ghaedizadeh et al., 2016, Ren et al., 2016, Liu et al., 2016,

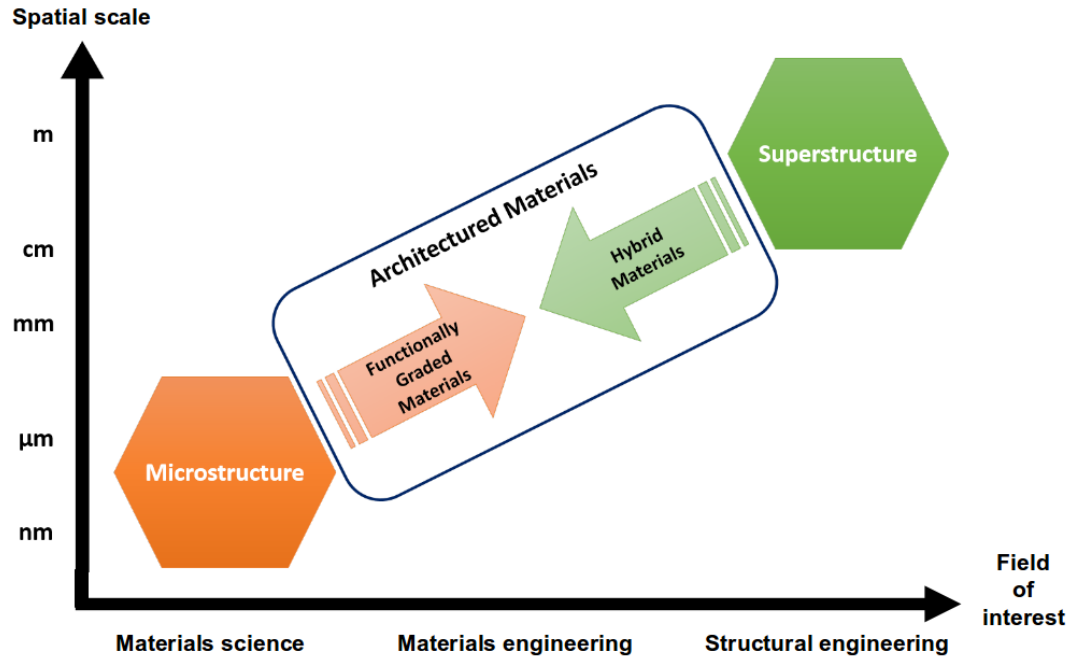

Figure 2.2: Characteristic lengths associated with architectured materials and different fields of interest for materials, adapted from [Bouaziz et al., 2008]

Dalaq et al., 2016, Osanov and Guest, 2016, Faure et al., 2017, Wang et al., 2017a].

The works presented in the present chapter stem from a certain school of thought that has been developed through previous collaborative research projects related to architectured materials, conducted in France under the influence of Prof. Y. Bréchet. The MAPO project (2005-2008), coordinated by CNRS and ONERA, aimed at developing architectured porous materials for structural, acoustic and insulation properties [Caty et al., 2008, Fallet et al., 2008]. Another project was the CPR MAM (2008-2011) (for multifunctional architectured materials), which led to further interesting results related to modelling [Trinh et al., 2012] and topological optimisation of architectured plates, as well as phase-changing materials for heat storage applications. The MANSART project (2009-2012), funded by ANR, aimed at exploring new tools to develop architectured materials for crashworthiness properties. Several architectured materials were considered to fulfil industrial requirements: entangled monofilament of perlitic steel [Courtois et al., 2012], sandwich composite structures [Kolopp et al., 2013], segmented interlocking structures, woven and non-woven textile composites [Lewandowski et al., 2012, Dirrenberger et al., 2014], as well as lattice-structures with negative Poisson's ratio (auxetics) [Dirrenberger et al., 2011, Dirrenberger et al., 2012, Dirrenberger et al., 2013]. Focus was made mostly on the characterisation and modelling of the materials listed. Optimisation of architectured sandwich materials was also investigated at ONERA [Leite et al., 2012a, Leite et al., 2012b]. From an industrial viewpoint, architectured materials have also been investigated: for instance, EDF collaborated on a study of metal-polymer multilayers for barrier properties [Garnier et al., 2009]; Airbus took

part in the MANSART project; ArcelorMittal R&D has been very active in the field of architectured materials, especially on the topic of processing and mechanical properties of architectured metallic materials [Bouaziz et al., 2008, Embury and Bouaziz, 2010, Chéhab et al., 2009, Cicoria et al., 2013, Bouaziz et al., 2013].

On an international scale, architectured materials have also been an exciting research topic in recent years, especially regarding the processing of architectured metallic foams [Brothers and Dunand, 2006, Erk et al., 2008] or multi-scale architectured ceramics [Mirkhalaf et al., 2014]. For architectured metallic sheets, the contribution of Embury's team at McMaster University is of prime importance [Embury and Bouaziz, 2010, Chéhab et al., 2009]. Apart from processing, most efforts have been focused on the modelling of architectured materials. In particular, the pioneering works done at Cambridge on truss-structures [Deshpande et al., 2001b] and metallic foams led to useful results for the modelling of architectured materials [Fleck et al., 2010]. The mechanical modelling of bio-inspired architectured materials has been pursued successfully by Dunlop's team at the Max Planck Institute of Colloids and Interfaces in Potsdam, and now at the University of Salzburg [Dunlop et al., 2010, Dunlop and Fratzl, 2010, Dunlop et al., 2011, Turcaud et al., 2011, Fratzl et al., 2013, Guiducci et al., 2014, Guiducci et al., 2015, Guiducci et al., 2016, Stoychev et al., 2016, Jayasankar et al., 2017]. Several works have demonstrated the interest for designing recursive or nested material architectures to achieve enhanced specific mechanical properties [Ajdari et al., 2012, Rayneau-Kirkhope et al., 2012]. Elastic instabilities have been considered for shape-generation of architectured materials, as showed by the work of Bertoldi's group in Harvard [Bertoldi et al., 2010, Shim et al., 2013]. In summary, architectured materials are subject to active research in coordinated research groups and industrial firms in France, as well as in world-class universities abroad. Given mature processing techniques, architectured materials are promised to a bright future in industrial applications due to their enticing customisable and multifunctional specific properties. Nevertheless, in most of the works cited, architectured materials are considered from the modelling and simulation viewpoint alone or, when experiments have been conducted, the materials have been processed with a trial-and-error empirical approach which is not satisfying in order to transfer this technology to the industry. Some of our efforts aim at tackling this problem by establishing a systematic computational approach for modelling, as well as a deterministically controlled processing route for architectured materials.

Therefore, the development of architectured materials is related to the availability of appropriate computational tools for both design and modelling, but also for computerised manufacturing as for the various additive manufacturing techniques considered for producing architectured materials. In order to foster the development of architectured materials within an industrial framework, the availability of modelling bricks describing the underlying behaviour of such materials, is a necessity in order for these to be used in structural simulation codes. We are aiming at developing product design methodologies taking into account the specificities of architectured materials. To do so, we focused on computational approaches to modelling and optimising architectured materials, as well as novel processing techniques.

2.2 Computational homogenisation of architectured materials

2.2.1 Constitutive equations

When heterogeneous materials are assumed to respond linearly to mechanical loading, constitutive relations are expressed locally for each phase in a linear elasticity framework using the generalized Hooke law:

$$\underset{\sim}{\boldsymbol{\sigma}} = \underset{\approx}{\boldsymbol{c}} : \underset{\sim}{\boldsymbol{\varepsilon}} \tag{2.1}$$

with $\underset{\sim}{\boldsymbol{\sigma}}$ second-order symmetric Cauchy stress tensor, $\underset{\sim}{\boldsymbol{\varepsilon}}$ second-order symmetric engineering strain tensor and $\underset{\approx}{\boldsymbol{c}}$, fourth-order positive definite tensor of elastic moduli, also known as the elastic stiffness tensor. It is possible to express strain as a function of stress using the Compliance tensor $\underset{\approx}{\boldsymbol{s}}$, which is defined as the inverse of tensor $\underset{\approx}{\boldsymbol{c}}$:

$$\underset{\sim}{\boldsymbol{\varepsilon}} = \underset{\approx}{\boldsymbol{s}} : \underset{\sim}{\boldsymbol{\sigma}} \quad \text{with,} \quad \underset{\approx}{\boldsymbol{s}} := \underset{\approx}{\boldsymbol{c}}^{-1} \tag{2.2}$$

such that,

$$\underset{\approx}{\boldsymbol{s}} \cdot \underset{\approx}{\boldsymbol{c}} = \underset{\approx}{\boldsymbol{I}} \tag{2.3}$$

with $\underset{\approx}{\boldsymbol{I}}$, fourth-order identity tensor operating on symmetric second-order tensors such that:

$$\underset{\approx}{\boldsymbol{I}} = \frac{1}{2}\left(\delta_{ik}\delta_{jl} + \delta_{il}\delta_{jk}\right) \underline{\boldsymbol{e}}_i \otimes \underline{\boldsymbol{e}}_j \otimes \underline{\boldsymbol{e}}_k \otimes \underline{\boldsymbol{e}}_l \tag{2.4}$$

The 81 components of c_{ijkl} can be thinned-down to 21 for the most anisotropic case (triclinic elasticity) due to symmetries of $\underset{\sim}{\boldsymbol{\sigma}}$ and $\underset{\sim}{\boldsymbol{\varepsilon}}$. By isomorphism, these 21 components can be written as a symmetric second-order tensor (matrix) c_{IJ} with 21 independent components using Voigt's notation:

$$\begin{bmatrix} \sigma_{11} \\ \sigma_{22} \\ \sigma_{33} \\ \sigma_{23} \\ \sigma_{31} \\ \sigma_{12} \end{bmatrix} = \begin{bmatrix} c_{11} & c_{12} & c_{13} & c_{14} & c_{15} & c_{16} \\ \bullet & c_{22} & c_{23} & c_{24} & c_{25} & c_{26} \\ \bullet & \bullet & c_{33} & c_{34} & c_{35} & c_{36} \\ \bullet & \bullet & \bullet & c_{44} & c_{45} & c_{46} \\ \bullet & \bullet & \bullet & \bullet & c_{55} & c_{56} \\ \bullet & \bullet & \bullet & \bullet & \bullet & c_{66} \end{bmatrix} \begin{bmatrix} \varepsilon_{11} \\ \varepsilon_{22} \\ \varepsilon_{33} \\ \gamma_{23} \\ \gamma_{31} \\ \gamma_{12} \end{bmatrix} \tag{2.5}$$

Engineering shear strain is used in the strain column-vector:

$$\gamma_{23} = 2\varepsilon_{23}$$
$$\gamma_{31} = 2\varepsilon_{31}$$
$$\gamma_{12} = 2\varepsilon_{12}$$

The matrix form of the compliance tensor is obtained by inverting Equation 2.5:

$$\begin{bmatrix} \varepsilon_{11} \\ \varepsilon_{22} \\ \varepsilon_{33} \\ \gamma_{23} \\ \gamma_{31} \\ \gamma_{12} \end{bmatrix} = \begin{bmatrix} s_{11} & s_{12} & s_{13} & s_{14} & s_{15} & s_{16} \\ \bullet & s_{22} & s_{23} & s_{24} & s_{25} & s_{26} \\ \bullet & \bullet & s_{33} & s_{34} & s_{35} & s_{36} \\ \bullet & \bullet & \bullet & s_{44} & s_{45} & s_{46} \\ \bullet & \bullet & \bullet & \bullet & s_{55} & s_{56} \\ \bullet & \bullet & \bullet & \bullet & \bullet & s_{66} \end{bmatrix} \begin{bmatrix} \sigma_{11} \\ \sigma_{22} \\ \sigma_{33} \\ \sigma_{23} \\ \sigma_{31} \\ \sigma_{12} \end{bmatrix} \tag{2.6}$$

The finite element code used in the applications is actually making use of the Mandel notation presented in Equations 2.7 and 2.8:

$$\begin{bmatrix} \sigma_{11} \\ \sigma_{22} \\ \sigma_{33} \\ \sqrt{2}\sigma_{23} \\ \sqrt{2}\sigma_{31} \\ \sqrt{2}\sigma_{12} \end{bmatrix} = \begin{bmatrix} c_{11} & c_{12} & c_{13} & \sqrt{2}c_{14} & \sqrt{2}c_{15} & \sqrt{2}c_{16} \\ \bullet & c_{22} & c_{23} & \sqrt{2}c_{24} & \sqrt{2}c_{25} & \sqrt{2}c_{26} \\ \bullet & \bullet & c_{33} & \sqrt{2}c_{34} & \sqrt{2}c_{35} & \sqrt{2}c_{36} \\ \bullet & \bullet & \bullet & 2c_{44} & 2c_{45} & 2c_{46} \\ \bullet & \bullet & \bullet & \bullet & 2c_{55} & 2c_{56} \\ \bullet & \bullet & \bullet & \bullet & \bullet & 2c_{66} \end{bmatrix} \begin{bmatrix} \varepsilon_{11} \\ \varepsilon_{22} \\ \varepsilon_{33} \\ \sqrt{2}\varepsilon_{23} \\ \sqrt{2}\varepsilon_{31} \\ \sqrt{2}\varepsilon_{12} \end{bmatrix} \tag{2.7}$$

The matrix form of the compliance tensor is obtained by inverting Equation 2.7:

$$\begin{bmatrix} \varepsilon_{11} \\ \varepsilon_{22} \\ \varepsilon_{33} \\ \sqrt{2}\varepsilon_{23} \\ \sqrt{2}\varepsilon_{31} \\ \sqrt{2}\varepsilon_{12} \end{bmatrix} = \begin{bmatrix} s_{11} & s_{12} & s_{13} & \sqrt{2}s_{14} & \sqrt{2}s_{15} & \sqrt{2}s_{16} \\ \bullet & s_{22} & s_{23} & \sqrt{2}s_{24} & \sqrt{2}s_{25} & \sqrt{2}s_{26} \\ \bullet & \bullet & s_{33} & \sqrt{2}s_{34} & \sqrt{2}s_{35} & \sqrt{2}s_{36} \\ \bullet & \bullet & \bullet & 2s_{44} & 2s_{45} & 2s_{46} \\ \bullet & \bullet & \bullet & \bullet & 2s_{55} & 2s_{56} \\ \bullet & \bullet & \bullet & \bullet & \bullet & 2s_{66} \end{bmatrix} \begin{bmatrix} \sigma_{11} \\ \sigma_{22} \\ \sigma_{33} \\ \sqrt{2}\sigma_{23} \\ \sqrt{2}\sigma_{31} \\ \sqrt{2}\sigma_{12} \end{bmatrix} \tag{2.8}$$

In the isotropic case, $\underset{\approx}{\boldsymbol{c}}$ can be rewritten as follows:

$$\underset{\approx}{\boldsymbol{c}} = 3k\underset{\approx}{\boldsymbol{J}} + 2\mu\underset{\approx}{\boldsymbol{K}} \tag{2.9}$$

with k bulk modulus, μ shear modulus, $\underset{\approx}{\boldsymbol{J}}$ and $\underset{\approx}{\boldsymbol{K}}$ respectively spherical and deviatoric fourth-order tensorial projectors such that,

$$\underset{\approx}{\boldsymbol{J}} = \frac{1}{3}\delta_{ij}\delta_{kl}\,\underline{\boldsymbol{e}}_i \otimes \underline{\boldsymbol{e}}_j \otimes \underline{\boldsymbol{e}}_k \otimes \underline{\boldsymbol{e}}_l \tag{2.10}$$

and

$$\underset{\approx}{\boldsymbol{K}} = \underset{\approx}{\boldsymbol{I}} - \underset{\approx}{\boldsymbol{J}} \tag{2.11}$$

2.2.2 Averaging relations

Let us consider a given volume element (VE) of volume V without voids or rigid inclusions, for the sake of simplicity. For the spatial average over V of a kinematically compatible strain field $\underset{\sim}{\boldsymbol{\varepsilon}}'$ which is defined as the symmetric part of the gradient of a kinematically admissible displacement field $\underline{\boldsymbol{u}}'$:

$$\begin{aligned}
\langle \underset{\sim}{\boldsymbol{\varepsilon}}' \rangle &= \frac{1}{V}\int_V \underset{\sim}{\boldsymbol{\varepsilon}}' dV = \frac{1}{V}\int_V u'_{(i,j)} dV \, \underline{\boldsymbol{e}}_i \otimes \underline{\boldsymbol{e}}_j \\
&= \frac{1}{V}\int_{\partial V} u'_{(i} n_{j)} dS \, \underline{\boldsymbol{e}}_i \otimes \underline{\boldsymbol{e}}_j \\
&= \frac{1}{V}\int_{\partial V} \underline{\boldsymbol{u}}' \overset{s}{\otimes} \underline{\boldsymbol{n}} \, dS
\end{aligned} \tag{2.12}$$

with $\underline{\boldsymbol{u}}' \overset{s}{\otimes} \underline{\boldsymbol{n}}$ and $u'_{(i,j)}$ denoting the symmetric part of the resulting tensor. If one considers now the spatial average of a statically admissible stress field $\underset{\sim}{\boldsymbol{\sigma}}^*$, *i.e.* $\underset{\sim}{\boldsymbol{\sigma}}^* . \nabla = \underline{\mathbf{0}}$ in V, it yields:

$$\begin{aligned}
\langle \underset{\sim}{\boldsymbol{\sigma}}^* \rangle &= \frac{1}{V}\int_V \underset{\sim}{\boldsymbol{\sigma}}^* dV = \frac{1}{V}\int_V \sigma^*_{ij} dV \, \underline{\boldsymbol{e}}_i \otimes \underline{\boldsymbol{e}}_j \\
&= \frac{1}{V}\int_V \sigma^*_{(ik} \delta_{j)k} dV \, \underline{\boldsymbol{e}}_i \otimes \underline{\boldsymbol{e}}_j \\
&= \frac{1}{V}\int_V \sigma^*_{(ik} x_{j),k} dV \, \underline{\boldsymbol{e}}_i \otimes \underline{\boldsymbol{e}}_j \\
&= \frac{1}{V}\int_{\partial V} \sigma^*_{(ik} n_k x_{j)} dS \, \underline{\boldsymbol{e}}_i \otimes \underline{\boldsymbol{e}}_j \\
&= \frac{1}{V}\int_{\partial V} \left(\underset{\sim}{\boldsymbol{\sigma}}^* \cdot \underline{\boldsymbol{n}}\right) \overset{s}{\otimes} \underline{\boldsymbol{x}} \, dS
\end{aligned} \tag{2.13}$$

From these averaging relations, we can define the elastic strain energy density $\mathscr{E}^{\mathrm{el}}$ such that,

$$\begin{aligned}
2\mathscr{E}^{\mathrm{el}} &= \langle \underset{\sim}{\boldsymbol{\sigma}}^* : \underset{\sim}{\boldsymbol{\varepsilon}}' \rangle \\
&= \frac{1}{V}\int_V \underset{\sim}{\boldsymbol{\sigma}}^* : \underset{\sim}{\boldsymbol{\varepsilon}}' dV \\
&= \frac{1}{V}\int_V \sigma^*_{ij} u'_{(i,j)} dV \\
&= \frac{1}{V}\int_V \left(\sigma^*_{ij} u'_i\right)_{,j} dV \\
&= \frac{1}{V}\int_{\partial V} \sigma^*_{ij} n_j u'_i dS \\
&= \frac{1}{V}\int_{\partial V} \left(\underset{\sim}{\boldsymbol{\sigma}}^* \cdot \underline{\boldsymbol{n}}\right) \cdot \underline{\boldsymbol{u}}' dS
\end{aligned} \tag{2.14}$$

2.2.3 Boundary conditions

It is necessary to set boundary conditions to the volume V considered in order to solve the constitutive equations in the case of statics. Let us consider three types of boundary conditions:

Kinematic uniform boundary conditions – KUBC

Displacement $\underline{\boldsymbol{u}}$ is prescribed for any material point $\underline{\boldsymbol{x}}$ on the boundary ∂V such that,

$$\underline{\boldsymbol{u}} = \underset{\sim}{\boldsymbol{E}} \cdot \underline{\boldsymbol{x}} \quad \forall \underline{\boldsymbol{x}} \in \partial V \tag{2.15}$$

with $\underset{\sim}{\boldsymbol{E}}$ second-order macroscopic strain tensor, which is symmetric and independent of $\underline{\boldsymbol{x}}$. It follows from Equations 2.15 and 2.12:

$$\langle \underset{\sim}{\boldsymbol{\varepsilon}} \rangle = \frac{1}{V} \int_V \underset{\sim}{\boldsymbol{\varepsilon}} dV = \underset{\sim}{\boldsymbol{E}} \tag{2.16}$$

The macroscopic stress tensor is then defined as the spatial average of the local stress field:

$$\underset{\sim}{\boldsymbol{\Sigma}} := \langle \underset{\sim}{\boldsymbol{\sigma}} \rangle = \frac{1}{V} \int_V \underset{\sim}{\boldsymbol{\sigma}} dV \tag{2.17}$$

Static uniform boundary conditions – SUBC

Traction $\underline{\boldsymbol{t}}$ is prescribed for any material point $\underline{\boldsymbol{x}}$ on ∂V such that,

$$\underline{\boldsymbol{t}} = \underset{\sim}{\boldsymbol{\Sigma}} \cdot \underline{\boldsymbol{n}} \quad \forall \underline{\boldsymbol{x}} \in \partial V \tag{2.18}$$

with $\underset{\sim}{\boldsymbol{\Sigma}}$ second-order macroscopic stress tensor, which is symmetric and independent of $\underline{\boldsymbol{x}}$. It follows from Equations 2.18 and 2.13:

$$\langle \underset{\sim}{\boldsymbol{\sigma}} \rangle = \frac{1}{V} \int_V \underset{\sim}{\boldsymbol{\sigma}} dV = \underset{\sim}{\boldsymbol{\Sigma}} \tag{2.19}$$

The macroscopic strain tensor is then defined as the spatial average of the local strain field:

$$\underset{\sim}{\boldsymbol{E}} := \langle \underset{\sim}{\boldsymbol{\varepsilon}} \rangle = \frac{1}{V} \int_V \underset{\sim}{\boldsymbol{\varepsilon}} dV \tag{2.20}$$

Periodic boundary conditions – PBC

For PBC, the displacement field $\underline{\boldsymbol{u}}$ can be dissociated into a part given by the macroscopic strain tensor $\underset{\sim}{\boldsymbol{E}}$ and a periodic fluctuation field for any material point $\underline{\boldsymbol{x}}$ of V, such that:

$$\underline{\boldsymbol{u}} = \underset{\sim}{\boldsymbol{E}} \cdot \underline{\boldsymbol{x}} + \underline{\boldsymbol{v}} \quad \forall \underline{\boldsymbol{x}} \in V \tag{2.21}$$

with $\underline{\boldsymbol{v}}$ the periodic fluctuations vector, *i.e.* taking the same value on two homologous points $\underline{\boldsymbol{x}}^+$ and $\underline{\boldsymbol{x}}^-$ of ∂V. Furthermore, the traction vector $\underline{\boldsymbol{t}} = \underset{\sim}{\boldsymbol{\sigma}} \cdot \underline{\boldsymbol{n}}$ fulfills anti-periodic conditions such that,

$$\underset{\sim}{\boldsymbol{\sigma}}^+ \cdot \underline{\boldsymbol{n}}^+ + \underset{\sim}{\boldsymbol{\sigma}}^- \cdot \underline{\boldsymbol{n}}^- = \underline{\mathbf{0}} \tag{2.22}$$

$$\underline{\boldsymbol{v}}^+ - \underline{\boldsymbol{v}}^- = \underline{\mathbf{0}} \tag{2.23}$$

A dual approach exists; it consists in prescribing a macroscopic stress to the cell. However we do not develop this approach here, *cf.* [Michel et al., 1999] for details.

2.2.4 Hill–Mandel condition

Let us consider a volume V with two independent local fields $\underset{\sim}{\boldsymbol{\varepsilon}}'$ and $\underset{\sim}{\boldsymbol{\sigma}}^*$ such that $\underset{\sim}{\boldsymbol{\varepsilon}}'$ is kinematically compatible and $\underset{\sim}{\boldsymbol{\sigma}}^*$ is statically admissible. If $\underset{\sim}{\boldsymbol{\sigma}}^*$ verifies SUBC, or $\underset{\sim}{\boldsymbol{\varepsilon}}'$ verifies KUBC, or if $\underset{\sim}{\boldsymbol{\sigma}}^*$ and $\underset{\sim}{\boldsymbol{\varepsilon}}'$ verify simultaneously the periodic boundary conditions, then:

$$\langle \underset{\sim}{\boldsymbol{\sigma}}^* : \underset{\sim}{\boldsymbol{\varepsilon}}' \rangle = \langle \underset{\sim}{\boldsymbol{\sigma}}^* \rangle : \langle \underset{\sim}{\boldsymbol{\varepsilon}}' \rangle \tag{2.24}$$

Thus, one obtains the following equivalence for the three types of boundary conditions:

$$\langle \underset{\sim}{\boldsymbol{\sigma}} : \underset{\sim}{\boldsymbol{\varepsilon}} \rangle = \langle \underset{\sim}{\boldsymbol{\sigma}} \rangle : \langle \underset{\sim}{\boldsymbol{\varepsilon}} \rangle \tag{2.25}$$

which corresponds to the Hill macrohomogeneity condition [Hill, 1967]. This ensures that the mechanical work density at the microscale is preserved while scaling up to the macroscopic level.

2.2.5 Effective properties vs. apparent properties

When determining the properties of volume V that is smaller than the RVE, apparent properties are considered. The apparent properties converge towards the effective properties once $V \geq V_{\text{RVE}}$, according to the definition of RVE introduced in Section 1.1.

The micromechanical linear elastic problem admits a unique solution, up to a rigid body displacement for SUBC and a periodic translation for PBC. Let us consider two fourth-order tensors $\underset{\approx}{\boldsymbol{A}}$ and $\underset{\approx}{\boldsymbol{B}}$ accounting respectively for strain localization and stress concentration:

$$\underset{\sim}{\boldsymbol{\varepsilon}}(\underline{\boldsymbol{x}}) = \underset{\approx}{\boldsymbol{A}}(\underline{\boldsymbol{x}}) : \underset{\sim}{\boldsymbol{E}} \qquad \forall \underline{\boldsymbol{x}} \in V \text{ and } \forall \underset{\sim}{\boldsymbol{E}} \tag{2.26}$$

and

$$\underset{\sim}{\boldsymbol{\sigma}}(\underline{\boldsymbol{x}}) = \underset{\approx}{\boldsymbol{B}}(\underline{\boldsymbol{x}}) : \underset{\sim}{\boldsymbol{\Sigma}} \qquad \forall \underline{\boldsymbol{x}} \in V \text{ and } \forall \underset{\sim}{\boldsymbol{\Sigma}} \tag{2.27}$$

such that,

$$\langle \underset{\approx}{\boldsymbol{A}} \rangle = \langle \underset{\approx}{\boldsymbol{B}} \rangle = \underset{\approx}{\boldsymbol{I}} \tag{2.28}$$

Let us consider the elastic moduli $\underset{\approx}{\boldsymbol{c}}(\underline{\boldsymbol{x}})$ and the compliances $\underset{\approx}{\boldsymbol{s}}(\underline{\boldsymbol{x}})$, then:

$$\underset{\sim}{\boldsymbol{\sigma}}(\underline{\boldsymbol{x}}) = \underset{\approx}{\boldsymbol{c}}(\underline{\boldsymbol{x}}) : \underset{\sim}{\boldsymbol{\varepsilon}}(\underline{\boldsymbol{x}}) \qquad \forall \underline{\boldsymbol{x}} \in V \tag{2.29}$$

and

$$\underset{\sim}{\boldsymbol{\varepsilon}}(\underline{\boldsymbol{x}}) = \underset{\approx}{\boldsymbol{s}}(\underline{\boldsymbol{x}}) : \underset{\sim}{\boldsymbol{\sigma}}(\underline{\boldsymbol{x}}) \qquad \forall \underline{\boldsymbol{x}} \in V \tag{2.30}$$

Thus,

$$\underset{\sim}{\boldsymbol{\Sigma}} = \langle \underset{\sim}{\boldsymbol{\sigma}} \rangle = \langle \underset{\approx}{\boldsymbol{C}} : \underset{\sim}{\boldsymbol{\varepsilon}} \rangle = \langle \underset{\approx}{\boldsymbol{c}} : \underset{\approx}{\boldsymbol{A}} : \underset{\sim}{\boldsymbol{E}} \rangle = \langle \underset{\approx}{\boldsymbol{c}} : \underset{\approx}{\boldsymbol{A}} \rangle : \underset{\sim}{\boldsymbol{E}} \tag{2.31}$$

and

$$\underset{\sim}{\boldsymbol{E}} = \langle \underset{\sim}{\boldsymbol{\varepsilon}} \rangle = \langle \underset{\approx}{\boldsymbol{S}} : \underset{\sim}{\boldsymbol{\sigma}} \rangle = \langle \underset{\approx}{\boldsymbol{s}} : \underset{\approx}{\boldsymbol{B}} : \underset{\sim}{\boldsymbol{\Sigma}} \rangle = \langle \underset{\approx}{\boldsymbol{s}} : \underset{\approx}{\boldsymbol{B}} \rangle : \underset{\sim}{\boldsymbol{\Sigma}} \tag{2.32}$$

We can define $\underset{\approx}{\boldsymbol{C}}^{\text{app}}_{E}$ and $\underset{\approx}{\boldsymbol{S}}^{\text{app}}_{\Sigma}$, fourth-order symmetric tensors, accounting respectively for the apparent elastic moduli and compliances of the volume V considered such that,

$$\underset{\approx}{\boldsymbol{C}}^{\text{app}}_{E} = \langle \underset{\approx}{\boldsymbol{c}} : \underset{\approx}{\boldsymbol{A}} \rangle \tag{2.33}$$

and

$$\underset{\approx}{\boldsymbol{S}}^{\text{app}}_{\Sigma} = \langle \underset{\approx}{\boldsymbol{s}} : \underset{\approx}{\boldsymbol{B}} \rangle \tag{2.34}$$

These equations show that homogenized properties are not usually obtained by a simple rule of mixture.

Also, one can define the apparent properties from the elastic strain energy density $\mathscr{E}^{el}$:

$$\mathscr{E}^{el} = \frac{1}{2} \langle \underset{\sim}{\boldsymbol{\sigma}} : \underset{\sim}{\boldsymbol{\varepsilon}} \rangle = \frac{1}{2} \langle \underset{\sim}{\boldsymbol{\varepsilon}} : \underset{\approx}{\boldsymbol{c}} : \underset{\sim}{\boldsymbol{\varepsilon}} \rangle = \frac{1}{2} \underset{\sim}{\boldsymbol{E}} : \langle \underset{\approx}{\boldsymbol{A}}^{T} : \underset{\approx}{\boldsymbol{c}} : \underset{\approx}{\boldsymbol{A}} \rangle : \underset{\sim}{\boldsymbol{E}} \tag{2.35}$$

and

$$\mathscr{E}^{el} = \frac{1}{2} \langle \underset{\sim}{\boldsymbol{\sigma}} : \underset{\sim}{\boldsymbol{\varepsilon}} \rangle = \frac{1}{2} \langle \underset{\sim}{\boldsymbol{\sigma}} : \underset{\approx}{\boldsymbol{s}} : \underset{\sim}{\boldsymbol{\sigma}} \rangle = \frac{1}{2} \underset{\sim}{\boldsymbol{\Sigma}} : \langle \underset{\approx}{\boldsymbol{B}}^{T} : \underset{\approx}{\boldsymbol{s}} : \underset{\approx}{\boldsymbol{B}} \rangle : \underset{\sim}{\boldsymbol{\Sigma}} \tag{2.36}$$

This way, we obtain a new definition of the apparent elastic moduli and compliances:

$$\underset{\approx}{\boldsymbol{C}}^{\text{app}}_{E} = \langle \underset{\approx}{\boldsymbol{A}}^{T} : \underset{\approx}{\boldsymbol{c}} : \underset{\approx}{\boldsymbol{A}} \rangle \tag{2.37}$$

and

$$\underset{\approx}{\boldsymbol{S}}^{\text{app}}_{\Sigma} = \langle \underset{\approx}{\boldsymbol{B}}^{T} : \underset{\approx}{\boldsymbol{s}} : \underset{\approx}{\boldsymbol{B}} \rangle \tag{2.38}$$

This new definition justifies the symmetric nature of the apparent elastic moduli and compliance tensors. By applying the Hill–Mandel lemma (*cf.* Section 2.2.4) one can prove the equivalence between direct and energetic definitions [Sanchez-Palencia and Zaoui, 1987].

According to [Sab, 1992], for an elementary volume V large enough ($V > V_{\text{RVE}}$), the apparent properties do not depend on the boundary conditions and match with the effective properties of the considered material, then:

$$\underset{\approx}{\boldsymbol{C}}^{\text{app}}_{\Sigma} = \underset{\approx}{\boldsymbol{S}}^{\text{app}-1}_{\Sigma} = \underset{\approx}{\boldsymbol{C}}^{\text{app}}_{E} = \underset{\approx}{\boldsymbol{S}}^{\text{app}-1}_{E} = \underset{\approx}{\boldsymbol{C}}^{\text{eff}} = \underset{\approx}{\boldsymbol{S}}^{\text{eff}-1} \tag{2.39}$$

For volumes ($V \geq V_{\text{RVE}}$), based on energetic considerations and the subadditivity property of the effective elastic moduli tensor, [Huet, 1990] proposed the so-called partition theorem. The effective properties can be bounded by the following inequalities:

$$\underset{\approx}{\boldsymbol{C}}^{\text{app}}_{\Sigma} \leq \underset{\approx}{\boldsymbol{C}}^{\text{eff}} \leq \underset{\approx}{\boldsymbol{C}}^{\text{app}}_{E} \tag{2.40}$$

$$\underset{\approx}{\boldsymbol{S}}^{\text{app}}_{E} \leq \underset{\approx}{\boldsymbol{S}}^{\text{eff}} \leq \underset{\approx}{\boldsymbol{S}}^{\text{app}}_{\Sigma} \tag{2.41}$$

These inequalities have to be considered in the sense of quadratic forms. For elementary volumes smaller than the RVE, using the same arguments but for partitions of different sizes, [Huet, 1990] derived hierarchical inequalities regarding apparent and effective properties. Coarse and fine partitions are considered and their respective statistical apparent properties are denoted by indices $_c$ and $_f$:

$$\underset{\approx}{\boldsymbol{C}}^{\text{Reuss}} \leq \underset{\approx}{\boldsymbol{C}}^{\text{app}}_{\Sigma f} \leq \underset{\approx}{\boldsymbol{C}}^{\text{app}}_{\Sigma c} \leq \underset{\approx}{\boldsymbol{C}}^{\text{eff}} \leq \underset{\approx}{\boldsymbol{C}}^{\text{app}}_{Ec} \leq \underset{\approx}{\boldsymbol{C}}^{\text{app}}_{Ef} \leq \underset{\approx}{\boldsymbol{C}}^{\text{Voigt}} \tag{2.42}$$

$$\underset{\approx}{\boldsymbol{S}}^{\text{Voigt}} \leq \underset{\approx}{\boldsymbol{S}}^{\text{app}}_{Ef} \leq \underset{\approx}{\boldsymbol{S}}^{\text{app}}_{Ec} \leq \underset{\approx}{\boldsymbol{S}}^{\text{eff}} \leq \underset{\approx}{\boldsymbol{S}}^{\text{app}}_{\Sigma c} \leq \underset{\approx}{\boldsymbol{S}}^{\text{app}}_{\Sigma f} \leq \underset{\approx}{\boldsymbol{S}}^{\text{Reuss}} \tag{2.43}$$

$\underset{\approx}{\boldsymbol{C}}^{\text{Voigt}}$, $\underset{\approx}{\boldsymbol{S}}^{\text{Voigt}}$, $\underset{\approx}{\boldsymbol{C}}^{\text{Reuss}}$ and $\underset{\approx}{\boldsymbol{S}}^{\text{Reuss}}$ refer to the classical Voigt and Reuss bounds [Voigt, 1889, Reuss, 1929]. The inequalities presented above can be used for verification of computational homogenisation results, as it was done for instance in [Kanit et al., 2003, Kanit et al., 2006] for elastic and thermal properties. Moreover, the bounds $\underset{\approx}{\boldsymbol{C}}^{\text{app}}_{\Sigma}$ and $\underset{\approx}{\boldsymbol{C}}^{\text{app}}_{E}$ are usually far apart when the contrast of properties between phases is large. If the microstructure features a matrix phase, tighter bounds can be obtained by choosing elementary volumes including only the matrix at the boundary, as shown in [Salmi et al., 2012a, Salmi et al., 2012b].

2.2.6 Computational homogenisation using the finite element method

In order to determine homogenized mechanical properties for a given microstructure, one has to solve boundary value problems in statics. The finite element (FE) method has proved to be quite an efficient technique to solve this kind of problems even in the case of highly nonlinear phenomena [Cailletaud et al., 2003, Besson et al., 2010, Geers and Yvonnet, 2016].

FE formulation of the principle of virtual work

Galerkin's approach for continuum mechanics is implemented and used with the principle of virtual work. In each of the n elements e, knowing the nodal displacements $\{u_e^*\}$, one can compute the virtual displacement field $\underline{\boldsymbol{u}}^*$ and the strain tensor $\underset{\sim}{\boldsymbol{\varepsilon}}$ as follows:

$$\underline{\boldsymbol{u}}^* = [N]\{u_e^*\} \tag{2.44}$$

and,

$$\underset{\sim}{\boldsymbol{\varepsilon}} = [B]\{u_e^*\} \tag{2.45}$$

with $[N]$, the shape function matrix and $[B]$, the matrix of shape function derivatives. Then, for all $\{u_e^*\}$ with prescribed body forces $\underline{\boldsymbol{f}}$ and surface forces $\underline{\boldsymbol{F}}$:

$$\sum_{e=1}^{n}\left(\int_{V_e}\underset{\sim}{\boldsymbol{\sigma}}\left(\{u_e^*\}\right)[B]\{u_e^*\}\,dV\right) = \sum_{e=1}^{n}\left(\int_{V_e}\underline{\boldsymbol{f}}\,[N]\{u_e^*\}\,dV + \int_{\partial V_e}\underline{\boldsymbol{F}}\,[N]\{u_e^*\}\,dS\right) \tag{2.46}$$

Thus,

$$\sum_{e=1}^{n}\left(\left\{\mathscr{F}_e^{\text{int}}\right\} - \left\{\mathscr{F}_e^{\text{ext}}\right\}\right)\{u_e^*\} = 0 \tag{2.47}$$

with $\left\{\mathscr{F}_e^{\text{int}}\right\}$ and $\left\{\mathscr{F}_e^{\text{ext}}\right\}$ respectively internal and external forces, in each element e, such that for the global problem:

$$\left\{\mathscr{F}^{\text{int}}\right\} = \int_{\Omega}[B]^T\underset{\sim}{\boldsymbol{\sigma}}\left(\{u_i^*\}\right)dV \tag{2.48}$$

and,

$$\left\{\mathscr{F}^{\text{ext}}\right\} = \int_{\Omega}[N]^T\underline{\boldsymbol{f}}\,dV + \int_{\partial\Omega}[N]^T\underline{\boldsymbol{F}}\,dS \tag{2.49}$$

Balance between internal and external forces is achieved with a Newton iterative algorithm using the stiffness matrix $[K]$:

$$\begin{aligned}[K] &= \frac{\partial\{\mathscr{F}^{\text{int}}\}}{\partial\{u_i^*\}} \\ &= \int_\Omega [B]^T \frac{\partial\{\sigma\}}{\partial\{\varepsilon\}} \frac{\partial\{\varepsilon\}}{\partial\{u_i^*\}} dV \\ &= \int_\Omega [B]^T \frac{\partial\{\sigma\}}{\partial\{\varepsilon\}} [B]\, dV \end{aligned} \tag{2.50}$$

which yields, for linear elastic problems:

$$[K] = \int_\Omega [B]^T [\underset{\approx}{\boldsymbol{c}}]\, [B]\, dV \tag{2.51}$$

Application to linear elasticity

In the case of linear elasticity within a volume V fulfilling RVE requirements, one can compute the effective elastic moduli $\underset{\approx}{\boldsymbol{C}}$ or compliances $\underset{\approx}{\boldsymbol{S}}$ using Equation 2.5 by prescribing either the macroscopic strain $\underset{\sim}{\boldsymbol{E}}$ or macroscopic stress $\underset{\sim}{\boldsymbol{\Sigma}}$:

$$\begin{bmatrix} \Sigma_{11} \\ \Sigma_{22} \\ \Sigma_{33} \\ \Sigma_{23} \\ \Sigma_{31} \\ \Sigma_{12} \end{bmatrix} = \begin{bmatrix} C_{11} & C_{12} & C_{13} & C_{14} & C_{15} & C_{16} \\ - & C_{22} & C_{23} & C_{24} & C_{25} & C_{26} \\ - & - & C_{33} & C_{34} & C_{35} & C_{36} \\ - & - & - & C_{44} & C_{45} & C_{46} \\ - & - & - & - & C_{55} & C_{56} \\ - & - & - & - & - & C_{66} \end{bmatrix} \begin{bmatrix} E_{11} \\ E_{22} \\ E_{33} \\ 2E_{23} \\ 2E_{31} \\ 2E_{12} \end{bmatrix} \tag{2.52}$$

$$\begin{bmatrix} E_{11} \\ E_{22} \\ E_{33} \\ 2E_{23} \\ 2E_{31} \\ 2E_{12} \end{bmatrix} = \begin{bmatrix} S_{11} & S_{12} & S_{13} & S_{14} & S_{15} & S_{16} \\ - & S_{22} & S_{23} & S_{24} & S_{25} & S_{26} \\ - & - & S_{33} & S_{34} & S_{35} & S_{36} \\ - & - & - & S_{44} & S_{45} & S_{46} \\ - & - & - & - & S_{55} & S_{56} \\ - & - & - & - & - & S_{66} \end{bmatrix} \begin{bmatrix} \Sigma_{11} \\ \Sigma_{22} \\ \Sigma_{33} \\ \Sigma_{23} \\ \Sigma_{31} \\ \Sigma_{12} \end{bmatrix} \tag{2.53}$$

Linear relations thus appear between macroscopic stress and strain, and can readily be used to build up effective compliance and elastic moduli tensors for a given microstructure. The formalism is similar for any linear property, *e.g.* thermal conductivity. Such an approach has been successfully implemented for architectured materials in [Jean and Engelmayr, 2010, Dirrenberger et al., 2013, Guiducci et al., 2014, Iltchev et al., 2015].

The element DOF method for periodic problems

In the case of periodic boundary conditions (*cf.* Section 2.2.3), there is an alternative to the FE formulation presented in Section 2.2.6. It consists in adding global DOFs shared by all elements. These DOFs correspond to the macroscopic strain components E_{ij} for displacements v_i, in addition to classical nodal DOFs. The balance equations can thus be written as follows:

$$\begin{aligned}
\int_V \sigma_{ij} u_{i,j} dV &= \int_V \sigma_{ij} (E_{ik} x_k + v_i)_{,j} dV \\
&= \int_V \sigma_{ij} E_{ij} dV + \int_V \sigma_{ij} v_{i,j} dV \\
&= \int_V \sigma_{ij} E_{ij} dV + \int_V \left(\sigma_{ij} v_i\right)_{,j} dV \\
&= \int_V \sigma_{ij} E_{ij} dV + \underbrace{\int_{\partial V} \sigma_{ij} v_i n_j dS}_{=0} \\
&= \int_V \sigma_{ij} dV E_{ij} \\
&= V \Sigma_{ij} E_{ij} \\
&= R E_{ij} E_{ij}
\end{aligned} \tag{2.54}$$

The FE problem left to solve concerns the homogeneous strain tensor E_{ij} and its dual RE_{ij}, which corresponds to the macroscopic reaction stress. Prescribing E_{ij} corresponds to the macroscopic strain approach, while prescribing RE_{ij} leads to the macroscopic stress approach. In that way, mixed macroscopic problems, *e.g.* tension, can be solved with periodic boundary conditions. Implementation of additional degrees of freedom in the FE framework is done as follows:

$$\{\underset{\sim}{\boldsymbol{\varepsilon}}\} = [B]\{u\} + \{\underset{\sim}{\boldsymbol{E}}\} \tag{2.55}$$

Also,

$$\{\underset{\sim}{\boldsymbol{\varepsilon}}\} = [B']\{u'\} \tag{2.56}$$

with

$$[B'] = \begin{bmatrix}
1 & & & & & & & \\
& 1 & & & & & & \\
& & 1 & & & & & \\
& & & 1 & & & & \\
& & & & 1 & & & \\
& & & & & 1 & & \\
& & & & & & N^i & \\
& & & & & & & \ddots
\end{bmatrix} \tag{2.57}$$

and

$$\{u\} = \begin{Bmatrix} E11 \\ E22 \\ E33 \\ E23 \\ E31 \\ E12 \\ u^i \\ \vdots \end{Bmatrix} \tag{2.58}$$

2.2.7 Conclusions

The strategy for computational homogenisation presented hereabove is complementary to the statistical approach introduced in Section 1.1 for stochastic media. The computational homogenisation technique using periodic boundary conditions allows to determine the effective properties of regular structures, *e.g.* lattice-like architectured materials. Although only elastic properties were introduced in the present section, this method also works for other physical properties, such as thermal conductivity [Dirrenberger et al., 2014], elastoplasticity [Dirrenberger et al., 2012], etc. In the next sections, a similar computational homogenisation approach is implemented in order to estimate the properties of various architectured materials.

2.3 Architectured auxetic hybrid lattice structures

This project is currently being developed in the context of Frédéric Albertini's PhD thesis, co-supervised by Cyrille Sollogoub and myself at PIMM, and Andrey Molotnikov at Monash University in Melbourne, Australia. This project was indeed started when A. Molotnikov came to PIMM as an invited professor of Arts et Métiers-ParisTech, for 1 month in December 2015.

2.3.1 Lattice structures

Among architectured materials, lattices are a combination of material and space. They are structures composed of a connected network of struts, that may be organized periodically in space, or not. They are generally used in cases where there is a need for high specific stiffness, or high specific strength [Evans et al., 2001, Deshpande et al., 2001a, Deshpande et al., 2001b, Kooistra et al., 2004, Côté et al., 2006, Ashby, 2006, Queheillalt et al., 2007, Evans et al., 2010, Fleck et al., 2010, Schaedler et al., 2011, Vigliotti and Pasini, 2012, Vigliotti and Pasini, 2013, Zok et al., 2016, Latture et al., 2018a, Latture et al., 2018b].

[Maxwell, 1864] gave the first general method for the static analysis of truss frameworks, based on the thermodynamical considerations of energy conservation, and Clapeyron's theorem, *i.e.* the

elastic energy of a strut being equal to the sum of the mechanical works of external forces. Following Maxwell, and the generalisation of his criterion for self-stressed truss frameworks by [Calladine, 1978], [Deshpande et al., 2001a] showed that depending on the network connectivity, lattice structures can be broken down into 2 separate groups: stretch-dominated and bending-dominated structures. So, for 3D lattices it yields Eq. 2.59:

$$M = b - 3j + 6 = s - m \tag{2.59}$$

with b the number of struts in a cell, j the number of frictionless vertices, s the number of self-stressed members, and m the number of mechanisms, both of the latter can be determined by finding the rank of the equilibrium matrix describing the framework in a full structural analysis [Pellegrino and Calladine, 1986]. If $M < 0$ the structure is bending-dominated; if $M \geq 0$ the structure is stretch-dominated.

Bending-dominated lattice structures

This group is characterised by low connectivity of the joints (number of struts that meet at a joint). The relative density $\rho^* = \frac{\rho_{\text{cell}}}{\rho_{\text{mat}}}$ of the cell is related to the slenderness $\frac{t}{L}$:

$$\frac{\rho_{\text{cell}}}{\rho_{\text{mat}}} = \rho^* \propto \left(\frac{t}{L}\right)^2 \tag{2.60}$$

This type of lattice cell, with a low-connectivity, is more likely to bend when loaded, leading to a low elastic modulus. [Gibson and Ashby, 1999] showed that relative modulus E^* is proportional to the square of the relative density:

$$\frac{E_{\text{cell}}}{E_{\text{mat}}} = E^* \propto \left(\frac{\rho_{\text{cell}}}{\rho_{\text{mat}}}\right)^2 \tag{2.61}$$

Due to the deformation mechanism involved with such topologies, the compressive stress-strain curve for a bending-dominated lattice, as shown in Fig. 2.3, reproduced from [Ashby, 2006], is characterised by a linear elastic behaviour, with modulus $\tilde{E}$, up to its elastic limit, at which point the cell edges yield plastically, buckle or fracture. The structure continues to collapse at a nearly constant stress $\tilde{\sigma}_{\text{pl}}$ until densification takes place.

Stretch-dominated structures

A well-known example of stretch-dominated lattice is the so-called octet truss, depicted in Fig. 2.4 introduced by Buckminster Fuller [Fuller, 1961]. Its mechanical behaviour has been thoroughly described by [Deshpande et al., 2001b]. The relative modulus E^* is directly proportional to the

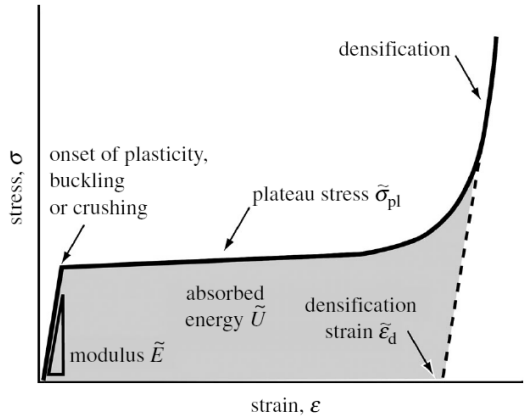

Figure 2.3: Typical compressive stress-strain curve for bending-dominated lattices [Ashby, 2006]

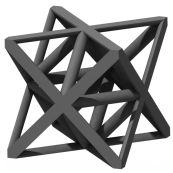

Figure 2.4: The octet truss unit-cell, proposed by [Fuller, 1961]

relative density:

$$\frac{E_{\text{cell}}}{E_{\text{mat}}} = E^* \propto \left(\frac{\rho_{\text{cell}}}{\rho_{\text{mat}}}\right) \tag{2.62}$$

Eq. 2.62 describes the fact that stretch-dominated lattices, for the same relative density, are exhibiting a higher stiffness than bending-dominated ones. The compressive stress-strain curve typical of a stretch-dominated lattice, as shown in Fig. 2.5, is characterised by a high stiffness and yield stress, followed by post-yield softening, resulting in a lower crashworthiness.

Energy absorption

The energy absorbed $\mathscr{E}_{\text{abs}}$ during the deformation of a structure can be evaluated from the stress-strain curve. It is equivalent to the plastic mechanical work evaluated until densification strain, noted ε_d:

$$\mathscr{E}_{\text{abs}} = \int_0^{\varepsilon_d} \sigma \, d\varepsilon \tag{2.63}$$

Energy absorption efficiency η is equal to the effective energy absorbed $\mathscr{E}_{\text{abs}}$, divided by the maximum theoretical energy absorption attainable for a given constitutive material, as defined in

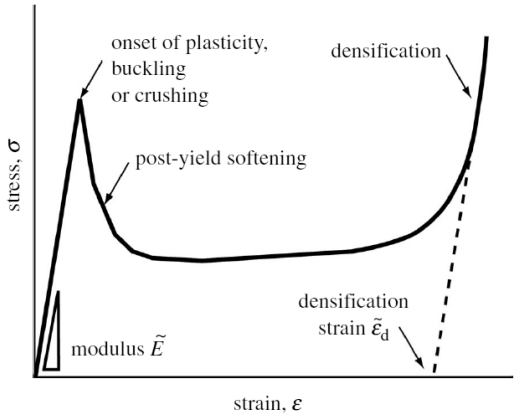

Figure 2.5: Typical compressive stress-strain curve for stretch-dominated lattices [Ashby, 2006]

[Schaedler et al., 2014]:

$$\eta = \frac{\int_0^{\varepsilon_d} \sigma \, d\varepsilon}{\sigma_{\text{tr}} 100\ \%} \tag{2.64}$$

The maximum theoretical energy absorption can be obtained by multiplying the maximum transmitted stress σ_{tr} until densification strain ε_d, *i.e.* the peak stress on Fig. 2.5. As stretch-dominated lattices present a high stress peak before softening, as seen in Fig. 2.5, their efficiency in terms of energy absorption is generally lower than the one of bending-dominated structures which exhibiting, ideally, a flat stress plateau, as shown in Fig. 2.3.

2.3.2 Additively manufactured lattice structures

Additively manufactured architectured lattice materials are of great interest for industrial applications for which weight is a key performance criterion, *i.e.* automotive, aerospace, biomedical, and defence sectors [Heinl et al., 2008, Suard et al., 2014, Peyre et al., 2015, Suard et al., 2015, Lhuissier et al., 2016, Zhang et al., 2017, Kalentics et al., 2017, Onal et al., 2018, Chauvet et al., 2018]. However, AM generates geometrical imperfections and surface roughness [Gharbi et al., 2014, Gong et al., 2015, Koutiri et al., 2018, Gunenthiram et al., 2018, Vayssette et al., 2018] that can cause dramatic decline of expected mechanical properties with regards to the idealised lattice structure, especially if stiffness or fatigue resistance are considered [Liu et al., 2017a]. Different strategies have been studied in the literature for mitigating the surface defects of additively manufactured metallic lattices: chemical etching, electro-erosion, mechanical polishing. A new proposition is explored in the present section: polymer coating or embedding of the metal struts, by analogy to the soft-hard nacre-like strategy for mitigating crack propagation, taking advantage of the surface roughness generated by AM [Kleffel and Drummer, 2017]. Such hybridisation strategies can be found in many examples of natural materials [Dunlop and Fratzl, 2010, Dunlop et al., 2011], and are being subject to many studies in bio-inspired materials [Wegst et al., 2015, Chen et al., 2012] that

demonstrate the pertinence of adding a soft phase within a rigid structure in order to improve its mechanical properties. Architectured materials are actually ubiquitous in biological materials as their functional properties are commonly related to a hierarchical organisation of structures, *i.e.* at multiple scales, each exhibiting their own characteristic length and time. Such complexity results in very efficient, lightweight, smart, adaptive materials which remain a source of inspiration for materials scientists and engineers to pin down the underlying mechanisms at work, in order to apply the same strategies in artificial materials [Munch et al., 2008, Luz and Mano, 2009, Naleway et al., 2015, Fratzl et al., 2016, Wang et al., 2016]. Classical bio-inspiration examples are the lotus leaf hydrophobicity [Barthlott and Neinhuis, 1997, Feng et al., 2002, Gao and McCarthy, 2006], gecko adhesion [Autumn et al., 2000, Yao and Gao, 2006, Autumn and Gravish, 2008], Euplectella aspergillum [Sundar et al., 2003, Aizenberg et al., 2005, Weaver et al., 2007, Fratzl and Weinkamer, 2007, Monn et al., 2015], ice-plant seed capsules [Parolin, 2006, Harrington et al., 2011, Elbaum and Abraham, 2014, Guiducci et al., 2015], or turtle shell [Krauss et al., 2009, Dunlop et al., 2011, Achrai et al., 2015, Chen et al., 2015, Djumas et al., 2016, Malik and Barthelat, 2016, Malik et al., 2017]. Each of these examples exhibits a specific spatial arrangement of phases at various scales, such that some of their overall materials properties have been improved in comparison to those of their constituents considered independently [Weaver and Ashby, 1996, Ashby and Bréchet, 2003, Weinkamer and Fratzl, 2016].

Besides processing of such architectured lattice structures, the present work brings experimental and numerical results concerning the mechanical behaviour for various types of lattices, including negative Poisson's ratio ones, also known as auxetics [Dirrenberger et al., 2011]. As a matter of fact, one engineering challenge is to predict the effective mechanical properties of architectured materials; we rely on computational homogenisation using FE analysis to do so when considering quasi-static behaviour; difficulties arise when analysing the effective damping behaviour. A straightforward solution is to rely on full-field FE dynamic simulation, accounting for both the intrinsic viscoelastic damping of the constitutive material, as well as the structural damping due to the geometrical definition of the lattice structure considered in the present work. Homogenised behaviour of architectured materials could thus be used in large structural computations, therefore enabling the dissemination of such materials in the industry. Comparison is made between the metal and hybrid lattice structure.

2.3.3 Materials and methods

So-called BCC (for body-centered cubic) lattice samples were produced out of Ti-6Al-4V alloy through selective laser melting (SLM) using a Concept Laser MLab printer with the optimised parameters listed in Table 2.1. One unit-cell corresponds to a cube of 3 mm side length. Each sample includes 5x5x5, *i.e.* 125 unit-cells, for a cube of 15 mm side length. Produced parts were wire-cut from the building plate, and used as-built without heat-treatment. Polyurethane[1] (PU) thermoset resin was used for embedding the metal lattices into a polymeric matrix within a

[1] Dalchem flexible casting polyurethane – Shore 40A

Laser power	95 W
Scan speed	600 mm.s^{-1}
Layer thickness	25 µm
Powder size distribution	10-50 µm

Table 2.1: Parameters used for SLM processing of Ti-6Al-4V

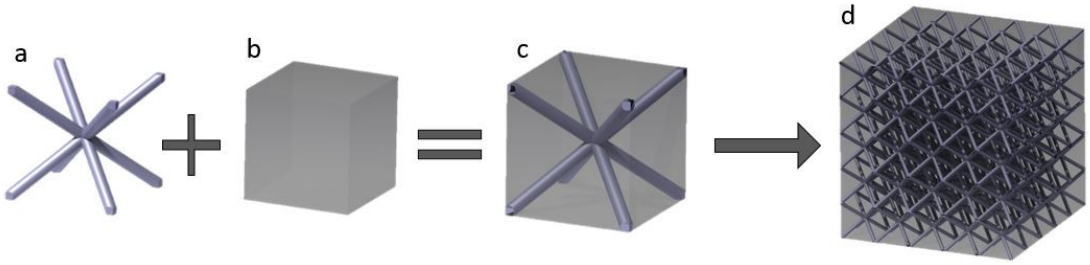

Figure 2.6: BCC unit-cell (a); PU matrix (b); hybrid unit-cell (c); hybrid architectured lattice (d)

silicone mould, as shown on Fig. 2.6, resulting in metal-polymer hybrid lattice structures.

2.3.4 Microstructural and mechanical characterisation

Microstructural characterisation of the as-built lattice structure was performed through X-ray microtomography at Laboratoire MATEIS in Lyon, France. The 3D reconstruction can be seen in Fig. 2.7. This characterisation allows to control inner porosity of printed specimen, as well as enables fine evaluation of the surface roughness, which is of prime importance for qualifying the metal-polymer interface.

In terms of mechanical behaviour characterisation, quasi-static compression tests were performed on 5x5x5 lattice cubic samples with a displacement-controlled electro-mechanical Instron machine equipped with a 10 kN load cell. Compression was performed up to 15% of macroscopic strain, *i.e.* 2.25 mm relative displacement between the top and bottom plates. A minimum of 3 samples were considered for each configuration, yielding similar results. The deformation patterns of the specimen during the test are shown on Fig. 2.8 and 2.9, respectively for the monolithic lattice, and the hybrid lattice structures, basically showing the same failure behaviour.

2.3.5 Simulation and computational homogenisation

FE simulations are currently being performed in order to further our understanding of the mechanics of hybrid lattice materials, although several difficulties may arise during this

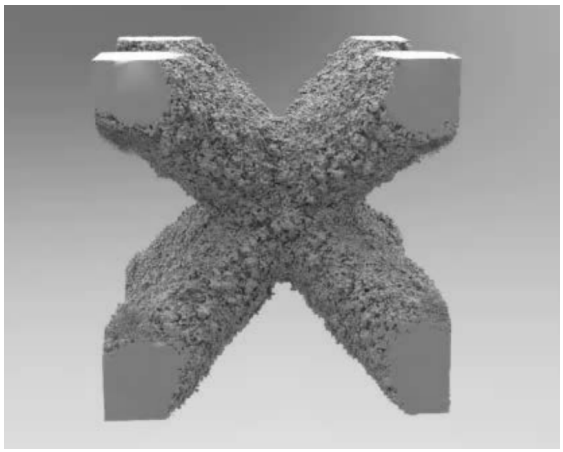

Figure 2.7: 3D reconstruction of one lattice unit-cell (3 mm side length, 1 mm strut diameter) characterised through μ-CT

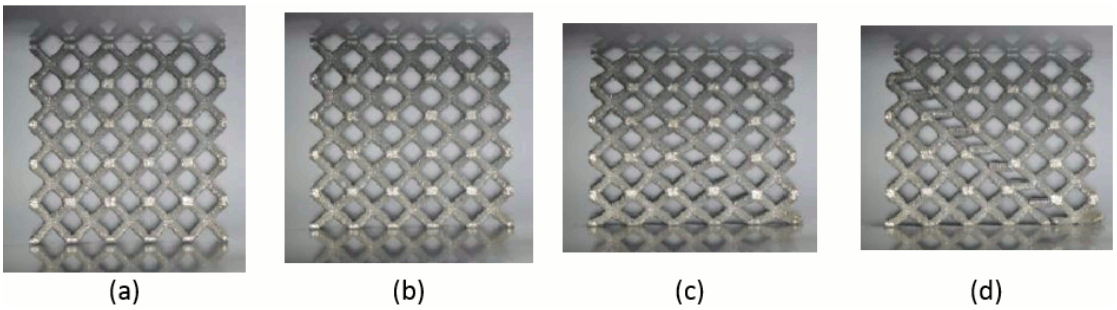

Figure 2.8: Different stages of quasi-static compression test on monolithic structure. Initial configuration (a); 5% total strain (b); 10% total strain (c); localisation and fracture (13%) (d)

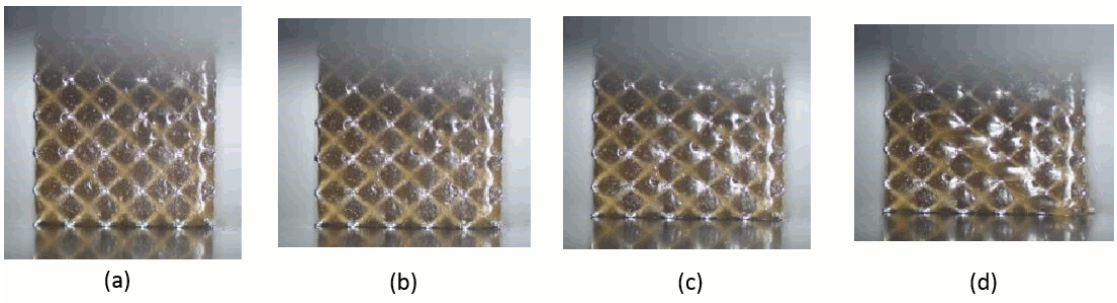

Figure 2.9: Different stages of quasi-static compression test on hybrid structure. Initial configuration (a); 3% total strain (b); 6% total strain (c); localisation and fracture (10%) (d)

step. The hyperelastic behaviour of the PU matrix complicates the choice of constitutive model and the identification of parameters. As a matter of fact many models are available [Boyce and Arruda, 2000, Marckmann and Verron, 2006] but choice has been made to rely on the Arruda-Boyce model [Arruda and Boyce, 1993] for its small number of parameters, its accu-

racy, and the fact that it is already implemented in the FE code used (Z-Set[2]). The elastoplastic behaviour of Ti-6Al-4V is identified based on tensile tests performed on 3D printed specimens, using an isotropic hardening model with two nonlinear potentials. As a first approach, interface between metal and polymer is assumed perfect, which is consistent with the experiments performed, in which no debonding was observed. Three sets of simulations are considered in this project: 1) Full-field structural FE simulation using an explicit geometrical description of the hybrid lattices; these computational experiments are aiming at accurately reproduce the actual experiments performed at Monash on the hybrids, either in compression or cyclic loading; they will serve as our reference calculations; 2) Nonlinear computational homogenisation on periodic unit-cells is performed up to failure, in order to precisely identify constitutive materials parameters, independently of the structural tests, avoiding boundary layer effects thanks to periodic boundary conditions; these calculations will also allow us to determine an homogeneous equivalent constitutive behaviour accounting for the effect of both material nonlinearities and the architecture; 3) Structural computations using the previously defined homogeneous equivalent behaviour in order to model the mechanical response of architectured hybrid lattices without explicitly describing their geometry; these computations will be validated by comparison with the reference calculations.

The early results introduced in the present section are an attempt at creating materials with enhanced functionality through hybridisation and architecture. Applications are envisioned regarding mechanical energy dissipation, either in monotonic or cyclic loading, but also damping by using the synergistic viscoelastic effect due to both the materials and the architecture. The availability of mechanical models able to describe the response of such materials is a necessity for these to be used in the industry. The further step will be to use multi-material topology optimisation in order to design smarter lattices than the ones used nowadays, which were designed on the ground of using monolithic materials.

2.4 Control of instabilities through architecture

Another promising application for architectured materials is the control of material instability propagation. Let us consider the archetypal NiTi shape memory alloy (SMA); the martensitic transformation giving rise to the shape memory effect is propagating via an unstable transformation front, moving according to the local stress state and microstructural heterogeneities [Shaw and Kyriakides, 1997, Bechle and Kyriakides, 2014, Bechle and Kyriakides, 2016]. As the material architecture can induce or mitigate stresses, it can potentially control the propagation of instabilities. Developing such an architectured material is one of the goals of the ANR-funded ALMARIS (Architecturation laser de matériaux superélastiques) project. In this context, Antoine-Emmanuel Viard (supervised by Samuel Forest at MINES-ParisTech, and myself) is exploring, in his PhD work, the possibilities of controlling instability propagation within NiTi-based architectured materials obtained through powder-

[2] http://www.zset-software.com

based additive manufacturing [Viard et al., 2018]. As the ability of printing NiTi is a goal of the project by itself [Haberland et al., 2014, Dadbakhsh et al., 2016, Elahinia et al., 2016, Gorgin Karajii et al., 2017], we focused on a simpler material in terms of mechanical modelling: mild steel. Although this material is not an SMA, it does exhibit inhomogeneous deformation characteristic of strain ageing, due to the phenomenon of Piobert-Lüders plastic banding [Piobert, 1842, Lüders, 1860, Lomer, 1952, Belotteau et al., 2009, Ballarin et al., 2009b, Ballarin et al., 2009a, Marais et al., 2012, Mazière et al., 2017], indicating dislocation movement inhibition by interstitial atoms [Cottrell and Bilby, 1949]. This phenomenon is characterised by the propagation of instabilities (plastic band) throughout the material; from a computational modelling viewpoint, the problem is very similar to the propagation of a martensitic transformation front. Any insight obtained from modelling the propagation of strain ageing instabilities could be useful for the simulation of SMAs [Kyriakides and Miller, 2000, Corona et al., 2002, Sun and Li, 2002, Sittner et al., 2005, Kyriakides et al., 2008, Jiang et al., 2017].

Early finite element simulation work resulted in the propagation of Piobert-Lüders plastic bands in simple structures, before studying architectured materials. This is done by considering an elastoplastic constitutive behaviour with a double nonlinear isotropic hardening function [Tsukahara and Iung, 1998, Kyriakides and Miller, 2000, Ballarin et al., 2009b, Marais et al., 2012, Mazière and Forest, 2015], as presented in Eq. 2.65:

$$R(p) = R_0 + Q_1\left(1 - e^{-b_1 p}\right) + Q_2\left(1 - e^{-b_2 p}\right) \tag{2.65}$$

with R_0 the yield stress, Q_i the hardening moduli, b_i phenomenological parameters, and p the accumulated plastic deformation. By considering simultaneously both a hardening modulus and a negative hardening modulus, *i.e.* softening modulus, one can obtain a constitutive behaviour typical of local instability propagation, with peak-stress and subsequent post-peak softening, as shown in Fig. 2.10. Let us simulate the tensile deformation of a mild-steel strip, with a small material defect in one element ($R_0^* = 0.99 R_0$) in order to localise the strain and initiate the instability. The instability is successfully simulated and propagates throughout the whole sample, initiating from the material inhomogeneity, as shown in Fig. 2.11. The macroscopic tensile curve for the same computational experiment, shown in Fig. 2.12, is characteristic of the behaviour of mild-steel exhibiting the peak-stress followed by serrations typical of the Piobert-Lüders band propagation. Once the maximum stress is reached, plastic deformation is localised in bands that are tilted at 54.7 deg, as predicted by plasticity theory [Hill, 1952, Rudnicki and Rice, 1975, Rice, 1976, Besson et al., 2010]. These are just some preliminary investigations, but the goals of this PhD work are three-fold: 1) implementing the superelastic constitutive developed in [Jiang et al., 2016], based on [Landis, 2003], for modelling the interactions between material instabilities and structural ones, within the Z-Set computational framework; 2) exploring various architectures, based on periodic unit-cells, and assessing their response to material instabilities, defining objective criteria for comparison, in order to chart a design map for architectured materials with instabilities; 3) validating the previous approach by producing architectured samples either 2D, with mild-steel using the platform that will be introduced in Section 2.7, or 3D using NiTi powder-based additive layer manufacturing.

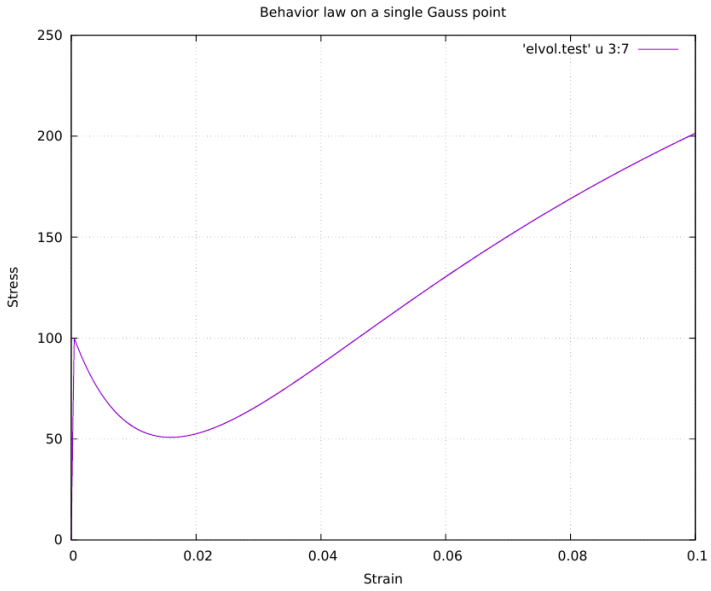

Figure 2.10: Local constitutive behaviour for Piobert-Lüders band propagation

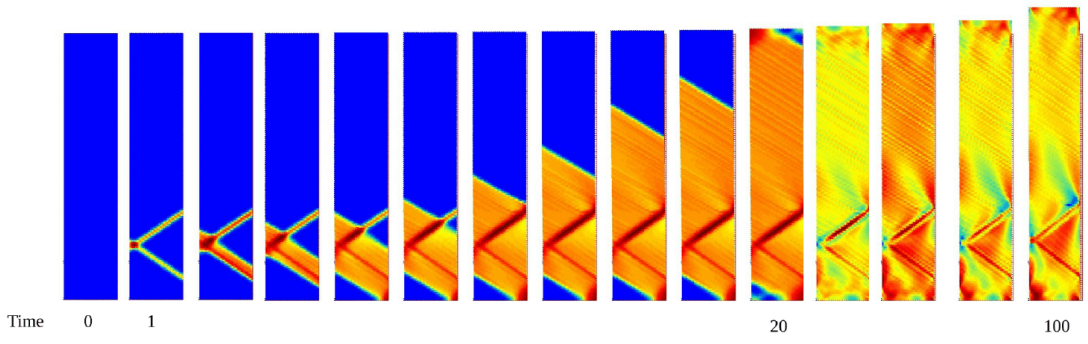

Figure 2.11: Simulation of the Piobert-Lüders band propagation within a simple structure in tension (colours indicate the equivalent plastic strain)

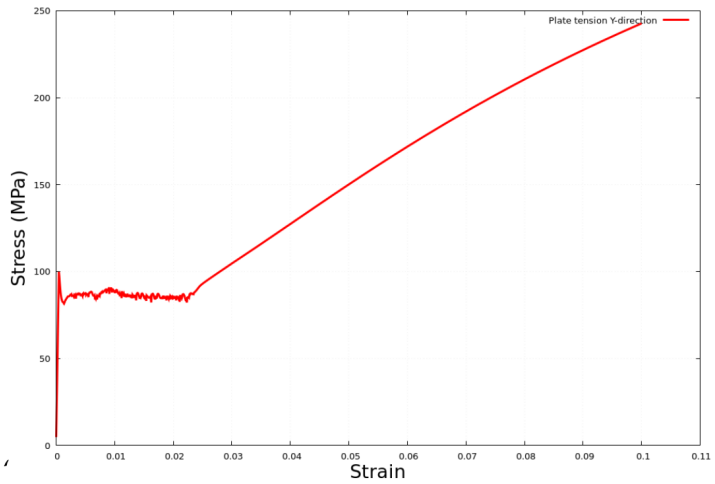

Figure 2.12: Macroscopic tensile curve of the experiment simulated in Fig. 2.11

2.5 Modelling architectured materials with generalised continua

The objective of this section is to address the problem of homogenisation methods for composite materials when the size of the constituents is not significantly smaller than the size of the whole structure, as in the case of architectured materials.

Classical homogenisation methods, based on Cauchy continua, break down if the structure contains a finite number of unit cells of the architectured material because of boundary layer effects, as well as inadequate effective moduli coming from the standard approach. As a consequence of the finite size of the system, macroscopic stress and strain fields cannot be regarded as uniform over the unit cell size. One can rely on generalized continuum theories. There are at least two ways to extend classical continuum mechanics [Toupin, 1962, Mindlin, 1964, Mindlin, 1965, Erigen, 1967, Mindlin and Eshel, 1968, Forest, 2005]:

- **Higher-order continua**: with this option the number of degrees of freedom is extended. These theories can model optical branches. The Cosserat elasticity in which local rotations are added as degrees of freedom belongs to this family [Cosserat and Cosserat, 1909]. This enhancement can be extended further to obtain the micromorphic elasticity [Green and Rivlin, 1964, Mindlin, 1964, Germain, 1973].
- **Higher-grade continua**: the alternative is to keep the same degrees of freedom but to add higher-order gradients of the displacement field into the energy density. Mindlin first strain-gradient elasticity (SGE) models [Mindlin, 1964, Mindlin and Eshel, 1968], and second strain gradient elasticity [Mindlin, 1965] belongs to this family.

These two types of generalised continua are summarised in Table 2.2.

In the context of a collaboration with my colleagues N. Auffray (MSME), G. Rosi (MSME), and

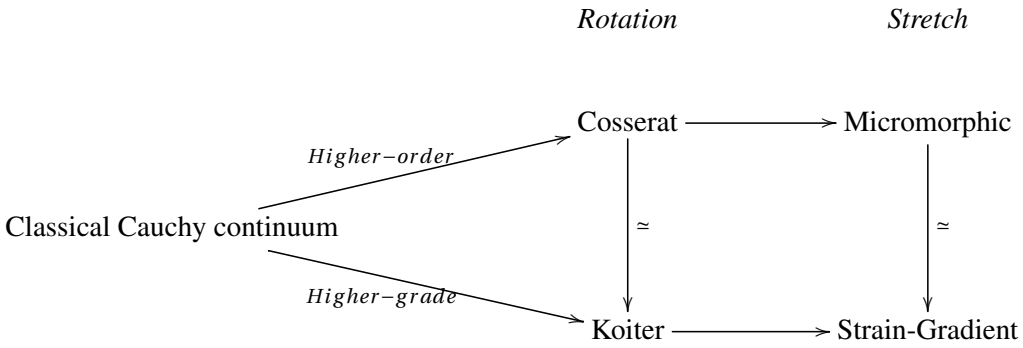

Table 2.2: Extensions of a Cauchy continuum. From the left to the right, *rotation* then *strech* are added to the kinematics. For higher-order continua these extensions are independent DOF, for higher-grade continua they are controlled by higher-order gradients of the displacement field.

M. Poncelet (LMT-Cachan), through the APHORISME project (Approche holiste de la chiralité dans les métamatériaux architecturés), we proposed to explore the validity and pertinence of such generalised continua models, based on full-field simulations, computational homogenisation, and actual experiments. A first effort, dealing with the complete tensorial description of 2D anisotropic strain-gradient elasticity, can be found in [Auffray et al., 2015]. In this paper spaces of fifth-order tensors involved in bidimensional SGE are studied. As a result complete sets of matrices representing these tensors in each one of their anisotropic system are provided. This paper completes and ends some previous studies on the subject providing an exhaustive description of the anisotropic 2D SGE. The proof is given that 2D SGE is divided into 14 non-equivalent anisotropic classes, 8 of which are isotropic for classical elasticity. The classification and matrix representations of the acoustical gyrotropic tensor are also provided, these results may find interesting applications to the study of wave propagation in dispersive architectured materials [Rosi and Auffray, 2016, Rosi et al., 2017, De Bellis and Bacigalupo, 2017, Bacigalupo and Gambarotta, 2017, Rosi et al., 2018, Lepidi and Bacigalupo, 2018]. This exhaustive 2D description was recently extended to the 3D case in [Auffray et al., 2018].

This preliminary work was necessary in order to determine which and how components of the coupling fifth-order tensor could be identified experimentally. Fig. 2.13 shows a preliminary design for a mechanical testing equipment capable of applying enriched boundary conditions to architectured materials samples in order to achieve specific loading states highlighting the effect of higher-order coupling tensorial components, hence enabling the possibility of an inverse identification process. Such approaches are currently being implemented in the PhD work of C. Morin at LMT-Cachan [Poncelet et al., 2018].

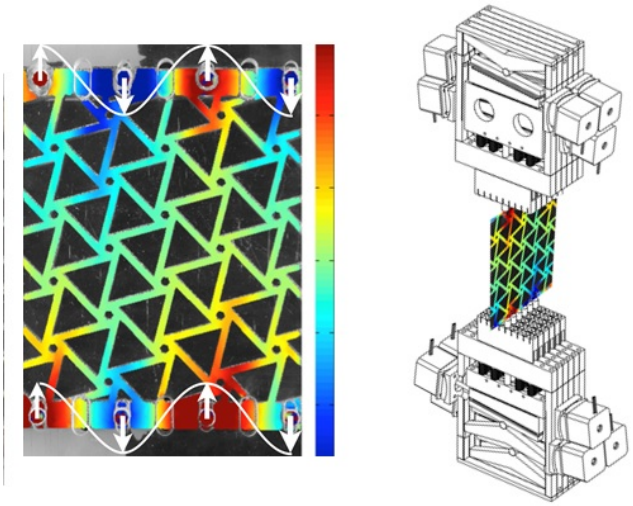

Figure 2.13: Preliminary design for a mechanical testing equipment capable of enriched boundary conditions

2.6 Shape optimisation for additive manufacturing

In the context of a collaboration with colleagues from the National University of Singapore (NUS), L.H. Poh, Z.P. Wang, and Y. Zhu, we got interested in the development of auxetics, *i.e.* architectured materials exhibiting a negative Poisson's ratio [Dirrenberger et al., 2011, Dirrenberger et al., 2012, Dirrenberger, 2012, Dirrenberger et al., 2013], and the possibilities of producing such materials thanks to the availability of additive manufacturing techniques. Our first contribution has been to consider the so-called star-shaped auxetics [Theocaris et al., 1997], and implementing an isogeometric analysis (IGA) method for optimising the shape of such auxetics while conserving their topology, in order to change the effective elastic properties, especially the Poisson ratio, and improving their manufacturability through additive manufacturing. The work published in [Wang et al., 2017b] is summarised hereafter. For the sake of clarity, most of the numerical details are avoided in the present manuscript; for an exhaustive description of the IGA and computational homogenisation scheme, please refer to the aforementioned paper. The figures in this section were produced by Zhen-Pei Wang during his post-doctoral stay at NUS.

A key challenge for the shape design of the proposed smoothed petal structures, is the proper integration between the curved geometrical description and the corresponding finite element analysis. Using non-uniform rational b-spline (NURBS) basis function as the shape function, the IGA [Hughes et al., 2005] is well suited for shape optimisation in terms of the exact geometrical description and enhanced sensitivity analysis [Cho and Ha, 2009, Qian, 2010]. Shape optimisation based IGA has been adopted for curved beam structures [Nagy et al., 2010, Nagy and Abdalla, 2011], vibrating membranes [Manh et al., 2011], fluid mechanics [Nørtoft and Gravesen, 2013, Park et al., 2013], shells [Nagy et al., 2013, Kiendl et al., 2014], photonic crystals [Qian and Sigmund, 2011], etc. Other works using NURBS as a tool for shape optimisation can be found in [Braibant and Fleury, 1984,

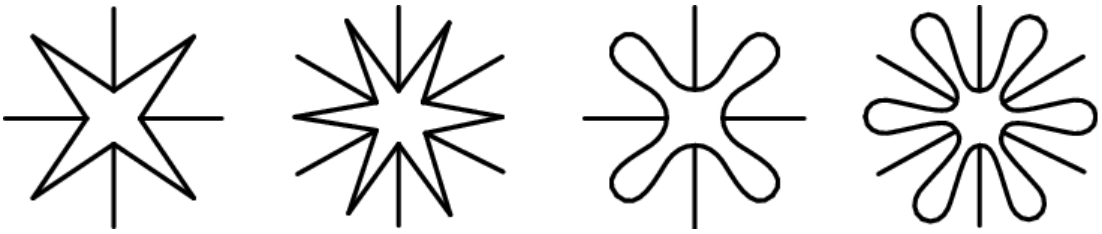

Figure 2.14: Star-shaped lattice (left), and new petal-shaped lattice design with 4 and 6 branches (right)

Zhang et al., 2010, Wang and Zhang, 2012, Cai et al., 2014].

Shape optimisation has been utilized for the design of auxetics [Wang et al., 2014, Clausen et al., 2015, Körner and Liebold-Ribeiro, 2015, Bacigalupo et al., 2016]. Departing from these established approaches, the present work adopts IGA for shape design optimisation of auxetic structures such that the curved features of the geometry can be naturally preserved. For practical engineering considerations, a geometry sizing constraint is introduced to ensure a minimum thickness, such that thin member connections do not surface. This geometry sizing constraint is difficult to implement in the context of IGAs due to the non-interpolatory nature of NURBS basis, which makes it a particularly interesting problem to solve.

In general, the effective elastic properties of periodic auxetic materials are not isotropic, as studied in [Dirrenberger et al., 2011, Dirrenberger et al., 2012, Dirrenberger et al., 2013, Bacigalupo and Gambarotta, 2014, Bacigalupo and De Bellis, 2015, Mukhopadhyay and Adhikari, 2016]. It is therefore essential to determine the full effective elastic modulus tensor for a given structure. This is done in the present work by means of computational homogenisation [Bornert et al., 2001, Besson et al., 2010, Dirrenberger et al., 2013], with periodic boundary conditions. As a special case, we consider a smoothed petal shape design with 6-fold symmetry, as shown in Fig. 2.14, in order to achieve in-plane isotropy, thus contributing to the pool of isotropic designs available in the literature [Larsen et al., 1997, Alderson et al., 2010].

2.6.1 Smoothed and manufacturable hinge-type vertices

In literature such as [Theocaris et al., 1997, Grima et al., 2005], star-shaped lattices are mostly modelled using truss or beam elements with the vertices treated as hinges or hinging springs. While these hinges or hinging springs are the underlying mechanisms leading to the auxetic behaviour, they are not amenable for the manufacturing process. A more desirable approach for manufacturing is to have a continuous unit cell structure, an example of which is depicted in Fig. 2.15(a) for a star-shaped structure with four vertices presented in [Theocaris et al., 1997]. Considering an isotropic elastic material (E=1; ν=0.3) with a unit member width, as shown in Fig. 2.15(a), an effective Poisson ratio of -0.144 is obtained. When subjected to a unity relative horizontal displacement, the deformed structure is plotted in Fig. 2.15(b) with the corresponding

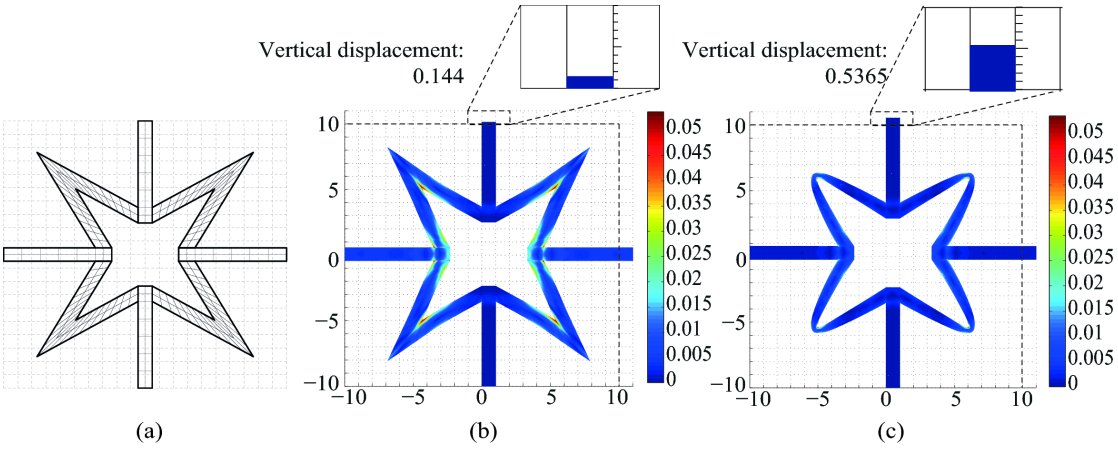

Figure 2.15: Star-shaped model from [Theocaris et al., 1997] built as a continuum of width 1 (a); the von Mises stress distribution of the star-shaped structure under a displacement of 1 applied to the right side (b); the von Mises stress distribution of the modified star-shaped structure under a displacement of 1 applied to the right side (c)

von Mises stress distribution. It can be observed that the auxetic behaviour is limited, with severe stress concentration at the connections.

For a slightly modified star-shaped lattice shown in Fig. 2.15(c) with smoothed vertices coupled with a varying width, an effective in-plane Poisson ratio of -0.537 is obtained. Applying the same boundary conditions for the modified unit-cell, its auxetic behaviour is improved, and stress concentration at connections reduced, as illustrated in Fig. 2.15(c). Comparing the auxetic behaviour of these two designs, it is clear that a compliant connection at the vertices can mimic the hinge effect. This sets the background for the following, where a proposed shape optimisation technique is utilized on a reference geometry with smooth connections, in order to design manufacturable auxetic structures.

2.6.2 Computational strategy

Starting from a reference petal-shaped structure, we seek an optimised shape which maximizes its auxetic property. To simplify the design problem, we consider only the exterior boundary of one petal, termed *parent petal* hereinafter, since the entire structure can be obtained through the patterning of parent petal and addition of connecting bars. Correspondingly, the control points characterising the exterior boundary of the parent petal are chosen as design variables. In order to evaluate the elastic properties of the lattice cell at each iteration, we rely on computational homogenisation using periodic boundary conditions [Dirrenberger, 2012].

NURBS have been used as a tool to describe and design geometry for decades. The combination of the basis function defined in the index space, and the control points located in the physical

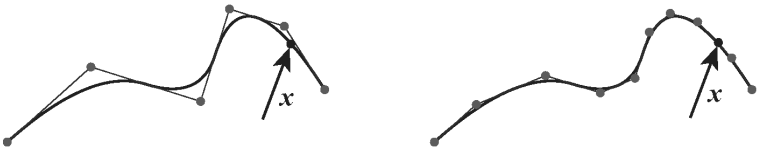

(a) Design discretization space (b) Analysis discretization space

Figure 2.16: Two levels of NURBS discretizations: Coarse discretisation for design (a); refined discretisation for analysis (b)

space, offers great flexibility in CAD modelling. Using the basis functions as the shape functions for finite element analysis, IGA integrates the CAE and CAD processes into one discretisation scheme. The isogeometric shape optimisation, which adopts the locations and weights of the control points as design variables, is naturally developed based on this integration between the two processes. For the design of the smoothed petal auxetic lattice, an isogeometric shape optimisation framework is well suited, since

- NURBS offer great flexibility and convenience in describing the geometry of the curved and smoothed petal auxetic structures;
- The curved geometry of the petal auxetic structure can be preserved exactly in the analysis, such that numerical errors are reduced;
- Less degrees of freedom are required for the analysis compared to the finite element discretisation of the curved geometry associated with a smoothed petal auxetic.

In the context of isogeometric shape optimisation, the NURBS model can be discretised differently for efficient analysis and design, as schematically shown in Fig. 2.16. In the design space, the geometry is updated with a coarse discretisation, in order to reduce the number of design variables. In the analysis space, a refined discretisation is utilised such that the state fields and geometrical features can be computed accurately. The continuous shape sensitivity, cf. [Wang et al., 2017b], is processed in both the design and the analysis spaces, *i.e.* the state variable fields and the geometrical features are calculated in the analysis space, while the design velocity is discretised in the design space such that the shape sensitivity is obtained with respect to the design control points. The two levels of discretisation can be achieved simply by inserting different numbers of knots in the NURBS index space. By prescribing appropriate geometrical constraints and implementing an adequate optimisation algorithm, shape optimisation is then performed.

2.6.3 Results

The design optimisation of the tetra-petals structure starts with an initial design that has a fixed interior boundary. The maximal curvature is 2 (equivalent to a radius of 0.5), which results in a reasonably smooth connection with low stress concentration. The gap between two arms is

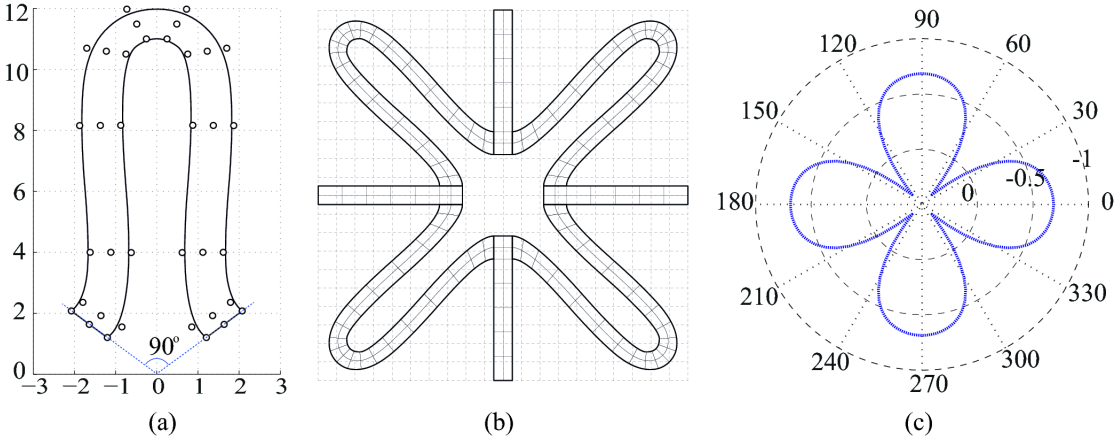

Figure 2.17: Petal shape and its corresponding control points (a), the full model (b), and the polar plot of the effective Poisson ratio for the initial design (c)

about 1.36. The initial design has a uniform width of 1 (see Fig. 2.17(b)) and an effective Poisson ratio of -0.6655 along the vertical and horizontal directions. The effective Poisson ratios along different directions are plotted in a polar coordinate system in Fig. 2.17(c), which indicates that the effective Poisson ratio of this structure is not isotropic.

The tetra-petals structure is optimised with both symmetric and sizing constraints considered. The macro strain of $\underset{\sim}{\boldsymbol{E}} = [1,\ 0,\ 0]^{\mathrm{T}}$ is used for the numerical homogenisation. For practical engineering considerations, the minimal width of the petals arms is set to be 0.5, which is half of its initial size. The optimised shape is shown in Fig. 2.18(a) with an effective Poisson ratio of -0.878 along both the vertical and horizontal directions. The effective Poisson ratio along different orientations are presented in a polar coordinate system in Fig. 2.18(b). From the polar plot, it can be seen that the auxetic behaviour of the optimised design has an overall better performance than the initial design. The comparison between the size bounding curve and the initial and optimised designs are plotted in Fig. 2.18(c), from which it can be observed that the sizing constraint is fully satisfied.

The same approach was applied to the so-called hexa-petals design, in order to reach an isotropic elastic behaviour. The hexa-petals lattice is optimised with both symmetric and sizing constraints imposed. A macro strain of $\underset{\sim}{\boldsymbol{E}} = [1,\ 0,\ 0]^{\mathrm{T}}$ is used for the numerical homogenisation. The minimal width of the petals arms is set to be 0.5. The optimised shape is shown in Fig. 2.19(a) with an effective Poisson ratio of -0.431. From the polar plot in Fig. 2.19(b), we observe that the auxetic behaviour of the optimised design is isotropic. An isotropic structure design can be very important for practical engineering applications in cases where the loading direction cannot be determined *a priori*. The comparison between the size bounding curve and the initial and optimised designs are plotted in Fig. 2.19(c), from which it can be seen the sizing constraint is fully satisfied. The iteration history of the objective function is plotted in Fig. 2.19(d).

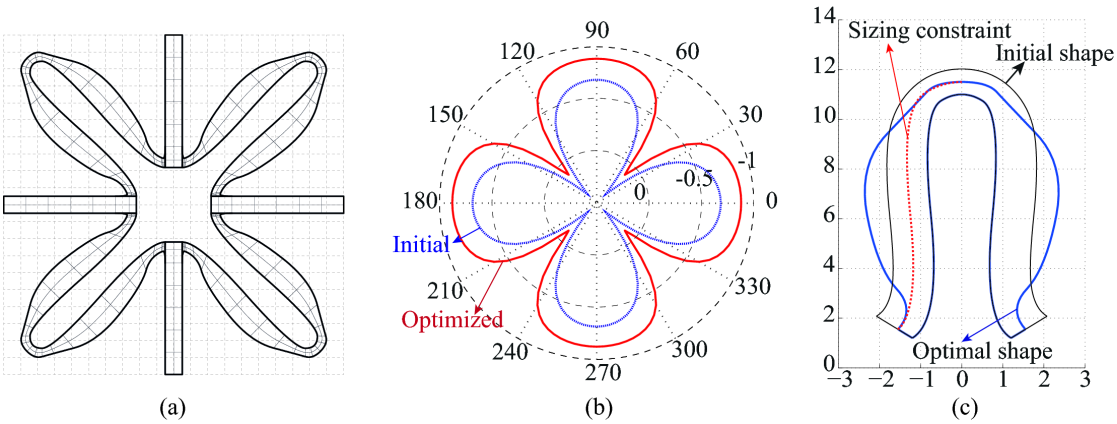

Figure 2.18: Full model of the optimised design (a); polar plot of the effective Poisson ratio for the optimised design (b); comparison between the size bounding polynomials, the initial and optimised designs (c)

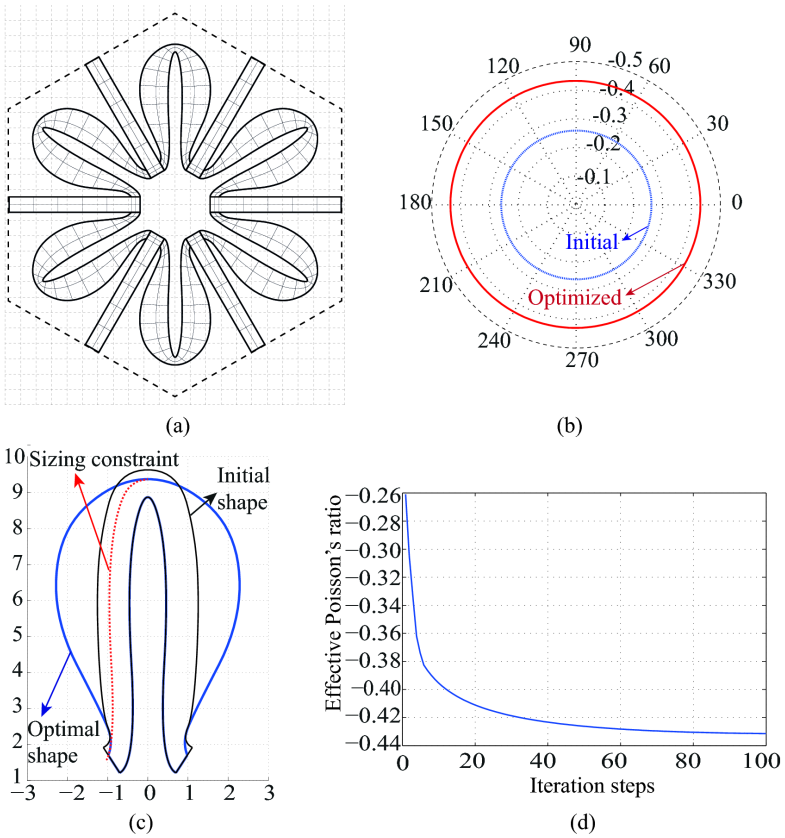

Figure 2.19: Full model of the optimised design (a); polar plot of the effective Poisson ratio for the optimised design (b); comparison between the size bounding polynomials, the initial and optimised designs (c); iteration history of the objective function (d)

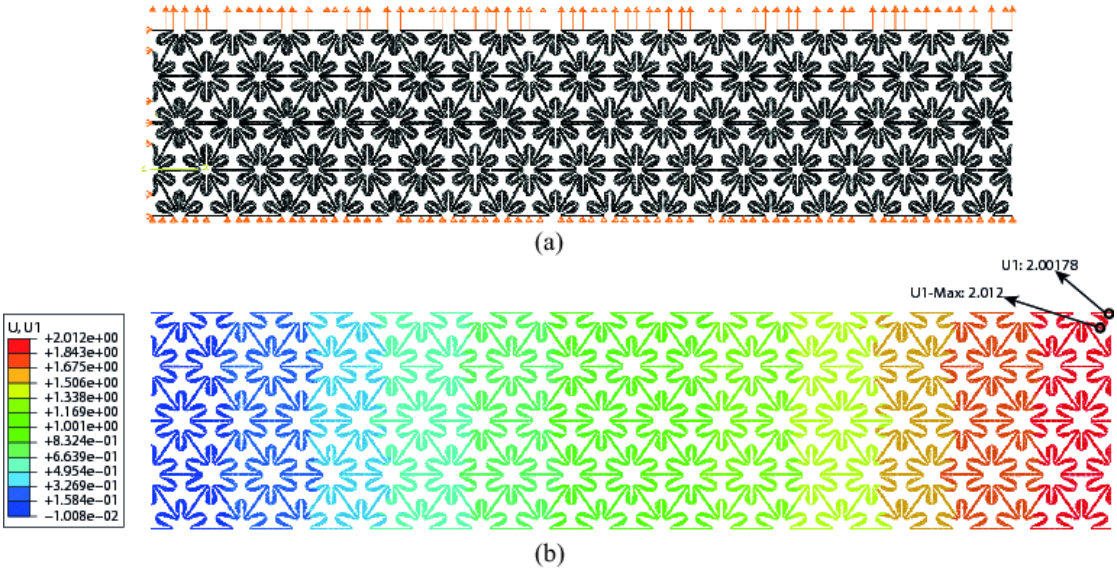

Figure 2.20: A periodic model with 16 by 4 units is loaded vertically with a unit relative displacement between the top and bottom surfaces, the vertical surfaces are constrained to remain plane (a); the horizontal displacement contour plot of the deformed structure (b)

To verify the auxetic behaviour of the optimised design, a periodic model with 16 by 4 units is loaded vertically with a unit relative displacement between the horizontal surfaces. The vertical surfaces are constrained to remain plane. The resultant relative horizontal displacement on the right surface is 2.00178. Given the specimen dimension of 343.86 by 74.448, the effective negative Poisson ratio therefore, is $\bar{\nu} = -\varepsilon_1/\varepsilon_2 = -(2.00178 \times 74.448)/(343.86 \times 1) = -0.433$, which agrees with the predicted value of the effective Poisson ratio reasonably well.

2.6.4 Conclusions

In the present section, we refer to the class of star-shaped designs, upon which a series of smoothed petal auxetics are proposed. These petal auxetic structures use smoothed connections to replace the sharp vertices. Shape optimisation within an isogeometric framework is performed to design the tetra- and hexa-petals structures. To impose the sizing constraint, a piece-wise bounding polynomial approach is proposed to overcome the difficulties associated with the non-interpolatory nature of NURBS basis. To the best of our knowledge, it seems from the literature that isogeometric shape optimisation had never been applied auxetics before this work. We note that the current modelling approach is not able to fully smooth the connection between a straight bar and a petal arm, which is a limitation of C^0 multi-patch modelling scheme used. This collaborative work is still going, the latest results were published in [Zhu et al., 2018, Wang et al., 2019].

This last example highlights the fact that processing constraints should be taken into account

while designing and modelling architectured materials, as it will condition the microstructure, the shape, and the scale of the material, and therefore the functionality of the component or structure to be manufactured (cf. Fig. 2.1).

2.7 Localised laser processing for metal sheets

Many industrial applications require new materials with enhanced specific properties, *i.e.* performance per unit of mass; this is especially true for the transportation and biomedical sectors. For instance, the automotive industry, with its ever increasing requirements regarding passenger safety and fuel consumption, is an edifying example: nowadays, classical steel-based material solutions are being challenged by new lightweight aluminium alloys and advanced composites. A response from steel manufacturers was the development of advanced high-strength steels (AHSS) for yield strength designed parts in order to reduce both thickness and mass. AHSS with very high strength (1000 MPa and more) commonly exhibit poor sheet formability hence limiting the mass reduction attainable. This is especially true for martensite-based AHSS such as dual-phase (DP), complex phase (CP) and martensitic (MS) steels, depending on their martensite content. The higher the martensite content, the lower the thin-sheet formability [Pierman et al., 2014, Lai et al., 2015, Lai et al., 2016]. In order to mitigate failure and tearing of thin-sheets during deformation-based forming (stamping, blanking, etc.), a possible solution is to rely on the concept of localised heat treatment in order to soften the material where needed by locally annealing martensite, hence changing the local yield strength/ductility trade-off [Bouaziz, 2013]. Introducing such geometrical discontinuities in terms of material behaviour is characteristic of architectured materials [Bouaziz et al., 2009].

Localised material processing methods, such as additive manufacturing, or localised laser heat treatment in the case of AHSS, appear as natural candidates for developing architectured materials. The potential for architectured dual-phase steel in terms of yield strength / ductility trade-off is indicated on Figure 2.21.

Dual-Phase (DP) steels are composite steels, in the sense that they include a ductile matrix phase (ferrite) reinforced by martensitic islands. The DP steel belongs to the 1st generation AHSS developed for the automotive industry in order to reduce vehicle mass, which is a critical factor for fuel consumption, while preserving passenger safety, thanks to high energy absorption. DP steels are currently being used commercially for automotive applications, but the forming and joining of higher grade such as DP980 and DP1180 has been problematic due to their very high volume fraction of martensite (as shown on Fig. 2.22 for a 1 mm thick sheet). Such problems can be overcome by the use of local laser processing. Since their inception in the early 1960s, lasers have brought a new form of energy in the industry and have thus been used in various applications. The materials processing techniques based on lasers are plethora [Steen, 2003]: cutting, welding, sintering, melting, peening, hardening, cleaning, marking, drilling, cladding, bending, etc. A possible explanation for such a wide range of process applications is the precision of spatial, time and energy control made possible with laser technology: when finely controlled, laser

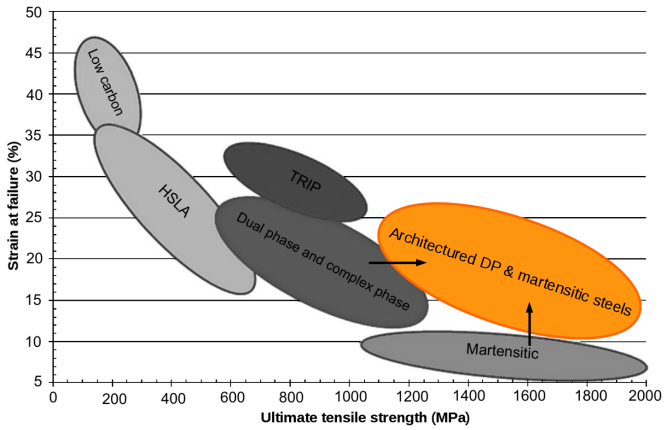

Figure 2.21: Elongation vs. strength for various AHSS, including architectured DP & martensitic steels, adapted from [Shome and Tumuluru, 2015]

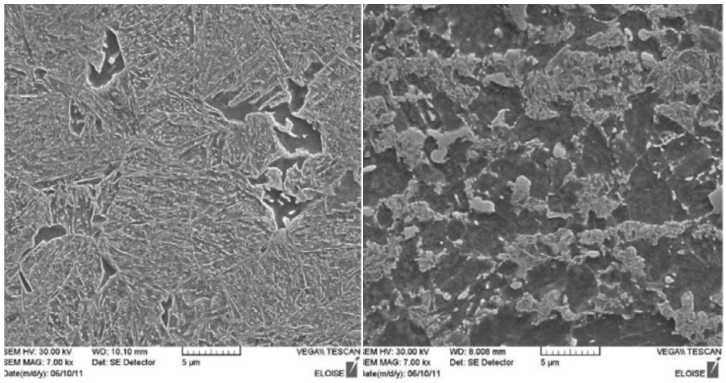

Figure 2.22: SEM micrographs of DP1180 base metal (left) and heat affected zone (right) after welding using 4kW Nd:YAG laser at 3.5m/min, adapted from ArcelorMittal internal report *in* [Shome and Tumuluru, 2015]. Bright grey denotes martensite, dark grey is ferrite.

processing can generate deterministically graded or homogeneous topographical, mechanical or metallurgical alterations, in surface or volume, depending on laser parameters, *i.e.* speed and power, as shown on Figure 10. In the context of the present work, laser materials processing is developed for the architecturation of DP steel sheets, by means of local laser heat treatment for altering the yield strength/ductility trade-off, which corresponds to the energy density range 20-50 J/mm^2 in order for the material to reach tempering temperatures 450-700°C . This range of temperature is typical of what can be found in the literature for heat-affected zones (HAZ) resulting from the laser welding of AHSS, especially DP steels [Shome and Tumuluru, 2015]. This type of treatment can be obtained using a diode laser source.

Laser heat treatment, is in itself a very wide field of research, as for traditional bulk heat treatment. It consists in inducing microstructural and metallurgical modifications by irradiating the sample with either a continuous or pulsed laser beam. While laser heat treatment has been a topic of research for more than four decades, a vast majority of the literature

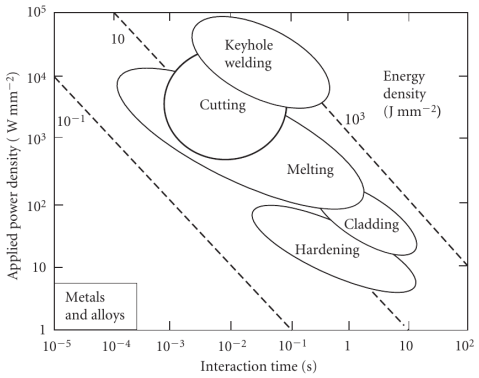

Figure 2.23: Thermal laser processing maps for metals and alloys, reproduced from [Ion, 2005]

is dedicated to hardening materials and enhancing wear resistance and fatigue life. Interestingly, softening, obtained by laser scanning overlap, is almost always seen as a problem, when reported [Iino and Shimoda, 1987, Hegge et al., 1990, Shome and Tumuluru, 2015]. An exception concerns the case of laser-assisted-shearing [Brecher and Emonts, 2010], in which the metal sheet is locally heated by the laser, while being punched, in order to facilitate the process by generating lower shearing forces and smaller edge warping, although this is not based on an actual microstructural softening. Softening is also aimed for with laser-assisted machining [Chryssolouris et al., 1997], which consists in turning or milling a material that has been heat-affected by laser, therefore enhancing the process. A thorough metallurgical study of laser-treated high-speed steels has been conducted by Russian scientists in the 1980s [D'yachenko et al., 1984, Gureev et al., 1990]. Their work showed that hardening or softening state is dependent on laser processing parameters, such as power and speed, and that softening is attainable in high-speed steel in single-pass laser processing. Tsay's team made significant contributions related to laser-annealing of steels, notably by demonstrating the positive effect of annealing on hydrogen embrittlement [Tsay and Yang, 2000], as well as its potential use for mitigating fatigue crack growth in stainless steels [Tsay et al., 2004]. [Capello and Previtali, 2009] studied the effect of laser heat treatment on formability, *i.e.* softening, for DP steels; they distinguished two regimes of metallurgical modification, annealing and tempering, that where attained below the melting temperature. Both treatments enhanced the ductility and lowered the yield strength of steel samples, as shown with tensile curves on Fig. 2.24. Also, an analytical model was proposed by the same authors for selecting process parameters in order to obtain one regime or another. This model could be helpful for calibrating the laser process parameters for softening. Most of the literature available on local laser heat treatment is dealing with the process of welding, and softening of the HAZ for high-strength DP steels is seen as a drawback, while we see it as a very smart opportunity to optimise forming processes and develop architectured materials. Laser welding metallurgy of DP steels has been studied by many groups, but most notably at McMaster University, ArcelorMittal [Baltazar Hernandez et al., 2011, Li et al., 2013] in terms of metallurgical and mechanical characterisation.

Using existing results in the welding and laser treatment literature, along with in-house knowledge

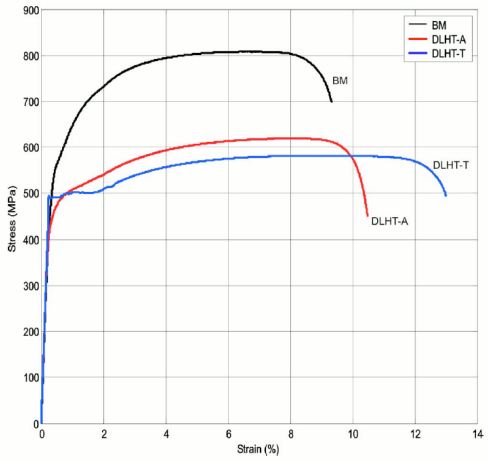

Figure 2.24: Tensile curves for dual phase steel samples that have been laser-tempered (DLHT-T) and laser-annealed (DLHT-A), and for untreated base metal (BM), reproduced from [Capello and Previtali, 2009]

of DP steel laser processing, based on experimental data and process simulation, parameters can be evaluated in order to reach local yield stress reduction, improved ductility and better formability. Also, tuning the local fracture toughness/yield stress trade-off enables crack path engineering for improved fatigue life. Before considering these applications, a thorough study is currently being conducted on the laser process parameters (speed, power, pulse duration, beam size, sheet thickness, roughness, and absorptivity) and their consequences in terms of microstructural features and mechanical properties. In order to do so, Pierre Lapouge, during his post-doctoral stay at PIMM, is working on the development of the laser processing platform for architectured materials, as well as microstructural and mechanical characterisation of architectured metal sheets. Some of his results on DP1180 steel are shown on Fig. 2.25 for 1 mm thick sheets, demonstrating the interest of such approach in terms of yield stress/ductility trade-off. This work is on-going through the ANR JCJC SCOLASTIC (Systematic Computational Optimisation and Local Laser Processing for Steel-Based Architectured Materials) project.

This is yet another example of how process can affect microstructure, shape, and scale, hence yielding new functional possibilities thanks to architecturation. Now, after having considered the microstructural scale, and the scale of architectured materials geometrical features, would it be beneficial to apply the various concepts explored in the present chapter to a larger, structural, architectural scale? We try to bring an answer to this question in the next chapter.

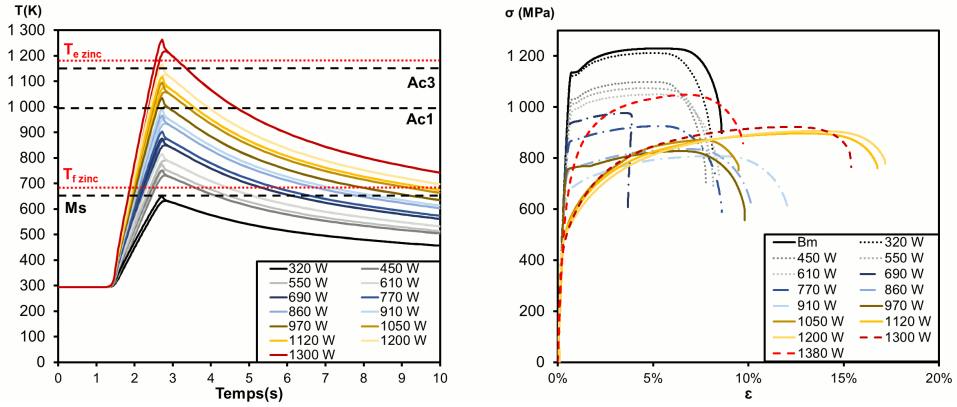

Figure 2.25: Laser processing curves for DP1180 steel samples (left) and the corresponding tensile curves (right)

3 Scaling up

I must Create a System. or be enslav'd by another Mans
I will not Reason & Compare: my business is to Create

— *William Blake, Jerusalem The Emanation of The Giant Albion (1820)*

3.1 Computation for design, modelling, and manufacturing

The merit of additive manufacturing is often summarised as its ability to produce shapes that result from a topology optimisation process. Topology optimisation aims at attaining the most efficient structure geometrically possible for a given set of requirements. It is a longstanding topic of research and development for engineers that can be traced back to the seminal work of [Michell, 1904] on frame structures one century ago, or even 30 years earlier with [Lévy, 1874], who gave the first proof for determinacy in statics for single-load trusses. The topic of optimisation has been active ever since. Nowadays, optimality in terms of industrial design is becoming more and more critical due to scarcity of material resources and the need for more efficient structures.

This technique has become well-established in the field of structural mechanics, especially when associated with FE simulation. Classical methods [Bendsøe and Kikuchi, 1988, Rozvany et al., 1995, Duysinx and Bendsøe, 1998], such as SIMP [Bendsøe and Sigmund, 2004] (Solid Isotropic Material with Penalisation) rely on node-based values to evaluate and optimise the geometry, *i.e.* the number of design variables is equal to the number of elements available in the model at initialisation. Then, the optimisation procedure consists in determining at each element if it should either stay a material element or become a void element, *i.e.* be removed. This technique has been applied to different scales: for instance with regards to the design of efficient building structures [Cui et al., 2003], or as a tool for designing micro- and nano-architectured materials [Zhou and Li, 2008]. Computation has been transforming the art of architectural practice into a field dominated by algorithms during the past 25 years

[Carpo, 2011, Carpo, 2013, Morel, 2014, Carpo, 2017, Bier, 2018].

Most computational approaches for topology optimisation used in engineering are gradient-based, they are also known as local approaches. In recent years, so-called global approaches emerged, and are currently subject to epistemological controversy in the optimisation community due to the lack of proof for global convergence, as well as inefficiency in comparison with classical gradient methods [Sigmund, 2011, Le Riche and Haftka, 2012]. Although the fact that being based on heuristics has been held against global approaches in structural mechanics, heuristics itself should not be considered a shortcoming but rather an epistemological hypothesis.

The computational framework being developed at PIMM relies on a global topology-optimisation approach making use of cellular automata, as well as FE for evaluating the cost function, which has to be minimised for given constraints, as depicted on Fig. 3.1, reproduced from [Tovar et al., 2006]. This evaluation step is straightforward since it consists in performing a FE computation on the generated model using predefined local constitutive behaviours, and averaging the response of the structure, to a given set of boundary conditions and applied loads, by the computational homogenisation method [Dirrenberger, 2012]. The topology optimisation step is somewhat more difficult as choices have to be made with regards to the many approaches available and the type of problem being dealt with. Several reviews are available on this topic, see for instance [Eschenauer and Olhoff, 2001, Bendsøe and Sigmund, 2004, Rozvany, 2009]. Most developments in topology optimisation dealt with the efficiency of structures, *i.e.* minimising the mass of materials while optimising the elastic stiffness of a structure under a given load, which means choosing between void and matter for any given point in the design space, either continuous [Allaire, 2002] or discrete [Bendsøe and Sigmund, 2004].

Architecturation patterns can be either continuous, discrete, periodic or random, therefore cellular automata (CA) seem like natural candidates for generating them. CA correspond to an evolving structure based on a regular lattice, they are characterised by 5 properties: lattice geometry and dimensionality, cellular neighbourhood, cell state, local rule of transition, and boundary conditions. CA have already been used for topological optimisation, but not for solving pattern-type problems [Hajela and Kim, 2001, Missoum et al., 2005, Hopman and Leamy, 2010]. An alternative method, the hybrid cellular automata (HCA) method, was proposed by [Tovar et al., 2004] by taking the best of both CA and SIMP. This method has been developed thoroughly for structural optimisation [Tovar et al., 2007]. A critical improvement to the CA approach was the implementation of multigrid methods in order to accelerate the convergence during optimisation [Kim et al., 2004, Zakhama et al., 2009]. The development of genetic algorithms in structural optimisation is known as evolutionary structural optimisation (ESO). It was first proposed by [Xie and Steven, 1993, Chu et al., 1996] in the early 1990s, but suffered from various drawbacks (lack of convergence, mesh-dependency) which were partially overcome by the bi-directional evolutionary structural optimisation (BESO) approach developed by the same team a decade later [Huang and Xie, 2007]. Other developments have been undertaken regarding genetic algorithms, *e.g.* in terms of multi-criterion optimisation [Canyurt and Hajela, 2010].

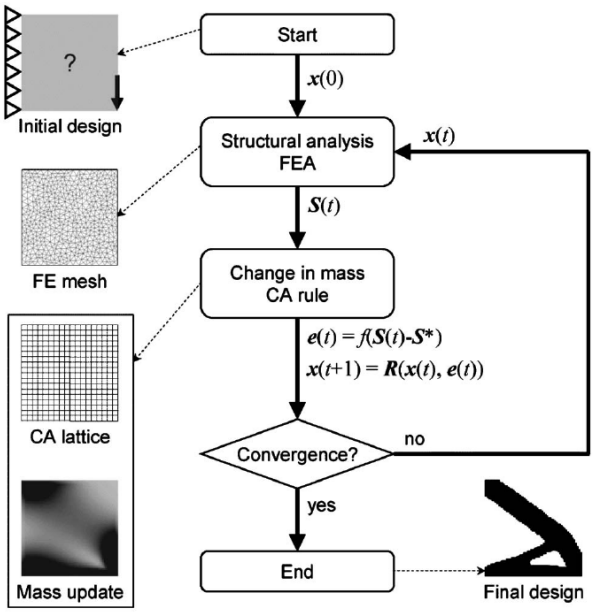

Figure 3.1: Hybrid cellular automaton algorithm. The algorithm starts with the definition of the design domain, material properties, load conditions, and the initial design $x(0)$. A finite element analysis (FEA) is performed to determine the mechanical stimuli and, therefore, the error signal operating on the automata, $e_i(t)$. The mass is updated according to the set of rules, $x(t+1) = R(x(t), e(t))$. The convergence is determined according to the change in the design variables and/or field variables. If there is no convergence, the process continues with a FEA performed on the updated design. Reproduced from [Tovar et al., 2006].

Therefore, a framework based on CA with a local rule of transition using the BESO approach, along with multigrid implementation appears like an appropriate option to design architectured materials, especially by the ability of such framework to deal with multiple scales of topology optimisation. In order to be of interest for architectured materials, the multiscale optimisation scheme must comply with optimising multiple anisotropic materials with nonlinear elastoplastic behaviour, which will yield nonlinearities in structural response of the architectured materials for various sets of requirements/cases of application.

Generating and modelling shapes for additive manufacturing follows specific rules, coming from both processing constraints, *e.g.* layer thickness, product dimensions, etc., and the functional properties of the produced part, *e.g.* mechanical strength, thermal conductivity, etc. An usual and straightforward method for generating an additive manufacturing building path is to use a 3D-to-2D slicing software. It consists in slicing the 3D shape, *i.e.* computer-aided design (CAD) file, of an object into flat thin layers of constant thickness which can be layered one up onto the other, *i.e.* computer-aided manufacturing (CAM) file. This results in a cantilever-method strategy. Each layer is then made of a contour line, as well as a filling pattern such as a honeycomb structure or a space-filling curve (Peano curve, Hilbert curve, etc.); the filling density can be adjusted for given requirements. This method is well-established for small-scale additive manufacturing.

3.2 Towards large-scale additive manufacturing

The industrial applications of small-scale additive manufacturing in production (in opposition to prototyping) concern either geometrically complex products in high value-adding sectors (biomedical, sports, aerospace) and/or parts made of costly materials, typically alloys which include Titanium, Nickel and/or Chrome in their composition. This type of additive manufacturing is usually powder-based, which is intrinsically costly, but enables very good spatial accuracy and microstructural control. Technologies such as direct metal laser sintering (DMLS), selective laser sintering (SLS), electron beam melting (EBM) or direct metal deposition (DMD) are taking off in high-end industries due to its cost-saving possibilities both in terms of reducing the number of manufacturing steps and the amount of materials used [Gutowski et al., 2009, Allwood et al., 2011, Yoon et al., 2014, Baumers et al., 2016, Ford and Despeisse, 2016].

The DEMOCRITE project (2014-2015, funded by HESAM Université) aimed at transposing such possibilities within an architectural context, *i.e.* developing large-scale additive manufacturing with the same level of material performance as conventional processing methods and comparable accuracy as DMLS, *i.e.* a spatial resolution circa 0.1 % of the building size, about 1 mm for a metre-wide printer. Our group at the PIMM lab explored the potential applications of large-scale additive manufacturing techniques to civil engineering structures. Thanks to this large-scale processing technique, one could apply the concept of architectured materials within an architectural context; multifunctional properties can be achieved for structural elements, by optimising geometry and material composition, as it was done in [Gosselin et al., 2016], for an enhanced thermal insulation case study regarding a structural wall element produced by large-

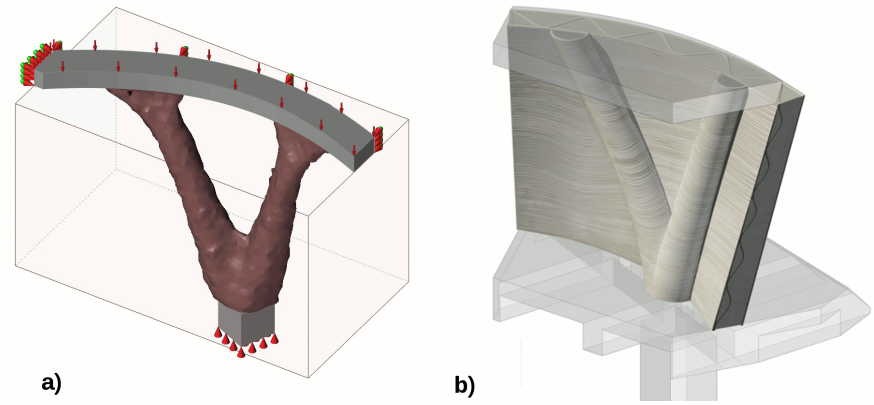

Figure 3.2: An example of implementation of topology optimisation in the DEMOCRITE project: a) Boundary conditions and results for the structural optimisation problem; b) Rendering of the actual multifunctional wall including both the structural and thermal insulation parts.

scale additive manufacturing. An example of topology optimisation based on the SIMP approach, performed during the DEMOCRITE project is given in Figure 3.2. The initial optimisation results (Fig. 3.2.a) were adapted and refined in order to fit the additive manufacturing constraints as well as the architectural scenario. The rendering shown on Fig. 3.2.b actually includes the visible layers of printed concrete resulting from the building process.

Based upon an understanding of the limitations identified in previous projects present in the literature, the DEMOCRITE project dealt with the large-scale additive manufacturing of selective deposition for ultra-high performance concrete (UHPC) [Duballet et al., 2016]. The 3D printing process involved is based on a Fused Deposition Modelling-like technique, in the sense that a material is deposited layer-by-layer through an extrusion printhead. The project also explored the possibilities offered by CAD and optimisation, and their integration within the product design process in the case of large-scale additive manufacturing. Thus, the introduced technology succeeded in solving many of the problems that could be found in the literature. Most notably, the process enabled the production of 3D large-scale complex geometries, without the use of temporary supports, as opposed to 2.5D examples found in the literature for concrete 3D printing [Khoshnevis, 2004, Buswell et al., 2007, Cesaretti et al., 2014].

Generating and modelling shapes for additive manufacturing follows specific rules, coming from both processing constraints, and functional objectives. According to [Gosselin et al., 2016], the concept of freeform commonly used in the literature is not adequate nor sufficient for describing concrete 3D printing. For a given printing process and automation complexity, one can attain specific types of topologies within a given time-frame and performance criterion for the material and/or structure to be built. Design conditions for large-scale additive manufacturing depend on many other parameters than just the properties of extruded cementitious materials; parameters such as the printing spatial resolution, overall size of parts to be printed, the environment, the presence of assembling steps, etc. A tentative classification of such relationships between

geometrical complexity, processing, and design is proposed in [Duballet et al., 2017]. The cantilever strategy, which is characteristic of small-scale additive manufacturing, is not appropriate for large-scale printing since it does not take into account the processing constraints and their impact on the performance of the printed structure. The building path should be adapted and optimised based on simulation results in order to take into account constraints and to exhibit more robustness for complex geometries.

The processing constraints depend mostly on the fresh material properties in its viscous state, as well as early-age behaviour, in interaction with the building strategy and the stiffness of the structure being built. On the other hand, functional requirements will depend on the properties of the hardened material, its durability [Lecampion et al., 2011], as well as the structural geometry for effective stiffness, and other functional properties such as thermal and sound insulation. See [Gosselin et al., 2016] for a geometrically induced thermal insulation case study. Both types of constraints have to be considered at the design stage.

Printing path generation is a critical step during the design phase. There are two main approaches to tool-path generation in the context of 3D printing:

- 3D-to-2D slicing, which is by far the most common method adopted, yields planar layers of equal thickness built on top of each other. This approach is not optimal from a design and structural viewpoint as it will induce cantilevers when two consecutive layers have different sizes and limit the attainable geometries;
- the tangential continuity method, which has been introduced in [Gosselin et al., 2016] in order to optimise the structure being built by creating layers of varying thickness. These layers exhibit a maximised surface area of contact between each other, hence stabilising the overall structure. Moreover, this method is actually exploiting the possibilities of the process in terms of printing speed and flow for generating variations in the layer thickness.

A driving force for additive manufacturing is its ability to produce more complex 3D shapes in comparison to casting or subtractive processes. This complexity allows to design optimal structures based on topology optimisation techniques. One of the main current challenges is to modify optimisation algorithms in order to account for the additive manufacturing constraints, especially with regards to the processing parameters and structural stability while printing. A possible answer to these challenges would be to consider the multiphysics phenomenon aspect of 3D printing, which involves the elastic stability of the overall structure being built, the kinetics of hydration, the evolving viscoplasticity of fresh cement, the evolution of temperature within the printing environment, etc. As a matter of fact, all these physical problems, with multiple time and space scales, can be modelled on their own, but coupling them generates complexity and uncertainty regarding the process of 3D printing. Therefore, efforts should be concentrated on understanding and modelling the printing process in its multiple physical aspects, only then optimisation will be fully integrated with the processing, which would virtually change the way 3D printed structures are conceived today. Indeed, the future of large-scale additive manufacturing

in architecture and construction might reside in smarter, more parsimonious use of 3D printing on specific parts of the printed object, where it is the most pertinent in order to take advantage of both the material properties and morphology of the structure being built.

An overview was given in Chapter 2 regarding the concept of architectured materials, and some examples were highlighting the importance of geometry at multiple scales, as well as the computational tools associated with the development of such materials. In fact, this development is made possible by both the computerisation of the designing step, and robotisation of the manufacturing step. This automation of the process theoretically allows for a higher accuracy and infinite customisation of materials and structures according to a given set of requirements. In this context, the top-down approach of architectured materials, *i.e.* going from the application down to the design of materials, becomes generalisable, hence yielding new opportunities for the built environment sector, *e.g.* in architectural design, structural engineers' calculations, or the logistics of a construction site, if building information modelling (BIM) is integrated. From an application viewpoint, one of the most critical point is indeed to be able to incorporate robotic actions within the BIM model.

3.3 Creating a technology company

Capitalising on the relative success of the DEMOCRITE project, a spin-off company, XtreeE[1], was created in order to develop and commercialise the 3D printing technology introduced. This mad idea would never have seen the light of day without the force of will of Philippe Morel, my partner in the DEMOCRITE project, who has always been at the forefront of things, including building up on the momentum of the DEMOCRITE project in order to create the company. I would never have gone doing research on such topic if it were not for the excitement of working with Philippe Morel, which I had the chance of doing from 2013. Although XtreeE is now developing in its own terms, it is important for me to acknowledge the initial input of Ph. Morel and EZCT Architecture & Design Research, which has been critical in helping the company survive and grow during its first year of existence. XtreeE was co-founded mainly by many individuals involved in the DEMOCRITE project, including graduate students from ENSA Paris-Malaquais, where Philippe Morel and Christian Girard were chairing the Digital Knowledge program. This was a first experience for me, and as painful as it has been since we have started pursuing this goal, it has been very rewarding from an intellectual and personal viewpoint. There is a satisfaction in looking at ideas once laid on paper being translated into real-life realisations, every scientist should have the opportunity to do so in his/her career, I was just very fortunate to do it on the first funded research project I have ever led. The company was officially created in December 2015; as of July 2018, it has generated 8 full-time jobs in the area of engineering, design, and project management. Most results from DEMOCRITE are gathered with details in [Gosselin et al., 2016, Dirrenberger, 2018].

[1] http://www.xtreee.com

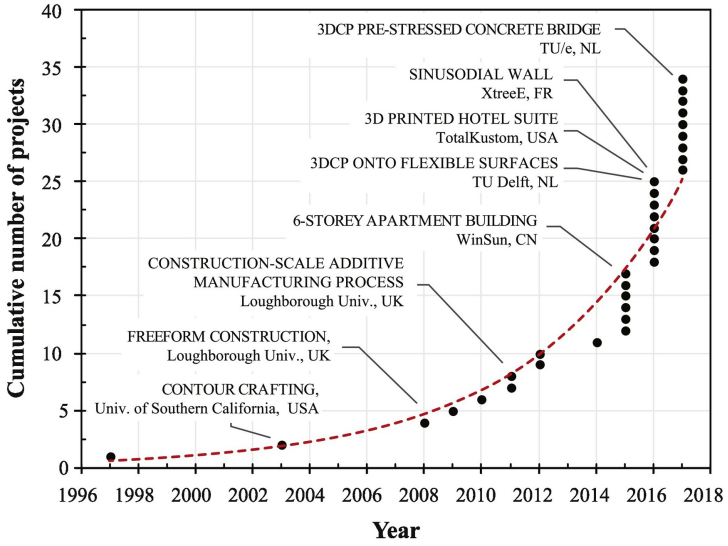

Figure 3.3: The rise of large-scale additive manufacturing for construction applications since the concept inception in 1997, reproduced from [Buswell et al., 2018]

3.3.1 A new playground for multidisciplinary research

Getting back to science, there are more questions that have stem from the technology developed in DEMOCRITE, than answers that have been brought by our research. Given the complex nature of large-scale additive manufacturing technology, multiple disciplinary research is developing around it. Unfortunately, due to the international context of scientific research, publication, and careers, multidisciplinarity[1], *i.e.* drawing on knowledge from other disciplines while staying within one discipline's boundaries, is the only way acceptable with regards to an academic career, although it may not be pertinent to actually solve problems related to large-scale AM. This is illustrated by the exponential number of research projects related to large-scale AM, or 3D concrete printing (3DCP), shown in Fig. 3.3, reproduced from [Buswell et al., 2018]. A holistic, *i.e.* transdisciplinary, approach integrating considerations from multiple fields at once, *e.g.* robotics, computer science, rheology, construction technology, chemistry, mechanics, design (but also ethics, energetics, architecture, urbanism, economy, aesthetics, marine biology (!), etc.), hence transcending the natural boundaries of say, materials science, might be necessary in order to solve actual problems. This transdisciplinary approach is reminiscent of the strategy adopted for the development of architectured materials [Bréchet, 2013]. From our short experience with XtreeE, every single project has needed a transdisciplinary approach. This duality between academic and industrial considerations is revealing of the current pressure on the international academic market, and the risk mitigation strategy adopted by most of the public funding bodies. There is probably something wrong when industry is considering riskier approaches to research than academia.

[1] I resort here to the definitions established by [Choi and Pak, 2006], for multidisciplinarity, interdisciplinarity, and transdisciplinarity.

3.3.2 Concrete formwork 3D printing

The large-scale robotic additive manufacturing process for concrete summarised in Fig. 3.4 was conceived during the DEMOCRITE project before being applied within the construction industry by XtreeE. Based on this process, a construction strategy was derived by XtreeE for concrete formwork 3D printing. The principle consists in only 3D printing the formwork necessary for casting another structural material such as ultra-high performance concrete for fibre-reinforced concrete, or insulation material, *e.g.* foamed concrete, for giving the part functionality, as shown on Fig. 3.5. The printed formwork is left in-place and becomes a so-called *lost formwork*. An optimal trade-off has to be taken into account from the early design steps as to the ratio of printed material within the built part, which can be critical for reaching economic viability. Depending on the application considered, concrete formwork 3D printing can be more efficient than either all-3D concrete printing, or traditional building techniques, from both a economic and/or building strategy viewpoint. This assertion is demonstrated in the following with a case study. More case studies can be found in [Gaudillière et al., 2018, Gaudillière et al., 2019].

3.3.3 Case study: Post in Aix-en-Provence, France

Context

The 4-m high freeform pillar shown on Fig. 3.6 is placed in the sports facilities of a school in Aix-en-Provence, France. It supports a concrete awning covering part of the playground. The sports facilities project was mandated by the Aix-Marseille Metropolis. The pillar, part of this larger project, was handled by the following people: Marc Dalibard as architect (also the architect for the whole sports facilities building), Artelia as structural engineering office, AD Concept as construction company, LafargeHolcim as material supplier and Fehr Architectural as UHPC concrete caster. For the construction of the pillar, the responsibilities of the actors were divided as follow: Marc Dalibard, as architect, was also the manager of the overall project, and defined the shape and placement of the pillar. Artelia, as structural engineer, supported XtreeE both during design and construction phases, and was tasked with defining the load case on which the topological optimisation would be based, as well as verifying the strength and stability of the printed pillar in accordance with the load case. LafargeHolcim supplied a specific 3D print concrete, developed with XtreeE in an earlier collaboration and Fehr Architectural casted UHPC inside the pillar, a task requiring a specific licence. Each one of the key players supported XtreeE in the definition of the fabrication strategy adopted for the pillar, by providing input regarding their field of expertise.

XtreeE identified a fabrication strategy for the post and adapted the printing system developed earlier according to the fabrication strategy and its requirements. During the design stages, XtreeE co-defined the load case for the topological optimisation with structural engineer Artelia and designed an exact shape for the pillar through the optimisation. In the fabrication stages, XtreeE coded the manufacturing files for the printing system and performed the manufacturing, before

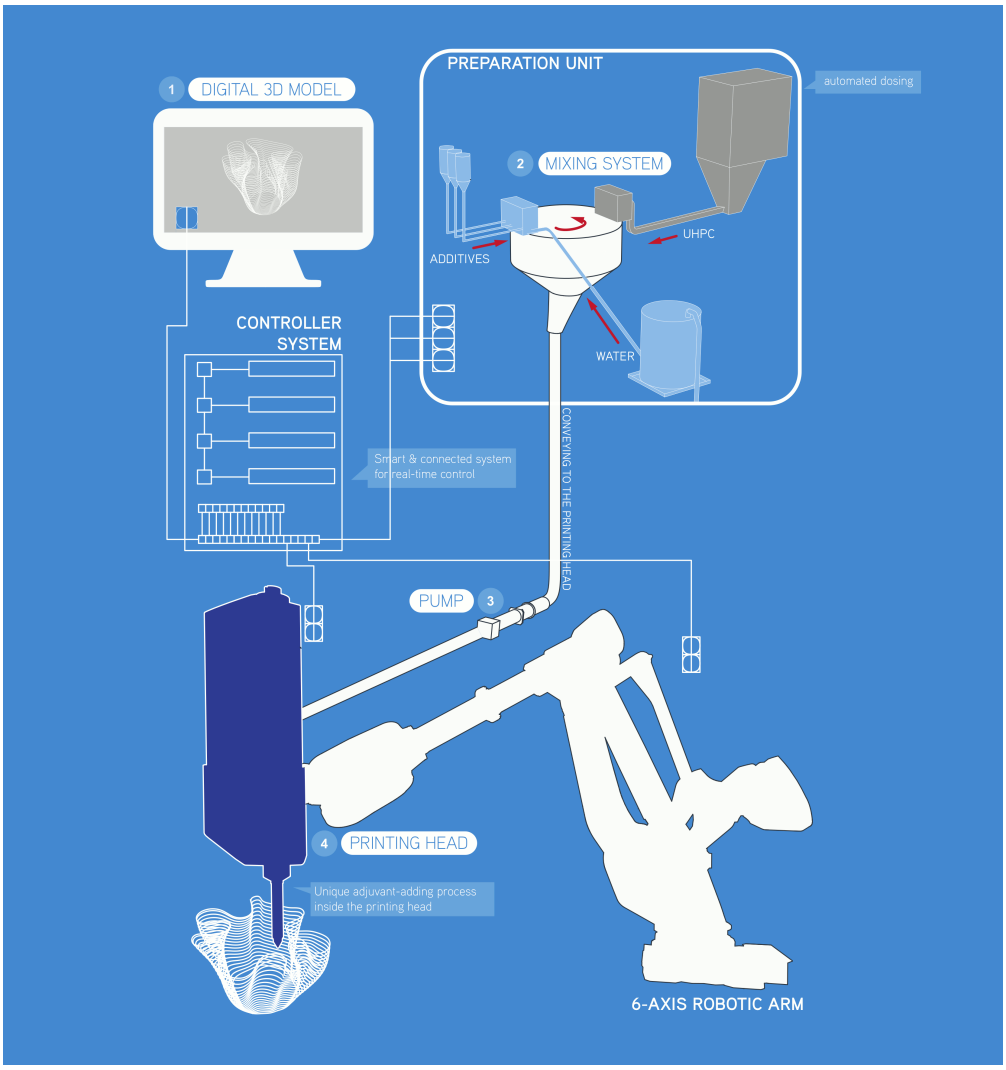

Figure 3.4: Workflow of the large-scale concrete additive manufacturing

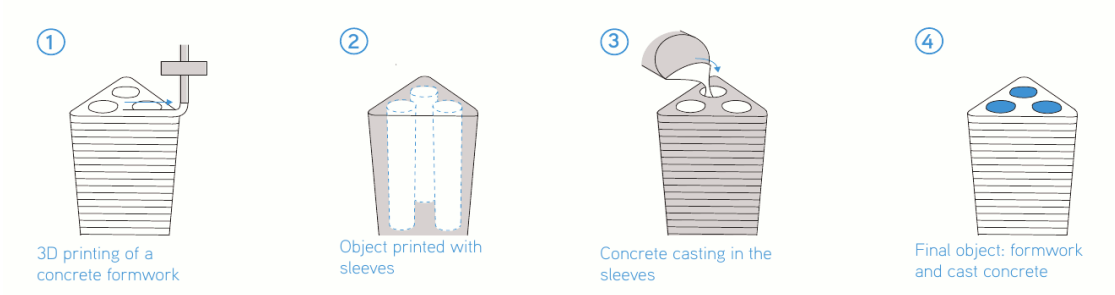

Figure 3.5: Schematic view of the concrete formwork 3D printing process

Figure 3.6: Post in Aix-en-Provence, photo by Lisa Ricciotti

co-supervising the placing of the pillar on site with architect Marc Dalibard.

Design

In the initial project designed by architect Marc Dalibard, a complex truss-shaped pillar supporting the roof was already planned. Although the idea of a complex truss-shaped pillar was featured, no viable design for the pillar existed at this stage of the project. XtreeE came in at this point and took over the design of the pillar, based on the sketches provided by the architect, starting from the algorithmic design developed by EZCT Architecture & Design Research. The design of the pillar is based as much on the formal intention highlighted in these sketches as on the constraints fixed by the building regulations in effect at the time and by the 3D printing manufacturing method. As no building regulation existed regarding 3D-printed items integrated in buildings at the time of construction, and to stick to the projected schedule, the choice was made to use the lost formwork manufacturing method. Instead of having to validate the pillar and its manufacturing method by using an ATEx (Experimental technical appreciation), a long and expensive procedure for experimental construction in France, the lost formwork made it possible to rely on existing building regulation on UHPC concrete. The main constraint of the 3D printing system developed by XtreeE for complex truss shapes as the pillar is the maximal inclination that can be given to printed geometries. In the case of the Aix-en-Provence pillar, this issue is avoided by printing supports at the same time than the geometry to enable any angle for the parts of the truss. To define the precise shape of the pillar, we relied on a topological optimisation method, to ensure an optimal use of matter in the truss. The entire circular volume containing the pillar is used as research space for the truss to develop, and the applied load case included the weight of the concrete awning supported by the pillar as well as site-specific constraints

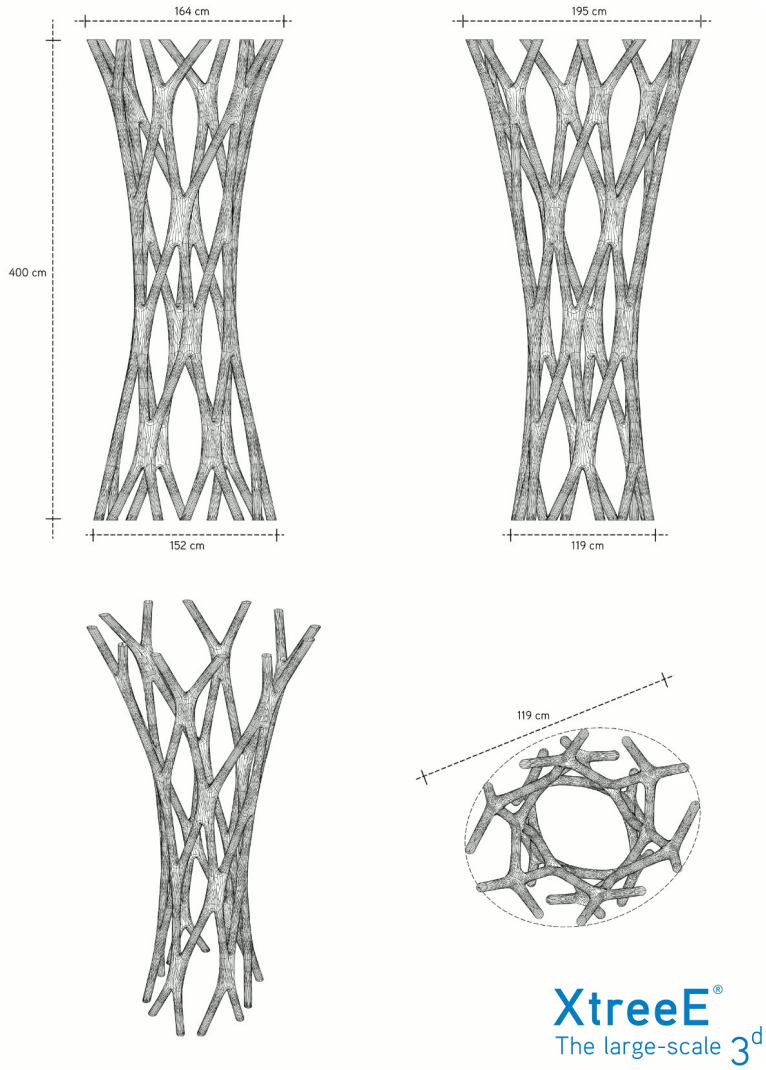

Figure 3.7: Final design of the pillar after topology optimisation

(wind, etc.). The resulting final shape is shown on Fig. 3.7. A more thorough examination of the possibilities offered by topology optimisation in the context of 3D concrete printing is available in [Duballet et al., 2018a].

Given the selected approach of lost formwork printing, the pillar is made of an outer shell that is 3D-printed and later filled with UHPC. The 3D-printing system in place at the time at XtreeE did not allow for printing the outer shell in one piece. Therefore, the pillar is divided in three smaller parts (cf. Fig. 3.8), each one to be filled with concrete and then assembled together to form the whole element. During casting, metallic female connectors are inserted in the concrete at each end of the parts. Male plugs are then used to connect the different parts of the pillar and assemble them.

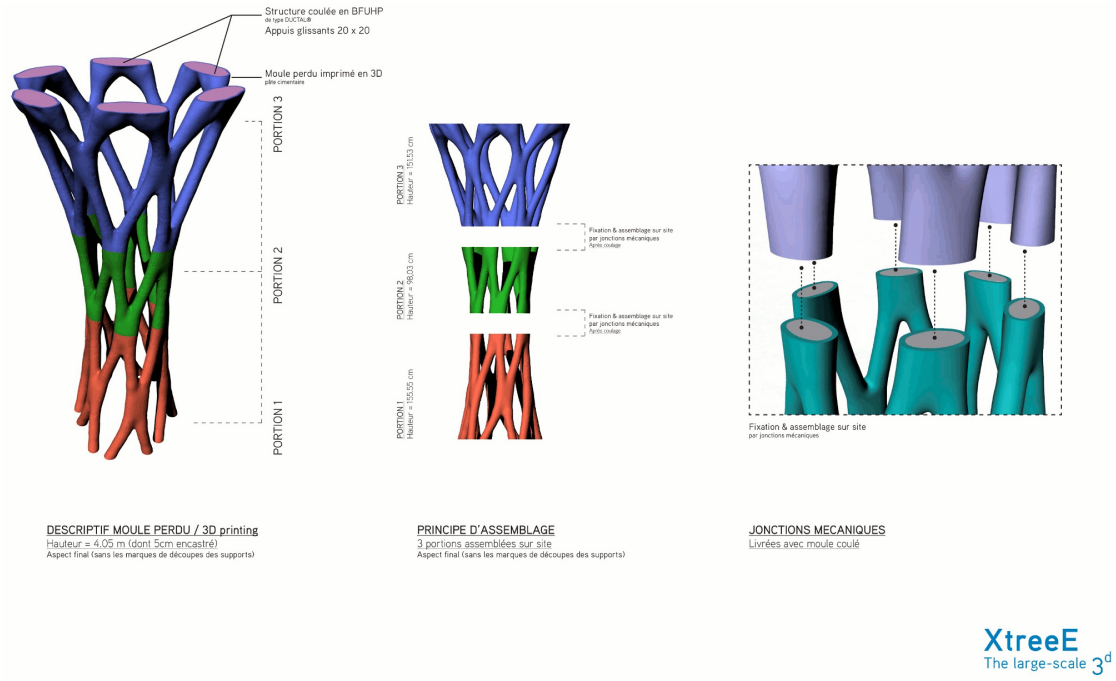

Figure 3.8: Splitting and assembling principles for the 3D-printed pillar system

Manufacturing

Manufacturing of the pillar includes several stages: 3D-printing the outer shell, at XtreeE's headquarters in the south of Paris, France, casting the UHPC and integrating the connectors, at the Fehr Architectural production facility in the north of France, and final assembly on site in Aix-en-Provence. 3D-printing the outer shell inside the facility allows, like for UHPC casting, a precise control and monitoring of the environment, to ensure ideal temperature and humidity conditions for the concrete to behave as expected. As a precaution, after running trials on smaller geometries similar to the pillar, it was decided to 3D-print the formwork in four parts rather than three. The concrete formwork took 15 hours to print in total, approximately 3 hours and 45 minutes for each part of the post. Setting time is typically comparable to the setting time of C60 concrete, *i.e.* about 2 hours. Once the formwork was successfully 3D-printed, an assembly trial was conducted at our facility to ensure the results were as precise as expected before shipping the parts. The casting of UHPC in each part of the pillar was then operated by the team of Fehr Architectural. In order to resist the hydrostatic pressure resulting from the casting, supports printed with the pillar were left in place until the UHPC set. The supports were then removed and the parts were shipped on site to Aix-en-Provence. The definitive assembling of the parts was performed there, before installing the pillar in place, with sliding supports on top and at its feets. Finally, on request of the architect, the pillar was given a smooth finish by coating it to cover the line pattern specific to 3D-printed objects. The difference of surface roughness is shown on Fig. 3.9.

Figure 3.9: Before (left) and after (right, photo by Lisa Ricciotti) surface smoothing obtained through manual coating.

Comparison to standard building methods

After completing the Aix-en-Provence pillar project, we conducted a study to compare our process for complex truss-shaped pillars fabrication to standard building methods. Two types of pillars are compared: a traditionally built pillar with complex shape, with geometry comparable to the Qatar National Convention Center pillars shown in Fig. 3.10, but at a smaller scale, and a more complex pillar in terms of shape, built with additive manufacturing lost formwork technique, such as the Aix-en-Provence pillar. The building process, and gain in terms of material, build time, and workforce, for both types of pillar is detailed in Fig. 3.11. The data for 3D-printing is based on the experience gained over the Aix-en-Provence pillar project, while the data for traditional casting technique using steel moulds is based on realistic values for implementation in the same socio-economic environment, *i.e.* Western Europe. It is noteworthy that the actual cost of steel moulds has not been considered, although it is likely to be the most costly aspect of a traditional casting technique. Even without considering the moulds, concrete formwork 3D printing emerges as a cost-effective alternative for pillar construction.

The table presented in Fig. 3.11 highlights the potential gain from several viewpoints, some more significant than others. A last element of comparison can be given by confronting the total production cost of the Aix-en-Provence pillar to the total production price of a traditionally built complex pillar: a 62,5% total cost gain is obtained, based on our information for the cost of the Aix-en-Provence pillar, and quotes obtained for a traditional manufacturing. One of the main reason for this cost difference, on top of the gain identified on time, materials, and workforce, is the absence of a specific material and shaping for the mould, hence eliminated by using the lost formwork method. Furthermore, comparison with the cost of pillars being built at the Nantes

Figure 3.10: Qatar National Convention Center, by architect Arata Isozaki in Doha, Qatar, exhibiting organic truss-shaped pillars.

train station in France, brings to light the fact that costs become comparable when building at least 18 identical pillars with a traditional mould manufacturing method. The Aix-en-Provence pillar has also provided input on possible improvements for the lost formwork method, including getting rid of the supports by advancing on the development of the 3D-printing system, gathering each of the manufacturing stages (3D-printing, casting, assembling) at the same place to reduce transportations, as well as setting up construction regulations for 3D-printed concrete structural parts.

The various advantages of large-scale additive manufacturing of ultra-high performance concrete, as well as the concrete formwork 3D printing technique, have been reviewed based on the analysis of Aix-en-Provence pillar case study taken from industrial construction project, performed using the XtreeE 3D printing technology. The multiple aspects of potential socio-economic gain for relying on additive manufacturing are three-fold: 1) materials saving by using the right amount of matter where needed, given that a multi-objective topology optimisation computational framework is available; 2) time saving by reducing the number of steps in the construction process, as well as being BIM-compatible for construction-planning strategies; 3) workforce saving by limiting on-site manual building steps, therefore enhancing safety on the construction site.

Although the lost formwork strategy allowed to get around experimental technical certification, further work should have to be conducted with certification authorities for the construction industry in order to define a legal and regulatory framework for 3D printed structures. The technological feats presented in this work are commercially available, but a legal framework and economic market are to be developed in order for the 3D printing technology to transfer into the mainstream construction industry.

XtreeE (3D-printing)	*Traditional method (Steel mould)*
MATERIAL CONSUMPTION	
3D-printable Concrete ..... 650 kg UHPC Concrete (Casting) ..... 1600 kg Steel Reinforcement (Fibers) ..... 50 kg *(+ 3D-printable concrete for supports)*	*UHPC Concrete (Casting) ..... 2250 kg* *Steel Reinforcement (Fibers) ..... 50 kg* *+ Steel for the mould*
Concrete consumption: -0 kg / -0,0%	
Steel consumption (mould): -100,0%	
MANUFACTURING PROCESS	
1. Digital design optimisation and process design ..... 3,0 days 2. 3D-printing of the outer shell in concrete ..... 2,0 days 3. Setting time ..... 1,0 days 4. Casting of concrete inside the shell ..... 1,0 days 5. Setting time ..... 5,0 days 6. Transportation to site ..... 0,5 days 7. Installation and assembly ..... 1,0 days 8. Coating ..... 2,0 days **Total** ..... 15,5 days	*1. Digital design optimisation and process design ..... 3,0 days* *2. Creation of a mannequin ..... 3,0 days* *3. Creation of a steel mould ..... 3,0 days* *4. Casting of concrete inside the mould ..... 1,0 days* *5. Setting time ..... 5,0 days* *6. Transportation to site ..... 0,5 days* *7. Installation ..... 1,0 days* *8. Coating ..... 2,0 days* *(+ discard & recycle the mannequin and mould)* ***Total ..... 18,5 days***
Manufacturing time: -3,0 days / -16,2 %	
WORKFORCE	
Designer / Engineer for toolpath design ..... 1 pers. - 3,0 days 3D printing supervisor ..... 1 pers. - 2,0 days 3D printing operator ..... 2 pers. - 2,0 days Concrete casting operator ..... 1 pers. - 1,0 days Transportation ..... --- external --- Assembly operator ..... 2 pers. - 1,0 days Coating operator ..... 1 pers. - 2,0 days **Total (FTE)** ..... 14,0 man.days	*Designer / Engineer for mould design ..... 1 pers. - 3,0 days* *Steel mould fabrication operator ..... 2 pers. - 5,0 days* *Concrete casting operator ..... 1 pers. - 1,0 days* *Transportation ..... --- external ---* *Assembly operator ..... 2 pers. - 1,0 days* *Coating operator ..... 1 pers. - 2,0 days* *Mould and mannequin recycling ..... --- external ---* ***Total (FTE) ..... 18,0 man.days***
Workforce use: -4,0 man.days / -22,2%	

Figure 3.11: Table of comparison between concrete formwork 3D printing vs. traditional concrete casting in steel moulds.

3.4 Masonry 4.0

In his PhD work at Laboratoire Navier under the supervision of Olivier Baverel (ENPC) and myself, Romain Duballet is exploring the possibilities brought by 3DCP in the context of construction [Duballet et al., 2018a, Duballet et al., 2018b]. As a matter of fact, beyond the demonstrative aspect of most projects considered in Fig. 3.3, very little has been done to actually prove and quantify the interest of using 3DCP in construction. If the fabrication process is in itself innovative, and very promising for the future of construction work, its impact on the fabricated object still remains marginal. The problem that we address here is the following: *how can this technology allow for a substantial reduction of overall concrete consumption in the building industry?* As a matter of fact, cement clinker production is responsible for about 8% of greenhouse gas emissions [Olivier et al., 2012]; the total production of concrete is equivalent to 1.5 m^3 per capita per year, half of which is used in China [U.S. Geological Survey, 2016]. As an answer in order to reduce overall cement consumption, a novel constructive approach based on robotic extrusion of mortar is introduced. Mortar is extruded only for its structural performances, but we take advantage of a novel assembly strategy of insulating blocks, that also serve as support for the printing.

Constrained masonry, the assembly technique of breeze blocks and mortar restrained in a reinforced concrete frame, is a very popular building system, especially for individual and collective housing, for it is at once cheap, fast and easily implemented. From a purely mechanical point of view, it is however quite inefficient. In the case of a one or two-storey house, the need in mechanical strength and elastic stiffness for the wall itself, considering the presence of the reinforced concrete frame, is indeed far lower than the breeze blocks/mortar system can provide. The main role of this staking is in fact to allow solid continuity between the concrete frames, for bracing purpose and to act as separating wall. Up to a limit, it could be said that the mortar between the blocks is the only needed element to provide strength. Such considerations leads us to the idea of assembling insulating blocks instead of breeze blocks, leaving the mechanical role to the mortar in-between, and getting thermal performances in addition. The new system for the wall is now a generalisation of the previous one: a continuous spatial structure in mortar, and thermal insulation in the negative space. The three questions to answer are then (a) Which shape for the mortar structure? (b) Can it be easily fabricated? (c) Are the overall performances meeting the set of requirements? The key aspect of the technique is to assemble specifically shaped insulating blocks by printing a mortar joint at the edges location (cf. Fig. 3.12). The mortar is extruded through a nozzle controlled by a robotic arm, as described in [Gosselin et al., 2016]. The mortar acts as joint for the insulating blocks, while they act as printing support for the mortar. At the end, tie columns and ring beams will ensure the masonry confinement. This approach is rather new in comparison with most examples of large-scale concrete 3D printing available [Labonnote et al., 2016, Duballet et al., 2017].

This system brings some shape constraints for the blocks, they must form a space tessellation, the edges of which will form a mortar space truss. Since this truss is printed on the blocks, it must not be done too close to verticality. In addition, for assembly purpose, the number of

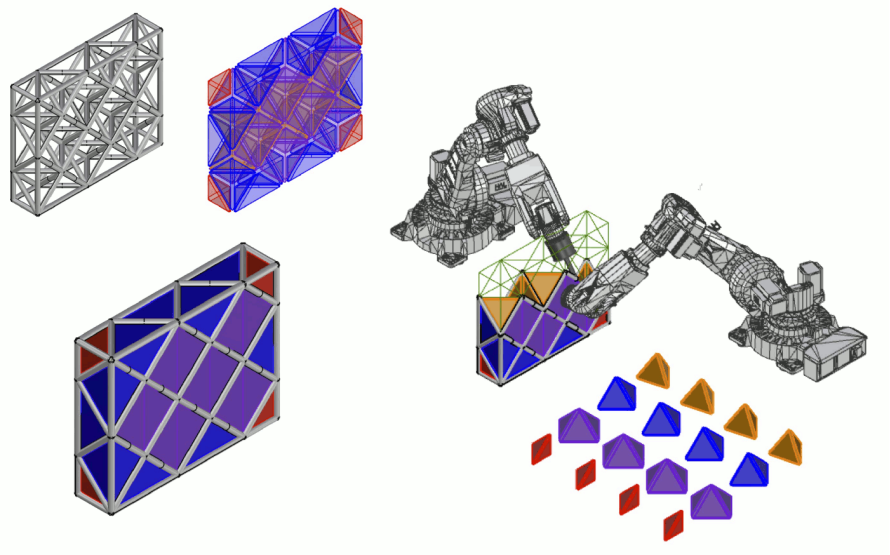

Figure 3.12: Automation in construction: two robots working together, one 3D printing concrete while the other is assembling blocks

crossing elements at each nodes must be limited. Coming back to the concept of lattice structures introduced in Section 2.3.1, we have conducted a comparison of different space tessellations. Thanks to this manufacturing technique it is realistic to hope for ultra-light space truss walls that drastically reduce concrete consumption while reaching current needs for thermal insulation. Different grid topologies are investigated for the concrete space truss in terms of structural efficiency and compatibility with the proposed manufacturing method. These topologies are taken from the edges of a space tessellation of the bounding box of the wall, so that a geometric duality with the polyhedral insulating blocks can be obtained. Considering that fresh mortar will be printed on the blocks, some geometrical configurations are to be avoided. We have retained five potential topologies that do not present internal vertical members that would be difficult to print, they are shown on Fig. 3.13.

We suppose that the lateral and horizontal frontier are supported, as for constrained masonry, and impose three load cases corresponding respectively to self-weight, overall lateral pressure (wind) and a specific horizontal point load of 2 kN. This last case has been taken from design methods for guardrails. The need for such verification comes from the attainable lightness for the wall (around 50 $kg.m^{-2}$). Traditional block work construction is indeed very often far more resistant that one could need, in non-seismic areas. In our case, this additional load case is critical. From possible structural failure, due to material stress, local and global buckling, in every case the tensile stress in members is the critical one. We conduct a heuristic calculation on each topology configuration with Grasshopper plug-in Octopus[2], evaluating the performance with regards to the following objectives: additional insulating thickness to reach target value, maximum tensile stress in members, and weight per unit area ($kg.m^{-2}$).

[2] http://www.food4rhino.com/app/octopus

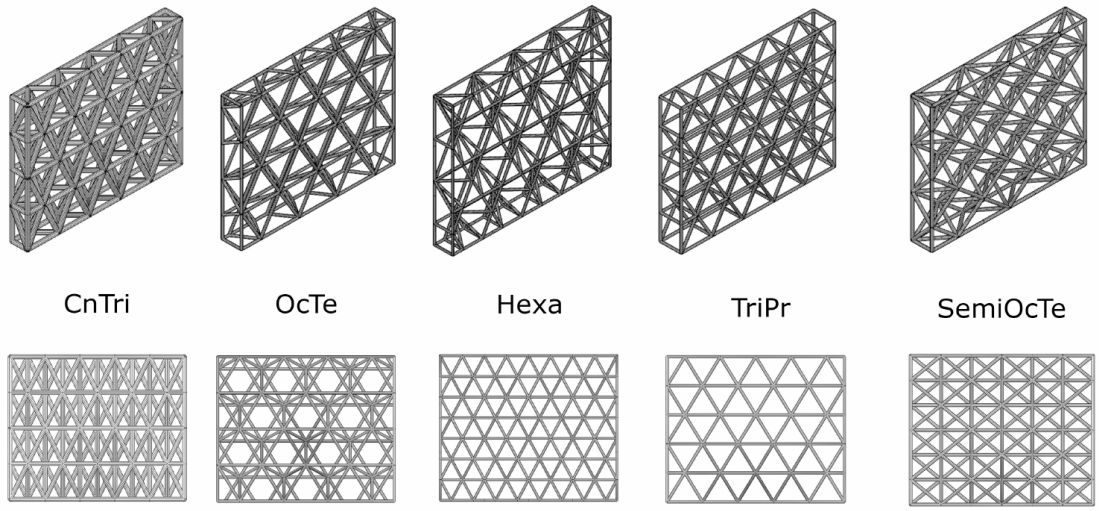

Figure 3.13: Various grid topologies for space truss tesselation

Wall system	Overall thickness (cm)	Weight (kg.m^{-2})	Thermal transmittance (W.m^{-2}.K^{-1})
Breeze blocks	40	180	0.1
Cellular concrete	56	150	0.09
Pre-wall	42	220	0.15
Printed truss	42	50	0.09

Table 3.1: Performance comparison with other systems

From the results, we obtain that the semi-octahedra/tetrahedra (SemiOctTe), octahedra/tetrahedra (OcTe), and counter running triangle (CnTri) exhibit the same performance for the criteria considered, although SemiOctTe might be the smarter choice due to its lower node valence in comparison to OcTe and CnTri, therefore simplifying manufacturing.

The system introduced in this section takes part in the global effort toward automation in construction, to build better and more efficiently, to face current needs in housing and to reduce environmental impact. This generic problem can be addressed at three main levels: a change in building materials themselves, a better geometrical control of build objects, and a transformation of building systems. Our proposition is a renewal of traditional constrained masonry system, by allowing it to handle more efficient geometries such as space trusses. The result is a relatively simple assembly system that allow great performances of produced objects, as shown in Table 3.1.

The presented building system can not only be seen as a renewal of traditional masonry, but also as a generalisation of 3DCP, when this term denotes only the stacking of extruded mortar layers to form an object. In fact, this technique, although studied under the assumption that it is an effort toward "free-form construction" [Pegna, 1997], depending on its explicit materialisation,

allows a certain family of shapes to be built, in a specific way, with a given technological mean. We have proposed elsewhere a classification of generalised robotic extrusion building methods [Duballet et al., 2017], taking into account not only the extrusion itself, but also different types of support and assembly strategies, as well as scale considerations. From that perspective, the present system is a generalised mortar printing approach, mixing assembly of external elements during the process, and making use of printing support left in place. Such considerations help us understand more precisely what those robotic techniques can become for tomorrow's construction.

This summarises my past contributions on the topic of large-scale additive manufacturing. Although somewhat different from the concerns of microstructural representativity, or design, modelling, and processing of architectured materials presented in Chapters 1 and 2, my research was motivated by the same transdisciplinary approach, driven by the same initial question: how can we use geometry to give rise to functionality? With the DEMOCRITE project and subsequent entrepreneurial adventures, we developed a new technology that is actually one, if not the only, means available to reach this end in civil engineering and architectural applications.

Future work Part III

4 General conclusions and proposal for future work

The fault, dear Brutus, is not in our stars,
But in ourselves, that we are underlings.

— *William Shakespeare, Julius Caesar, Act 1, Scene 2 (1599)*

4.1 General conclusions

In the previous three chapters, a selective overview was given concerning the research I have been conducting at PIMM since 2013. We have seen that morphology, as the study of shapes, is ubiquitous in materials science, and mechanics of materials and structures, independently of the scale considered, as shown in the various examples introduced. As morphology depends on material processing, it can actually be used in an inverse manner in order to help us further our understanding of processing, as it was done in Section 1.2. When it comes to architectured materials, they are countless implications of morphology, *e.g.* just to name a few: node connectivity in lattice structures, which will unilaterally determinate the mechanical response (bending or stretch-dominated) of the unit-cell as introduced in Section 2.3; morphology can also have an effect on the kinematics of architectured, *e.g.* due to chirality, and implicate the need for an enriched description of the homogeneous equivalent behaviour of such materials, as stated in Section 2.5. At the architectural scale, the availability of large-scale additive manufacturing for cementitious materials, allowing for new, lighter structural morphologies is fundamentally changing the way structures and buildings are being designed and manufactured, as demonstrated throughout Chapter 3. Here are a few proposals for future work to be conducted at PIMM.

4.2 Mechanical behaviour of architectured materials

Studying the mechanical behaviour of architectured materials already constitutes the core of my research activity, hopefully it will continue to do so. Several questions are considered for investigation, having already been introduced in Chapter 2:

- Modelling architectured materials with nonlinear constitutive behaviour, although studied in [Dirrenberger et al., 2012] this question remains relatively untouched, most of the literature being focused on linear elasticity [Schaedler and Carter, 2016, Muth et al., 2017], and elastic buckling [Shan et al., 2015, Liu et al., 2016, Bertoldi, 2017]. We intend to tackle this problem through computational homogenisation, introducing elastoplasticity and superelasticity components, as in the PhD work of A.-E. Viard;

- Harnessing the potential of hybrids and multiphase architectured materials, by combining synergistically, in a deterministic manner, hybridisation and geometrical effects. Again, this topic of research is relatively new, in the sense that such architectures were not attainable without additive manufacturing [Dalaq et al., 2016, Al-Ketan et al., 2017, Song et al., 2018, Al-Ketan et al., 2018b, Al-Ketan et al., 2018a]. It does seem quite promising from an application viewpoint, from counterbalancing defects from AM [Hedayati et al., 2017], as in F. Albertini's PhD work, to enhanced damping behaviour [Jung and Diebels, 2016, Haghpanah et al., 2017, Weaver et al., 2017] for the aerospace industry, as explored in a current research project with CNES;

- Integrating microstructural information at the scale of architectured materials. As a matter of fact, additive manufacturing is an amazing tool to create architectures, but it also generates intense gradients of temperature during the process, inducing heterogeneous microstructures. One could aim for thermomechanical treatments in order to recover more common microstructures, or consider additive manufacturing as a new playground for metallurgy and polymer science. By controlling the process, one might enable microstructural engineering [Niendorf et al., 2014, Wei et al., 2017], and thus architecturation at multiple scales. Integrating these different scales in a deterministic computational framework is the objective of the SCOLASTIC ANR JCJC project.

4.3 Hierarchical morphologies

When looking at natural materials, one cannot but admire the strategies implemented by natural selection for functionality, *i.e.* survival, in biological systems [Arzt, 2006, Liu et al., 2017b]. Several recurring structural elements have been identified [Fratzl, 2007, Naleway et al., 2015], entangled in various combinations at multiple scale within such materials. Although, we have only just begun to fathom the mechanisms at play within biological structures, additive manufacturing techniques allow to artificially replicate some of these features within engineering materials [Melchels et al., 2012, Kolewe et al., 2013, Fu et al., 2014, Frølich et al., 2017,

Velasco-Hogan et al., 2018]. Being already involved with AM techniques, this is a potentially fruitful research direction I intend on taking, in collaboration with Andrey Molotnikov and Neil Cameron at Monash University, and Cyrille Sollogoub at PIMM, with whom we started working on 3D printing using nanoarchitectured filament produced by coextrusion. Regarding actual biomaterials morphology, and the mechanics of biological systems, we intend on collaborating with John W.C. Dunlop at Salzburg University, *e.g.* on the effect of architecture on the growth of cells [Dunlop et al., 2010, Nerger et al., 2017, Xie et al., 2017]. The concept of bioinspired hierarchical morphologies can be very useful in architectural applications in order to enhance the efficiency of structures [Lakes, 1993, Tsui, 1999, Dollens, 2005, Arciszewski and Kicinger, 2005, Fratzl and Weinkamer, 2007, Roudavski, 2009, Gibson, 2012, Knippers and Speck, 2012, Schleicher et al., 2015, Charpentier et al., 2017].

4.4 Morphological and functional grammars for architectured materials

With architectured materials comes the question of design methodology. As a matter of fact, most attempts at designing architectured materials were empirical, relying on trial-and-error, as well as the very effective and valuable engineer intuition. Some partial solutions were brought to this problem most notably in the form of topology optimisation [Bendsøe and Sigmund, 1995, Bendsøe and Sigmund, 2004], hence replacing the design problem by a computational one. Therefore, a systematic methodology framework is needed in order for these materials to diffuse in industrial applications. From this observation, a rationalised formalism relating morphology to function should be developed following the methodology summarised in [Flemming et al., 1992], similarly to the work of rationalisation that has been pursued in product design [Winsor and MacCallum, 1994, Hsiao and Chen, 1997, Agarwal and Cagan, 1998, Hirtz et al., 2002], functional taxonomies [Stahovich et al., 1993, Kirschman and Fadel, 1998], or in art [Stiny and Gips, 1971, Cenani and Cagdas, 2006] and architecture with shape grammars [Stiny and Mitchell, 1978, March and Stiny, 1985], grammar for discrete structures [Shea and Cagan, 1999], as well as making grammars [Knight and Stiny, 2015], or the pattern language developed by Christopher Alexander for architecture [Alexander, 1977]. Shape grammars are rule-based systems made for describing and generating design. Such an approach seems not having been explored in the field of materials engineering so far. Shape grammars can be used to generate evolution rules for cellular automata [Wolfram, 1984, Wolfram, 2002, Speller et al., 2007], which themselves can be used for design generation and optimisation. Although a rather long-term ambition, results emerging from such research could enable artificial intelligence design for architectured materials, a way that has already been explored in structural design [Fenves and Baker, 1987, Shea and Cagan, 1997]. This proposal for research is the fruit of my own experience and reflection, influenced by multiple conversations with engineers, architects, designers, philosophers... setting my future research in line with the global trend of technological, computational, convergence between design, engineering, science, art, and humanities [Eames and Eames, 1973, Negroponte, 1995, Oxman and Oxman, 2010, Ingold, 2013].

References (489)

[Achrai et al., 2015] Achrai B, Bar-On B, and Wagner HD (2015). *Biological armors under impact—effect of keratin coating, and synthetic bio-inspired analogues*. Bioinspiration & biomimetics, vol. 10 n° 1, pp 016009. 62

[Agarwal and Cagan, 1998] Agarwal M. and Cagan J. (1998). *A blend of different tastes: the language of coffeemakers*. Environment and Planning B: Planning and Design, vol. 25 n° 2, pp 205–226. 107

[Aizenberg et al., 2005] Aizenberg Joanna, Weaver James C, Thanawala Monica S, Sundar Vikram C, Morse Daniel E, and Fratzl Peter (2005). *Skeleton of Euplectella sp.: structural hierarchy from the nanoscale to the macroscale*. Science, vol. 309 n° 5732, pp 275–278. 62

[Ajdari et al., 2012] Ajdari A., Jahromi B. H., Papadopoulos J., Nayeb-Hashemi H., and Vaziri A. (2012). *Hierarchical honeycombs with tailorable properties*. International Journal of Solids and Structures, vol. 49 n° 11-12, pp 1413–1419. 47

[Al-Ketan et al., 2018a] Al-Ketan O., Al-Rub R. K. A., and Rowshan R. (2018a). *The effect of architecture on the mechanical properties of cellular structures based on the IWP minimal surface*. Journal of Materials Research, vol. 33 n° 3, pp 343–359. 106

[Al-Ketan et al., 2017] Al-Ketan O., Assad M. A., and Al-Rub R. K. A. (2017). *Mechanical properties of periodic interpenetrating phase composites with novel architected microstructures*. Composite Structures, vol. 176, pp 9–19. 106

[Al-Ketan et al., 2018b] Al-Ketan O., Soliman A., AlQubaisi A. M., and Al-Rub R. K. A. (2018b). *Nature-Inspired Lightweight Cellular Co-Continuous Composites with Architected Periodic Gyroidal Structures*. Advanced Engineering Materials, vol. 20 n° 2, pp 1700549. 106

[Alderson et al., 2010] Alderson A., Alderson K. L., Attard D., Evans K. E., Gatt R., Grima J. N., Miller W., Ravirala N., Smith C. W., and Zied K. (2010). *Elastic constants of 3-, 4- and 6-connected chiral and anti-chiral honeycombs subject to uniaxial in-plane loading*. Composites Science and Technology, vol. 70 n° 7, pp 1042–1048. 71

[Alexander, 1977] Alexander C. (1977). *A pattern language: towns, buildings, construction*. Oxford University Press. 107

[Allaire, 2002] Allaire G. (2002). *Shape Optimization by the Homogenization Method*. Springer. 44, 45, 84

[Allwood et al., 2011] Allwood J. M., Ashby M. F., Gutowski T. G., and Worrell E. (2011). *Material efficiency: A white paper*. Resources, Conservation and Recycling, vol. 55 n° 3, pp 362–381. 86

[Altendorf et al., 2012] Altendorf H., Decencière E., Jeulin D., De Sa Peixoto P., Deniset-Besseau A., Angelini E., Mosser G., and Schanne-Klein M.-C. (2012). *Imaging and 3D morphological analysis of collagen fibrils*. Journal of Microscopy, vol. 247 n° 2, pp 161–175. 16

[Altendorf et al., 2014] Altendorf H., Jeulin D., and Willot F. (2014). *Influence of the fiber geometry on the macroscopic elastic and thermal properties*. International Journal of Solids and Structures, vol. 51 n° 23-24, pp 3807–3822. 15, 23

[Andreassen et al., 2014] Andreassen E., Lazarov B.S., and Sigmund O. (2014). *Design of manufacturable 3D extremal elastic microstructure*. Mechanics of Materials, vol. 69 n° 1, pp 1–10. 46

[Andreaus et al., 2016] Andreaus U., dell'Isola F., Giorgio I., Placidi L., Lekszycki T., and Rizzi N. L. (2016). *Numerical simulations of classical problems in two-dimensional (non) linear second gradient elasticity*. International Journal of Engineering Science, vol. 108, pp 34–50. 45

[Arciszewski and Kicinger, 2005] Arciszewski T. and Kicinger R. (2005). *Innovation in Civil and Structural Engineering Computing*, chapter Structural Design Inspired by Nature, pp 25–48. Saxe-Coburg Publications, Stirling, UK. 107

[Arruda and Boyce, 1993] Arruda E. M. and Boyce M. C. (1993). *A three-dimensional constitutive model for the large stretch behavior of rubber elastic materials*. Journal of the Mechanics and Physics of Solids, vol. 41 n° 2, pp 389–412. 64

[Arzt, 2006] Arzt E. (2006). *Biological and artificial attachment devices: Lessons for materials scientists from flies and geckos*. Materials Science and Engineering: C, vol. 26 n° 8, pp 1245–1250. 106

[Asadpoure et al., 2017] Asadpoure A., Tootkaboni M., and Valdevit L. (2017). *Topology optimization of multiphase architected materials for energy dissipation*. Computer Methods in Applied Mechanics and Engineering, vol. 325, pp 314–329. 45

[Ashby, 2006] Ashby M. F. (2006). *The properties of foams and lattices*. Philosophical Transactions of the Royal Society A: Mathematical, Physical and Engineering Sciences, vol. 364 n° 1838, pp 15–30. 58, 59, 60, 61

[Ashby and Bréchet, 2003] Ashby M. F. and Bréchet Y. (2003). *Designing hybrid materials*. Acta Materialia, vol. 51, pp 5801–5821. 5, 43, 45, 62

[Auffray et al., 2015] Auffray N., Dirrenberger J., and Rosi G. (2015). *A complete description of bi-dimensional anisotropic strain-gradient elasticity*. International Journal of Solids and Structures, vol. 69-70, pp 195–210. 45, 69

[Auffray et al., 2018] Auffray N., He Q. C., and Le Quang H. (2018). *Complete symmetry classification and compact matrix representations for 3D strain gradient elasticity*. International Journal of Solids and Structures. in press. 69

[Autumn and Gravish, 2008] Autumn Kellar and Gravish Nick (2008). *Gecko adhesion: evolutionary nanotechnology*. Philosophical Transactions of the Royal Society of London A: Mathematical, Physical and Engineering Sciences, vol. 366 n° 1870, pp 1575–1590. 62

[Autumn et al., 2000] Autumn Kellar, Liang Yiching A, Hsieh S Tonia, Zesch Wolfgang, et al. (2000). *Adhesive force of a single gecko foot-hair*. Nature, vol. 405 n° 6787, pp 681. 62

[Bacigalupo and De Bellis, 2015] Bacigalupo A. and De Bellis M. L. (2015). *Auxetic anti-tetrachiral materials: equivalent elastic properties and frequency band-gaps*. Composite Structures, vol. 131, pp 530–544. 71

[Bacigalupo and Gambarotta, 2014] Bacigalupo A. and Gambarotta L. (2014). *Homogenization of periodic hexa- and tetrachiral cellular solids*. Composite Structures, vol. 116, pp 461–476. 71

[Bacigalupo and Gambarotta, 2017] Bacigalupo A. and Gambarotta L. (2017). *Wave propagation in non-centrosymmetric beam-lattices with lumped masses: Discrete and micropolar modeling*. International Journal of Solids and Structures, vol. 118, pp 128–145. 69

[Bacigalupo et al., 2016] Bacigalupo A., Lepidi M., Gnecco G., and Gambarotta L. (2016). *Optimal design of auxetic hexachiral metamaterials with local resonators*. Smart Materials and Structures, vol. 25 n° 5, pp 054009. 71

[Bafekrpour et al., 2015] Bafekrpour E., Dyskin A., Pasternak E., Molotnikov A., and Estrin Y. (2015). *Internally architectured materials with directionally asymmetric friction*. Scientific Reports, vol. 5, pp 10732. 43

[Bafekrpour et al., 2014] Bafekrpour E., Molotnikov A., Weaver J. C., Brechet Y., and Estrin Y. (2014). *Responsive materials: A novel design for enhanced machine-augmented composites*. Scientific Reports, vol. 4, pp 3783. 43

[Ballarin et al., 2009a] Ballarin V., Perlade A., Lemoine X., Bouaziz O., and Forest S. (2009a). *Mechanisms and modeling of bake-hardening steels: Part II. Complex loading paths*. Metallurgical and Materials Transactions A: Physical Metallurgy and Materials Science, vol. 40 n° 6, pp 1375–1382. 66

[Ballarin et al., 2009b] Ballarin V., Soler M., Perlade A., Lemoine X., and Forest S. (2009b). *Mechanisms and modeling of bake-hardening steels: Part I. Uniaxial tension*. Metallurgical and Materials Transactions A: Physical Metallurgy and Materials Science, vol. 40 n° 6, pp 1367–1374. 66

[Baltazar Hernandez et al., 2011] Baltazar Hernandez V., Nayak S., and Zhou Y. (2011). *Tempering of Martensite in Dual-Phase Steels and Its Effects on Softening Behavior*. Metallurgical and Materials Transactions A: Physical Metallurgy and Materials Science, vol. 42, pp 3115–3129. 79

[Barbe et al., 2001] Barbe F., Decker L., Jeulin D., and Cailletaud G. (2001). *Intergranular and intragranular behavior of polycrystalline aggregates. Part I: F.E. model*. International Journal of Plasticity, vol. 17, pp 513–536. 29, 30, 31

[Bargmann et al., 2018] Bargmann S., Klusemann B., Markmann J., Schnabel J. E., Schneider K., Soyarslan C., and Wilmers J. (2018). *Generation of 3D representative volume elements for heterogeneous materials: a review*. Progress in Materials Science, vol. 96, pp 322–384. 9

[Barthlott and Neinhuis, 1997] Barthlott W. and Neinhuis C. (1997). *Purity of the sacred lotus, or escape from contamination in biological surfaces*. Planta, vol. 202 n° 1, pp 1–8. 62

[Bathias and Paris, 2004] Bathias C. and Paris P.C. (2004). *Gigacycle fatigue in mechanical practice*. CRC Press. 41

[Baumers et al., 2016] Baumers M., Dickens P., Tuck C., and Hague R. (2016). *The cost of additive manufacturing: machine productivity, economies of scale and technology-push*. Technological Forecasting & Social Change, vol. 102, pp 193–201. 86

[Bechle and Kyriakides, 2014] Bechle N. J. and Kyriakides S. (2014). *Localization in NiTI tubes under bending*. International Journal of Solids and StructureS, vol. 51 n° 5, pp 967–980. 65

[Bechle and Kyriakides, 2016] Bechle N. J. and Kyriakides S. (2016). *Evolution of localization in pseudoelastic NiTi tubes under biaxial stress states*. International Journal of Plasticity, vol. 82, pp 1–31. 65

[Belotteau et al., 2009] Belotteau J., Berdin C., Forest S., Parrot A., and Prioul C. (2009). *Mechanical behavior and crack tip plasticity of a strain aging sensitive steel*. Materials Science & Engineering, A: Structural Materials: Properties, Microstructure and Processing, vol. 526 n° 1-2, pp 156–165. 66

[Bendsøe and Kikuchi, 1988] Bendsøe M.P. and Kikuchi N. (1988). *Generating optimal topologies in structural design using a homogenization method*. Computer Methods in Applied Mechanics and Engineering, vol. 71 n° 2, pp 197–224. 83

[Bendsøe and Sigmund, 2004] Bendsøe M.P. and Sigmund O. (2004). *Topology Optimization*. Springer. 44, 45, 83, 84, 107

[Bendsøe and Sigmund, 1995] Bendsøe M. P. and Sigmund O. (1995). *Optimization of structural topology, shape, and material*. Springer, Berlin. 107

[Benedetti and Barbe, 2013] Benedetti I. and Barbe F. (2013). *Modelling polycrystalline materials: an overview of three-dimensional grain-scale mechanical models*. Journal of Multiscale Modelling, vol. 5 n° 1, pp 1350002. 9

[Beran, 1968] Beran M. J. (1968). *Statistical Continuum Theories*. Wiley. 10

[Berdin et al., 2013] Berdin C., Yao Z. Y., and Pascal S. (2013). *Internal stresses in polycrystalline zirconia: Microstructure effects*. Computational Materials Science, vol. 70, pp 140–144. 9

[Bertoldi, 2017] Bertoldi K. (2017). *Harnessing instabilities to design tunable architected cellular materials*. Annual Review of Materials Research, vol. 47, pp 51–61. 106

[Bertoldi et al., 2010] Bertoldi K., Reis P.M., Willshaw S., and Mullin T. (2010). *Negative Poisson's Ratio Behavior Induced by an Elastic Instability*. Advanced Materials, vol. 22 n° 3, pp 361–366. 47

[Besson et al., 2010] Besson J., Cailletaud G., Chaboche J.-L., Forest S., and Blétry M. (2010). *Non-Linear Mechanics of Materials*, vol. 167 of *Solid Mechanics and Its Applications*. Springer. 9, 55, 66, 71

[Bier, 2018] ed. Bier H. (2018). *Robotic Building*, vol. 1 of *Springer Series in Adaptive Environments*. Springer Nature. 84

[Bironeau, 2016] Bironeau A. (2016). *Films multinanocouches de polymères amorphes coextrudés : élaboration, caractérisation et stabilité des nanocouches*. Thèse de Doctorat, Ecole nationale supérieure d'arts et métiers-ENSAM. 16

[Bironeau et al., 2016] Bironeau A., Dirrenberger J., Sollogoub C., Miquelard-Garnier G., and Roland S. (2016). *Evaluation of morphological representative sample sizes for nanolayered polymer blends*. Journal of Microscopy, vol. 264 n° 1, pp 48–58. 15, 16

[Bironeau et al., 2017] Bironeau A., Salez T., Miquelard-Garnier G., and Sollogoub C. (2017). *Existence of a critical layer thickness in PS/PMMA nanolayered films*. Macromolecules, vol. 50 n° 10, pp 4064–4073. 16

[Blanche et al., 2015] Blanche A., Chrysochoos A., Ranc N., and Favier V. (2015). *Dissipation assessments during dynamic very high cycle fatigue tests*. Experimental Mechanics, vol. 55, pp 699–709. 41

[Bornert et al., 2001] Bornert M., Bretheau T., and Gilormini P. (2001). *Homogénéisation en mécanique des matériaux, Tome 1 : Matériaux aléatoires élastiques et milieux périodiques*. Hermès. 9, 71

[Bouaziz, 2013] Bouaziz O. (2013). *Geometrically induced strain hardening*. Scripta Materialia, vol. 68 n° 1, pp 28–30. 77

[Bouaziz et al., 2009] Bouaziz O., Allain S., Barcelo D., and Niang R. (2009). *Strengthening by plastic corrugated reinforcements: an efficient way for strain-hardening improvement by architecture*. In : MRS Proceedings, 1188, n° 1188-LL05-01. 77

[Bouaziz et al., 2008] Bouaziz O., Bréchet Y., and Embury J. D. (2008). *Heterogeneous and Architectured Materials: A Possible Strategy for Design of Structural Materials*. Advanced Engineering Materials, vol. 10 n° 1-2, pp 24–36. 43, 45, 46, 47

[Bouaziz et al., 2013] Bouaziz O., Masse J. P., Allain S., Orgéas L., and Latil P. (2013). *Compression of crumpled aluminum thin foils and comparison with other cellular materials*. Materials Science & Engineering, A: Structural Materials: Properties, Microstructure and Processing, vol. 570, pp 1–7. 44, 47

[Boufarguine et al., 2013] Boufarguine M., Guinault A., Miquelard-Garnier G., and Sollogoub C. (2013). *PLA/PHBV films with improved mechanical and gas barrier properties*. Macromolecular Materials and Engineering, vol. 298 n° 10, pp 1065–1073. 16

[Boulanger et al., 2004] Boulanger T., Chrysochoos A., Mabru C., and Galtier A. (2004). *Calorimetric analysis of dissipative and thermoelastic effects associated with the fatigue behavior of steels*. International Journal of Fatigue, vol. 26, pp 221–229. 41

[Boyce and Arruda, 2000] Boyce M. C. and Arruda E. M. (2000). *Constitutive models of rubber elasticity: a review*. Rubber Chemistry and Technology, vol. 73 n° 3, pp 504–523. 64

[Braibant and Fleury, 1984] Braibant V. and Fleury C. (1984). *Shape optimal design using B-splines*. Computer Methods in Applied Mechanics and Engineering, vol. 44 n° 3, pp 247–267. 71

[Brecher and Emonts, 2010] Brecher C. and Emonts M. (2010). *Laser-assisted shearing: new process developments for the sheet metal industry*. International Journal of Advanced Manufacturing Technology, vol. 48, pp 133–141. 79

[Bréchet and Embury, 2013] Bréchet Y. and Embury J. D. (2013). *Architectured materials: Expanding materials space*. Scripta Materialia, vol. 68 n° 1, pp 1–3. 43, 45

[Bréchet, 2013] Bréchet Y. J. M. (2013). *Materials Design Inspired by Nature- Function Through Inner Architecture*, chapter Architectured Materials: An Alternative to Microstructure Control for Structural Materials Design? A Possible Playground for Bio-inspiration?, pp 1–16. RSC Publishing. 90

[Brothers and Dunand, 2006] Brothers A. H. and Dunand D. C. (2006). *Density-Graded Cellular Aluminum*. Advanced Engineering Materials, vol. 8 n° 9, pp 805–809. 47

[Buswell et al., 2007] Buswell R.A., Soar R.C., Gibb A.G.F., and Thorpe A. (2007). *Freeform Construction: Mega-scale Rapid Manufacturing for construction*. Automation in Construction, vol. 16, pp 224–231. 87

[Buswell et al., 2018] Buswell R. A., Leal de Silva W., Jones S. Z., and Dirrenberger J. (2018). *3D printing using concrete extrusion: A roadmap for research*. Cement and Concrete Research, vol. 112, pp 37–49. 90

[Cai et al., 2014] Cai S.-Y., Zhang W. H., Zhu J. H., and Gao T. (2014). *Stress constrained shape and topology optimization with fixed mesh: A B-spline finite cell method combined with level set function*. Computer Methods in Applied Mechanics and Engineering, vol. 278, pp 361–387. 71

[Cailletaud, 1992] Cailletaud G. (1992). *A micromechanical approach to inelastic behaviour of metals*. International Journal of Plasticity, vol. 8, pp 55–73. 31

[Cailletaud et al., 2003] Cailletaud G., Forest S., Jeulin D., Feyel F., Galliet I., Mounoury V., and Quilici S. (2003). *Some elements of microstructural mechanics*. Computational Materials Science, vol. 27, pp 351–374. 9, 30, 32, 55

[Cailletaud et al., 1994] Cailletaud G., Jeulin D., and Rolland P. (1994). *Size effect on elastic properties of random composites*. Engineering Computations, vol. 11 n° 2, pp 99–110. 12, 14, 41

[Calladine, 1978] Calladine C. R. (1978). *Buckminster Fuller's "tensegrity" structures and Clerk Maxwell's rules for the construction of stiff frames*. International Journal of Solids and Structures, vol. 14 n° 2, pp 161–172. 59

[Canyurt and Hajela, 2010] Canyurt O. E. and Hajela P. (2010). *Cellular genetic algorithm technique for the multicriterion design optimization*. Structural and Multidisciplinary Optimization, vol. 40, pp 201–214. 84

[Capello and Previtali, 2009] Capello E. and Previtali B. (2009). *Enhancing dual phase steel formability by diode laser heat treatment*. Journal of Laser Applications, vol. 21 n° 1, pp 1–9. 79, 80

[Carpo, 2011] Carpo M. (2011). *The alphabet and the algorithm*. MIT Press, Cambridge, MA. 84

[Carpo, 2013] ed. Carpo M. (2013). *The digital turn in architecture 1992-2012*. John Wiley & Sons. 84

[Carpo, 2017] Carpo M. (2017). *The Second Digital Turn: Design Beyond Intelligence*. MIT Press, Cambridge, MA. 84

[Carreker and Hibbard, 1953] Carreker R.P. and Hibbard W. R. Jr. (1953). *Tensile deformation of high-purity copper as a function of temperature, strain rate and grain size*. Acta Metallurgica, vol. 1, pp 656–663. 35

[Caty et al., 2008] Caty O., Maire E., and Bouchet R. (2008). *Fatigue of metal hollow spheres structures*. Advanced Engineering Materials, vol. 10 n° 3, pp 179–184. 43, 46

[Cenani and Cagdas, 2006] Cenani S. and Cagdas G. (2006). *Shape grammar of geometric islamic ornaments*. In : Proceedings of the 24th eCAADe. 107

[Cesaretti et al., 2014] Cesaretti G., Dini E., Kestelier X. De, Colla V., and Pambaguian L. (2014). *Building components for an outpost on the Lunar soil by means of a novel 3D printing technology*. Acta Astronautica, vol. 93, pp 430–450. 87

[Challis et al., 2008] Challis V. J., Roberts A. P., and Wilkins A. H. (2008). *Design of three dimensional isotropic microstructures for maximized stiffness and conductivity*. International Journal of Solids and Structures, vol. 45, pp 4130–4146. 45

[Charpentier et al., 2017] Charpentier V., Hannequart P., Adriaenssens S., Baverel O., Viglino E., and Eisenman S. (2017). *Kinematic amplification strategies in plants and engineering*. Smart Materials and Structures, vol. 26 n° 6, pp 063002. 107

[Chauvet et al., 2018] Chauvet E., Kontis P., Jägle E. A., Gault B., Raabe D., Tassin C., Blandin J.-J., Dendievel R., Vayre B., Abed S., and Martin G. (2018). *Hot cracking mechanism affecting a non-weldable Ni-based superalloy produced by selective electron Beam Melting*. Acta Materialia, vol. 142, pp 82–94. 61

[Chéhab et al., 2009] Chéhab B., Zurob H., Embury D., Bouaziz O., and Bréchet Y. (2009). *Compositionally Graded Steels: A Strategy for Materials Development*. Advanced Engineering Materials, vol. 11 n° 12, pp 992–999. 47

[Chen et al., 2015] Chen I. H., Yang W., and Meyers M.-A. (2015). *Leatherback sea turtle shell: A tough and flexible biological design*. Acta Biomaterialia, vol. 28, pp 2–12. 62

[Chen et al., 2012] Chen P. Y., McKittrick J., and Meyers M. A. (2012). *Biological materials: functional adaptations and bioinspired designs*. Progress in Materials Science, vol. 57 n° 8, pp 1492–1704. 61

[Chen et al., 2014] Chen Y., Liu X. N., Hu G. K., Sun Q. P., and Zheng Q. S. (2014). *Micropolar continuum modelling of bi-dimensional tetrachiral lattices*. Proceedings of the Royal Society A: Mathematical, Physical and Engineering Sciences, vol. 470 n° 2165, pp 20130734. 45

[Cho and Ha, 2009] Cho S. and Ha S.-H. (2009). *Isogeometric shape design optimization: Exact geometry and enhanced sensitivity*. Structural and Multidisciplinary Optimization, vol. 38 n° 1, pp 53–70. 70

[Choi and Pak, 2006] Choi B. C. and Pak A. W. (2006). *Multidisciplinarity, interdisciplinarity and transdisciplinarity in health research, services, education and policy: 1. Definitions, objectives, and evidence of effectiveness*. Clinical and Investigative Medicine, vol. 29 n° 6, pp 351. 90

[Chrysochoos et al., 2008] Chrysochoos A., Berthel B., Latourte F., Pagano S., Wattrisse B., and Weber B. (2008). *Local energy approach to steel fatigue*. Strain, vol. 44, pp 327–334. 41

[Chrysochoos et al., 1989] Chrysochoos A., Maisonneuve O., Martin G., Caumon H., and Chezeaux J.-C. (1989). *Plastic and dissipated work and stored energy*. Nuclear Engineering and Design, vol. 114, pp 323–333. 35

[Chrysochoos and Martin, 1989] Chrysochoos A. and Martin G. (1989). *Tensile test microcalorimetry for thermomechanical behaviour law analysis*. Materials Science and Engineering, vol. A108, pp 25–32. 36

[Chrysochoos et al., 2009] Chrysochoos A., Wattrisse B., Muracciole J.-M., and Kaim Y.E. (2009). *Fields of stored energy associated with localized necking to steel*. Journal of Mechanics of Materials and Structures, vol. 4, pp 245–262. 36

[Chryssolouris et al., 1997] Chryssolouris G., Anifantis N., and Karagiannis S. (1997). *Laser Assisted Machining: An Overview*. Journal of Manufacturing Science and Engineering, vol. 119, pp 766–769. 79

[Chu et al., 1996] Chu D. N., Xie Y. M., Hira A., and Steven G. P. (1996). *Evolutionary structural optimization for problems with stiffness constraints*. Finite Elements in Analysis and Design, vol. 21 n° 4, pp 239–251. 84

[Cicoria et al., 2013] Cicoria R., Chehab B., and Zurob H. (2013). *Diffusion as a method for producing architectured materials*. Scripta Materialia, vol. 68 n° 1, pp 17–21. 47

[Clausen et al., 2015] Clausen A., Wang F., Jensen J. S., Sigmund O., and Lewis J. A. (2015). *Topology Optimized Architectures with Programmable Poisson's Ratio over Large Deformations*. Advanced Materials, vol. 27 n° 37, pp 5523–5527. 71

[Connesson et al., 2011] Connesson N., Maquin F., and Pierron F. (2011). *Experimental energy balance during the first cycles of cyclically loaded specimens under the conventional yield stress*. Experimental Mechanics, vol. 51, pp 23–44. 41

[Corona et al., 2002] Corona E., Shaw J. A., and Iadicola M. A. (2002). *Buckling of steel bars with Lüders bands*. International Journal of Solids and Structures, vol. 39 n° 13-14, pp 3313–3336. 66

[Cosserat and Cosserat, 1909] Cosserat E. and Cosserat F. (1909). *Théorie des corps déformables*. Hermann. 68

[Côté et al., 2006] Côté F., Deshpande V. S., Fleck N. A., and Evans A. G. (2006). *The compressive and shear responses of corrugated and diamond lattice materials*. International Journal of Solids and Structures, vol. 43 n° 20, pp 6220–6242. 58

[Cottrell and Bilby, 1949] Cottrell A. H. and Bilby B. A. (1949). *Dislocation theory of yielding and strain ageing of iron*. Proceedings of the Physical Society. Section A, vol. 62 n° 1, pp 49. 66

[Courtois et al., 2012] Courtois L., Maire E., Perez M., Rodney D., Bouaziz O., and Bréchet Y. (2012). *Mechanical properties of monofilament entangled materials*. Advanced Engineering Materials, vol. 14 n° 12, pp 1128–1133. 43, 46

[Cruzado et al., 2017] Cruzado A., Llorca J., and Segurado J. (2017). *Modeling cyclic deformation of inconel 718 superalloy by means of crystal plasticity and computational homogenization*. International Journal of Solids and Structures, vol. 122–123, pp 148–161. 29, 30, 32

[Cruzado et al., 2018] Cruzado A., Lucarini S., Llorca J., and Segurado J. (2018). *Microstructure-based fatigue life model of metallic alloys with bilinear Coffin-Manson behavior*. International Journal of Fatigue, vol. 107, pp 40–48. 29, 30

[Cui et al., 2003] Cui C., Ohmori H., and Sasaki M. (2003). *Computational morphogenesis of 3D structures by extended ESO method*. Journal of the International Association for Shell and Spatial Structures, vol. 44 n° 1, pp 51–61. 83

[Dadbakhsh et al., 2016] Dadbakhsh S., Speirs M., Van Humbeeck J., and Kruth J. P. (2016). *Laser additive manufacturing of bulk and porous shape-memory NiTi alloys: From processes to potential biomedical applications*. MRS Bulletin, vol. 41 n° 10, pp 765–774. 66

[Dalaq et al., 2016] Dalaq A. S., Abueidda D. W., Al-Rub R. K. Abu, and Jasiuk I. M. (2016). *Finite element prediction of effective elastic properties of interpenetrating phase composites with architectured 3D sheet reinforcements*. International Journal of Solids and Structures, vol. 83, pp 169–182. 46, 106

[De Bellis and Bacigalupo, 2017] De Bellis M. L. and Bacigalupo A. (2017). *Auxetic behavior and acoustic properties of microstructured piezoelectric strain sensors*. Smart Materials and Structures, vol. 26 n° 8, pp 085037. 69

[Decker et al., 1998] Decker L., Jeulin D., and Tovena I. (1998). *3D morphological analysis of the connectivity of a porous medium*. Acta Stereologica, vol. 17 n° 1, pp 107–112. 9

[dell'Isola et al., 2017] dell'Isola F., Della Corte A., and Giorgio I. (2017). *Higher-gradient continua: The legacy of Piola, Mindlin, Sedov and Toupin and some future research perspectives*. Mathematics and Mechanics of Solids, vol. 22 n° 4, pp 852–872. 45

[Deshpande et al., 2001a] Deshpande V. S., Ashby M. F., and Fleck N. A. (2001a). *Foam topology: bending versus stretching dominated architectures*. Acta Materialia, vol. 49 n° 6, pp 1035–1040. 58, 59

[Deshpande et al., 2001b] Deshpande V. S., Fleck N. A., and Ashby M. F. (2001b). *Effective properties of the octet-truss lattice material*. Journal of the Mechanics and Physics of Solids, vol. 49 n° 8, pp 1747–1769. 47, 58, 59

[di Paola, 2010] di Paola F. (2010). *Modélisation multi-échelles du comportement thermo-élastique de composites à particules sphériques*. Thèse de Doctorat, Ecole Centrale Paris. 14

[Diard et al., 2005] Diard O., Leclercq S., Rousselier G., and Cailletaud G. (2005). *Evaluation of finite element based analysis of 3D multicrystalline material plasticity: Application to crystal plasticity model identification and the study of stress and strain fields near grain boundaries*. International Journal of Plasticity, vol. 21, pp 691–722. 31

[Dirrenberger, 2012] Dirrenberger J. (2012). *Effective properties of architectured materials*. Thèse de Doctorat, MINES-ParisTech, Paris. 44, 70, 72, 84

[Dirrenberger, 2018] Dirrenberger J. (2018). *Robotic Building*, vol. 1 of *Springer Series in Adaptive Environments*, chapter From Architectured Materials to Large-Scale Additive Manufacturing, pp 79–96. Springer Nature. 89

[Dirrenberger et al., 2012] Dirrenberger J., Forest S., and Jeulin D. (2012). *Elastoplasticity of auxetic materials*. Computational Materials Science, vol. 64, pp 57–61. 46, 58, 70, 71, 106

[Dirrenberger et al., 2013] Dirrenberger J., Forest S., and Jeulin D. (2013). *Effective elastic properties of auxetic microstructures: anisotropy and structural applications*. International Journal of Mechanics and Materials in Design, vol. 9 n° 1, pp 21–33. 46, 56, 70, 71

[Dirrenberger et al., 2014] Dirrenberger J., Forest S., and Jeulin D. (2014). *Towards gigantic RVE sizes for stochastic fibrous networks*. International Journal of Solids and Structures, vol. 51 n° 2, pp 359–376. 15, 16, 30, 41, 43, 46, 58

[Dirrenberger et al., 2011] Dirrenberger J., Forest S., Jeulin D., and Colin C. (2011). *Homogenization of periodic auxetic materials*. Procedia Engineering, vol. 10, pp 1847–1852. 11th International Conference on the Mechanical Behavior of Materials (ICM11). 46, 62, 70, 71

[Djumas et al., 2016] Djumas L., Molotnikov A., Simon G. P., and Estrin Y. (2016). *Enhanced mechanical performance of bio-inspired hybrid structures utilising topological interlocking geometry*. Scientific Reports, vol. 6, pp 26706. 43, 62

[Djumas et al., 2017] Djumas L., Simon G. P., Estrin Y., and Molotnikov A. (2017). *Deformation mechanics of non-planar topologically interlocked assemblies with structural hierarchy and varying geometry*. Scientific Reports, vol. 7 n° 1, pp 11844. 43

[Dollens, 2005] Dollens D. (2005). *A System of Digital-Botanic Architecture*. Leonardo, vol. 38 n° 1, pp 15–21. 107

[Doškàř et al., 2018] Doškàř M., Zeman J., Jarušková D., and Novàk J. (2018). *Wang tiling aided statistical determination of the Representative Volume Element size of random heterogeneous materials*. European Journal of Mechanics A/Solids, vol. 70, pp 280–295. 15

[Doudard et al., 2010] Doudard C., Calloch S., Hild F., and Roux S. (2010). *Identification of heat source fields from infrared thermography: determination of 'self-heating' in a dual-phase steel by using a dog bone sample*. Mechanics of Materials, vol. 42, pp 55–62. 41

[Drugan and Willis, 1996] Drugan W. J. and Willis J. R. (1996). *A Micromechanics-Based Nonlocal Constitutive Equation and Estimates of Representative Volume Element Size for Elastic Composites*. Journal of the Mechanics and Physics of Solids, vol. 44 n° 4, pp 497–524. 10

[Duballet et al., 2017] Duballet R., Baverel O., and Dirrenberger J. (2017). *Classification of building systems for concrete 3D printing*. Automation in Construction, vol. 83, pp 247–258. 88, 99, 102

[Duballet et al., 2018a] Duballet R., Baverel O., and Dirrenberger J. (2018a). *Humanizing Digital Reality*, chapter Design of Space Truss Based Insulating Walls for Robotic Fabrication in Concrete, pp 453–461. Springer. 94, 99

[Duballet et al., 2018b] Duballet R., Baverel O., and Dirrenberger J. (2018b). *Space truss masonry walls with robotic mortar extrusion*. In : Proceedings of the IASS Symposium 2018, Creativity in Structural Design, July 16-20, 2018, MIT, Boston, USA, eds. Mueller C. and Adriaenssens S. International Association for Shell and Spatial Structures. 99

[Duballet et al., 2016] Duballet R., Gosselin C., and Roux P. (2016). *Additive Manufacturing and Multi-Objective Optimization of Graded Polystyrene Aggregate Concrete Structures*. In : Modelling Behaviour- Design Modelling Symposium 2015, eds. Thomsen M.R., Tamke M., Gengnagel C., Faircloth B., and Scheurer F. Springer. 87

[Dunlop and Fratzl, 2010] Dunlop J.W.C. and Fratzl P. (2010). *Biological composites*. Annual Review of Materials Research, vol. 40, pp 1–24. 47, 61

[Dunlop et al., 2011] Dunlop J.W.C., Weinkamer R., and Fratzl P. (2011). *Artful interfaces within biological materials*. MaterialsToday, vol. 14 n° 3, pp 70–78. 47, 61, 62

[Dunlop et al., 2010] Dunlop J. W. C., Fischer F. D., Gamsjäger E., and Fratzl P. (2010). *A theoretical model for tissue growth in confined geometries*. Journal of the Mechanics and Physics of Solids, vol. 58, pp 1073–1087. 47, 107

[Duysinx and Bendsøe, 1998] Duysinx P. and Bendsøe M. P. (1998). *Topology optimization of continuum structures with local stress constraints*. International Journal for Numerical Methods in Engineering, vol. 43 n° 8, pp 1453–1478. 83

[D'yachenko et al., 1984] D'yachenko V. S., Tverdokhlebov G. N., and Korosteleva A. A. (1984). *Features of laser heat treatment of high-speed steel tools*. Metal Science and Heat Treatment, vol. 26 n° 9, pp 675–679. 79

[Dyskin et al., 2001] Dyskin A. V., Estrin Y., Kanel-Belov A. J., and Pasternak E. (2001). *Toughening by Fragmentation - How Topology Helps*. Advanced Engineering Materials, vol. 3, pp 885–888. 43

[Eames and Eames, 1973] Eames C. and Eames R. (1973). *A computer perspective*. Harvard University Press, Cambridge, MA. 107

[Elahinia et al., 2016] Elahinia M., Moghaddam N. S., Andani M. T., Amerinatanzi A., Bimber B. A., and Hamilton R. F. (2016). *Fabrication of NiTi through additive manufacturing: A review*. Progress in Materials Science, vol. 83, pp 630–663. 66

[Elbaum and Abraham, 2014] Elbaum R. and Abraham Y. (2014). *Insights into the microstructures of hygroscopic movement in plant seed dispersal*. Plant Science, vol. 223, pp 124–133. 62

[Embury and Bouaziz, 2010] Embury D. and Bouaziz O. (2010). *Steel-Based Composites: Driving Forces and Classifications*. Annual Review of Materials Research, vol. 40, pp 213–241. 44, 47

[Erigen, 1967] Erigen A. C. (1967). *Mathematical Fundamentals of Fracture*, vol. 2 of *Fracture: an advanced treatise*, chapter Theory of micropolar elasticity, pp 621–629. Academic Press, New York. 68

[Erk et al., 2008] Erk K. A., Dunand D. C., and Shull K. R. (2008). *Titanium with controllable pore fractions by thermoreversible gelcasting of TiH2*. Acta Materialia, vol. 56 n° 18, pp 5147–5157. 47

[Eschenauer and Olhoff, 2001] Eschenauer H. A. and Olhoff N. (2001). *Topology optimization of continuum structures: A review*. Applied Mechanics Reviews, vol. 54 n° 4, pp 331–390. 84

[Escoda et al., 2015] Escoda J., Jeulin D., Willot F., and Toulemonde C. (2015). *Three-dimensional morphological modelling of concrete using multiscale Poisson polyhedra*. Journal of Microscopy, vol. 258 n° 1, pp 31–48. 9

[Estrin et al., 2011] Estrin Y., Dyskin A. V., and Pasternak E. (2011). *Topological interlocking as a material design concept*. Materials Science and Engineering, vol. C31, pp 1189–1194. 43

[Estrin et al., 2003] Estrin Y., Dyskin A. V., Pasternak E., Khor H. C., and Kanel-Belov A. J. (2003). *Topological interlocking of protective tiles for the space shuttle*. Philosophical Magazine Letters, vol. 83, pp 351–355. 43

[Evans et al., 2010] Evans A. G., He M., Deshpande V. S., Hutchinson J. W., Jacobsen A. J., and Carter W. B. (2010). *Concepts for enhanced energy absorption using hollow micro-lattices*. International Journal of Impact Engineering, vol. 37 n° 9, pp 947–959. 58

[Evans et al., 2001] Evans A. G., Hutchinson J. W., Fleck N. A., Ashby M. F., and Wadley H. N. G. (2001). *The topological design of multifunctional cellular metals*. Progress in Materials Science, vol. 46 n° 3-4, pp 309–327. 58

[Fallet et al., 2008] Fallet A., Lhuissier P., Salvo L., and Bréchet Y. (2008). *Mechanical behaviour of metallic hollow spheres foam*. Advanced Engineering Materials, vol. 10 n° 9, pp 858–862. 43, 46

[Faure et al., 2017] Faure A., Michailidis G., Parry G., Vermaak N., and Estevez R. (2017). *Design of thermoelastic multi-material structures with graded interfaces using topology optimization*. Structural and Multidisciplinary Optimization, vol. 56 n° 4, pp 823–837. 46

[Feng et al., 2018] Feng J., Zhang Z., Bironeau A., Guinault A., Miquelard-Garnier G., Sollogoub, C.and Olah A., and Baer E. (2018). *Breakup behavior of nanolayers in polymeric multilayer systems—Creation of nanosheets and nanodroplets*. Polymer, vol. 143, pp 19–27. 16

[Feng et al., 2002] Feng L., Li S., Li Y., Li H., Zhang L., Zhai J., Song Y., Liu B., Jiang L., and Zhu D. (2002). *Super-hydrophobic surfaces: from natural to artificial*. Advanced Materials, vol. 14 n° 24, pp 1857–1860. 62

[Feng et al., 2015] Feng Y., Siegmund T., Habtour E., and Riddick J. (2015). *Impact mechanics of topologically interlocked material assemblies*. International Journal of Impact Engineering, vol. 75, pp 140–149. 43

[Fenves and Baker, 1987] Fenves S. J. and Baker N. C. (1987). *Spatial and Functional Representation Language for Structural Design*. In : Expert Systems in Computer-Aided Design, IFIP 5.2, North-Holland. Elsevier Science. 107

[Fleck et al., 2010] Fleck N. A., Deshpande V. S., and Ashby M. F. (2010). *Micro-architectured materials: past, present and future*. Proceedings of the Royal Society A: Mathematical, Physical and Engineering Sciences, vol. 466 n° 2121, pp 2495–2516. 47, 58

[Flemming et al., 1992] Flemming U., Adams J., Carlson C., Coyne R., Fenves S., Finger S., Ganeshan R., Garrett J., Gupta A., Reich Y., Siewiorek D., Sturges R., and abd R. Woodbury D. Thomas (1992). *Computational models for form-function synthesis in engineering design*. Technical Report 48-25-92, Engineering Design Research Center, Carnegie Mellon University, Pittsburgh, PA. 107

[Ford and Despeisse, 2016] Ford S and Despeisse M (2016). *Additive manufacturing and sustainability: an exploratory study of the advantages and challenges*. Journal of Cleaner Production, vol. 137, pp 1573–1587. 86

[Forest, 2005] Forest S. (2005). *Mechanics of generalized continua and heterogeneous materials*. Les Presses de l'Ecole des Mines de Paris. 68

[François et al., 2012] François D., Pineau A., and Zaoui A. (2012). *Mechanical Behaviour of Materials, Volume 1: Micro- and Macroscopic Constitutive Behaviour*, vol. 180 of *Solid Mechanics and Its Applications*. Springer. 9

[Fratzl, 2007] Fratzl P. (2007). *Biomimetic materials research: what can we really learn from nature's structural materials?* Journal of the Royal Society Interface, vol. 4 n° 15, pp 637–642. 106

[Fratzl et al., 2013] eds. Fratzl P., Dunlop J.W.C., and Weinkamer R. (2013). *Materials Design Inspired by Nature- Function Through Inner Architecture*. RSC Publishing. 47

[Fratzl et al., 2016] Fratzl P., Kolednik O., Fischer F. D., and Dean M. N. (2016). *The mechanics of tessellations–bioinspired strategies for fracture resistance*. Chemical Society Reviews, vol. 45 n° 2, pp 252–267. 62

[Fratzl and Weinkamer, 2007] Fratzl P.r and Weinkamer R. (2007). *Nature's hierarchical materials*. Progress in Materials Science, vol. 52 n° 8, pp 1263–1334. 62, 107

[Freeman, 2002] Freeman A. J. (2002). *Materials by design and the exciting role of quantum computation/simulation*. Journal of Computational and Applied Mathematics, vol. 149 n° 1, pp 27–56. 44

[Fritzen et al., 2013] Fritzen F., Forest S., Kondo D., and Böhlke T. (2013). *Computational homogenization of porous materials of Green type*. Computational Mechanics, vol. 52 n° 1, pp 121–134. 9

[Frølich et al., 2017] Frølich S., Weaver J. C., Dean M. N., and Birkedal H. (2017). *Uncovering Nature's Design Strategies through Parametric Modeling, Multi-Material 3D Printing, and Mechanical Testing*. Advanced Engineering Materials, vol. 19 n° 6, pp e201600848. 107

[Fu et al., 2014] Fu K., Moreno D., Yang M., and Wood K. L. (2014). *Bio-inspired design: an overview investigating open questions from the broader field of design-by-analogy*. Journal of Mechanical Design, vol. 136 n° 11, pp 111102. 107

[Fuller, 1961] Fuller B. R. (1961). *Synergetic building construction*. 59, 60

[Gao and McCarthy, 2006] Gao L. and McCarthy T. J. (2006). *The "lotus effect" explained: two reasons why two length scales of topography are important*. Langmuir, vol. 22 n° 7, pp 2966–2967. 62

[Garnier et al., 2009] Garnier G., Chehab B., Yrieix B., Bréchet Y., and Flandin L. (2009). *On the essential work of fracture in polymer–metal multilayers*. Journal of Materials Science, vol. 44 n° 20, pp 5537–5543. 46

[Gaudillière et al., 2018] Gaudillière N., Duballet R., Bouyssou C., Mallet A., Roux Ph., Zakeri M., and Dirrenberger J. (2018). chapter Large-Scale Additive Manufacturing of Ultra-High-Performance Concrete of Integrated Formwork for Truss-Shaped Pillars, pp 459–472. Springer. 91

[Gaudillière et al., 2019] Gaudillière N., Duballet R., Bouyssou C., Mallet A., Roux Ph., Zakeri M., and Dirrenberger J. (2019). chapter Building applications using lost formworks obtained through large-scale additive manufacturing of ultra-high performance concrete. Elsevier. 91

[Geers and Yvonnet, 2016] Geers M. G. D. and Yvonnet J. (2016). *Multiscale modeling of microstructure–property relations*. MRS Bulletin, vol. 41 n° 8, pp 610–616. 45, 55

[Gérard et al., 2009] Gérard C., N'Guyen F., Osipov N., Cailletaud G., Bornert M., and Caldemaison D. (2009). *Comparison of experimental results and finite element simulation of strain localization scheme under cyclic loading*. Computational Materials Science, vol. 46 n° 3, pp 755–760. 31

[Germain, 1973] Germain P (1973). *The method of virtual power in continuum mechanics. Part 2: Microstructure*. SIAM Journal of Applied Mathematics, vol. 25 n° 3, pp 556–575. 68

[Ghaedizadeh et al., 2016] Ghaedizadeh A., Shen J., Ren X., and Xie Y. M. (2016). *Tuning the Performance of Metallic Auxetic Metamaterials by Using Buckling and Plasticity*. Materials, vol. 9 n° 54, pp 1–17. 46

[Gharbi et al., 2014] Gharbi M., Peyre P., Gorny C., Carin M., Morville S., Le Masson P., Carron D., and Fabbro R. (2014). *Influence of a pulsed laser regime on surface finish induced by the direct metal deposition process on a Ti64 alloy*. Journal of Materials Processing Technology, vol. 214 n° 2, pp 485–495. 61

[Gibson and Ashby, 1999] Gibson L.J. and Ashby M.F. (1999). *Cellular Solids*. Cambridge University Press, 2 edition. 59

[Gibson, 2012] Gibson L. J. (2012). *The hierarchical structure and mechanics of plant materials*. Journal of the Royal Society Interface, vol. 9, pp 2749–2767. 107

[Gillner and Münstermann, 2017] Gillner K. and Münstermann S. (2017). *Numerically predicted high cycle fatigue properties though representative volume elements of the microstructure*. International Journal of Fatigue, vol. 105, pp 219–234. 30

[Gitman et al., 2007] Gitman I. M., Askes H., and Sluys L. J. (2007). *Representative volume: Existence and size determination*. Engineering Fracture Mechanics, vol. 74, pp 2518–2534. 10

[Gong et al., 2015] Gong H., Rafi K., Gu H., Ram G. J., Starr T., and Stucker B. (2015). *Influence of defects on mechanical properties of Ti–6Al–4V components produced by selective laser melting and electron beam melting*. Materials and Design, vol. 86, pp 545–554. 61

[Gorgin Karajii et al., 2017] Gorgin Karajii Z., Speirs M., Dadbakhsh S., Kruth J. P., Weinans H., Zadpoor A. A., and Amin Yavari S. (2017). *Additively manufactured and surface biofunctionalized porous nitinol*. ACS Applied Materials & Interfaces, vol. 9 n° 2, pp 1293–1304. 66

[Gosselin et al., 2016] Gosselin C., Duballet R., Roux Ph., Gaudillière N., Dirrenberger J., and Morel Ph. (2016). *Large-Scale 3D Printing of Ultra-High Performance Concrete– A New Processing Route for Architects and Builders*. Materials and Design, vol. 100, pp 102–109. 86, 87, 88, 89, 99

[Green and Rivlin, 1964] Green A.E. and Rivlin R.S. (1964). *Multipolar continuum mechanics*. Archive for Rational Mechanics and Analysis, vol. 17 n° 2, pp 113–147. 68

[Grima et al., 2005] Grima JN, Gatt R, Alderson A, and Evans KE (2005). *On the potential of connected stars as auxetic systems*. Molecular Simulation, vol. 31 n° 13, pp 925–935. 71

[Guest and Prévost, 2006] Guest J. K. and Prévost J. H. (2006). *Optimizing multifunctional materials: design of microstructures for maximized stiffness and fluid permeability*. International Journal of Solids and Structures, vol. 43 n° 22-23, pp 7028–7047. 45

[Guiducci et al., 2014] Guiducci L., Fratzl P., Bréchet Y., and Dunlop J.W.C. (2014). *Pressurized honeycombs as soft-actuators: a theoretical study*. Journal of the Royal Society Interface, vol. 11, pp 20140458. 47, 56

[Guiducci et al., 2016] Guiducci L., Razghandi K., Bertinetti L., Turcaud S., Rüggeberg M., Weaver J. C., Fratzl P., Burgert I., and Dunlop J. W. C. (2016). *Honeycomb Actuators Inspired by the Unfolding of Ice Plant Seed Capsules*. PloS one, vol. 11 n° 11, pp e0163506. 47

[Guiducci et al., 2015] Guiducci L., Weaver J. C., Bréchet Y. J., Fratzl P., and Dunlop J. W. C. (2015). *The geometric design and fabrication of actuating cellular structures*. Advanced Materials Interfaces, vol. 2 n° 11, pp 1500011. 47, 62

[Gunenthiram et al., 2018] Gunenthiram V., Peyre P., Schneider M., Dal M., Coste F., Koutiri I., and Fabbro R. (2018). *Experimental analysis of spatter generation and melt-pool behavior during the powder bed laser beam melting process*. Journal of Materials Processing Technology, vol. 251, pp 376–386. 61

[Guo et al., 2015] Guo Q., Guo X., Fan J., Syed R., and Wu C. (2015). *An energy method for rapid evaluation of high cycle fatigue parameters based on intrinsic dissipation*. International Journal of Fatigue, vol. 80, pp 136–144. 41

[Gureev et al., 1990] Gureev D. M., Mednikov S. I., Shukhostanov V. K., and Yamshchikov S. V. (1990). *Influence of laser tempering on the characteristics of surface layers of tool steels*. Soviet Journal of Quantum Electronics, vol. 20 n° 8, pp 1003–1006. 79

[Gutowski et al., 2009] Gutowski T. G., Branham M. S., Dahmus J. B., Jones A. J., Thiriez A., and Sekulic D. P. (2009). *Thermodynamic analysis of resources used in manufacturing processes*. Environmental Science & Technology, vol. 43 n° 5, pp 1584–1590. 86

[Haberland et al., 2014] Haberland C., Elahinia M., Walker J. M., Meier H., and Frenzel J. (2014). *On the development of high quality NiTi shape memory and pseudoelastic parts by additive manufacturing*. Smart Materials and Structures, vol. 23 n° 10, pp 104002. 66

[Haghpanah et al., 2017] Haghpanah B., Shirazi A., Salari-Sharif L., Izard A. G., and Valdevit L. (2017). *Elastic architected materials with extreme damping capacity*. Extreme Mechanics Letters, vol. 17, pp 56–61. 106

[Hajela and Kim, 2001] Hajela P. and Kim B. (2001). *On the use of energy minimization for CA based analysis in elasticity*. Structural and Multidisciplinary Optimization, vol. 23, pp 24–33. 84

[Harrington et al., 2011] Harrington MJ, Razghandi K, Ditsch F, Guiducci L, Rueggeberg M, Dunlop JWC, Fratzl P, Neinhuis C, and Burgert I (2011). *Origami-like unfolding of hydro-actuated ice plant seed capsules*. Nature communications, vol. 2, pp 337. 62

[Hashin, 1983] Hashin Z. (1983). *Analysis of Composite Materials - A Survey*. Journal of Applied Mechanics, vol. 50, pp 481–505. 10

[Hazanov, 1998] Hazanov S. (1998). *Hill condition and overall properties of composites*. Archive of Applied Mechanics, vol. 68, pp 385–394. 36

[Hazanov and Huet, 1994] Hazanov S. and Huet C. (1994). *Order Relationships for Boundary Conditions Effect in Heterogeneous Bodies Smaller than the Representative Volume*. Journal of the Mechanics and Physics of Solids, vol. 42 n° 12, pp 1995–2011. 36

[Hedayati et al., 2017] Hedayati R., Janbaz S., Sadighi M., Mohammadi-Aghdam M., and Zadpoor A. A. (2017). *How does tissue regeneration influence the mechanical behavior of additively manufactured porous biomaterials?* Journal of the Mechanical Behavior of Biomedical Materials, vol. 65, pp 831–841. 106

[Hegge et al., 1990] Hegge H. J., Beurs H. De, Noordhuis J., and Hosson J. T. M. De (1990). *Tempering of Steel during Laser Treatment*. Metallurgical and Materials Transactions A: Physical Metallurgy and Materials Science, vol. 21, pp 987–995. 79

[Heinl et al., 2008] Heinl P., Müller L., Körner C., Singer R. F., and Müller F. A. (2008). *Cellular Ti–6Al–4V structures with interconnected macro porosity for bone implants fabricated by selective electron beam melting*. Acta Biomaterialia, vol. 4 n° 5, pp 1536–1544. 61

[Henry and Pimenta, 2018] Henry J. and Pimenta S. (2018). *Increasing damage tolerance in composites using hierarchical brick-and-mortar microstructures*. Journal of the Mechanics and Physics of Solids, vol. 118, pp 322–340. 43

[Hersant and Jeulin, 1976] Hersant T. and Jeulin D. (1976). *L'échantillonnage dans les analyses quantitatives d'images. Exemples d'application aux mesures des teneurs de phases dans les agglomérés et des inclusions dans les aciers*. Mémoires et Etudes Scientifiques de la Revue de Métallurgie, vol. 73, pp 503. 17

[Hill, 1963] Hill R. (1963). *Elastic Properties of Reinforced Solids: Some Theoretical Principles*. Journal of the Mechanics and Physics of Solids, vol. 11, pp 357–372. 10

[Hill, 1967] Hill R. (1967). *The essential structure of constitutive laws for metal composites and polycrystals*. Journal of the Mechanics and Physics of Solids, vol. 15, pp 79–95. 33, 52

[Hill, 1952] Hill R. T. (1952). *On discontinuous plastic states, with special reference to localized necking in thin sheets*. Journal of the Mechanics and Physics of Solids, vol. 1 n° 1, pp 19–30. 66

[Hirtz et al., 2002] Hirtz J., Stone R. B., McAdams D. A., Szykman S., and Wood K. L. (2002). *A functional basis for engineering design: reconciling and evolving previous efforts*. Research in Engineering Design, vol. 13 n° 2, pp 65–82. 107

[Hopkins et al., 2016] Hopkins J. B., Shaw L. A., Weisgraber T. H., Farquar G. R., Harvey C. D., and Spadaccini C. M. (2016). *Design of Nonperiodic Microarchitectured Materials That Achieve Graded Thermal Expansions*. Journal of Mechanisms and Robotics, vol. 8 n° 5, pp 051010. 46

[Hopman and Leamy, 2010] Hopman R. K. and Leamy M. J. (2010). *Triangular Cellular Automata for Computing Two-Dimensional Elastodynamic Response on Arbitrary Domains*. Journal of Applied Mechanics, vol. 78 n° 2, pp 021020. 84

[Hor et al., 2014] Hor A., Saintier N., Robert C., Palin-Luc T., and Morel F. (2014). *Statistical assessment of multiaxial HCF criteria at the grain scale*. International Journal of Fatigue, vol. 67, pp 151–158. 9

[Hsiao and Chen, 1997] Hsiao S. W. and Chen C. H. (1997). *A semantic and shape grammar based approach for product design*. Design Studies, vol. 18 n° 3, pp 275–296. 107

[Huang and Xie, 2007] Huang X. and Xie Y. M. (2007). *Convergent and mesh-independent solutions for bi-directional evolutionary structural optimization method*. Finite Elements in Analysis and Design, vol. 43 n° 14, pp 1039–1049. 84

[Huet, 1990] Huet C. (1990). *Application of Variational Concepts to Size Effects in Elastic Heterogeneous Bodies*. Journal of the Mechanics and Physics of Solids, vol. 38 n° 6, pp 813–841. 16, 33, 54

[Huet, 1997] Huet C. (1997). *An integrated micromechanics and statistical continuum thermodynamics approach for studying the fracture behaviour of microcracked heterogeneous materials with delayed response*. Engineering Fracture Mechanics, vol. 58 n° 5-6, pp 459–556. 36

[Hughes et al., 2005] Hughes T. J. R., Cottrell J. A., and Bazilevs Y. (2005). *Isogeometric analysis: CAD, finite elements, NURBS , exact geometry and mesh refinement*. Computer Methods in Applied Mechanics and Engineering, vol. 194 n° 39, pp 4135–4195. 70

[Iino and Shimoda, 1987] Iino Y. and Shimoda K. (1987). *Effect of overlap pass tempering on hardness and fatigue behaviour in laser heat treatment of carbon steel*. Journal of Materials Science Letters, vol. 6 n° 10, pp 1193–1194. 79

[Iltchev et al., 2015] Iltchev A., Marcadon V., Kruch S., and Forest S. (2015). *Computational homogenisation of periodic cellular materials: Application to structural modelling*. International Journal of Mechanical Sciences, vol. 93, pp 240–255. 56

[Ingold, 2013] Ingold T. (2013). *Making: Anthropology, archaeology, art and architecture*. Routledge. 107

[Ion, 2005] Ion J.C. (2005). *Laser Processing of Engineering Materials*. Elsevier, Oxford. 79

[Jayasankar et al., 2017] Jayasankar A. K., Seidel R., Naumann J., Guiducci L., Hosny A., Fratzl P., Weaver J. C., Dunlop J. W. C., and Dean M. N. (2017). *Mechanical behavior of idealized, stingray-skeleton-inspired tiled composites as a function of geometry and material properties*. Journal of the Mechanical Behavior of Biomedical Materials, vol. 73, pp 86–101. 47

[Jean and Engelmayr, 2010] Jean A. and Engelmayr G. C. (2010). *Finite element analysis of an accordion-like honeycomb scaffold for cardiac tissue engineering*. Journal of Biomechanics, vol. 43, pp 3035–3043. 56

[Jean et al., 2011a] Jean A., Jeulin D., Forest S., Cantournet S., and N'Guyen F. (2011a). *A multiscale microstructure model of carbon black distribution in rubber*. Journal of Microscopy, vol. 241 n° 3, pp 243–260. 9, 11, 15, 30

[Jean et al., 2011b] Jean A., Willot F., Cantournet S., Forest S., and Jeulin D. (2011b). *Large-scale Computations of Effective Elastic Properties of Rubber with Carbon Black Fillers*. International Journal for Multiscale Computational Engineering, vol. 9 n° 3, pp 271–303. 15

[Jeulin, 1991] Jeulin D. (1991). *Modèles de Fonctions Aléatoires Multivariables*. Sciences de la Terre, vol. 30, pp 225–256. 14

[Jeulin, 2000] Jeulin D. (2000). *Random texture models for material structures*. Statistics and Computing, vol. 10 n° 2, pp 121–132. 9

[Jeulin, 2001] Jeulin D. (2001). *Caractérisation Morphologique et Modèles de Structures Aléatoires*, vol. 1 of *Homogénéisation en Mécanique des Matériaux*, chapter 4, pp 95–132. Hermès. 12

[Jeulin, 2011] Jeulin D. (2011). *Variance scaling of Boolean random varieties*. Technical report, Centre de Morphologie Mathématique. N/10/11/MM (2011), hal-00618967, version 1. 15

[Jeulin, 2016] Jeulin D. (2016). *Power Laws Variance Scaling of Boolean Random Varieties*. Methodology and Computing in Applied Probability, vol. 18 n° 4, pp 1065–1079. 26

[Jeulin and Ostoja-Starzewski, 2001] Jeulin D. and Ostoja-Starzewski M. (2001). *Mechanics of Random and Multiscale Microstructures*. CISM Courses. Springer. 9, 12

[Jiang et al., 2016] Jiang D., Bechle N. J., Landis C. M., and Kyriakides S. (2016). *Buckling and recovery of NiTi tubes under axial compression*. International Journal of Solids and Structures, vol. 80, pp 52–63. 66

[Jiang et al., 2017] Jiang D., Kyriakides S., Landis C. M., and Kazinakis K. (2017). *Modeling of propagation of phase transformation fronts in NiTi under uniaxial tension*. European Journal of Mechanics A/Solids, vol. 64, pp 131–142. 66

[Jung and Diebels, 2016] Jung A. and Diebels S. (2016). *Synthesis and mechanical properties of novel Ni/PU hybrid foams: a new economic composite material for energy absorbers*. Advanced Engineering Materials, vol. 18 n° 4, pp 532–541. 106

[Kalentics et al., 2017] Kalentics N., Boillat E., Peyre P., Ćirić-Kostić S., Bogojević N., and Logé R. E. (2017). *Tailoring residual stress profile of selective laser melted parts by laser shock peening*. Additive Manufacturing, vol. 16, pp 90–97. 61

[Kanit et al., 2003] Kanit T., Forest S., Galliet I., Mounoury V., and Jeulin D. (2003). *Determination of the Size of the Representative Volume Element for Random Composites: Statistical and Numerical Approach*. International Journal of Solids and Structures, vol. 40, pp 3647–3679. 9, 11, 14, 15, 17, 20, 23, 28, 30, 31, 40, 41, 54

[Kanit et al., 2006] Kanit T., N'Guyen F., Forest S., Jeulin D., Reed M., and Singleton S. (2006). *Apparent and effective physical properties of heterogeneous materials: Representativity of samples of two materials from food industry*. Computer Methods in Applied Mechanics and Engineering, vol. 195, pp 3960–3982. 9, 15, 54

[Kazmierczak et al., 2007] Kazmierczak T., Song H., Hiltner A., and Baer E. (2007). *Polymeric one-dimensional photonic crystals by continuous coextrusion*. Macromolecular Rapid Communications, vol. 28 n° 23, pp 2210–2216. 16

[Kerns et al., 1999] Kerns J., Hsieh A., Hiltner A., and Baer E. (1999). *Mechanical behavior of polymer microlayers*. Macromolecular Symposia, vol. 147 n° 1, pp 15–25. 16

[Khakalo and Niiranen, 2017] Khakalo S. and Niiranen J. (2017). *Isogeometric analysis of higher-order gradient elasticity by user elements of a commercial finite element software*. Computer-Aided Design, vol. 82, pp 154–169. 45

[Khandelwal et al., 2015] Khandelwal S., Siegmund T., Cipra R. J., and Bolton J. S. (2015). *Adaptive mechanical properties of topologically interlocking material systems*. Smart Materials and Structures, vol. 24 n° 4, pp 045037. 43

[Khoshnevis, 2004] Khoshnevis B (2004). *Automated construction by contour crafting- related robotics and information technologies*. Automation in Construction, vol. 13, pp 5–19. 87

[Kiendl et al., 2014] Kiendl J., Schmidt R., Wüchner R., and Bletzinger K.-U. (2014). *Isogeometric shape optimization of shells using semi-analytical sensitivity analysis and sensitivity weighting*. Computer Methods in Applied Mechanics and Engineering, vol. 274, pp 148–167. 70

[Kim et al., 2004] Kim S., Abdalla M. M., Gürdal Z., and Jones M. (2004). *Multigrid Accelerated Cellular Automata for Structural Design Optimization: A 1-D Implementation*. In : 45th AIAA/ASME/ASCE/AHS/ASC Structures, Structural Dynamics and Materials Conference, Palm Springs, California, 2004. 84

[Kirschman and Fadel, 1998] Kirschman C. F. and Fadel G. M. (1998). *Classifying functions for mechanical design*. Journal of Mechanical Design, vol. 120 n° 3, pp 475–482. 107

[Kleffel and Drummer, 2017] Kleffel T. and Drummer D. (2017). *Investigating the suitability of roughness parameters to assess the bond strength of polymer-metal hybrid structures with mechanical adhesion*. Composites Part B; Engineering, vol. 117, pp 20–25. 61

[Knight and Stiny, 2015] Knight T. and Stiny G. (2015). *Making grammars: from computing with shapes to computing with things*. Design Studies, vol. 41, pp 8–28. 107

[Knippers and Speck, 2012] Knippers J. and Speck T. (2012). *Design and construction principles in nature and architecture*. Bioinspiration & biomimetics, vol. 7 n° 1, pp 015002. 107

[Kolewe et al., 2013] Kolewe M. E., Park H., Gray C., Ye X., Langer R., and Freed L. E. (2013). *3D structural patterns in scalable, elastomeric scaffolds guide engineered tissue architecture*. Advanced Materials, vol. 25 n° 32, pp 4459–4465. 107

[Kolopp et al., 2013] Kolopp A., Rivallant S., and Bouvet C. (2013). *Experimental study of sandwich structures as armour against medium-velocity impacts*. International Journal of Impact Engineering, vol. 61, pp 24–35. 43, 46

[Kooistra et al., 2004] Kooistra G. W., Deshpande V. S., and Wadley H. N. (2004). *Compressive behavior of age hardenable tetrahedral lattice truss structures made from aluminium*. Acta Materialia, vol. 52 n° 14, pp 4229–4237. 58

[Körner and Liebold-Ribeiro, 2015] Körner C. and Liebold-Ribeiro Y. (2015). *A systematic approach to identify cellular auxetic materials*. Smart Materials and Structures, vol. 24 n° 2, pp 025013. 46, 71

[Kotani and Ikeda, 2016] Kotani M. and Ikeda S. (2016). *Materials inspired by mathematics*. Science and Technology of Advanced Materials, vol. 17 n° 1, pp 253–259. 46

[Koutiri et al., 2018] Koutiri I., Pessard E., Peyre P., Amlou O., and De Terris T. (2018). *Influence of SLM process parameters on the surface finish, porosity rate and fatigue behavior of as-built Inconel 625 parts*. Journal of Materials Processing Technology, vol. 255, pp 536–546. 61

[Kowalski et al., 2016] Kowalski N., Delannay L., Yan P., and Remacle J. F. (2016). *Finite element modeling of periodic polycrystalline aggregates with intergranular cracks*. International Journal of Solids and Structures, vol. 90, pp 60–68. 9

[Krause et al., 2012] Krause T., Molotnikov A., Carlesso M., Rente J., Rezwan K., Estrin Y., and Koch D. (2012). *Mechanical properties of topologically interlocked structures with elements produced by freeze gelation of ceramic slurries*. Advanced Engineering Materials, vol. 14 n° 5, pp 335–341. 43

[Krauss et al., 2009] Krauss S., Monsonego-Orsan E., Zelzer E., Fratzl P., and Shahar R. (2009). *Mechanical Function of a Complex Three-Dimensional Suture Joining the Bony Elements in the Shell of the Red-Ear ed Slider Turtle*. Advanced Materials, vol. 21, pp 407–412. 62

[Kyriakides and Miller, 2000] Kyriakides S. and Miller J. E. (2000). *On the propagation of Lüders bands in steel strips*. Journal of Applied Mechanics, vol. 67 n° 4, pp 645–654. 66

[Kyriakides et al., 2008] Kyriakides S., Ok A., and Corona E. (2008). *Localization and propagation of curvature under pure bending in steel tubes with Lüders bands*. International Journal of Solids and Structures, vol. 45 n° 10, pp 3074–3087. 66

[La Rosa and Risitano, 2000] La Rosa G. and Risitano A. (2000). *Thermographic methodology for rapid determination of the fatigue limit of materials and mechanical components*. International Journal of Fatigue, vol. 22, pp 65–73. 41

[Labonnote et al., 2016] Labonnote N., Ronnquist A., Manum B., and Rüther P. (2016). *Additive construction: State-of-the-art, challenges and opportunities*. Automation in Construction, vol. 72, pp 347–366. 99

[Lai et al., 2015] Lai Q., Bouaziz O., Gouné M., Brassart L., Verdier M., Parry G., Perlade A., Bréchet Y., and Pardoen T. (2015). *Damage and fracture of dual-phase steels: Influence of martensite volume fraction*. Materials Science & Engineering, A: Structural Materials: Properties, Microstructure and Processing, vol. 646, pp 322–331. 77

[Lai et al., 2016] Lai Q., Brassart L., Bouaziz O., M. Gouné, M. Verdier, Parry G., Perlade A., Bréchet Y., and Pardoen T. (2016). *Influence of martensite volume fraction and hardness on the plastic behavior of dual-phase steels: Experiments and micromechanical modeling*. International Journal of Plasticity, vol. 80, pp 187–203. 77

[Lakes, 1993] Lakes R. S. (1993). *Materials with structural hierarchy*. Nature, vol. 361, pp 511–515. 107

[Landis, 2003] Landis C. M. (2003). *On the strain saturation conditions for polycrystalline ferroelastic materials*. Journal of Applied Mechanics, vol. 70 n° 4, pp 470–478. 66

[Lantuéjoul, 1991] Lantuéjoul C. (1991). *Ergodicity and Integral Range*. Journal of Microscopy, vol. 161, pp 387–403. 12, 14

[Lantuéjoul, 2002] Lantuéjoul C. (2002). *Geostatistical Simulation: Models and Algorithms*. Springer. 12

[Larsen et al., 1997] Larsen UD, Signund O, and Bouwsta S (1997). *Design and fabrication of compliant micromechanisms and structures with negative Poisson's ratio*. Journal of Microelectromechanical Systems, vol. 6 n° 2, pp 99–106. 71

[Laszczyk et al., 2009] Laszczyk L., Dendievel R., Bouaziz O., Bréchet Y., and Parry G. (2009). *Design of Architectured Sandwich Core Materials using Topological Optimization Methods*. In : Symposium LL – Architectured Multifunctional Materials, vol. 1188 of *MRS Proceedings*. 46

[Latture et al., 2018a] Latture R. M., Begley M. R., and Zok F. W. (2018a). *Design and mechanical properties of elastically isotropic trusses*. Journal of Materials Research, vol. 33 n° 3, pp 249–263. 58

[Latture et al., 2018b] Latture R. M., Rodriguez R. X., Holmes Jr L. R., and Zok F. W. (2018b). *Effects of nodal fillets and external boundaries on compressive response of an octet truss*. Acta Materialia, vol. 149, pp 78–87. 58

[Le Riche and Haftka, 2012] Le Riche R. and Haftka R. T. (2012). *On global optimization articles in SMO*. Structural and Multidisciplinary Optimization, vol. 46, pp 627–629. 84

[Lebée and Sab, 2012] Lebée A. and Sab K. (2012). *Homogenization of thick periodic plates: Application of the Bending-Gradient plate theory to a folded core sandwich panel*. International Journal of Solids and Structures, vol. 49 n° 19-20, pp 2778–2792. 45

[Lecampion et al., 2011] Lecampion B., Vanzo J., Ulm F.-J., Huet B., Germay C., Khalfallah I., and Dirrenberger J. (2011). *EVOLUTION OF PORTLAND CEMENT MECHANICAL PROPERTIES EXPOSED TO CO2-RICH FLUIDS: INVESTIGATION AT DIFFERENT SCALES*. In : MPPS 2011, Symposium on Mechanics and Physics of Porous Solids : A tribute to Pr. Olivier Coussy. IFSTTAR. 88

[Leite et al., 2012a] Leite P., Thomas M., and Bréchet Y. (2012a). *Optimal design of a lightweight sandwich panel for mechanical and thermal properties*. In : MS&T '12, Proceedings of the Materials Science and Technology Conference, Pittsburgh, Pennsylvania, USA, 7-11 October 2012. 46

[Leite et al., 2012b] Leite P., Thomas M., Simon F., and Bréchet Y. (2012b). *Optimal design of an asymmetrical sandwich panel for acoustical and mechanical properties*. In : Proceedings of the ESDA2012, 11th Biennal conference on Engineering Systems Design and Analysis, Nantes, France, 1-4 July 2012. 46

[Lepidi and Bacigalupo, 2018] Lepidi M. and Bacigalupo A. (2018). *Parametric design of the band structure for lattice materials*. Meccanica, vol. 53 n° 3, pp 613–628. 69

[Lévy, 1874] Lévy M. (1874). *La statique graphique et ses applications aux constructions*. Gauthier-Villars, Paris. 83

[Lewandowski et al., 2012] Lewandowski M., Amiot M., and Perwuelz A. (2012). *Development and Characterization of 3D Nonwoven Composites*. Materials Science Forum, vol. 714, pp 131–137. 43, 46

[Lhuissier et al., 2016] Lhuissier P., De Formanoir C., Martin G., Dendievel R., and Godet S. (2016). *Geometrical control of lattice structures produced by EBM through chemical etching: Investigations at the scale of individual struts*. Materials and Design, vol. 110, pp 485–493. 61

[Li et al., 2013] Li J., Nayak S., Biro E., Panda S., Goodwin F., and Zhou Y. (2013). *Effects of weld line position and geometry on the formability of laser welded high strength low alloy and dual-phase steel blanks*. Materials and Design, vol. 52, pp 757–766. 79

[Li et al., 2014] Li X., McKenna G. B., Miquelard-Garnier G., Guinault A., Sollogoub C., Regnier G., and Rozanski A. (2014). *Forced assembly by multilayer coextrusion to create oriented graphene reinforced polymer nanocomposites*. Polymer, vol. 55 n° 1, pp 248–257. 16

[Liu et al., 2016] Liu J., Gu T., Shan S., Kang S. H., Weaver J. C., and Bertoldi K. (2016). *Harnessing buckling to design architected materials that exhibit effective negative swelling*. Advanced Materials, vol. 28 n° 31, pp 6619–6624. 46, 106

[Liu et al., 2017a] Liu L., Kamm P., García-Moreno F., Banhart J., and Pasini D. (2017a). *Elastic and failure response of imperfect three-dimensional metallic lattices: the role of geometric defects induced by Selective Laser Melting*. Journal of the Mechanics and Physics of Solids, vol. 107, pp 160–184. 61

[Liu et al., 2003] Liu R., Jin Y., Hiltner A., and Baer E. (2003). *Probing nanoscale polymer interactions by forced-assembly*. Macromolecular Rapid Communications, vol. 24 n° 16, pp 943–948. 16

[Liu et al., 2017b] Liu Z., Meyers M. A., Zhang Z., and Ritchie R. O. (2017b). *Functional gradients and heterogeneities in biological materials: Design principles, functions, and bioinspired applications*. Progress in Materials Science, vol. 88, pp 467–498. 106

[Lomer, 1952] Lomer W. M. (1952). *The yield phenomenon in polycrystalline mild steel*. Journal of the Mechanics and Physics of Solids, vol. 1 n° 1, pp 64–73. 66

[Lüders, 1860] Lüders W. (1860). *Über die Äusserung der Elasticität an stahlartigen Eisenstäben und Stahlstäben, und über eine beim Biegen solcher Stäbe beobachtete Molecularbewegung*. Dinglers Polytechnisches Journal, vol. 5, pp 18–22. 66

[Luong, 1995] Luong M. (1995). *Infrared thermographic scanning of fatigue in metals*. Nuclear Engineering and Design, vol. 158, pp 363–376. 41

[Luz and Mano, 2009] Luz G. M. and Mano J. F. (2009). *Biomimetic design of materials and biomaterials inspired by the structure of nacre*. Philosophical Transactions of the Royal Society of London A: Mathematical, Physical and Engineering Sciences, vol. 367 n° 1893, pp 1587–1605. 62

[Madi et al., 2007] Madi K., Forest S., Boussuge M., Gailliègue S., Lataste E., Buffière J.-Y., Bernard D., and Jeulin D. (2007). *Finite element simulations of the deformation of fused-cast refractories based on X-ray computed tomography*. Computational Materials Science, vol. 39, pp 224–229. 9, 15

[Madi et al., 2005] Madi K., Forest S., Cordier P., and Boussuge M. (2005). *Numerical study of creep in two-phase aggregates with a large rheology contrast: implications for the lower mantle*. Earth and Planetary Science Letters, vol. 237 n° 1-2, pp 223–238. 15

[Madi et al., 2006] Madi K., Forest S., Jeulin D., and Boussuge M. (2006). *Estimating RVE sizes for 2D/3D viscoplastic composite materials*. In : Matériaux 2006. 30, 34, 38, 40

[Malik and Barthelat, 2016] Malik IA and Barthelat F (2016). *Toughening of thin ceramic plates using bioinspired surface patterns*. International Journal of Solids and Structures, vol. 97, pp 389–399. 62

[Malik et al., 2017] Malik IA, Mirkhalaf M, and Barthelat F (2017). *Bio-inspired "jigsaw"-like interlocking sutures: Modeling, optimization, 3D printing and testing*. Journal of the Mechanics and Physics of Solids, vol. 102, pp 224–238. 62

[Manh et al., 2011] Manh N. D., Evgrafov A., Gersborg A. R., and Gravesen J. (2011). *Isogeometric shape optimization of vibrating membranes*. Computer Methods in Applied Mechanics and Engineering, vol. 200 n° 13, pp 1343–1353. 70

[Marais et al., 2012] Marais A., Mazière M., Forest S., Parrot A., and Le Delliou P. (2012). *Identification of a strain-aging model accounting for Lüders behavior in a C-Mn steel*. Philosophical Magazine, vol. 92 n° 28-30, pp 3589–3617. 66

[March and Stiny, 1985] March L. and Stiny G. (1985). *Spatial systems in architecture and design: some history and logic*. Environment and Planning B: Planning and Design, vol. 12 n° 1, pp 31–53. 107

[Marckmann and Verron, 2006] Marckmann G. and Verron E. (2006). *Comparison of hyperelastic models for rubber-like materials*. Rubber Chemistry and Technology, vol. 79 n° 5, pp 835–858. 64

[Martin et al., 2014] Martin G., Ochoa N., Saï K., Hervé-Luanco E., and Cailletaud G. (2014). *A multiscale model for the elastoviscoplastic behavior of Directionally Solidified alloys: Application to FE structural computations*. International Journal of Solids and Structures, vol. 51 n° 5, pp 1175–1187. 29, 30

[Mather et al., 2012] Mather A., Cipra R., and Siegmund T. (2012). *Structural integrity during remanufacture of a topologically interlocked material*. International Journal of Structural Integrity, vol. 3 n° 1, pp 61–78. 43

[Matheron, 1971] Matheron G. (1971). *The Theory of Regionalized Variables and its Applications*. Les Cahiers du Centre de Morphologie Mathématique de Fontainebleau. Ecole des Mines de Paris. 11, 12

[Matheron, 1975] Matheron G. (1975). *Random Sets and Integral Geometry*. J. Wiley. 12

[Matheron, 1989] Matheron G. (1989). *Estimating and Choosing*. Springer-Verlag, Berlin. 14

[Matouš et al., 2017] Matouš K., Geers M. G. D., Kouznetsova V. G., and Gillman A. (2017). *A review of predictive nonlinear theories for multiscale modeling of heterogeneous materials*. Journal of Computational Physics, vol. 330, pp 192–220. 45

[Maxwell, 1864] Maxwell J. C. (1864). *On the calculation of the equilibrium and stiffness of frames*. The London, Edinburgh, and Dublin Philosophical Magazine and Journal of Science, vol. 27 n° 182, pp 294–299. 58

[Mazière and Forest, 2015] Mazière M. and Forest S. (2015). *Strain gradient plasticity modeling and finite element simulation of Lüders band formation and propagation*. Continuum Mechanics and Thermodynamics, vol. 27 n° 1-2, pp 83–104. 66

[Mazière et al., 2017] Mazière M., Luis C., Marais A., Forest S., and Gaspérini M. (2017). *Experimental and numerical analysis of the Lüders phenomenon in simple shear*. International Journal of Solids and Structures, vol. 106, pp 305–314. 66

[Melchels et al., 2012] Melchels F. P., Domingos M. A., Klein T. J., Malda J., Bartolo P. J., and Hutmacher D. W. (2012). *Additive manufacturing of tissues and organs*. Progress in Polymer Science, vol. 37 n° 8, pp 1079–1104. 107

[Méric et al., 1991] Méric L., Poubanne P., and Cailletaud G. (1991). *Single crystal modeling for structural calculations. Part 1: Model presentation*. Journal of Engineering Materials and Technology, vol. 113, pp 162–170. 31

[Mezeix et al., 2009] Mezeix L., Bouvet C., Huez J., and Poquillon D. (2009). *Mechanical behavior of entangled fibers and entangled cross-linked fibers during compression*. Journal of Materials Science, vol. 44 n° 14, pp 3652–3661. 43

[Michel et al., 1999] Michel J.-C., Moulinec H., and Suquet P. (1999). *Effective properties of composite materials with periodic microstructure: a computational approach*. Computer Methods in Applied Mechanics and Engineering, vol. 172, pp 109–143. 52

[Michell, 1904] Michell A. G. M. (1904). *The limit of economy of material in frame structures*. Philosophical Magazine, vol. 8 n° 6, pp 589–597. 83

[Mindlin, 1964] Mindlin R.D. (1964). *Micro-structure in linear elasticity*. Archive for Rational Mechanics and Analysis, vol. 16 n° 1, pp 51–78. 68

[Mindlin, 1965] Mindlin R.D. (1965). *Second gradient of strain and surface-tension in linear elasticity*. International Journal of Solids and Structures, vol. 1 n° 4, pp 417–438. 68

[Mindlin and Eshel, 1968] Mindlin R.D. and Eshel N.N. (1968). *On first strain-gradient theories in linear elasticity*. International Journal of Solids and Structures, vol. 4 n° 1, pp 109–124. 68

[Miquelard-Garnier et al., 2013] Miquelard-Garnier G., Guinault A., Fromonteil D., Delalande S., and Sollogoub C. (2013). *Dispersion of carbon nanotubes in polypropylene via multilayer coextrusion: Influence on the mechanical properties*. Polymer, vol. 54 n° 16, pp 4290–4297. 16

[Mirkhalaf et al., 2014] Mirkhalaf M., Khayer Dastjerdi A., and Barthelat F. (2014). *Overcoming the brittleness of glass through bio-inspiration and micro-architecture*. Nature Communications, vol. 5, pp 3166. 47

[Missoum et al., 2005] Missoum S., Gürdal Z., and Setoodeh S. (2005). *Study of a new local update scheme for cellular automata in structural design*. Structural and Multidisciplinary Optimization, vol. 29, pp 103–112. 84

[Molotnikov et al., 2007] Molotnikov A., Estrin Y., Dyskin A. V., Pasternak E., and Kanel-Belov A. J. (2007). *Percolation mechanism of failure of a planar assembly of interlocked osteomorphic elements*. Engineering Fracture Mechanics, vol. 74, pp 1222–1232. 43

[Molotnikov et al., 2013] Molotnikov A., Gerbrand R., Bouaziz O., and Estrin Y. (2013). *Sandwich panels with a core segmented into topologically interlocked elements*. Advanced Engineering Materials, vol. 15 n° 8, pp 728–731. 43

[Molotnikov et al., 2015] Molotnikov A., Gerbrand R., Qi Y., Simon G. P., and Estrin Y. (2015). *Design of responsive materials using topologically interlocked elements*. Smart Materials and Structures, vol. 24 n° 2, pp 025034. 43

[Monn et al., 2015] Monn MA, Weaver JC, Zhang T, Aizenberg J, and Kesari H (2015). *New functional insights into the internal architecture of the laminated anchor spicules of Euplectella aspergillum*. Proceedings of the National Academy of Sciences, vol. 112 n° 16, pp 4976–4981. 62

[Morel, 2014] Morel P. (2014). *Computation or Revolution*. Architectural Design, vol. 84 n° 3, pp 76–87. 84

[Mukhopadhyay and Adhikari, 2016] Mukhopadhyay T. and Adhikari S. (2016). *Effective in-plane elastic properties of auxetic honeycombs with spatial irregularity*. Mechanics of Materials, vol. 95, pp 204–222. 71

[Munch et al., 2008] Munch E., Launey M. E., Alsem D. H., Saiz E., Tomsia A. P., and Ritchie R. O. (2008). *Tough, bio-inspired hybrid materials*. Science, vol. 322 n° 5907, pp 1516–1520. 62

[Musienko et al., 2007] Musienko A., Tatschl A., Schmidegg K., Kolednik O., Pippan R., and Cailletaud G. (2007). *Three-dimensional finite element simulation of a polycrystalline copper specimen*. Acta Materialia, vol. 55 n° 12, pp 4121–4136. 31

[Muth et al., 2017] Muth J. T., Dixon P. G., Woish L., Gibson L. J., and Lewis J. A. (2017). *Architected cellular ceramics with tailored stiffness via direct foam writing*. Proceedings of the National Academy of Sciences, vol. 114 n° 8, pp 1832–1837. 106

[Nagy et al., 2010] Nagy A. P., Abdalla M. M., and Gürdal Z. (2010). *Isogeometric sizing and shape optimisation of beam structures*. Computer Methods in Applied Mechanics and Engineering, vol. 199 n° 17, pp 1216–1230. 70

[Nagy and Abdalla, 2011] Nagy A. P. and Abdalla, M. M.and Gürdal Z. (2011). *Isogeometric design of elastic arches for maximum fundamental frequency*. Structural and Multidisciplinary Optimization, vol. 43 n° 1, pp 135–149. 70

[Nagy et al., 2013] Nagy A. P., Ijsselmuiden S. T., and Abdalla M. M. (2013). *Isogeometric design of anisotropic shells: Optimal form and material distribution*. Computer Methods in Applied Mechanics and Engineering, vol. 264, pp 145–162. 70

[Naleway et al., 2015] Naleway S.E., Porter M.M., McKittrick J., and Meyers M.A. (2015). *Structural design elements in biological materials: application to bioinspiration*. Advanced Materials, vol. 27 n° 37, pp 5455–5476. 62, 106

[Negroponte, 1995] Negroponte N. (1995). *Being Digital*. Alfred A. Knopf, New York. 107

[Nerger et al., 2017] Nerger B. A., Siedlik M. J., and Nelson C. M. (2017). *Microfabricated tissues for investigating traction forces involved in cell migration and tissue morphogenesis*. Cellular and Molecular Life Sciences, vol. 74 n° 10, pp 1819–1834. 107

[Niendorf et al., 2014] Niendorf T., Leuders S., Riemer A., Brenne F., Tröster T., Richard H. A., and Schwarze D. (2014). *Functionally graded alloys obtained by additive manufacturing*. Advanced Engineering Materials, vol. 16 n° 7, pp 857–861. 106

[Niezgoda et al., 2010] Niezgoda S. R., Turner D. M., Fullwood D. T., and Kalidindi S. R. (2010). *Optimized structure based representative volume element sets reflecting the ensemble-averaged 2-point statistics*. Acta Materialia, vol. 58 n° 13, pp 4432–4445. 15

[Nørtoft and Gravesen, 2013] Nørtoft P. and Gravesen J. (2013). *Isogeometric shape optimization in fluid mechanics*. Structural and Multidisciplinary Optimization, vol. 48 n° 5, pp 909–925. 70

[Olivier et al., 2012] Olivier J., Janssens-Maenhout G., and Peters J. (2012). *Trends in global CO2 emissions; 2012 Report*. PBL Netherlands Environmental Assessment Agency. 99

[Olson, 2001] Olson G. B. (2001). *Beyond discovery: design for a new material world*. Calphad, vol. 25 n° 2, pp 175–190. 44

[Onal et al., 2018] Onal E., Frith J. E., Jurg M., Wu X., and Molotnikov A. (2018). *Mechanical Properties and In Vitro Behavior of Additively Manufactured and Functionally Graded Ti6Al4V Porous Scaffolds*. Metals, vol. 8 n° 4, pp 200. 61

[Osanov and Guest, 2016] Osanov M. and Guest J. K. (2016). *Topology optimization for architected materials design*. Annual Review of Materials Research, vol. 46, pp 211–233. 46

[Ostoja-Starzewski, 2002] Ostoja-Starzewski M. (2002). *Microstructural Randomness Versus Representative Volume Element in Thermomechanics*. Journal of Applied Mechanics, vol. 69 n° 1, pp 25–35. 10

[Ostoja-Starzewski, 2008] Ostoja-Starzewski M. (2008). *Microstructural Randomness and Scaling in Mechanics of Materials*. Mordern Mechanics and Mathematics. Chapman & Hall/CRC. 9

[Oumarou et al., 2011] Oumarou M., Jeulin D., and Renard J. (2011). *Etude statistique multi-échelle du comportement élastique et thermique d'un composite thermoplastique*. Revue des composites et des matériaux avancés, vol. 21, pp 221–254. 15

[Oxman and Oxman, 2010] Oxman R. and Oxman R. (2010). *New structuralism: design, engineering and architectural technologies*. Architectural Design, vol. 80 n° 4, pp 14–23. 107

[Park et al., 2013] Park B.-U., Seo Y.-D., Sigmund O., and Youn S.-K. (2013). *Shape optimization of the stokes flow problem based on isogeometric analysis*. Structural and Multidisciplinary Optimization, vol. 48 n° 5, pp 965–977. 70

[Parolin, 2006] Parolin P. (2006). *Ombrohydrochory: Rain-operated seed dispersal in plants–With special regard to jet-action dispersal in Aizoaceae*. Flora-Morphology, Distribution, Functional Ecology of Plants, vol. 201 n° 7, pp 511–518. 62

[Pegna, 1997] Pegna J. (1997). *Exploratory investigation of solid freeform construction*. Automation in Construction, vol. 5, pp 427–437. 101

[Pelissou et al., 2009] Pelissou C., Baccou J., Monerie Y., and Perales F. (2009). *Determination of the size of the representative volume element for random quasi-brittle composites*. International Journal of Solids and Structures, vol. 46, pp 2842–2855. 15, 16, 30

[Pellegrino and Calladine, 1986] Pellegrino S. and Calladine C. R. (1986). *Matrix analysis of statically and kinematically indeterminate frameworks*. International Journal of Solids and Structures, vol. 22 n° 4, pp 409–428. 59

[Peng et al., 2018] Peng X. L., Husser E., Huang G. Y., and Bargmann S. (2018). *Modeling of surface effects in crystalline materials within the framework of gradient crystal plasticity*. Journal of the Mechanics and Physics of Solids, vol. 112, pp 508–522. 9

[Peyre et al., 2015] Peyre P., Rouchausse Y., Defauchy D., and Régnier G. (2015). *Experimental and numerical analysis of the selective laser sintering (SLS) of PA12 and PEKK semi-crystalline polymers*. Journal of Materials Processing Technology, vol. 225, pp 326–336. 61

[Peyrega et al., 2011] Peyrega C., Jeulin D., Delisée C., and Malvestio J. (2011). *3D morphological characterization of phonic insulation fibrous media*. Advanced Engineering Materials, vol. 13 n° 3, pp 156–164. 9

[Phung et al., 2014] Phung N.L., Favier V., Ranc N., Vales F., and Mughrabi H. (2014). *Very high cycle fatigue of copper: Evolution, morphology and locations of surface slip markings*. International Journal of Fatigue, vol. 63, pp 68–77. 41

[Pierman et al., 2014] Pierman A. P., Bouaziz O., Pardoen T., Jacques P. J., and Brassart L. (2014). *The influence of microstructure and composition on the plastic behaviour of dual-phase steels*. Acta Materialia, vol. 73, pp 298–311. 77

[Piobert, 1842] Piobert G. (1842). *Mémorial de l'Artillerie*, vol. 5, chapter Expérience sur la pénétration des projectiles dans le fer forgé, pp 502–509. Bachelier. 66

[Piollet, 2014] Piollet E. (2014). *Amortissement non-linéaire des structures sandwichs à matériau d'âme en fibres enchevêtrées*. Thèse de Doctorat, ISAE, Toulouse. 43

[Piollet et al., 2013] Piollet E., Michon G., and Poquillon D. (2013). *Nonlinear vibration behavior of sandwich beams with entangled fiber core material*. In : ASME 2013 International Design Engineering Technical Conferences and Computers and Information in Engineering Conference, pp V008T13A013–V008T13A013. American Society of Mechanical Engineers. 43

[Piollet et al., 2016] Piollet E., Poquillon D., and Michon G. (2016). *Dynamic hysteresis modelling of entangled cross-linked fibres in shear*. Journal of Sound and Vibration, vol. 383, pp 248–264. 43

[Placidi et al., 2017] Placidi L., Barchiesi E., and Della Corte A. (2017). *Mathematical Modelling in Solid Mechanics*, vol. 69 of *Advanced Structured Materials*, chapter Identification of Two-Dimensional Pantographic Structures with a Linear D4 Orthotropic Second Gradient Elastic Model Accounting for External Bulk Double Forces, pp 211–232. Springer, Singapore. 45

[Placidi and El Dhaba, 2015] Placidi L. and El Dhaba A. R. (2015). *Semi-inverse method à la Saint-Venant for two-dimensional linear isotropic homogeneous second-gradient elasticity*. Mathematics and Mechanics of Solids, vol. 22 n° 5, pp 919–937. 45

[Poncelet et al., 2018] Poncelet M., Somera A., Morel C., Jailin C., and Auffray N. (2018). *An experimental evidence of the failure of Cauchy elasticity for the overall modeling of a non-centro-symmetric lattice under static loading*. International Journal of Solids and Structures, vol. 147, pp 223–237. 69

[Qian, 2010] Qian X. (2010). *Full analytical sensitivities in NURBS based isogeometric shape optimization*. Computer Methods in Applied Mechanics and Engineering, vol. 199 n° 29, pp 2059–2071. 70

[Qian and Sigmund, 2011] Qian X. and Sigmund O. (2011). *Isogeometric shape optimization of photonic crystals via Coons patches*. Computer Methods in Applied Mechanics and Engineering, vol. 200 n° 25, pp 2237–2255. 70

[Queheillalt et al., 2007] Queheillalt D., Deshpande V., and Wadley H. (2007). *Truss waviness effects in cellular lattice structures*. Journal of Mechanics of Materials and Structures, vol. 2 n° 9, pp 1657–1675. 58

[Quey et al., 2011] Quey R., Dawson P.R., and Barbe F. (2011). *Large-scale 3D random polycrystals for the finite element method: Generation, meshing and remeshing*. Computer Methods in Applied Mechanics and Engineering, vol. 200, pp 1729–1745. 31

[Rayneau-Kirkhope et al., 2012] Rayneau-Kirkhope D., Mao Y., and Farr R. (2012). *Ultralight Fractal Structures from Hollow Tubes*. Physical Review Letters, vol. 109, pp 204301. 47

[Ren et al., 2016] Ren X., Shen J., Ghaedizadeh A., Tian H., and Xie Y. M. (2016). *A simple auxetic tubular structure with tuneable mechanical properties*. Smart Materials and Structures, vol. 5 n° 6, pp 065012. 46

[Reuss, 1929] Reuss A. (1929). *Berechnung der Fließgrenze von Mischkristallen auf Grund der Plastizitätsbedingung für Einkristalle*. Zeitschrift für angewandte Mathematik und Mechanik, vol. 9 n° 1, pp 49–58. 54

[Rice, 1976] Rice J. R. (1976). *The localization of plastic deformation*. In : Proceedings of 14th International Conference Theoretical and Applied Mechanics, ed. Koiter W., pp 207–220, Delft, North–Holland, Amsterdam. 66

[Robert et al., 2012] Robert C., Saintier N., Palin-Luc T., and Morel F. (2012). *Micro-mechanical modelling of high cycle fatigue behaviour of metals under multiaxial loads*. Mechanics of Materials, vol. 55, pp 112–129. 29

[Rodney et al., 2016] Rodney D., Gadot B., Martinez O. R., Du Roscoat S. R., and Orgéas L. (2016). *Reversible dilatancy in entangled single-wire materials*. Nature Materials, vol. 15 n° 1, pp 72. 43

[Roland et al., 2016] Roland S., Miquelard-Garnier G., Gervais M., Guinault A., and Sollogoub C. (2016). *Controlling the order of triblock copolymer via confinement induced by forced self-assembly*. Materials Today Communications, vol. 6, pp 37–43. 16

[Rosi and Auffray, 2016] Rosi G. and Auffray N. (2016). *Anisotropic and dispersive wave propagation within strain-gradient framework*. Wave Motion, vol. 63, pp 120–134. 45, 69

[Rosi et al., 2018] Rosi G., Placidi L., and Auffray N. (2018). *On the validity range of strain-gradient elasticity: a mixed static-dynamic identification procedure*. European Journal of Mechanics A/Solids, vol. 69, pp 179–191. 69

[Rosi et al., 2017] Rosi G., Scala I., Nguyen V.H., and Naili S. (2017). *Wave propagation in strain gradient poroelastic medium with microinertia: closed-form and finite element solutions*. Zeitschrift für angewandte Mathematik und Physik, vol. 63 n° 3, pp 58. 69

[Roters et al., 2011] Roters F., Eisenlohr P., Bieler T. R., and Raabe D. (2011). *Crystal plasticity finite element methods: in materials science and engineering*. John Wiley & Sons. 29, 32

[Roudavski, 2009] Roudavski S. (2009). *Towards morphogenesis in architecture*. International Journal of Architectural Computing, vol. 7 n° 3, pp 345–374. 107

[Rougier et al., 1993] Rougier Y., Stolz C., and Zaoui A. (1993). *Représentation spectrale en viscoélasticité linéaire des matériaux hétérogènes*. Comptes Rendus de l'Académie des Sciences - Série II, vol. 316, pp 1517–1522. 34

[Rozvany, 2009] Rozvany G. I. N. (2009). *A critical review of established methods in structural topology optimization*. Structural and Multidisciplinary Optimization, vol. 37, pp 217–237. 84

[Rozvany et al., 1995] Rozvany G. I. N., Bendsøe M. P., and Kirsch U. (1995). *Layout optimization of structures*. Applied Mechanics Reviews, vol. 48 n° 2, pp 41–119. 83

[Rudnicki and Rice, 1975] Rudnicki J. W. and Rice J. R. (1975). *Conditions for the localization of deformation in pressure-sensitive dilatant materials*. Journal of the Mechanics and Physics of Solids, vol. 23 n° 6, pp 371–394. 66

[Sab, 1992] Sab K. (1992). *On the homogenization and the simulation of random materials*. European Journal of Mechanics, A/Solids, vol. 11 n° 5, pp 585–607. 10, 11, 33, 54

[Salmi et al., 2012a] Salmi M., Auslender F., Bornert M., and Fogli M. (2012a). *Apparent and effective mechanical properties of linear matrix-inclusion random composites: Improved bounds for the effective behavior*. International Journal of Solids and Structures, vol. 49, pp 1195–1211. 16, 54

[Salmi et al., 2012b] Salmi M., Auslender F., Bornert M., and Fogli M. (2012b). *Various estimates of Representative Volume Element sizes based on a statistical analysis of the apparent behavior of random linear composites*. Comptes-Rendus de l'Académie des Sciences - Serie IIb : Mécanique, vol. 340, pp 230–246. 16, 54

[Salonitis et al., 2017] Salonitis K., Chantzis D., and Kappatos V. (2017). *A hybrid finite element analysis and evolutionary computation method for the design of lightweight lattice components with optimized strut diameter*. The International Journal of Advanced Manufacturing Technology, vol. 90 n° 9-12, pp 2689–2701. 45

[Sanchez-Palencia and Zaoui, 1987] Sanchez-Palencia E. and Zaoui A. (1987). *Homogenization techniques for composite media*, vol. 272 of *Lecture Notes in Physics*. Springer-Verlag. 54

[Sarac et al., 2014] Sarac B., Wilmers J., and Bargmann S. (2014). *Property optimization of porous metallic glasses via structural design*. Materials Letters, vol. 134, pp 306–310. 43

[Schaare et al., 2009] Schaare S., Riehemann W., and Estrin Y. (2009). *Damping properties of an assembly of topologically interlocked cubes*. Materials Science & Engineering, A: Structural Materials: Properties, Microstructure and Processing, vol. 521-522, pp 380–383. 43

[Schaedler and Carter, 2016] Schaedler T. A. and Carter W. B. (2016). *Architected Cellular Materials*. Annual Review of Materials Research, vol. 46, pp 187–210. 44, 106

[Schaedler et al., 2011] Schaedler T. A., Jacobsen A. J., Torrents A., Sorensen A. E., Lian J., Greer J. R., Valdevit L., and Carter W. B. (2011). *Ultralight Metallic Microlattices*. Science, vol. 334 n° 6058, pp 962–965. 44, 58

[Schaedler et al., 2014] Schaedler T. A., Ro C. J., Sorensen A. E., Eckel Z., Yang S. S., Carter W. B., and Jacobsen A. J. (2014). *Designing metallic microlattices for energy absorber applications*. Advanced Engineering Materials, vol. 16 n° 3, pp 276–283. 61

[Schleicher et al., 2015] Schleicher S., Lienhard J., Poppinga S., Speck T., and Knippers J. (2015). *A methodology for transferring principles of plant movements to elastic systems in architecture*. Computer-Aided Design, vol. 60, pp 105–117. 107

[Shan et al., 2015] Shan S., Kang S. H., Raney J. R., Wang P., Fang L., Candido F., Lewis J. A., and Bertoldi K. (2015). *Multistable architected materials for trapping elastic strain energy*. Advanced Materials, vol. 27 n° 29, pp 4296–4301. 106

[Shaw and Kyriakides, 1997] Shaw J. A. and Kyriakides S. (1997). *On the nucleation and propagation of phase transformation fronts in a NiTi alloy*. Acta Materialia, vol. 45 n° 2, pp 683–700. 65

[Shea and Cagan, 1997] Shea K. and Cagan J. (1997). *Innovative dome design: Applying geodesic patterns with shape annealing*. Artificial Intelligence for Engineering Design, Analysis and Manufacturing, vol. 11 n° 5, pp 379–394. 107

[Shea and Cagan, 1999] Shea K. and Cagan J. (1999). *Languages and semantics of grammatical discrete structures*. Artificial Intelligence for Engineering Design, Analysis and Manufacturing, vol. 13 n° 4, pp 241–251. 107

[Shenoy et al., 2008] Shenoy M., Tjiptowidjojo Y., and McDowell D.L. (2008). *Microstructure-sensitive modeling of polycrystalline IN 100*. International Journal of Plasticity, vol. 24 n° 10, pp 1694–1730. 29, 30

[Shenoy et al., 2007] Shenoy M., Zhang J., and McDowell D.L. (2007). *Estimating fatigue sensitivity to polycrystalline Ni-base superalloy microstructures using a computational approach*. Fatigue and Fracture of Engineering Materials and Structures, vol. 30, pp 889–904. 29, 30

[Shim et al., 2013] Shim J., Shan S., Košmrlj A., Kang S. H., Chen E. R., Weaver J. C., and Bertoldi K. (2013). *Harnessing instabilities for design of soft reconfigurable auxetic/chiral materials*. Soft Matter, vol. 9 n° 34, pp 8198–8202. 47

[Shome and Tumuluru, 2015] Shome M. and Tumuluru M. (2015). *Welding and joining of advanced high strength steels*. Number 85 in Welding and Other Joining Technologies. Woodhead. 78, 79

[Sigmund, 2011] Sigmund O. (2011). *On the usefulness of non-gradient approaches in topology optimization*. Structural and Multidisciplinary Optimization, vol. 43, pp 589–596. 84

[Sittner et al., 2005] Sittner P., Liu Y., and Novák V. (2005). *On the origin of Lüders-like deformation of NiTi shape memory alloys*. Journal of the Mechanics and Physics of Solids, vol. 53 n° 8, pp 1719–1746. 66

[Smith and Torquato, 1988] Smith P. and Torquato S. (1988). *Computer simulation results for the two-point probability function of composite media*. Journal of Computational Physics, vol. 76 n° 1, pp 176–191. 9

[Song et al., 2018] Song J., Gao L., Cao K., Zhang H., Xu S., Jiang C., Surjadi J. U., Xu Y., and Lu Y. (2018). *Metal-coated hybrid meso-lattice composites and their mechanical characterizations*. Composite Structures, vol. 203, pp 750–763. 106

[Soyarslan et al., 2018] Soyarslan C., Bargmann S., Pradas M., and Weissmüller J. (2018). *3D stochastic bicontinuous microstructures: Generation, topology and elasticity*. Acta Materialia, vol. 149, pp 326–340. 9

[Speller et al., 2007] Speller T. H., Whitney D., and Crawley E. (2007). *Using shape grammar to derive cellular automata rule patterns*. Complex Systems, vol. 17 n° 1-2, pp 79–102. 107

[Stahovich et al., 1993] Stahovich T. F., Davis R., and Shrobe H. (1993). *An ontology of mechanical devices*. In : Proceedings of the 1993 AAAI National Conference on Artificial Intelligence. 107

[Stanzl-Tschegg et al., 2007] Stanzl-Tschegg S., Mughrabi H., and Schoenbauer B. (2007). *Life time and cyclic slip of copper in the VHCF regime*. International Journal of Fatigue, vol. 29, pp 2050–2059. 41

[Steen, 2003] Steen W. M. (2003). *Laser material processing—an overview*. Journal of Optics A: Pure and Applied Optics, vol. 5, pp S3–S7. 77

[Stiny and Gips, 1971] Stiny G. and Gips J. (1971). *Shape grammars and the generative specification of painting and sculpture*. In : IFIP Congress, vol. 2. 107

[Stiny and Mitchell, 1978] Stiny G. and Mitchell W. J. (1978). *The palladian grammar*. Environment and planning B: Planning and design, vol. 5 n° 1, pp 5–18. 107

[Stoychev et al., 2016] Stoychev G., Guiducci L., Turcaud S., Dunlop J. W. C., and Ionov L. (2016). *(2016). Hole-Programmed Superfast Multistep Folding of Hydrogel Bilayers*. Advanced Functional Materials, vol. 26 n° 42, pp 7733–7739. 47

[Suard et al., 2014] Suard M., Lhuissier P., Dendievel R., Blandin J.J., Vignat F., and Villeneuve F. (2014). *Towards stiffness prediction of cellular structures made by electron beam melting (EBM)*. Powder Metallurgy, vol. 57, pp 190–195. 61

[Suard et al., 2015] Suard M., Martin G., Lhuissier P., Dendievel R., Vignat F., Blandin J.J., and Villeneuve F. (2015). *Mechanical equivalent diameter of single struts for the stiffness prediction of lattice structures produced by Electron Beam Melting*. Additive Manufacturing, vol. 8, pp 124–131. 61

[Sun and Li, 2002] Sun Q. P. and Li Z. Q. (2002). *Phase transformation in superelastic NiTi polycrystalline micro-tubes under tension and torsion—from localization to homogeneous deformation*. International Journal of Solids and Structures, vol. 39 n° 13-14, pp 3797–3809. 66

[Sundar et al., 2003] Sundar VC, Yablon AD, Grazul JL, Ilan M, and Aizenberg J (2003). *Fibre-optical features of a glass sponge*. Nature, vol. 424 n° 6951, pp 899–900. 62

[Sweeney et al., 2015] Sweeney C.A., O'Brien B., Dunne F.P.E., McHugh P.E., and Leen S.B. (2015). *Micro-scale testing and micromechanical modelling for high cycle fatigue of CoCr stent material*. Journal of the Mechanical Behavior of Biomedical Materials, vol. 46, pp 244–260. 29, 30

[Teferra and Graham-Brady, 2018] Teferra K. and Graham-Brady L. (2018). *A random field-based method to estimate convergence of apparent properties in computational homogenization*. Computer Methods in Applied Mechanics and Engineering, vol. 330, pp 253–270. 30

[Teixeira-Pinto et al., 2016] Teixeira-Pinto J., Nadot-Martin C., Touchard F., Gueguen M., and Castagnet S. (2016). *Towards the size estimation of a Representative Elementary Domain in semi-crystalline polymers*. Mechanics of Materials, vol. 95, pp 116–124. 15

[Terada et al., 2000] Terada K., Hori M., Kyoya T., and Kikuchi N. (2000). *Simulation of the multi-scale convergence in computational homogenization approaches*. International Journal of Solids and Structures, vol. 37, pp 2285–2311. 10

[Theocaris et al., 1997] Theocaris P.S., Stavroulakis G.E., and Panagiotopoulos P.D. (1997). *Negative Poisson's ratios in composites with star-shaped inclusions: a numerical homogenization approach*. Archive of Applied Mechanics, vol. 67, pp 274–286. 70, 71, 72

[Tollar, 1966] Tollar J. (1966). *Interfacial surface generator*. 16

[Torabian et al., 2017a] Torabian N., Favier V., Dirrenberger J., Adamski F., Ziaei-Rad S., and Ranc N. (2017a). *Correlation of the high and very high cycle fatigue response of ferrite based steels with strain rate-temperature conditions*. Acta Materialia, vol. 134, pp 40–52. 41

[Torabian et al., 2016a] Torabian N., Favier V., Ziaei-Rad S., Adamski F., Dirrenberger J., and Ranc N. (2016a). *Self-Heating Measurements for a Dual-Phase Steel under Ultrasonic Fatigue Loading for stress amplitudes below the conventional fatigue limit*. Procedia Structural Integrity, vol. 2, pp 1191–1198. 41

[Torabian et al., 2016b] Torabian N., Favier V., Ziaei-Rad S., Dirrenberger J., Adamski F., and Ranc N. (2016b). *Thermal response of DP600 dual-phase steel under ultrasonic fatigue loading*. Materials Science & Engineering, A: Structural Materials: Properties, Microstructure and Processing, vol. 677, pp 97–105. 41

[Torabian et al., 2017b] Torabian N., Favier V., Ziaei-Rad S., Dirrenberger J., Adamski F., and Ranc N. (2017b). *Fatigue and Fracture Test Planning, Test Data Acquisitions and Analysis*, vol. STP1598, chapter Calorimetric Studies and Self-Heating Measurements for a Dual-Phase Steel Under Ultrasonic Fatigue Loading, pp 81–93. ASTM. 41

[Torquato, 1998] Torquato S. (1998). *Morphology and effective properties of disordered heterogeneous media*. International Journal of Solids and Structures, vol. 35 n° 19, pp 2385–2406. 9

[Torquato, 2001] Torquato S. (2001). *Random Heterogeneous Materials*. Springer. 9

[Toupin, 1962] Toupin R. A. (1962). *Elastic materials with couple-stresses*. Archive for Rational Mechanics and Analysis, vol. 11 n° 1, pp 385–414. 68

[Tovar et al., 2004] Tovar A., Niebur G. L., Sen M., Renaud J. E., and Sanders B. (2004). *Bone structure adaptation as a cellular automaton optimization process*. In : 45th AIAA/ASME/ASCE/AHS/ASC Structures, Structural Dynamics & Materials Conference, Palm Springs, California, 2004. 84

[Tovar et al., 2007] Tovar A., Patel N. M., Kaushik A. K., and Renaud J. E. (2007). *Optimality Conditions of the Hybrid Cellular Automata for Structural Optimization*. AIAA Journal, vol. 45 n° 3, pp 673–683. 84

[Tovar et al., 2006] Tovar A., Patel N. M., Niebur G. L., Sen M., and Rennaud J. E. (2006). *Topology Optimization Using a Hybrid Cellular Automaton Method With Local Control Rules*. Journal of Mechanical Design, vol. 128, pp 1205–1216. 84, 85

[Trinh et al., 2012] Trinh D. K., Jänicke R., Auffray N., Diebels S., and Forest S. (2012). *Evaluation of generalized continuum substitution models for heterogeneous materials*. International Journal of Multiscale Computational Engineering, vol. 10 n° 6, pp 527–549. 45, 46

[Tsay et al., 2004] Tsay L. W., Liu Y. C., Lin D. Y., and Young M. C. (2004). *The use of laser surface-annealed treatment to retard fatigue crack growth of austenitic stainless steel*. Materials Science & Engineering, A: Structural Materials: Properties, Microstructure and Processing, vol. 384, pp 177–183. 79

[Tsay and Yang, 2000] Tsay L. W. and Yang T. Y. (2000). *Reduction of hydrogen embrittlement in an ultra-high-strength steel by laser surface annealing*. Fatigue and Fracture of Engineering Materials and Structures, vol. 23 n° 4, pp 325–333. 79

[Tsui, 1999] Tsui E. (1999). *Evolutionary Architecture: Nature as a Basis for Design*. John Wiley, New York. 107

[Tsukahara and Iung, 1998] Tsukahara H. and Iung T. (1998). *Finite element simulation of the Piobert–Lüders behavior in an uniaxial tensile test*. Materials Science & Engineering, A: Structural Materials: Properties, Microstructure and Processing, vol. 248 n° 1-2, pp 304–308. 66

[Turcaud et al., 2011] Turcaud S., Guiducci L., Fratzl P., Dunlop J. W. C., and Bréchet Y. (2011). *An excursion into the design space of biomimetic architectured biphasic actuators*. International Journal of Materials Research, vol. 102 n° 6, pp 607–612. 47

[U.S. Geological Survey, 2016] U.S. Geological Survey (2016). *Mineral commodity summaries 2016*. U.S. Geological Survey. 99

[Vayssette et al., 2018] Vayssette B., Saintier N., Brugger C., Elmay M., and Pessard E. (2018). *Surface roughness of Ti-6Al-4V parts obtained by SLM and EBM: Effect on the High Cycle Fatigue life*. Procedia Engineering, vol. 213, pp 89–97. 61

[Velasco-Hogan et al., 2018] Velasco-Hogan A., Xu J., and Meyers M. A. (2018). *Additive Manufacturing as a Method to Design and Optimize Bioinspired Structures*. Advanced Materials, vol. Early View, pp 1800940. 107

[Vermaak et al., 2014] Vermaak N., Michailidis G., Parry G., Estevez R., Allaire G., and Bréchet Y. (2014). *Material interface effects on the topology optimizationof multi-phase structures using a level set method*. Structural and Multidisciplinary Optimization, vol. 50 n° 4, pp 623–644. 46

[Viard et al., 2018] Viard A. E., Dirrenberger J., and Forest S. (2018). *Propagating Instabilities in Architectured Materials*. In : 6th European Conference on Computational Mechanics (ECCM 6), 11-15 June 2018, Glasgow, UK. 66

[Vicente et al., 2016] Vicente W. M., Zuo Z. H., Pavanello R., Calixto T. K. L., Picelli R., and Xie Y. M. (2016). *Concurrent topology optimization for minimizing frequency responses of two-level hierarchical structures*. Computer Methods in Applied Mechanics and Engineering, vol. 301, pp 116–136. 45

[Vigliotti and Pasini, 2012] Vigliotti A. and Pasini D. (2012). *Stiffness and strength of tridimensional periodic lattices*. Computer Methods in Applied Mechanics and Engineering, vol. 229, pp 27–43. 58

[Vigliotti and Pasini, 2013] Vigliotti A. and Pasini D. (2013). *Mechanical properties of hierarchical lattices*. Mechanics of Materials, vol. 62, pp 32–43. 58

[Voigt, 1889] Voigt W. (1889). *Ueber die Beziehung zwischen den beiden Elasticitätsconstanten isotroper Körper*. Annalen der Physik und Chemie, vol. 38, pp 573–587. 54

[Wang et al., 2016] Wang B., Yang W., McKittrick J., and Meyers M. A. (2016). *Keratin: Structure, mechanical properties, occurrence in biological organisms, and efforts at bioinspiration*. Progress in Materials Science, vol. 76, pp 229–318. 62

[Wang and Zhang, 2012] Wang D. and Zhang W.-H. (2012). *A bispace parameterization method for shape optimization of thin-walled curved shell structures with openings*. International Journal for Numerical Methods in Engineering, vol. 90 n° 13, pp 1598–1617. 71

[Wang et al., 2014] Wang F., Sigmund O., and Jensen J. S. (2014). *Design of materials with prescribed nonlinear properties*. Journal of the Mechanics and Physics of Solids, vol. 69, pp 156–174. 71

[Wang et al., 2009] Wang H., Keum J., Hiltner A., and Baer E. (2009). *Confined crystallization of PEO in nanolayered films impacting structure and oxygen permeability*. Macromolecules, vol. 42 n° 18, pp 7055–7066. 16

[Wang et al., 2015] Wang H., Pietrasanta A., Jeulin D., Willot F., Faessel M., Sorbier L., and Moreaud M. (2015). *Modelling mesoporous alumina microstructure with 3D random models of platelets*. Journal of Microscopy, vol. 260 n° 3, pp 287–301. 23

[Wang et al., 2017a] Wang Y., Xu H., and Pasini D. (2017a). *Multiscale isogeometric topology optimization for lattice materials*. Computer Methods in Applied Mechanics and Engineering, vol. 316, pp 568–585. 46

[Wang et al., 2019] Wang Z.-P., Poh L.H., Zhu Y., Dirrenberger J., and Forest S. (2019). *Systematic design of tetra-petals auxetic structures with stiffness constraint*. 76

[Wang et al., 2017b] Wang Z. P., Poh L. H., Dirrenberger J., Zhu Y., and Forest S. (2017b). *Isogeometric shape optimization of smoothed petal auxetic structures via computational periodic homogenization*. Computer Methods in Applied Mechanics and Engineering, vol. 323, pp 250–271. 45, 70, 73

[Weaver et al., 2007] Weaver J.C., Aizenberg J., Fantner G. E., Kisailus D., Woesz A., Allen P., Fields K., Porter M. J., Zok F. W., Hansma P. K., Fratzl P., and Morse D. E. (2007). *Hierarchical assembly of the siliceous skeletal lattice of the hexactinellid sponge Euplectella aspergillum*. Journal of Structural Biology, vol. 158 n° 1, pp 93–106. 62

[Weaver et al., 2017] Weaver J. S., Kalidindi S. R., and Wegst U. G. (2017). *Structure-processing correlations and mechanical properties in freeze-cast Ti-6Al-4V with highly aligned porosity and a lightweight Ti-6Al-4V-PMMA composite with excellent energy absorption capability*. Acta Materialia, vol. 132, pp 182–192. 106

[Weaver and Ashby, 1996] Weaver P. M. and Ashby M. F. (1996). *The optimal selection of material and section-shape*. Journal of Engineering Design, vol. 7 n° 2, pp 129–150. 44, 62

[Wegst et al., 2015] Wegst U. G., Bai H., Saiz, E and Tomsia A. P., and Ritchie R. O. (2015). *Bioinspired structural materials*. Nature Materials, vol. 14 n° 1, pp 23. 61

[Wei et al., 2017] Wei K., Wang Z., and Zeng X. (2017). *Preliminary investigation on selective laser melting of Ti-5Al-2.5 Sn α-Ti alloy: From single tracks to bulk 3D components*. Journal of Materials Processing Technology, vol. 244, pp 73–85. 106

[Weinkamer and Fratzl, 2016] Weinkamer R. and Fratzl P. (2016). *Solving conflicting functional requirements by hierarchical structuring-–Examples from biological materials*. MRS Bulletin, vol. 41 n° 9, pp 667–671. 62

[Winsor and MacCallum, 1994] Winsor J. and MacCallum K. (1994). *A review of functionality modelling in design*. The Knowledge Engineering Review, vol. 9 n° 2, pp 163–199. 107

[Wolfram, 1984] Wolfram S. (1984). *Cellular automata as models of complexity*. Nature, vol. 311 n° 5985, pp 419. 107

[Wolfram, 2002] Wolfram S. (2002). *A new kind of science*. Wolfram Media, Champaign, IL. 107

[Xie et al., 2017] Xie R., Hu J., Guo X., Ng F., and Qin T. (2017). *Topographical control of preosteoblast culture by shape memory foams*. Advanced Engineering Materials, vol. 19 n° 1, pp 1600343. 107

[Xie and Steven, 1993] Xie Y. M. and Steven G. P. (1993). *A simple evolutionary procedure for structural optimization*. Computers & Structures, vol. 49, pp 885–896. 84

[Xu et al., 2016a] Xu B., Huang X., Zhou S. W., and Xie Y. M. (2016a). *Concurrent topological design of composite thermoelastic macrostructure and microstructure with multi-phase material for maximum stiffness*. Composite Structures, vol. 150, pp 84–102. 45

[Xu et al., 2016b] Xu S., Shen J., Zhou S., Huang X., and Xie Y. M. (2016b). *Design of lattice structures with controlled anisotropy*. Materials and Design, vol. 93, pp 443–447. 45

[Yang, 2018] Yang S. (2018). *Very High Cycle Fatigue of Pure Copper*. Thèse de Doctorat, Ecole nationale supérieure d'arts et métiers-ENSAM. 29

[Yang et al., 2019] Yang S., Dirrenberger J., Monteiro E., and Ranc N. (2019). *Representative volume element size determination for viscoplastic properties in polycrystalline materials*. International Journal of Solids and Structures, vol. 158, pp 210–219. 29, 31, 36

[Yao and Gao, 2006] Yao H. and Gao H. (2006). *Mechanics of robust and releasable adhesion in biology: Bottom-up designed hierarchical structures of gecko*. Journal of the Mechanics and Physics of Solids, vol. 54 n° 6, pp 1120–1146. 62

[Yeong and Torquato, 1998] Yeong C. L. Y. and Torquato S. (1998). *Reconstructing random media*. Physical Review E, vol. 57 n° 1, pp 495. 9

[Yoon et al., 2014] Yoon H. S., Lee J. Y., Kim H. S., Kim M. S., Kim E. S., Shin Y. J., Chu W. S., and Ahn S. H. (2014). *A comparison of energy consumption in bulk forming, subtractive, and additive processes: Review and case study*. International Journal of Precision Engineering and Manufacturing-Green Technology, vol. 1 n° 3, pp 261–279. 86

[Zakhama et al., 2009] Zakhama R., Abdalla M. M., Smaoui H., and Gürdal Z. (2009). *Multi-grid implementation of cellular automata for topology optimization of continuum structures*. Computer Modeling in Engineering and Sciences, vol. 51 n° 1, pp 1–24. 84

[Zeman and Šejnoha, 2007] Zeman J. and Šejnoha M. (2007). *From random microstructures to representative volume elements*. Modelling and Simulation in Materials Science and Engineering, vol. 15 n° 4, pp S325. 15

[Zhang et al., 2010] Zhang W. H., Wang D., and Yang J.-G. (2010). *A parametric mapping method for curve shape optimization on 3D panel structures*. International Journal for Numerical Methods in Engineering, vol. 84 n° 4, pp 485–504. 71

[Zhang et al., 2017] Zhang X. Y., Fang G., and Zhou J. (2017). *Additively manufactured scaffolds for bone tissue engineering and the prediction of their mechanical behavior: A review*. Materials, vol. 10 n° 1, pp 50. 61

[Zhou and Li, 2008] Zhou S. and Li Q. (2008). *Design of graded two-phase microstructures for tailored elasticity gradients*. Journal of Materials Science, vol. 43, pp 5157–5167. 83

[Zhu et al., 2016] Zhu Y., Bironeau A., Restagno F., Sollogoub C., and Miquelard-Garnier G. (2016). *Kinetics of thin polymer film rupture: model experiments for a better understanding of layer breakups in the multilayer coextrusion process*. Polymer, vol. 90, pp 156–164. 16

[Zhu et al., 2018] Zhu Y., Wang Z. P., and Poh L. H. (2018). *Auxetic hexachiral structures with wavy ligaments for large elasto-plastic deformation*. Smart Materials and Structures, vol. 27 n° 5, pp 055001. 76

[Zok et al., 2016] Zok F. W., Latture R. M., and Begley M. R. (2016). *Periodic truss structures*. Journal of the Mechanics and Physics of Solids, vol. 96, pp 184–203. 58

Justin DIRRENBERGER

Associate Professor at Cnam
PIMM Laboratory
Arts et Métiers-ParisTech/Cnam/CNRS UMR 8006
151, boulevard de l'Hôpital
75013 Paris, France
+33 144246101
justin.dirrenberger@lecnam.net

Expertise

- **Mechanics of materials**, additive manufacturing, architectured materials, modelling.

Professional Experience

- **Associate Professor**, Conservatoire National des Arts et Métiers, Paris, France (since Sep. 2013)
- **Co-founder & scientific advisor**, XtreeE, Paris, France (since Sep. 2015)
  Technological solutions for large-scale additive manufacturing.
- **Research Engineer**, Centre des Matériaux, MINES-ParisTech, Evry, France (Oct. 2009 – June 2013)
  Computational homogenisation of mechanical and thermal properties of architectured materials.
- **Research Engineer**, Carbon Services, Schlumberger Ltd., Clamart, France (Feb. – Aug. 2009)
  Study of Portland cement carbonation in the context of CO_2 sequestration.
- **Research Engineer**, EPFL, Lausanne, Switzerland (Mar. – Aug. 2008)
  Modeling of the particle size distribution effect on mechanical properties in cement paste.

Education

- **Ph.D.** in Materials Science & Engineering, **MINES-ParisTech**, Paris (2012)
  Supervised by Prof. S. Forest and Prof. D. Jeulin.
- **Diplôme d'ingénieur** in Materials Science & Engineering, **Polytech' Paris-Sud**, Orsay (2009)
- **M.Sc.** in Materials Science & Engineering, **Université Paris-Sud**, Saclay (2009)

Awards

- FEMS Communication Award for Excellence in MSE, 1st runner-up (Jul. 2018)
- Jean Rist medal from SF2M (Oct. 2017)
- French-Australia Science Innovation Collaboration (FASIC) grant (Dec. 2016)
- National Young Academic Researcher Grant (ANR JCJC) (2015 – 2020)
- Doctoral scholarship from MINES-ParisTech (Oct. 2009 – Dec. 2012)
- Research fellowship from EPFL, Lausanne, Switzerland (Mar. – Aug. 2008)

Scientific Output

- 16 articles in international peer-reviewed journals
- 5 papers in international peer-reviewed conference proceedings
- 8 scholarly book chapters, 1 patent
- 39 invited lectures out of 90+ oral communications, seminars, workshops, etc.

Representative Publications

- N. Torabian, V. Favier, **J. Dirrenberger**, F. Adamski, S. Ziaei-Rad, and N. Ranc. Correlation of the high and very high cycle fatigue response of ferrite based steels with strain rate-temperature conditions. *Acta Mater.*, vol. **134**, 2017, pp. 40-52
- R. Duballet, O. Baverel, and **J. Dirrenberger**. Classification of building systems for concrete 3D printing. *Automation in Construction*, vol. **83**, 2017, pp. 247-258

Scientific Responsabilities

- Supervision of 5 PhD candidates (2 defended, 3 on-going).
- Project leader for various funded projects : SCOLASTIC (250k€, ANR JCJC), ALMARIS (160k€, ANR PRCE), DEMOCRITE (150k€, Comue Hésam Université) et APHORISME (50k€, F2M-CNRS).
- Member of Mécamat (2010- elected board member since 2016), Euromech (2010-), and SF2M (2011- education committee member).

Scientific output

Justin DIRRENBERGER, Associate Professor, Cnam

January 7, 2019

A Refereed journal articles (17)

A17. M. De Angelo, M. Spagnuolo, F. D'Annibale, A. Pfaff, K. Hoschke, A. Misra, C. Dupuy, P. Peyre, **J. Dirrenberger**, and M. Pawlikowski. The macro behavior of pantographic sheets depends mainly on their microstructure. *Continuum Mechanics and Thermodynamics (under review)*

A16. E. Ernault, **J. Dirrenberger**, E. Richaud, and B. Fayolle. Prediction of stress induced by heterogeneous oxidation in epoxy/amine networks. *Polymer Degradation and Stability (revision)*

A15. Z.P. Wang, L.H. Poh, Y. Zhu, **J. Dirrenberger**, and S. Forest. Systematic design of tetra-petals auxetic structures with stiffness constraint. *Materials and Design (revision)*

A14. R. Duballet, O. Baverel, and **J. Dirrenberger**. Space truss masonry walls with robotic mortar extrusion. *Structures (in press)* http://doi.org/10.1016/j.istruc.2018.11.003

A13. R.A. Buswell, W.R. Leal de Silva, S.Z. Jones, and **J. Dirrenberger**. 3D printing using concrete extrusion: A roadmap for research. *Cement and Concrete Research*, volume **112**, 2018, pp. 37-49 http://doi.org/10.1016/j.cemconres.2018.05.006

A12. S. Yang, **J. Dirrenberger**, E. Monteiro, and N. Ranc. Representative volume element size determination for viscoplastic and dissipative properties in polycrystalline materials. *International Journal of Solids and Structures*, volume **158**, 2019, pp. 210-219 https://doi.org/10.1016/j.ijsolstr.2018.09.011

A11. R. Duballet, O. Baverel, and **J. Dirrenberger**. Classification of building systems for concrete 3D printing. *Automation in Construction*, volume **83**, 2017, pp. 247-258 http://doi.org/10.1016/j.autcon.2017.08.018

A10. N. Torabian, V. Favier, **J. Dirrenberger**, F. Adamski, S. Ziaei-Rad, and N. Ranc. Correlation of the high and very high cycle fatigue response of ferrite based steels with strain rate-temperature conditions. *Acta Materialia*, volume **134**, 2017, pp. 40-52 http://doi.org/10.1016/j.actamat.2017.05.064

A9. Z.P. Wang, L.H. Poh, **J. Dirrenberger**, S. Forest, and Y. Zhu. Isogeometric shape optimization of smoothed petal auxetic structures via computational periodic homogenization. *Computational Methods in Applied Mechanics and Engineering*, volume **323**, 2017, pp. 250-271 http://doi.org/10.1016/j.cma.2017.05.013

A8. N. Torabian, V. Favier, S. Ziaei-Rad, **J. Dirrenberger**, F. Adamski, and N. Ranc. Thermal Response of DP600 Dual-Phase Steel under Ultrasonic Fatigue Loading. *Materials Science and Engineering: A*, volume **677**, 2016, pp. 97-105 http://dx.doi.org/10.1016/j.msea.2016.09.025

A7. A. Bironeau, **J. Dirrenberger**, C. Sollogoub, G. Miquelard-Garnier and S. Roland. Evaluation of morphological representative sample sizes for nanolayered polymer blends. *Journal of Microscopy*, volume **264**(1), 2016, pp.48-58 http://dx.doi.org/10.1111/jmi.12415

A6. C. Gosselin, R. Duballet, Ph. Roux, N. Gaudillière, **J. Dirrenberger** and Ph. Morel. Large-Scale 3D Printing of Ultra-High Performance Concrete– A New Processing Route for Architects and Builders. *Materials & Design*, volume **100**, 2016, pp. 102-109 http://dx.doi.org/10.1016/j.matdes.2016.03.097

A5. N. Auffray, **J. Dirrenberger** and G. Rosi. A complete description of bi-dimensional anisotropic strain-gradient elasticity. *International Journal of Solids and Structures*, volume **69-70**, 2015, pp. 195-206 http://dx.doi.org/10.1016/j.ijsolstr.2015.04.036

A4. **J. Dirrenberger**, S. Forest and D. Jeulin. Towards gigantic RVE sizes for stochastic fibrous networks. *International Journal of Solids and Structures*, volume **51**(2), 2014, pp. 359-376 http://dx.doi.org/10.1016/j.ijsolstr.2013.10.011

A3. **J. Dirrenberger**, S. Forest and D. Jeulin. Effective elastic properties of auxetic microstructures: anisotropy and structural applications. *International Journal of Mechanics and Materials in Design*, volume **9**(1), 2013, pp. 21-33 http://dx.doi.org/10.1007/s10999-012-9192-8

A2. **J. Dirrenberger**, S. Forest and D. Jeulin. Elastoplasticity of auxetic materials. *Computational Materials Science*, volume **64**, 2012, pp. 57-61 http://dx.doi.org/10.1016/j.commatsci.2012.03.036

A1. **J. Dirrenberger**, S. Forest, D. Jeulin and C. Colin. Homogenization of periodic auxetic materials. *Procedia Engineering*, volume **10**, 2011, pp. 1852-1857 http://dx.doi.org/10.1016/j.proeng.2011.04.307

B Refereed conference proceedings (5)

R5. **J. Dirrenberger**. From Architectured Materials to the Development of Large-scale Additive Manufacturing. *SPOOL*, volume **4**(1), 2017, ISSN 2215-0900 https://doi.org/10.7480/spool.2017.1.1910

R4. N. Torabian, V. Favier, S. Ziaei-Rad, F. Adamski, **J. Dirrenberger** and N. Ranc. Self-Heating Measurements for a Dual-Phase Steel under Ultrasonic Fatigue Loading for Stress Amplitudes below the Conventional Fatigue Limit. *Procedia Structural Integrity*, volume **2**, 2016, pp. 1191-1198 http://dx.doi.org/10.1016/j.prostr.2016.06.152

R3. G. Rosi, N. Auffray and **J. Dirrenberger**. Wave propagation in the framework of strain gradient continua: the example of hexachiral materials. *22ème Congrès Français de Mécanique*, Lyon, France, August 2015 http://hdl.handle.net/2042/57379

R2. N. Gaudillière, **J. Dirrenberger**, O. Baverel and C. Sollogoub. Additive Manufacturing for the Development of an Assembling System for Gridshells. In *What's the Matter? Materiality and Materialism at the Age of Computation*, 2014, ed. M. Voyatzaki, pp. 195-210, ISBN: 978-960-89320-6-7

R1. **J. Dirrenberger**, S. Forest and D. Jeulin. Effective properties of auxetics made using selective laser melting. *Matériaux & Techniques*, volume **100**, S1, 2012, pp. 172-173

C Scholarly book chapters (7)

B7. N. Gaudillière, R. Duballet, C. Bouyssou, A. Mallet, Ph. Roux, M. Zakeri, and **J. Dirrenberger**. Building applications using lost formworks obtained through large-scale additive manufacturing of ultra-high performance concrete. In *3D Concrete Printing Technology*, eds. J. Sanjayan, et al., Elsevier, 2019, *(in press)*

B6. **J. Dirrenberger**, S. Forest and D. Jeulin. Computational homogenization of architectured materials. In *ArchiMats: Architectured Materials in Nature and Engineering*, 2019, eds. Y. Bréchet, R. Dendievel, J. Dunlop, Y. Estrin, P. Fratzl *(revision)*

B5. N. Gaudillière, R. Duballet, C. Bouyssou, A. Mallet, Ph. Roux, M. Zakeri, and **J. Dirrenberger**. Large-Scale Additive Manufacturing of Ultra-High-Performance Concrete of Integrated Formwork for Truss-Shaped Pillars. In *Robotic Fabrication in Architecture, Art and Design 2018*, eds. J. Willmann, P. Block, M. Hutter, K. Byrne, T. Schork. ROBARCH 2018. Springer, 2019, pp. 459–472 http://dx.doi.org/10.1007/978-3-319-92294-2_35

B4. **J. Dirrenberger**. From Architectured Materials to Large-Scale Additive Manufacturing. In *Robotic Building*, ed. H. Bier. Springer Series in Adaptive Environments, Springer International Publishing, 2018, pp. 79–96 http://dx.doi.org/10.1007/978-3-319-70866-9_4

B3. R. Duballet, O. Baverel, and **J. Dirrenberger**. Design of Space Truss Based Insulating Walls for Robotic Fabrication in Concrete. In *Humanizing Digital Reality*, eds. K. De Rycke, et al., Springer, Singapore, 2018, pp. 453–461 http://dx.doi.org/10.1007/978-981-10-6611-5_39

B2. N. Torabian, V. Favier, S. Ziaei-Rad, **J. Dirrenberger**, F. Adamski and N. Ranc. Calorimetric Studies and Self-Heating Measurements for a Dual-Phase Steel Under Ultrasonic Fatigue Loading. In *Fatigue and Fracture Test Planning, Test Data Acquisitions, and Analysis*, ASTM STP1598, Z. Wei, K. Nikbin, P. McKeighan, and G. Harlow, Eds., ASTM International, West Conshohocken, PA, 2017, pp. 81–93 `http://dx.doi.org/10.1520/STP159820160053`

B1. B. Lecampion, J. Vanzo, F.J. Ulm, B. Huet, C. Germay, I. Khalfallah and **J. Dirrenberger**. Evolution of Portland cement mechanical properties exposed to CO2-rich fluids: Experimental investigation at different scales. In *MPPS 2011, Symposium on Mechanics and Physics of Porous Solids : A tribute to Pr. Olivier Coussy, Marne-la-Vallée, 18-20 avril 2011*, 2011, 406p `http://hal.archives-ouvertes.fr/hal-00595113/`

D Patent (1)

P1. **J. Dirrenberger**, K. Mathis, and F. Masson. Amortisseur auxétique. Patent application n°17 58682, 19 September 2017. *patent pending*

E Refereed conference lectures (35)

C35. **J. Dirrenberger**, S. Yang, E. Monteiro, and N. Ranc. Representative volume element size determination for viscoplastic polycrystalline aggregates. *SES 2018 - 55th Annual Technical meeting*, Madrid, Spain, October 2018.

C34. **J. Dirrenberger**, F. Albertini, C. Sollogoub, and A. Molotnikov. Architectured hybrid auxetic lattice structures. *IUTAM Symposium on Architectured Materials Mechanics*, Chicago, IL, USA, September 2018.

C33. **J. Dirrenberger**. Large-scale additive manufacturing: Challenges and opportunities for innovation. *1st RILEM International Conference on Concrete and Digital Fabrication*, **Invited keynote lecture**, Zurich, Switzerland, September 2018.

C32. N. Gaudillière, R. Duballet, C. Bouyssou, A. Mallet, Ph. Roux, M. Zakeri, and **J. Dirrenberger**. Large-Scale Additive Manufacturing of Ultra-High-Performance Concrete of Integrated Formwork for Truss-Shaped Pillars. *ROB-ARCH 2018*, Zurich, Switzerland, September 2018.

C31. **J. Dirrenberger**. Bio-inspired hybrid architectured materials obtained through additive manufacturing. *Euromat Junior Conference, FEMS Communication Award for Excellence in MSE lecture*, **Invited lecture**, Budapest, Hungary, July 2018.

C30. **J. Dirrenberger**, S. Yang, E. Monteiro, and N. Ranc. Representative volume element size determination for viscoplastic polycrystalline materials. *10th European Solid Mechanics Conference*, Bologna, Italy, July 2018.

C29. **J. Dirrenberger**, F. Albertini, C. Sollogoub, and A. Molotnikov. Bio-inspired architectured hybrid lattice structures. *International workshop in honor of Dominique Jeulin, Physics and mechanics of random structures: from morphology to material properties*, **Invited lecture**, Oléron, France, June 2018.

C28. **J. Dirrenberger**, S. Yang, E. Monteiro, and N. Ranc. Representative volume element size determination for viscoplastic polycrystalline materials. *Engineering Mechanics Institute Conference 2018*, Cambridge, MA, USA, May 2018.

C27. **J. Dirrenberger**, S. Yang, E. Monteiro, and N. Ranc. Representative Volume Element Size for Viscoplastic Properties in Polycrystalline Copper. *16th European Mechanics of Materials Conference*, Nantes, France, March 2018.

C26. **J. Dirrenberger**. Large-scale additive manufacturing as a disruptive force in the construction industry. *1st Asia-Pacific International Conference on Additive Manufacturing*, **Invited lecture**, Melbourne, Australia, December 2017.

C25. **J. Dirrenberger**, Y. Qi, and A. Molotnikov. Preliminary results on the mechanical behavior of hybrid architectured lattice structures. *Journées annuelles de la SF2M*, **Jean Rist medal Invited keynote lecture**, Lyon, France, October 2017.

C24. E. Ernault, **J. Dirrenberger**, E. Richaud, and B. Fayolle. Embrittlement and stress-strain field induced by oxidation: case of epoxy amine networks. *32nd PDDG (Polymer Degradation Discussion Group) conference*, Taormina, Italy, September 2017.

C23. S. Yang, N. Ranc, E. Monteiro and **J. Dirrenberger**. Intrinsic dissipation process during very high cycle fatigue tests on pure Copper. *7th International Conference on Very High Cycle Fatigue*, Dresden, Germany, July 2017.

C22. **J. Dirrenberger**, Y. Qi, and A. Molotnikov. Bio-inspired architectured hybrid lattice structures. *5th International Conference on Material Modelling*, Rome, Italy, June 2017.

C21. Z.P. Wang, L.H. Poh, **J. Dirrenberger**, Y. Zhu, and S. Forest. Designing Smoothed Petal Auxetic Structures Using Isogeometric Shape Optimization. *5th International Conference on Material Modelling*, Rome, Italy, June 2017.

C20. E. Ernault, **J. Dirrenberger**, E. Richaud, and B. Fayolle. Simulation du comportement chemo-mécanique de réseaux époxy lors de leur oxydation hétérogène. *27th DEPOS (Déformation des Polymères Solides) conference*, Dourdan, France, March 2017.

C19. A. Bironeau, **J. Dirrenberger**, C. Sollogoub, G. Miquelard-Garnier and S. Roland. Evaluation of morphologically representative sample sizes for nanolayered polymer blends. *15th European Mechanics of Materials Conference*, Brussels, Belgium, September 2016.

C18. **J. Dirrenberger**. Representative Volume Element Size Determination for Viscoplastic Properties in Polycrystalline Aggregates. *10th Mechanics of Time-Dependent Materials Conference*, Paris, France, May 2016.

C17. **J. Dirrenberger**, S. Forest and D. Jeulin. Towards Gigantic RVE sizes for 3D stochastic fibrous networks. *1st European-Latin-American Conference of Theoretical and Applied Mechanics*, La Havane, Cuba, February 2016.

C16. N. Auffray, G. Rosi and **J. Dirrenberger**. Wave propagation in the framework of strain gradient continua. *French-German workshop on Extended continuum theories for the numerically efficient modeling of multi-scale phenomena*, Ruhr-Universität Bochum, Germany, September 2015.

C15. G. Rosi, N. Auffray and **J. Dirrenberger**. Wave propagation in the framework of strain gradient continua: the example of hexachiral materials. *22ème Congrès Français de Mécanique*, Lyon, France, August 2015.

C14. **J. Dirrenberger**, S. Forest and D. Jeulin. Towards Gigantic RVE sizes for 3D stochastic fibrous networks. *9th European Solid Mechanics Conference*, Leganés-Madrid, Spain, July 2015.

C13. G. Rosi, N. Auffray and **J. Dirrenberger**. Wave Propagation in Hexachiral Lattices Modeled as Strain Gradient Continua. *9th European Solid Mechanics Conference*, Leganés-Madrid, Spain, July 2015.

C12. **J. Dirrenberger**. Representative Volume Element Size for Viscoplastic Properties in Face-Centered Cubic Metals. *4th International Conference on Material Modeling*, Berkeley, California, May 2015.

C11. **J. Dirrenberger**. Mécanique des matériaux auxétiques. **Invited lecture**, *Mini-symposium « Mécanique des matériaux architecturés », 12ème Colloque National en Calcul de Structures*, Giens, France, May 2015.

C10. **J. Dirrenberger**, L. Callen, V. Favier and O. Castelnau. Computational Investigation of Micro-Macro Rate Sensitivity Equivalence in Polycrystalline Copper. *24th International Workshop on Computational Mechanics of Materials*, Madrid, Spain, October 2014.

C9. **J. Dirrenberger**. From Materials Engineering to the Computational Development of Architectured Materials. *What's the Matter- Materiality and Materialism at the Age of Computation*, **Invited keynote lecture**, Barcelona, Spain, September 2014.

C8. N. Gaudillière, **J. Dirrenberger**, O. Baverel and C. Sollogoub. Additive Manufacturing for the Development of an Assembling System for Gridshells. *What's the Matter? Materiality and Materialism at the Age of Computation*, Barcelona, Spain, September 2014.

C7. **J. Dirrenberger**, L. Callen, V. Favier and O. Castelnau. RVE size for viscoplastic properties in polycrystalline aggregates. *14th European Mechanics of Materials Conference*, Gothenburg, Sweden, August 2014.

C6. **J. Dirrenberger**, S. Forest and D. Jeulin. RVE size determination for 3D stochastic fibrous networks. *Journées Matériaux Numériques*, Loches, France, February 2013.

C5. **J. Dirrenberger**, S. Forest and D. Jeulin. Effective properties of auxetics made using selective laser melting. *Journées annuelles de la SF2M*, **Invited keynote lecture**, Paris, France, October 2012.

C4. **J. Dirrenberger**, S. Forest and D. Jeulin. Statistical determination of RVE sizes and effective properties for stochastic fibrous networks. *6th European Congress on Computational Methods in Applied Sciences and Engineering*, Vienna, Austria, September 2012.

C3. **J. Dirrenberger**, S. Forest and D. Jeulin. Modelling of auxetic materials with periodic microstructure. *8th European Solid Mechanics Conference*, Graz, Austria, July 2012.

C2. **J. Dirrenberger**, S. Forest and D. Jeulin. Elastoplasticity of auxetic materials. *21st International Workshop on Computational Mechanics of Materials*, Limerick, Ireland, August 2011.

C1. **J. Dirrenberger**, S. Forest, D. Jeulin and C. Colin. Homogenization of periodic auxetic materials. *11th International Conference on Mechanical Behaviour of Materials*, Como, Italy, June 2011.

F Invited lectures, seminars, workshops, etc. (54)

L54. **J. Dirrenberger**, S. Yang, E. Monteiro, and N. Ranc. Representative volume element size determination for viscoplastic polycrystalline materials. *DGM workshop on micromechanics*, Wuppertal, Germany, December 2018.

L53. **J. Dirrenberger**. Additive manufacturing for architecture materials. **Invited lecture** *Rencontres Franciliennes de Mécanique*, Dammarie-les-Lys, France, June 2018.

L52. R. Duballet, O. Baverel, and **J. Dirrenberger**. Large-scale additive manufacturing and architecture. **Invited lecture** *Rencontres Franciliennes de Mécanique*, Dammarie-les-Lys, France, June 2018.

L51. F. dell'Isola, M. Spagnuolo, C. Dupuy, P. Peyre, and **J. Dirrenberger**. Pantographic structures, an example of collaboration between France and Italy. *Réseau National de Connaissances*, **Invited lecture**, Paris, France, February 2018.

L50. **J. Dirrenberger**, S. Forest, D. Jeulin, F. Willot, and M. Faessel. Representative Volume Element Size Determination for Elasticity & Viscoplasticity. **Invited lecture** *Colloque Mécamat 2018*, Aussois, France, January 2018.

L49. **J. Dirrenberger**. From architectured materials to the development of large-scale additive manufacturing. **Invited lecture** *UPEM*, Marne-la-Vallée, France, December 2017.

L48. **J. Dirrenberger**. Hybrid architectured materials: an example of fruitful collaboration between France and Australia. *AFRAN Forum*, **Invited keynote lecture**, Canberra, Australia, December 2017.

L47. **J. Dirrenberger**. The future of architectured materials: Opportunities for innovation and international collaboration. *EDTAS Advanced Materials & Manufacturing*, **Invited keynote lecture**, Melbourne, Australia, November 2017.

L46. **J. Dirrenberger**, Y. Qi, and A. Molotnikov. Preliminary results on the mechanical behavior of bioinspired hybrid architectured lattice structures. *Réseau National de Connaissances*, **Invited lecture**, Angers, France, June 2017.

L45. **J. Dirrenberger**. XtreeE– the Large-Scale 3D-Printing company. *Ecole Nationale Supérieure d'Architecture de Paris-La Villette*, Paris, France, May 2017.

L44. **J. Dirrenberger**, S. Forest, D. Jeulin. Towards gigantic RVE sizes for 3D stochastic fibrous networks. *Monash University, Department of Materials Science*, Melbourne, Australia, December 2016.

L43. **J. Dirrenberger**. From architectured materials to the development of large-scale additive manufacturing. **Invited lecture** *TU Delft*, Delft, The Netherlands, November 2016.

L42. **J. Dirrenberger**. From architectured materials to the development of large-scale additive manufacturing. **Invited lecture** *ENS Paris-Saclay*, Cachan, France, November 2016.

L41. **J. Dirrenberger**, N. Auffray, M. Poncelet and G. Rosi. Approche holliste de la chiralité dans les métamatériaux architecturés. **Invited lecture** *Rencontres Franciliennes de Mécanique*, Dammarie-les-Lys, France, June 2016.

L40. **J. Dirrenberger**. Fabrication additive et grande échelle: le projet DEMOCRITE. **Invited lecture** *ENPC Alumni, Maison des Ponts*, Paris, France, May 2016.

L39. **J. Dirrenberger**. Architectured materials: A short overview. **Invited lecture** *National University of Singapore*, Singapore, April 2016.

L38. **J. Dirrenberger**. Modelling the behaviour of auxetic materials. *National University of Singapore*, Singapore, April 2016.

L37. **J. Dirrenberger**. Modelling the plastic behaviour of auxetic materials. **Invited lecture** *Centre National d'Études Spatiales*, Paris, France, March 2016.

L36. **J. Dirrenberger**. Matériaux, computation et architectures. **Invited lecture** *École Nationale Supérieure d'Architecture Paris-Malaquais*, Paris, France, February 2016.

L35. **J. Dirrenberger**. Modelling the plastic behaviour of auxetic materials. **Invited lecture** *Unité de Mécanique, ENSTA-ParisTech*, Palaiseau, France, February 2016.

L34. **J. Dirrenberger**. Towards gigantic RVE sizes for 3D stochastic fibrous networks. **Invited lecture** *Laboratoire de Mathématique Nicolas Oresme, Université de Caen Basse-Normandie*, Caen, France, December 2015.

L33. A. Bironeau, **J. Dirrenberger**, C. Sollogoub, G. Miquelard-Garnier, S. Roland. Evaluation of morphologically representative sample sizes for nanolayered polymer blends. **Invited lecture** *Centre for Molecular and Macromolecular Studies, Polish Academy of Sciences*, Łódź, Poland, November 2015.

L32. **J. Dirrenberger**. Matériaux pour la construction durable. **Invited lecture**, *Séminaire du DPEA Architecture post-carbone, Ecole d'Architecture de la Ville et des Territoires*, Marne-la-Vallée, France, October 2015.

L31. **J. Dirrenberger**. Projet DEMOCRITE : Démonstrateur technologique pour une fabrication additive à grande échelle. **Invited lecture**, Salon *3D Print*, Lyon, France, September 2015.

L30. **J. Dirrenberger**. Possibilities offered by 3D printing for the development of architectured and metamaterials. **Invited lecture**, *International Workshop on Metamaterials*, Marne-la-Vallée, France, April 2015.

L29. **J. Dirrenberger**. Computation, robotique et impression 3D en ingénierie des matériaux. **Invited lecture**, *Ecole Supérieure des Beaux-Arts Tours Angers Le Mans*, Le Mans, France, April 2015.

L28. **J. Dirrenberger**, S. Forest, D. Jeulin. Towards gigantic RVE sizes for 3D stochastic fibrous networks. *Séminaire du laboratoire MSME à l'Université Paris-Est*, Marne-la-Vallée, France, January 2015.

L27. **J. Dirrenberger**, G. Miquelard-Garnier, C. Sollogoub, S. Roland, P. Peyre, T. Gu, O. Castelnau, A. Guinault, G. Regnier. From nano- to macroscale applications: multiple processing routes for architectured materials. *Architectured Biomaterials, Medical and Tissue Engineering Symposium*, Berlin, Germany, December 2014.

L26. **J. Dirrenberger**. From Materials Engineering to the Computational Development of Architectured Materials. **Invited lecture**, *Hyperbody Media Studies Lectures, TU Delft*, Delft, Netherlands, November 2014.

L25. **J. Dirrenberger**. Matériaux pour la construction durable. **Invited lecture**, *Séminaire du DPEA Architecture post-carbone, Ecole d'Architecture de la Ville et des Territoires*, Marne-la-Vallée, France, November 2014.

L24. **J. Dirrenberger**. Matériaux architecturés par fabrication additive. *Séminaire de l'institut Carnot ARTS, ENSAM*, Paris, France, May 2014.

L23. **J. Dirrenberger**. L'impression 3D, un rendez-vous manqué ? **Invited lecture**, *Séminaire "Société de la connaissance et innovation", Master Affaires Publiques, SciencesPo*, Paris, France, April 2014.

L22. **J. Dirrenberger**. Towards gigantic RVE sizes for 3D stochastic fibrous networks. *Séminaire du laboratoire PIMM à l'École Nationale Supérieure d'Arts et Métiers*, Paris, France, March 2014.

L21. **J. Dirrenberger**. Introduction to architectured materials. **Invited lecture**, *Composite Chair Workshop, AA[n+1]Lab*, Paris, France, March 2014.

L20. **J. Dirrenberger**. Matériaux et construction durable. **Invited lecture**, *Séminaire du DPEA Architecture post-carbone, Ecole d'Architecture de la Ville et des Territoires*, Marne-la-Vallée, France, November 2013.

L19. **J. Dirrenberger**. Towards gigantic RVE sizes for 3D stochastic fibrous networks. *Journées "Problématiques multi-échelles dans les milieux fibreux" du GDR 3MF-Mécanique Multi-échelles des Milieux Fibreux*, Grenoble, France, June 2013.

L18. **J. Dirrenberger**. Towards gigantic RVE sizes for 3D stochastic fibrous networks. **Invited lecture**, *Institut Jean Le Rond d'Alembert, Université Pierre et Marie Curie*, Paris, France, May 2013.

L17. **J. Dirrenberger**. Introduction to architectured materials. **Invited lecture**, *RFR Group*, Paris, France, March 2013.

L16. **J. Dirrenberger**, S. Forest and D. Jeulin. Effective thermal properties of 3D stochastic fibrous networks. *Workshop on Architectured Materials at Collège de France*, Paris, France, February 2013.

L15. **J. Dirrenberger**. Introduction to architectured materials. **Invited lecture**, *The Bartlett School of Architecture, University College London*, London, UK, February 2013.

L14. **J. Dirrenberger**, S. Forest and D. Jeulin. RVE size determination for 3D stochastic fibrous networks. *Colloquium at Université Paris-Est*, Marne-la-Vallée, France, January 2013.

L13. **J. Dirrenberger**, S. Forest and D. Jeulin. Effective Properties of Architectured Materials: Periodic Auxetics and Stochastic Networks of Infinite Fibres. *Seminar at Centre des Matériaux, MINES-ParisTech*, Evry, France, June 2012.

L12. **J. Dirrenberger**, S. Forest and D. Jeulin. Homogenization methods for architectured materials. *Roundtable on architectured materials, MINES-ParisTech*, Paris, France, May 2012.

L11. **J. Dirrenberger**. Introduction to architectured materials. *Roundtable on architectured materials, MINES-ParisTech*, Paris, France, May 2012.

L10. **J. Dirrenberger**, S. Forest, D. Jeulin, M. Faessel and F. Willot. Etude de la taille du VER pour l'homogénéisation de milieux fibreux poissoniens. *Séminaire du département Mécanique et Matériaux, MINES-ParisTech*, Paris, France, Feb. 2012.

L9. **J. Dirrenberger**, S. Forest, D. Jeulin, M. Faessel and F. Willot. Effective properties of architectured materials. *Séminaire du groupe Comportement et Calcul de Structures, Centre des Matériaux, MINES-ParisTech*, Evry, France, Nov. 2011.

L8. **J. Dirrenberger**, S. Forest, D. Jeulin, C. Colin, J.-D. Bartout, M. Faessel and F. Willot. Effective properties of architectured materials. *ArchiMat 2011, 1st International School on Architectured Materials*, Autrans, France, May 2011.

L7. **J. Dirrenberger**, S. Forest, D. Jeulin, M. Faessel and F. Willot. Modélisation de milieux fibreux aléatoires enchevêtrés et estimation de VER. *Journées thématiques MECAMAT*, Sophia-Antipolis, France, May 2011.

L6. **J. Dirrenberger**, S. Forest, D. Jeulin, C. Colin, J.-D. Bartout and M. Faessel. Propriétés effectives des matériaux architecturés. *Colloque Mécamat 2011*, Aussois, France, Jan. 2011.

L5. **J. Dirrenberger** and S. Forest. Homogénéisation numérique de microstructures périodiques avec Zébulon/Z-Set. *Club Zébulon*, Evry, France, Dec. 2010.

L4. **J. Dirrenberger**, S. Forest and D. Jeulin. Propriétés effectives des matériaux architecturés : cas périodique et cas aléatoire. *École thématique CE2M10 "Changement d'échelles en mécanique des matériaux"*, Briançon, France, Aug. 2010.

L3. **J. Dirrenberger**, S. Forest, D. Jeulin and C. Colin. Propriétés mécaniques effectives des matériaux architecturés par simulation numérique massive et prototypage rapide. *Journées annuelles de la SF2M*, Paris, France, June 2010.

L2. **J. Dirrenberger**, S. Forest, F. N'Guyen and D. Jeulin. Modélisation de microstructures aléatoires et notion de volume élémentaire représentatif. *Colloque Mécamat 2010*, Aussois, France, Jan. 2010.

L1. **J. Dirrenberger**, K. Scrivener, S. Bishnoi and A. Guidoum. Effects of Particle Size Distribution on Mechanical Properties of Cement Paste at Early Age. *Junior EUROMAT 2008*, Lausanne, Switzerland, July 2008.

G Doctoral courses (2)

D2. **J. Dirrenberger**. Introduction to computational homogenization for fibrous media. *Models of Generalized Continua characterized by Quasi-Inextensible Fibrous Structures*, **Invited lecture**, Arpino, Italy, Septembre 2016.

D1. **J. Dirrenberger**, S. Forest, D. Jeulin. Towards gigantic RVE sizes for 3D stochastic fibrous networks. *Models of Generalized Continua characterized by Quasi-Inextensible Fibrous Structures*, **Invited lecture**, Arpino, Italy, Septembre 2016.

H Technical reports (5)

T5. **J. Dirrenberger**. Architectured material concepts for launcher-satellite damping connection. *CNES*, Paris, France, 2017.

T4. **J. Dirrenberger**. Effective properties of architectured materials. PhD thesis, *MINES-ParisTech*, Paris, France, 2012. `http://pastel.archives-ouvertes.fr/pastel-00797363/fr/`

T3. **J. Dirrenberger** and S. Forest. Simulation et homogénéisation de microstructures périodiques. *Centre des Matériaux, MINES-ParisTech*, Evry, France, 2010.

T2. **J. Dirrenberger**. Durable Oil-Well Cement for Safe and Reliable CO_2 Storage. MSc thesis, *Université Paris-Sud XI*, Orsay, France, 2009.

T1. **J. Dirrenberger** and I. Khalfallah. Physico-chemical investigation of the carbonation reaction in oil-well cements for CO_2 storage application. Technical report, *Schlumberger Ltd.*, Clamart, France, 2009.

Résumé des activités d'enseignement, de recherche et de responsabilités académiques

Justin DIRRENBERGER, MCF au CNAM

18 septembre 2018

A Activités pédagogiques

Depuis septembre 2013, j'ai rejoint l'équipe pédagogique "Matériaux industriels" du Conservatoire National des Arts et Métiers à Paris en tant que maître de conférences avec un service d'enseignement de 192 heures équivalent TD (HED). Le CNAM ayant une mission de formation tout au long de la vie, j'ai l'occasion d'enseigner à des publics très variés en termes d'âge et de niveau. Ainsi, mon service est réparti de la sorte : 25% en cours du soir (après 18h) et du samedi, 25% en formation continue et 50% en formation d'ingénieurs par alternance. J'ai initié et dirige pour l'année 2016 un stage de formation continue en fabrication additive dans le cadre des formations CACEMI, en partenariat avec le CNRS, ainsi qu'une formation d'ingénieurs par apprentissage, spécialité matériaux, habilitée par la CTI, qui démarre en septembre 2018. Par ailleurs, je suis responsable des unités d'enseignement (UE) en mécanique des matériaux et des structures, matériaux composites, sélection des matériaux et des procédés, et technologie avancée des matériaux. À titre d'exemple, j'ai pu revoir en profondeur l'UE de matériaux composites, en y incorporant notamment des études de cas, des travaux pratiques (mise en œuvre, caractérisation mécanique et méthodes numériques) et des projets de recherche bibliographique.. Enfin, je suis responsable à l'échelle nationale de la licence en science et génie des matériaux du Cnam. À l'Ensam Paris, j'ai développé une unité d'enseignement d'expertise (spécialisation de 3ème année), co-habilitée par le département Digital Knowledge de l'École d'Architecture de Paris-Malaquais. Cette formation, qui fut la première en France dans une école d'ingénieurs à porter sur la fabrication additive et ses domaines connexes (matériaux, conception, mécanique, robotique), a remporté un franc succès et forme aujourd'hui environ 60 étudiants par an. Ceci est un exemple parmi d'autres témoignant de ma capacité à innover en tant qu'enseignant en initiant ou en faisant évoluer des contenus pédagogiques. Par ailleurs, j'ai eu l'opportunité d'enseigner dans d'autres institutions, notamment l'École des Ponts (Introduction à la fabrication additive), à l'École des mines des Paris (Homogénéisation numérique), en écoles d'architecture (Sélection des matériaux, introduction à la science des matériaux), ou encore à SciencesPo Paris (séminaire sur la fabrication additive). Vous trouverez ci-dessous le détail de ma charge d'enseignement sur les 3 dernières années universitaires.

Année 2017/2018

Conservatoire National des Arts et Métiers (**271 HED**)
- Responsabilité nationale du diplôme de Licence en Science et Génie des Matériaux du CNAM (10 HED)
- MTX103 - Matériaux : notions fondamentales (20 HED)
- MTX104 - Composites hautes performances (69 HED)
- MTX231 - Technologie avancée des matériaux (34 HED)
- MMC116 - Travaux pratiques en métallurgie (8 HED)
- EICNAM - FIP Aéronautique - Matériaux métalliques pour l'aéronautique (33 HED)
- CACEMI - Formation continue - Stage d'initiation à la fabrication additive (24 HED)
- Tutorat d'apprentis ingénieurs (64 HED)
- Responsabilités administratives (9 HED).

Autres institutions (**19 HED**)
- Arts et Métiers-ParisTech : Cours sur la mécanique des composites, en Master MAGIS (3 HED).
- MINES-ParisTech : Cours d'homogénéisation (8 HED).
- Ponts-ParisTech : Cours de matériaux et introduction à la fabrication additive (8 HED).

Année 2016/2017

Conservatoire National des Arts et Métiers (**198 HED**)
— Responsabilité nationale du diplôme de Licence en Science et Génie des Matériaux du CNAM (10 HED)
— MTX103 - Matériaux : notions fondamentales (15 HED)
— MTX104 - Composites hautes performances (64 HED)
— EICNAM - FIP Aéronautique - Matériaux métalliques pour l'aéronautique (30 HED)
— CACEMI - Formation continue - Stage d'initiation à la fabrication additive (25 HED)
— Tutorat d'apprentis ingénieurs (48 HED)
— Responsabilités administratives (6 HED).

Autres institutions (**34 HED**)
— Arts et Métiers-ParisTech : Cours sur la mécanique des composites, en Master MAGIS (3 HED).
— Ecole d'Architecture de la Ville et des Territoires : Cours sur la sélection des matériaux et la construction durable (3 HED).
— MINES-ParisTech : Cours d'homogénéisation (8 HED).
— Ponts-ParisTech : Cours de matériaux et introduction à la fabrication additive (20 HED).

Année 2015/2016

Conservatoire National des Arts et Métiers (**216 HED**)
— Responsabilité nationale du diplôme de Licence en Science et Génie des Matériaux du CNAM (10 HED)
— MTX103 - Matériaux : notions fondamentales (20 HED)
— MTX104 - Composites hautes performances (64 HED)
— MTX231 - Technologie avancée des matériaux (24 HED)
— MMC114 - Comportement mécanique et intégrité des structures (16 HED)
— EICNAM - FIP Aéronautique - Matériaux métalliques pour l'aéronautique (30 HED)
— CACEMI - Formation continue - Stage d'initiation à la fabrication additive (16 HED)
— Tutorat d'apprentis ingénieurs (32 HED)
— Responsabilités administratives (4 HED).

Autres institutions (**37 HED**)
— Arts et Métiers-ParisTech : Unité d'Enseignement en fabrication additive et matériaux (20 HED).
— Arts et Métiers-ParisTech : Cours sur la mécanique des composites, en Master MAGIS (3 HED).
— Ecole d'Architecture de Paris-Malaquais : Cours sur les matériaux architecturés (3 HED).
— Ecole d'Architecture de la Ville et des Territoires : Cours sur la sélection des matériaux et la construction durable (3 HED).
— MINES-ParisTech : Cours d'homogénéisation (8 HED).

B Activités de recherche

Ma thématique de recherche porte initialement sur la mécanique des matériaux hétérogènes et plus spécifiquement la mécanique des matériaux architecturés, sujet que j'ai abordé dès 2009 au cours de ma thèse avec Samuel Forest et Dominique Jeulin à l'École des Mines de Paris. Depuis 2013, je suis membre du laboratoire PIMM (Procédés et Ingénierie en Mécanique et Matériaux), UMR Arts et Métiers-ParisTech/CNAM/CNRS, ce qui m'a permis d'enrichir mon champ de recherche à travers des collaborations internes, mais aussi à l'échelle régionale, nationale et internationale. Les différents projets et collaborations peuvent être regroupés ci-dessous de façon thématique, selon les axes de recherche suivants :
— Matériaux architecturés, métamatériaux, auxétiques, matériaux cellulaires
— Fabrication additive, procédés innovants, microstructure induite
— Optimisation topologique, morphologie structurale, géométrie
— Mécanique non-linéaire, fatigue, durabilité des matériaux et des structures
— Calcul de microstructures, homogénéisation numérique, milieux aléatoires

Projet APHORISME Le projet APHORISME (Approche holiste de la chiralité dans les métamatériaux architecturés) est financé à hauteur de 50 k€ par le CNRS et l'ENSAM, via la Fédération Francilienne de Mécanique- Matériaux, Structures et Procédés et son AAP Coup de pouce 2014. Ce projet commun entre 3 laboratoires (PIMM, LMT-Cachan et MSME) a pour objectif de développer une campagne expérimentale originale visant à mettre en

évidence les effets de la chiralité dans les matériaux architecturés, dont le comportement mécanique ne peut être décrit par l'élasticité classique de Cauchy. Le but est donc de discriminer expérimentalement les différentes descriptions disponibles en termes de milieux continus généralisés dans le cas des matériaux auxétiques à symétrie rotationnelle d'ordre 6. Ce projet s'inscrit dans une thématique de recherche qui met en effervescence la communauté scientifique internationale depuis quelques années : les métamatériaux. Initialement restreints au champ des matériaux fonctionnels, les métamatériaux mécaniques présentent un enjeu majeur tant du point de vue fondamental qu'applicatif. En dynamique, certaines architectures internes peuvent générer des matériaux invisibles acoustiquement. Ces thématiques vont tendre à se développer au cours des prochaines années, et ce projet permet de créer un noyau dur géographiquement cohérent sur le sujet, tant sur les aspects théoriques (MSME), expérimentaux (LMT) que numériques (PIMM). Decembre 2014-Decembre 2016.

Projet DEMOCRITE J'ai eu le privilège de porter le projet DEMOCRITE (Démonstrateur technologique pour une fabrication additive à grande échelle), financé à hauteur de 150k euros par l'IDEX Paris Nouveaux Mondes, via la ComUE Hésam Université et son AAP Synergie 2014. Ce projet, rassemblant 5 partenaires (CNAM, ENSAM, ENSCI-Les Ateliers, INRIA Sophia-Antipolis et ENSA Paris-Malaquais), vise, par une approche rationnelle et transdisciplinaire, à développer un démonstrateur technologique pour la fabrication additive à grande échelle, basée sur l'utilisation de matériaux énergétiquement sobres. Le projet DEMOCRITE vise à concilier les exigences de l'impression 3D de bureau et de la fabrication additive industrielle (i.e. flexibilité et coût réduit d'un côté, hautes performances mécaniques, prédictibilité et précision de l'autre), tout en développant un démonstrateur technologique de grande taille, permettant de produire des éléments de structures architecturales de forme complexe à l'échelle 1 :1. Les recherches ont principalement été menées, en collaboration entre le laboratoire PIMM et le département Digital Knowledge de l'ENSA Paris-Malaquais, sur la faisabilité technique de la fabrication additive avec un volume de travail de l'ordre du mètre cube.

Plusieurs voies ont été explorées en termes de matériaux : argiles, bétons haute performance grâce à un partenariat avec LafargeHolcim. Ces choix nous ont permis de produire des démonstrateurs à l'échelle 1 :1 dans le cadre de projets d'élèves-architectes, qui ont donné lieu d'une part à une production scientifique, et d'autre part à un intérêt de la part du monde industriel, très intéressé par la technologie développée. La plateforme développée dans le projet DEMOCRITE aura ainsi rempli ses 3 fonctions annoncées dans le projet initial : substrat pour la recherche, outil pédagogique, vitrine technologique. Le projet a donné lieu à la création en décembre 2015 d'une start-up développant la fabrication additive grande échelle : XtreeE. Financement PNM-14-SYNG-0002. Octobre 2014-Juin 2016.

En septembre 2018, l'entreprise a bientôt trois années d'existence en réalisant un chiffre d'affaire de 276k€ sur l'exercice 2016, et 491k€ en 2017. L'activité générée a créé 8 emplois au sein d'XtreeE dans le domaine de l'ingénierie et de la conception. L'entreprise a levé avec succès 1,1 million d'euros en janvier 2017 et 1 million d'euros en juin 2018 pour assurer son développement.

Collaboration avec Monash University J'ai récemment initié une collaboration avec Andrey Molotnikov et son équipe à Monash University, située à Melbourne en Australie, qui se trouve être une des meilleures universités de recherche australiennes, notamment sur la fabrication additive et les matériaux architecturés multifonctionnels. Andrey Molotnikov a été professeur invité au laboratoire PIMM sur mon invitation pendant le mois de décembre 2015. Parmi les projets de recherche que nous développons ensemble, celui portant sur le développement de nouveaux matériaux multi-architecturés par coextrusion et fabrication additive, en collaboration avec des collègues du PIMM, est particulièrement important. Selon le cahier des charges visé, des "smart pellets" ou du jonc architecturé sont produits par coextrusion multi-nanocouches, afin d'être utilisés en fabrication additive de type FDM ou en extrusion à grande échelle, permettant ainsi une architecturation à plusieurs échelles, ou hiérarchique : motif nanométrique, diamètre du granulé ou du filament et longueur caractéristique du matériau architecturé. Les applications visées sont multiples : matériaux cellulaires à rigidité optimisée, propriétés antagonistes rigidité/conductivité, treillis à dissipation viscoélastique. Le projet a fait l'objet d'un financement initial du PHC FASIC qui m'a permis de travailler 15 jours à Monash en Décembre 2016 (bourse de l'ambassade de France en Australie). Septembre 2016-Septembre 2018.

Thèse de Romain Duballet / Collaboration avec Navier et LafargeHolcim Dans le cadre de la chaire industrielle LafargeHolcim "Science des Matériaux pour la Construction Durable" aux Ponts et Chaussées, et en réponse au projet DEMOCRITE, la thèse de Romain Duballet a démarré en octobre 2015, sous ma direction et celle d'Olivier Baverel, équipe MSA (Matériaux et Structures Architecturés) de l'UMR Navier aux Ponts. Cette thèse porte sur

les potentialités offertes en architecture par la fabrication additive à grande échelle de structures hiérarchiques optimisées en béton ultra-haute performance et en assemblages multi-matériaux. Romain développe des outils d'optimisation topologique prenant en compte l'échelle du matériau jusqu'à la morphologie structurale du bâti, incluant les contraintes constructives propres à la fabrication additive, en accord avec un discours architectural innovant visant à générer de la fonction par une géométrie ingénieuse, comme pour les matériaux architecturés, mais en explorant d'autres échelles ici. Ce projet m'a permis de tisser des liens privilégiés avec Navier. Octobre 2015-Mars 2019.

Projet SCOLASTIC / Collaboration avec ArcelorMittal Le projet SCOLASTIC consiste à développer des matériaux métalliques architecturés innovants par une approche systématique de type materials-by-design, basée sur la génération et l'optimisation de motifs déterministes d'architecturation. Chaque motif est utilisé pour un traitement laser correspondant à un cahier des charges unique. Le cas des aciers dual-phase est considéré ici, dans le but de contrôler, par architecturation, l'anisotropie plastique, la localisation des déformations pour une meilleure formabilité, ainsi que l'émoussement de fissures et l'amélioration de la durée de vie en fatigue, en comparaison au matériau non-traité. Pour cela, un cadre numérique nécessaire à l'obtention des motifs optimisés, ainsi qu'un dispositif expérimental de traitement laser, sont développés. Les échantillons obtenus sont caractérisés, afin d'alimenter la modélisation multi-échelles des matériaux architecturés et de permettre ainsi à l'approche proposée d'acquérir un caractère prédictif. Ce projet ANR JCJC a été financé lors de la campagne 2016 à hauteur de 250k€. ArcelorMittal est partenaire du projet, car la technologie développée semble prometteuse pour l'emboutissage des tôles aciers à très haute limite d'élasticité. Financement ANR-16-CE08-0009. Janvier 2017-Décembre 2021.

Post-doc de Zhenpei Wang / Collaboration NUS et MINES-ParisTech Dans le cadre d'une collaboration internationale initiée en 2015 par le professeur Leong Hien Poh de National University of Singapore avec Samuel Forest à l'École des Mines de Paris et moi-même, un post-doctorant, Zhenpei Wang, a été recruté à NUS pour travailler sur l'optimisation topologique de matériaux architecturés cellulaires métalliques en élasticité et en plasticité compressible anisotrope, en se basant sur l'homogénéisation numérique par méthode des éléments finis et en ayant recours à des algorithmes d'optimisation méta-heuristiques. Dans la continuité de travaux entrepris depuis 2013, Zhenpei travaille en étroite collaboration avec moi. J'ai ainsi pu partir en mission à NUS en avril 2016. Septembre 2015-Décembre 2017.

Projet ALMARIS Le projet ALMARIS (Architecturation laser de matériaux superélastiques) est un projet de recherche collaboratif financé par l'ANR (à hauteur de 160k€ pour le PIMM), porté par l'ONERA (DMSM) et regroupant le Centre des Matériaux de MINES-ParisTech, le laboratoire PIMM, le LASMIS (UTT) et l'entreprise PolyShape. L'utilisation d'alliages à mémoire de forme dans le domaine aéronautique semble prometteuse pour diverses applications : la superélasticité pour des fonctions de dissipation d'énergie vibratoire, l'effet mémoire simple sens pour des absorbeurs de choc réutilisables, ou l'effet mémoire double sens pour des actionneurs de contrôle de la forme des voilures aéronautiques. Le principal frein d'intégration de ces alliages est la difficulté à les usiner dans des géométries complexes. Les procédés de fabrication additive offrent la possibilité de créer des géométries 3D de forme complexe d'un seul tenant, intégrant une architecture interne ainsi que des systèmes d'attache. Par ailleurs, à l'instar d'un stent, l'architecturation de la matière permet de créer des changements de formes d'amplitude non accessible avec un matériau dense. L'objectif de ce projet est donc de concevoir par voie SLM (Selective Laser Melting) des architectures modèles à grande amplitude de déformation en optimisant à la fois la forme et le matériau constitutif. Ma contribution au projet consiste à développer une modélisation constitutive adaptée, notamment avec une prise en compte de la superélasticité en vue d'une optimisation topologique des structures cellulaires envisagées. Financement ANR-16-CE08-0001. Janvier 2017-Décembre 2021.

C Responsabilités académiques

Représentant au conseil des formations du Cnam (collège B) depuis juin 2018

Représentant au conseil d'UMR (collège B) depuis janvier 2015

Reviewer pour les revues suivantes `https://publons.com/a/709704/` **:**

- *Advanced Engineering Materials*
- *ASME Journal of Engineering Materials and Technology*

— *Automation in Construction*
— *Composite Structures*
— *Computers & Structures*
— *Construction and Building Materials*
— *Engineering Fracture Mechanics*
— *Engineering Structures*
— *Finite Elements in Analysis and Design*
— *International Journal of Solids and Structures*
— *International Journal of Mechanical Sciences*
— *Materials*
— *Materials and Design*
— *Materials Today Communications*
— *Meccanica*
— *ZAMM - Zeitschrift für Angewandte Mathematik und Mechanik*

Membre des sociétés savantes suivantes :
— SF2M (2013-)
— Mécamat (2010-), représentant élu au CA de l'association depuis janvier 2016
— Euromech (2010-)

Participation aux groupes de travail suivants :
— GdR 3MF (Mécanique Multi-échelle des Milieux Fibreux) depuis janvier 2013
— GT Mécamat "Approches probabilistes en mécanique des matériaux" depuis mai 2010
— RNC (Réseaux Nationaux de Compétences) ENSAM : Fabrication Additive, Fatigue, et Matériaux Composites depuis janvier 2015

Participation aux comités de sélection suivants :
— MCF au CNAM (section 28/33) en 2014
— MCF à l'INSA Lyon (section 33/60) en 2016
— MCF au CNAM (section 28/33) en 2016

D Activités d'encadrement

Post-docs (5) :

5. Encadrement de **Federica ONGARO** (PhD, Queen's University London) sur la conception de matériaux architecturés pour applications spatiales (11/2017-11/2019), financement CNES
4. Encadrement de **Pierre LAPOUGE** (PhD, Univ. Grenoble) sur l'architecturation laser de tôles métalliques (06/2017-06/2019), projet ANR JCJC SCOLASTIC
3. Co-encadrement de **Zhenpei WANG** (PhD, TU Delft) avec Samuel Forest (MINES-ParisTech) et Leong Hien Poh (National University of Singapore) sur l'optimisation topologique de matériaux architecturés cellulaires métalliques (03/2016-09/2017), financement gouvernement singapourien
2. Co-encadrement de **Yilin ZHU** (PhD, Chengdu University) avec Samuel Forest (MINES-ParisTech) et Leong Hien Poh (National University of Singapore) sur l'homogénéisation numérique multi-échelle de milieux à longueurs internes (03/2016-09/2017), financement gouvernement singapourien
1. Co-encadrement de **Sébastien TURCAUD** (PhD, Grenoble-INP) en contrat de recherche au PIMM et au LMT-Cachan sur la mécanique des metamatériaux chiraux à coefficient de Poisson négatif (03/2015-09/2015), financement Coup de Pouce 2014, fédération francilienne de mécanique

Doctorants (5) :

5. Co-encadrement (70%) avec Samuel Forest (ENSMP, 30%) d'**Antoine-Emmanuel VIARD**, en thèse au PIMM sur le contrôle de la propagation d'instabilités par l'architecturation des matériaux (à partir de 09/2017), financement CDD CNRS 3 ans (projet ANR ALMARIS).

4. Co-encadrement (70%) avec Cyrille Sollogoub (30%) de **Frédéric ALBERTINI**, en thèse au PIMM sur la modélisation de structures micro-treillis hybrides pour applications d'amortissement (à partir de 09/2017), en collaboration avec Monash University (Australie), financement contrat doctoral spécifique normalien.
3. Co-encadrement (50%) avec Nicolas Ranc (50%) de **Shaobo YANG**, en thèse au PIMM sur la fatigue à très grand nombre du cuivre polycristallin (à partir de 10/2015), financement China Scholarship Council-ParisTech.
2. Co-encadrement (50%) avec Olivier Baverel (50%) de **Romain DUBALLET**, en thèse entre les laboratoires PIMM et Navier (Ponts-ParisTech) sur la fabrication additive à grande échelle de structures architecturées en béton (à partir de 10/2015), financement Chaire LafargeHolcim (Navier).
1. Co-encadrement (50%) avec Véronique Favier (50%) de **Noushin TORABIAN**, en thèse au laboratoire PIMM sur la fatigue à très grand nombre de cycles d'aciers dual-phase (11/2014-06/2017), financement bourse de thèse du gouvernement iranien.

Stages (14) :

14. Encadrement (100%) de **Frédéric ALBERTINI** (M2 MAGIS, ENS Paris-Saclay), en stage de fin d'études au laboratoire PIMM, sur l'architecturation laser de matériaux super-élastiques et optimisation topologique (02/2017-07/2017).
13. Encadrement (70%) de **Niki NOURI** (Double diplôme ENSAM-Karlsruhe Institute of Technology), en stage au laboratoire PIMM, sur l'architecturation de tôles métalliques par traitement laser localisé (02/2017-05/2017).
12. Encadrement (100%) de **Regina MUTZ** (M2 MAGIS, double diplôme ENSAM-Karlsruhe Institute of Technology), en stage de fin d'études au laboratoire PIMM, sur l'architecturation de tôles métalliques par traitement laser localisé et optimisation topologique (02/2016-08/2016).
11. Encadrement (70%) de **Antonios CHOLERIDIS** (M2 MAGIS), en stage de fin d'études au laboratoire PIMM, sur la caractérisation et la modélisation de la rupture dans les composites à matrice métallique (02/2015-08/2015).
10. Encadrement (100%) de **Yoann ANGILELLA** (M2 MSE Orsay), en stage de fin d'études au laboratoire PIMM, sur le développement d'un matériau architecturé photovoltaïque bioinspiré. (03/2014-09/2014).
9. Encadrement (100%) de **Guillaume LANGLET** (M2 MAMI), en stage de fin d'études au laboratoire PIMM sur l'élaboration par co-extrusion et la caractérisation microstructurale de fil composites pour la fabrication additive FDM. (02/2014-09/2014).
8. Encadrement (70%) de **Lucas CALLEN** (M2 MAGIS), en stage de fin d'études au laboratoire PIMM, sur la modélisation numérique d'agrégats polycristallins de cuivre et l'étude de l'impact de la microstructure sur la sensibilité à la vitesse de déformation effective dans le cas d'applications en fatigue (02/2014-08/2014).
7. Encadrement (100%) de **Paul DEFIEZ** (Double diplôme ENSAM-Karlsruhe Institute of Technology), en stage au laboratoire PIMM, sur la conception et l'optimisation topologique de matériaux cellulaires pour cœurs de structures sandwiches (02/2015-05/2015).
6. Encadrement (80%) de **Patrick MOLL** (Double diplôme ENSAM-Karlsruhe Institute of Technology), en stage au laboratoire PIMM, sur la modélisation numérique par morphologique mathématique de mélanges polymères PS-PMMA extrudés (02/2014-05/2014).
5. Encadrement (50%) de **Matthieu BERTEAUX** (Double diplôme ENSAM-Karlsruhe Institute of Technology), en stage au laboratoire PIMM, sur la caractérisation des propriétés mécaniques et rhéologiques de mélanges polymères PS-PMMA extrudés (02/2014-05/2014).
4. Encadrement (50%) de **Christoph HELLMANN** (Double diplôme ENSAM-Karlsruhe Institute of Technology), en stage au laboratoire PIMM, sur la conception d'une imprimante 3D à grande échelle basée sur un procédé d'extrusion de polymères (02/2014-05/2014).
3. Encadrement (50%) de **Jaqueline OLIVEIRA GOUVEIA** (Echange Brésil-CNAM, Equipe Systèmes Mécaniques), en stage au laboratoire PIMM, sur la fabrication et la caractérisation microstructurale de mélanges polymères PS-PMMA extrudés (01/2014-06/2014).
2. Encadrement (80%) de **Nadja GAUDILLIERE** (élève-architecte, ENSA Paris-Malaquais, en partenariat avec le laboratoire Navier, Ecole des Ponts-ParisTech), en stage au laboratoire PIMM, sur la conception et la fabrication par impression 3D de pièces d'assemblage pour structures légères de type gridshell (03/2014-07/2014).

1. Encadrement (60%) de **Nanjunda S. VELU** (BSc NITK, via le programme Campus France-Inde Georges Charpak), en stage au laboratoire PIMM sur l'étude des mélanges polymères PS-PMMA extrudés (05/2014-08/2014).

E Autres

Expert auprès du MENESR pour le crédit impôt recherche

Co-fondateur de l'entreprise XtreeE, spécialisée dans la fabrication additive à grande échelle

Conseiller scientifique auprès de XtreeE depuis décembre 2015

Organisation d'un atelier international sur les matériaux architecturés en mai 2012 à Paris

Organisation du colloque d'Aussois 2021 de l'association Mécamat sur la mécanique des matériaux architecturés

Participation à l'organisation de la conférence internationale ICMM2 à MINES-ParisTech en septembre 2011

Participation, au sein de l'agence d'architecture EZCT (Paris), à la réalisation d'un projet pour le concours international d'avant-garde architecturale *ArchiLab* organisé par le FRAC Centre, de mars à juillet 2013. L'œuvre fait aujourd'hui partie de la collection permanente du Centre National d'Art et de Culture Georges-Pompidou

SORBONNE UNIVERSITÉ

Vers une approche intégrée pour le développement des matériaux architecturés

Résumé: Les matériaux architecturés au sens d'Ashby et Bréchet sont obtenus par un processus de conception visant à remplir un cahier des charges spécifique à travers une fonctionnalité, un comportement ou une performance, induits par un arrangement morphologique particulier entre plusieurs phases. La plupart des matériaux architecturés ont été obtenus grâce à de bonnes idées d'ingénieurs et/ou par une approche empirique difficilement transférable à l'industrie. L'ambition du présent mémoire d'habilitation est de présenter des travaux œuvrant à définir une approche déterministe et systématique pour le développement de tels matériaux, par une compréhension du lien entre morphologie à différentes échelles et comportements effectifs. Plus spécifiquement, le lien entre procédés innovants et architecture des matériaux et des structures est exploré. Enfin, le dialogue raisonné entre caractérisation, modélisation et simulation numérique permet de proposer de nouvelles approches pour la conception de matériaux architecturés.

Mots-clés: matériaux architecturés ; mécanique des matériaux ; modélisation

Towards an integrated approach for the development of architectured materials

Abstract: Architectured materials, in the definition of Ashby and Bréchet, are obtained from a design process aiming at fulfilling a specific set of requirements through a given functionality, behaviour, or performance, induced via a particular morphological arrangement between multiple material phases. Most of the available architectured materials were obtained thanks to engineers' ideas and/or through an empirical trial-and-error approach, hardly transferable to the industry. The objective of the present habilitation is to present a synthesis of results aiming at defining a deterministic and systematic approach towards the development of such materials, via an understanding of the relation between morphology at multiple scales, and effective behaviours. Specifically, the relation between innovative processing and the architecture of materials and structures is explored. Finally, a dialogue between characterisation, modelling, and numerical simulation enables the proposal of new approaches for the design of architectured materials.

Keywords: architectured materials; mechanics of materials; modelling

HDR